

**INTERACTION EFFECTS IN HIGH-MOBILITY Si MOSFETs**  
**AT ULTRA-LOW TEMPERATURES**

by

NIKOLAI N. KLIMOV

A Dissertation submitted to the  
Graduate School-New Brunswick  
Rutgers, The State University of New Jersey  
in partial fulfillment of the requirements  
for the degree of  
Doctor of Philosophy  
Graduate Program in Physics and Astronomy  
written under the direction of  
Prof. Michael Gershenson  
and approved by

---

---

---

---

---

New Brunswick, New Jersey

October, 2008

# **ABSTRACT OF THE DISSERTATION**

## **Interaction effects in high-mobility Si MOSFETs at ultra-low temperatures**

**By Nikolai N. Klimov**

**Dissertation Directors: Michael Gershenson**

This dissertation focuses on the experimental study of the anomalous “metallic” behavior of the conductivity observed in high-mobility two-dimensional (2D) electron systems at low carrier densities ( $n$ ) and temperatures ( $T$ ). This intriguing phenomenon seems to defy one of the paradigms of our understanding of electron transport in 2D, the scaling theory of localization that claims that all electron states in 2D are localized. Our experimental object is the high-mobility silicon metal-insulator-oxide field effect transistor (Si MOSFET) in which this anomalous behavior is the most pronounced in comparison with other high-mobility devices.

We have explored in details the conductivity ( $\sigma$ ) in high-mobility Si MOSFETs over wide ranges of electron densities  $n = (2-30) \times 10^{11} \text{ cm}^{-2}$ , temperatures  $T = 30 \text{ mK} - 4 \text{ K}$ , and magnetic fields  $B = 0-5 \text{ T}$ . The low-temperature behavior of  $\sigma$  in these systems is shaped by the interaction effects, which are amplified by the valley degeneracy and the interaction-driven renormalization of electron parameters. While exploring the temperature and magnetic field dependences of  $\sigma$  far from the strongly localized regime ( $(\sigma \gg e^2/h)$ ), we observed for the first time the crossover between the “metallic” ( $d\sigma/dT < 1$ ) and “insulating” ( $d\sigma/dT > 1$ ) regimes with

lowering temperature below  $\sim 0.3$  K. We have attributed this crossover to the modification of the interaction correction to  $\sigma$  at low  $T$  caused by a non-zero valley splitting and inter-valley scattering. All relevant quantities have been measured in independent experiments. In particular, the intervalley scattering rate  $\tau_V^{-1}$  has been extracted from the analysis of weak localization magnetoresistance. We found that the intervalley scattering rate is temperature-independent and the ratio  $\tau_V/\tau$  increases monotonically with decreasing the electron density ( $\tau$  is the momentum relaxation time). These observations suggest that the roughness of the Si-SiO<sub>2</sub> interface plays the major role in intervalley scattering. The detailed analysis of the  $\sigma(T, B_{\parallel})$  data conducted with no adjustable parameters shows that the theory of interaction corrections to the conductivity of disordered systems adequately describes the experimental data at intermediate temperatures. At the same time, our data indicate that for better agreement with the experiment at low temperatures, the theory should take into account inter-valley scattering that strongly affect the interaction corrections in multi-valley systems.

## Acknowledgements

I would like to give the deepest gratitude to my adviser Professor Michael Gershenson. Thank you, Misha, for your careful and tactful guidance, for your enormous help over all 6 years of my studying at Rutgers University. I have learned a lot from you starting from different experimental techniques to how to approach to a given scientific problem. Inspiring discussions with you and your advices how to deal with the scientific problem outlined in this thesis helped tremendously in my work. I feel very honored and fortunate to be your student. It was a pleasure to work under your guidance.

I am very grateful to Professor Harry Kojima for great patience while teaching me cryogenic techniques and helping me to solve different experimental problems related to low-temperature experiment. All measurements in this dissertation were done on Harry's dilution refrigerator.

I deeply appreciate Professor Vladimir Pudalov's help, who have also guided me during my academic research. I also thank him for providing the unique high-mobility Si MOSFET samples, without which none of the work presented in this dissertation would be possible.

I thank the faculty members of my defense committee, Ron Ransome, Premi Chandra and Natan Andrei, for the contribution to my dissertation work, for valuable advices and suggestions during committee report meetings. I deeply thank Professor Sergey Vitkalov for being my external committee member. I appreciate my defense committee members for their time and effort in my study.



Many thanks to all members of Misha's laboratory who have helped me in different ways over the years: Sergey Pereverzev, Joshua Paramanandam, Eva Dupont-Ferrier, Sergey Gladchenko, David Olaya, Jian Wei.

I thank the faculty and staff members at Department of Physics and Astronomy helping me through my Ph.D. study.

I thank my friends for their help and encouragement, (Andrey Bayrashev, Andrei Malashevich, Evgeny Andriyash, Alexey Soluyanov, Viktor Oudovenko, Joni Gawlikowski, Antonina Toropova, and many others).

Especially I thank my parents, Nikolai Klimov and Galina Klimova, my sister, Anastasiya Klimova, and my wife, Daria Klimova, for their love, psychological support, and encouragement. Without them, this Ph.D dissertation would not be possible.

Thank you all for your participation in my Ph.D. study!

Nikolai

# Table of Content

<b>ABSTRACT OF THE DISSERTATION .....</b>	<b>ii</b>
<b>Acknowledgements .....</b>	<b>iv</b>
<b>List of Figures.....</b>	<b>xi</b>
<b>List of Abbreviations.....</b>	<b>xiv</b>
<b>1. Introduction.....</b>	<b>1</b>
1.1. Semiconductor electronics .....	1
1.2. Si Metal-Oxide-Semiconductor Field Effect Transistor .....	2
1.3. Anomalous “metallic” conductivity in high-mobility low-density Si MOSFETs .....	4
1.4. Theoretical approach to the problem of the “metallicity” in 2D .....	8
1.5. Summary of the results obtained in this dissertation .....	10
<b>2. Quantum effects in the conductivity of two-dimensional systems.....</b>	<b>18</b>
2.1. Non-interacting 2D electron systems.....	20
2.1.1. Weak localization .....	20
2.1.2. Scaling theory of localization.....	26
2.2. Interacting 2D electron systems.....	31
2.2.1. Wigner-Seitz radius, the role of interaction in 2D systems.....	31
2.2.2. Electron-electron interaction in the diffusive regime.....	34
2.2.3. Electron-electron interaction in the ballistic regime .....	37

2.2.4.	EEI in the crossover between the ballistic and diffusive regimes.....	38
2.2.5.	Interaction corrections to the conductivity within Zala-Narozhny-Aleiner theory .....	40
<b>3.</b>	<b>Metal Oxide Semiconductor Field Effect Transistor .....</b>	<b>47</b>
3.1.	Si MOSFET device .....	47
3.1.1.	Basic principles of operation of n-channel Si MOSFET.....	47
3.1.2.	Band structure of (001) Si MOSFET .....	51
3.2.	Transport properties of Si MOSFETs .....	54
3.2.1.	Low $\mu$ , high $n$ Si MOSFETs.....	54
3.2.2.	High $\mu$ , high $n$ Si MOSFETs .....	56
3.2.3.	High $\mu$ , low $n$ Si MOSFETs .....	59
<b>4.</b>	<b>Experimental technique.....</b>	<b>67</b>
4.1.	Experimental set-up .....	67
4.1.1.	Ruthenium oxide thermometer.....	68
4.1.2.	Cross-magnetic field technique.....	69
4.1.3.	Isolation of the experimental set-up from external electromagnetic noise (grounding and filtering).....	72
4.1.4.	Samples studied in this work.....	74
4.2.	Sample characterization .....	75
4.2.1.	Density of 2D electrons.....	76

4.2.2.	Temperature of 2D electrons .....	80
4.2.3.	Valley splitting in (001) Si MOSFET .....	82
<b>5.</b>	<b>Renormalization of electron parameters due to electron-electron interactions .....</b>	<b>84</b>
5.1.	Spin susceptibility .....	84
5.1.1.	$\chi^*$ from the analysis of SdH oscillations .....	86
5.1.2.	$\chi^*$ from measurement of the field of complete spin polarization .....	88
5.1.3.	$\chi^*$ from the analysis of magnetization .....	90
5.2.	Effective mass .....	90
5.3.	Renormalization of Landé g-factor and the FL parameter $F_0^\sigma$ .....	95
<b>6.</b>	<b>Experimental study of intervalley scattering time and WL in Si-based 2D structures .....</b>	<b>97</b>
6.1.	Introduction.....	97
6.2.	Experiment.....	98
6.3.	Fitting the data with Hikami-Larkin-Nagaoka theory .....	99
6.4.	Fitting the data with the ballistic theory .....	103
6.4.1.	Ballistic theory of WL corrections for a two-valley system..	103
6.4.2.	Data analysis using the ballistic theory .....	106
6.5.	Results and discussion .....	110
6.5.1.	Phase breaking time .....	110

6.5.2.	Prefactor $\alpha$ .....	112
6.5.3.	Intervalley scattering time: Independence of temperature ....	112
6.5.4.	Intervalley scattering time: density and sample dependence	114
6.5.5.	Analysis of possible errors in $\tau_v$ .....	115
6.6.	Conclusions.....	117
<b>7.</b>	<b>Experimental study of the low-temperature conductivity of high-<math>\mu</math> Si MOSFETs .....</b>	<b>119</b>
7.1.	Introduction.....	119
7.2.	Sample characterization and data analysis.....	120
7.2.1.	Samples characterization.....	120
7.2.2.	Temperature dependence of the conductivity at $B_{  }=0$ .....	123
7.2.3.	Temperature dependence of the conductivity at $B_{  } \neq 0$ .....	126
7.2.4.	Magnetoconductivity.....	128
7.2.5.	The $F_0^\sigma(\mathbf{n})$ dependence .....	130
7.3.	Conclusion .....	134
<b>8.</b>	<b>Quenched disorder effects in electron transport in Si MOSFETs in the dilute regime .....</b>	<b>136</b>
8.1.	Introduction.....	136
8.2.	Experiment.....	138
8.3.	Temperature dependence of resistivity for different cooldowns.....	138
8.4.	In-plane magnetoresistance for different cooldowns .....	142

8.5. Conclusions.....	148
<b>9. Summary.....</b>	<b>151</b>
<b>APPENDIX A (Shubnikov-de Haas oscillations) .....</b>	<b>155</b>
<b>APPENDIX B (ZNA theory) .....</b>	<b>162</b>
<b>APPENDIX C (WL theory for a two-valley system).....</b>	<b>165</b>
<b>References.....</b>	<b>168</b>
<b>Curriculum Vitae .....</b>	<b>177</b>

## List of Figures

1.1. The first point contact transistor .....	2
1.2. Intel 65 nm Si MOSFET.....	2
1.3. Schematic diagram of Si MOSFET .....	4
1.4. $\rho(T)$ of a high- $\mu$ Si MOSFET in a wide range of electron densities.....	6
1.5. $\rho(B_{\parallel})$ of a high- $\mu$ Si MOSFET and the suppression of the “metallicity” by $B_{\parallel}$ .....	7
1.6. Conductivity vs. temperature for Si MOSFET sample Si6-14. ....	12
1.7. Intervalley scattering time (density and temperature dependences). ....	13
1.8. Renormalization of Fermi-liquid parameter $F_0^{\sigma}$ in Si MOSFETs .....	14
1.9. Cooldown-specific $\rho(T)$ - dependences in the vicinity of 2D MIT .....	15
1.10. Cooldown-specific $\rho(B_{\parallel}^2)$ dependences in the vicinity of 2D MIT .....	15
1.11. Temperature dependences of the frequency of SdH oscillations.....	16
2.1. Mechanism of weak localization. ....	22
2.2. Magnetoresistance of thin Mg film for different temperatures.....	26
2.3. The wavefunctions of extended and localized states. ....	28
2.4. Schematic behavior of scaling function in different dimensions.....	30
2.5. Phase diagram for Si MOSFETs.....	33
2.6. Scattering by Friedel oscillation .....	41
2.7. Dimensionless $f(x)$ - and $t(x; F_0^{\sigma})$ - functions .....	42
2.8. EEI correction to the conductivity for a one-valley system.....	43
3.1. Principles of operation of Si MOSFET.....	48
3.2 Constant energy surfaces in $k$ space for silicon .....	52
3.3. $\rho(T)$ of low- $\mu$ Si MOSFETs at relatively high electron densities.....	55
3.4. WL magnetoconductance of Si MOSFETs.....	55

3.5. $\rho(T)$ of high- $\mu$ Si MOSFETs at relatively high electron densities.....	57
3.6. Resistivity vs. temperature of high- $\mu$ Si MOSFETs at relatively high $n$ .....	57
3.7. Conductivity vs temperature of of high- $\mu$ Si MOSFETs at relatively high $n$ .....	58
3.8. $\sigma(T)$ of high- $\mu$ Si MOSFET sample at high $n$ .....	59
3.9. Conductivity vs temperture of high- $\mu$ Si MOSFETs at low $n$ .....	60
3.10. 2D MIT and anoumalous “metallic” behavior in high- $\mu$ Si MOSFET .....	61
3.11. $\rho(T)$ of high- and low- disordered Si MOSFETs s .....	62
3.12. Strong in-plane magnetoresistance of high- $\mu$ Si MOSFET .....	63
3.13. Supression of the “metallicity” by in-plane magnetic field in Si MOSFET .....	65
4.1. Calibration curve of $RuO_2$ thermometer RO2254.....	69
4.2. Cross-magnetic field set-up. ....	70
4.3. Available range of magnetic fields $B_{  }$ and $B_{\perp}$ . In our experimental set-up .....	71
4.4. Magnetic field profiles for the split coil and the large solenoid .....	71
4.5. Filtering of wires connected to the Si MOSFET sample. ....	73
4.6. Hall bar geometry of our Si MOSFET samples.....	76
4.7. Sample charachterization: $n(V_g)$ .....	79
4.8. SdH oscillations for sample Si6-14 at different temperatures. ....	81
4.9. Temperature dependence of the amplitude of SdH oscillations .....	81
4.10. Estimation of valley splitting fror samples Si6-14 and Si1-46 .....	83
5.1. Renormalized spin susceptibility in Si MOSFETEs.....	85
5.2. Examples of fitting SdH oscillations using the LK theory .....	87
5.3. Renormalized effective mass in Si MOSFETs.. ....	91
5.4. Renormalized $\chi^*$ , $m^*$ , $g^*$ and $F_0^\sigma$ in Si MOSFEETs.....	96
6.1. Examples of WL MR for Si6-14, Si39, and Si40 Si MOSFET samples .....	101



6.2. Analysis of WL MC of Si40 Si MOSFET using HLN theory .....	102
6.3. WL correction for a two-valley system .....	105
6.4. Comparison between the WL MC for sample Si40 and the ballistic theory. ....	107
6.5. Errors of extracted $\tau_v/\tau$ -values from WL MC data.....	109
6.6. Temperature dependence of $\tau_\phi$ extracted from WL MC data.....	111
6.7. Temperature dependence of intervalley scattering time in Si MOSFETs .....	113
6.8. Density dependence of the intervalley scattering in Si MOSFETs.....	113
7.1. $\sigma(T, B_{  }=0)$ for the sample Si6-14 at various electron densities .....	124
7.2. $\sigma(T, B_{  }\neq 0)$ for the samples Si6-14 and Si1-46 at various electron densities. ....	127
7.3. $\rho(B_{  })$ for sample Si6-14 at different electron densities and temperatures.. ....	129
7.4. The $F_0^\sigma$ values obtained from the analysis of the $\sigma(T)$ and $\sigma(B_{  })$ . ....	131
8.1. Mobility of Si6-14 vs. the gate voltage for different cooldowns.....	140
8.2. Cooldown-specific $\rho(T)$ dependences of Si6-14 in the vicinity of 2D MIT .....	141
8.3. Difference between resistivity values for two different cooldowns vs. $T^{-1}$ .....	142
8.4. Cooldown-specific $\rho(B_{  }^2)$ dependences in the vicinity of 2D MIT. ....	144
8.5. Resistivity vs. in-plane magnetic field for different cooldowns .....	145
8.6. SdH oscillations for Si6-14: the shift of the frequency of oscillations with $T$ ....	146
8.7. Temperature dependences of the frequency of SdH oscillations.....	147
A1. Landau quantization in a perpendicular magnetic field .....	156
A2. Occupation of Landau levels in a $B_\perp$ .....	157
A3. Variation of Fermi level as a function of magnetic field for 2DEG. ....	158
A4. Zeeman splitting of Landau levels for spin up and spin down states .....	159
A5. Typical SdH oscillations for Si6-14 with and without $B_{  }$ .....	160

## List of Abbreviations

MOSFET	Metal-oxide-semiconductor field effect transistor
MIT	Metal-insulator transition
1D,2D,3D	One-, two- and three-dimensional
2DEG	Two-dimensional electron gas
EEI	Electron-electron interaction
MC	Magnetoconductance
MR	Magnetoresistance
NMR	Negative magnetoresistance
QC	Quantum corrections
SdH	Shubnikov-de Haas
WL	Weak localization
FL	Fermi-liquid
DoS	Density of states
RG	Renorm group
HLN	Hikami-Larkin-Nagaoka
ZNA	Zala-Narozhny-Aleiner
GM	Gornyi-Mirlin
LK	Lifshitz-Kosevich
$F_0^\sigma$	Fermi-liquid interaction parameter
$r_s$	Wigner-Seitz radius
$B$	Magnetic field
$B_{\parallel}$	In-plane magnetic field
$B_{\perp}$	Magnetic field normal to the plane of a 2D system
$D$	Diffusion constant
$l$	Mean free path
$L_B$	Magnetic length
$L_\varphi$	Phase coherence length
$v_F$	Fermi velocity

$k_F$	Fermi wavevector
$\lambda_F$	Fermi wavelength
$E_F$	Fermi energy
$\mu$	Electron mobility
$m_b$	Electron band mass
$m^*$	Electron effective mass
$g_b$	Bare factor Landé
$g^*$	Effective Landé g-factor
$\chi_b$	Band value of the spin susceptibility
$\chi^*$	Renormalized spin susceptibility
$E_{ee}$	Coulomb energy
$\tau$	Momentum relaxation time (mean free time)
$\tau_q$	Elastic quantum scattering time
$\tau_\varphi$	Phase relaxation time
$\tau_V$	Intervalley scattering time
$\Delta_V$	Valley splitting
$\sigma$	Electrical conductivity
$\sigma_D$	Drude conductivity
$\rho$	Electrical resistivity
$R_\square$	Resistance per square
$T_D$	Dingle temperature
$\Phi$	Magnetic flux
$\Phi_0$	Magnetic flux quantum
$E_Z$	Zeeman energy
$n$	Electron density
$n_c$	Critical density of the metal-insulator transition
$\mu_B$	Bohr magneton
$\omega_c$	Cyclotron frequency

# 1. Introduction

## 1.1. Semiconductor electronics

Today it is impossible to imagine our life without electronic devices. They are everywhere: televisions, VCRs, stereos, telephones, refrigerators, washers and dryers, microwave ovens, alarm systems, fax machines, not to mention a vast number of electronic devices used in the high-tech industry. Many people know that electronic circuits, or microchips, are underneath the fancy covers of these devices, but not everyone realizes that millions of tiny semiconductor devices, called transistors, are hidden from our eyes inside every microchip. A school textbook can give a definition of a transistor as follow: “Transistor is a tiny electronic device to control the flow of electricity. It has two key abilities: the first is to amplify an electric signal, and the second is to switch on or off (1 or 0), letting current through or blocking it as necessary.”

The first point-contact transistor was invented at Bell Telephones Laboratories in 1947 by William Shockley, John Bardeen and Walter Brattain.<sup>1</sup> Prior to the invention of the transistor the only alternative to current regulation and switching functions was a vacuum tube, which could only be miniaturized to a certain extent, and wasted a lot of energy in the form of heat. Figure 1.1 shows the first point-contact transistor. It consisted of germanium and gold contacts, held in place by a plastic frame. The transistor could amplify an electric current like a vacuum tube but its power consumption was very low. Later, William Shockley developed a *p-n* junction and a bipolar transistor,<sup>2</sup> which were both easier to understand theoretically and

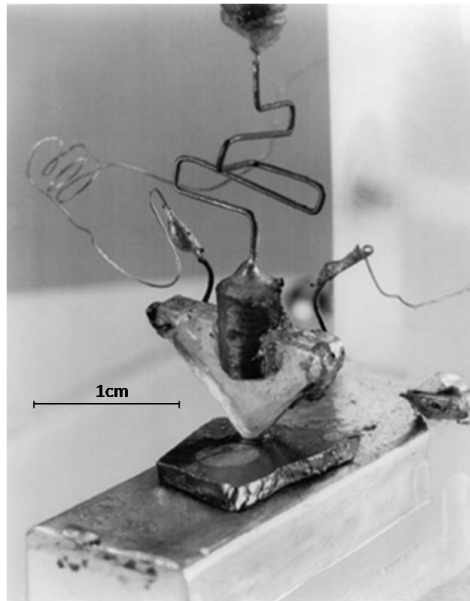


Figure 1.1. The first point contact transistor<sup>3</sup>, developed in 1947 by researchers at the US Bell Telephone Laboratories. (Adopted from Ref. 4)



Figure 1.2. Transmission electron micrograph of Intel 65 nm Si MOSFET. (Adopted from Ref. 5).

could be fabricated more reliably. The invention of the transistor was probably the most important discovery of the 20th century. This invention ignited a huge research effort in solid state electronics. Bardeen, Shockley and Brattain received the Nobel Prize in Physics, 1956, “for the research in semiconductors and a discovery of the transistor effect”. After the invention of bipolar transistor the number of semiconductor devices has increased tremendously. Today, semiconductor devices serve as a foundation as one of the largest industries in the world – the electronics industry.

## 1.2. Si Metal-Oxide-Semiconductor Field Effect Transistor

Since the discovery of the first transistor in 1947 its size has decreased dramatically. For example, a modern Intel Pentium IV processor has about 55 million transistors, which are fabricated using 160 nm technology. The smallest transistor

currently used in industry is 65 nm in length (Figure 1.2), which is about five orders of magnitude smaller than the very first transistor.

Among all electronic components in digital and analog circuits a Si metal–oxide–semiconductor field effect transistor, or Si MOSFET, is by far the most common transistor in use. A transistor is formed of  $p$ - or  $n$ -type semiconductor, an oxide layer, and a metal film deposited on top of the oxide [Figure 1.3(a)]. The MOSFET has also two additional terminals, the source (S) and the drain (D), which are connected to highly doped regions. Those regions have a type ( $p$ - or  $n$ -) opposite to the type of a bulk semiconductor, and serve as a source of charge carries. Two  $p$ - $n$  junctions facing each other, formed by the highly doped regions (located under the source and the drain terminals) and the bulk semiconductor, block an electrical current ( $I_{SD}$ ) between S and D when the device is “off”.

When a sufficient electric voltage  $V_g$  is applied between the gate and source terminals, the bottom of the conduction band  $E_C$  bends below the Fermi level  $E_F$  near the Si-SiO<sub>2</sub> interface and a triangular potential well is formed between the Si-SiO<sub>2</sub> interface and the conduction band [Figure 1.3(b)]. Electrons near the interface occupy the states with  $E_C < E < E_F$  in this potential well, forming the inversion layer. The energy spectrum of electrons in the well is quantized and consists of energy subbands. Within each subband, electrons can move freely only in the  $xy$ -plane parallel to the interface. At low temperatures and not-too-high electron densities, only the lowest subband is occupied, and a two-dimensional electron gas (2DEG) is formed. Thus, at  $V_g \geq V_{th}$ , where  $V_{th}$  is the threshold voltage, the source and the drain are connected by a conducting 2D inversion layer.

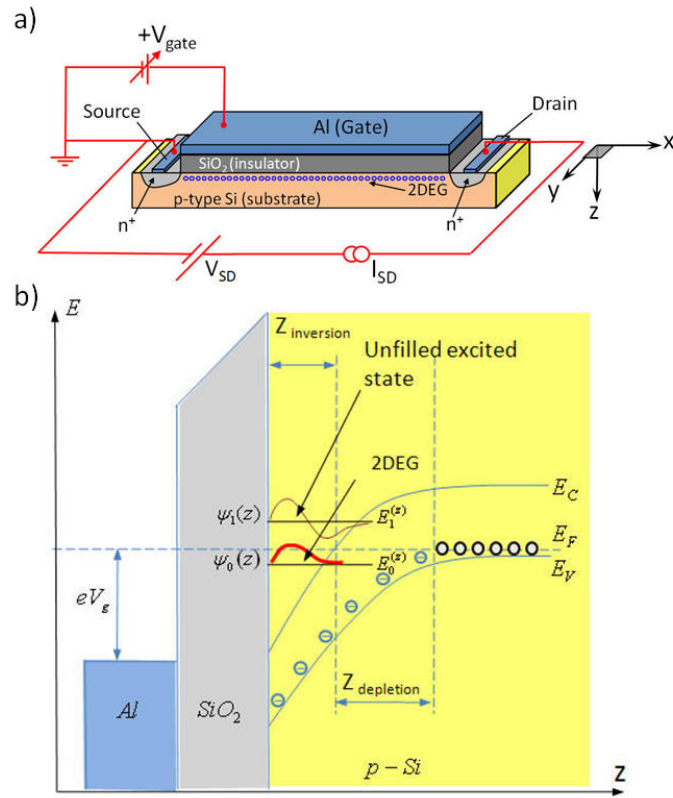


Figure 1.3. Si MOSFET: (a) schematic diagram; (b) band-edge diagram.

With applying an electrical field between the source and the drain, the current flows through this 2D layer. The concentration of charge carriers in the inversion layer is directly related to an applied gate voltage. Thus, by varying  $V_g$  it is possible to control continuously  $I_{SD}$ .<sup>a</sup>

### 1.3. Anomalous “metallic” conductivity in high-mobility low-density Si MOSFETs

Besides being the main building block of the modern electronic<sup>5</sup> industry, semiconductor devices are wonderful tools for studying low-dimensional physics. The

<sup>a</sup> A detailed description of the principles of operation of Si MOSFET will be presented in Sec. 3.1.

quantum phenomena discovered in two-dimensional (2D) carrier devices are fascinating. Despite their technological importance, some of the fundamental electronic properties of these 2D systems are not yet fully understood. Although people have been studying such devices for more than half a century,<sup>6</sup> Si MOSFETs bring many surprises.

According to the scaling theory of localization, which describes the flow of the dimensionless conductance  $g$  with the system size  $L$ ,<sup>7,8</sup> at  $T = 0$  all electron states are localized in 2D, and the ground state is an insulator. Depending on the degree of disorder the conductivity decreases either logarithmically (in the case of weak disorder), or exponentially (in the case of strong disorder) as temperature is decreased. A logarithmic decrease of the conductivity in 2D as  $T \rightarrow 0$  is governed jointly by two mechanisms: a quantum interference of electron wavefunctions propagating along loop-like trajectories in opposite directions, the weak localization effect (WL),<sup>7,8</sup> and an electron-electron interaction (EEI).<sup>9,10</sup> The localization behavior was experimentally observed in many low-mobility 2D systems (see for example Ref. 11) and was consistent with WL and EEI theories. This left no doubt in the validity of the scaling theory for the weakly interacting systems,<sup>7,8</sup> and the statement “there is no true metallic state, and, hence, there is no a metal-to-insulator transition (MIT) in 2D” was well accepted in the scientific community until the mid-1990s.

The progress in technology allowed the fabrication of Si MOSFETs with a very high mobility. These devices have shown an unexpected anomalous “metallic” behavior at low temperatures below  $T_F \equiv E_F / k_B$ : at relatively high electron densities the resistivity  $\rho$  of such devices *decreases* with cooling<sup>12,13</sup>. This decrease of the



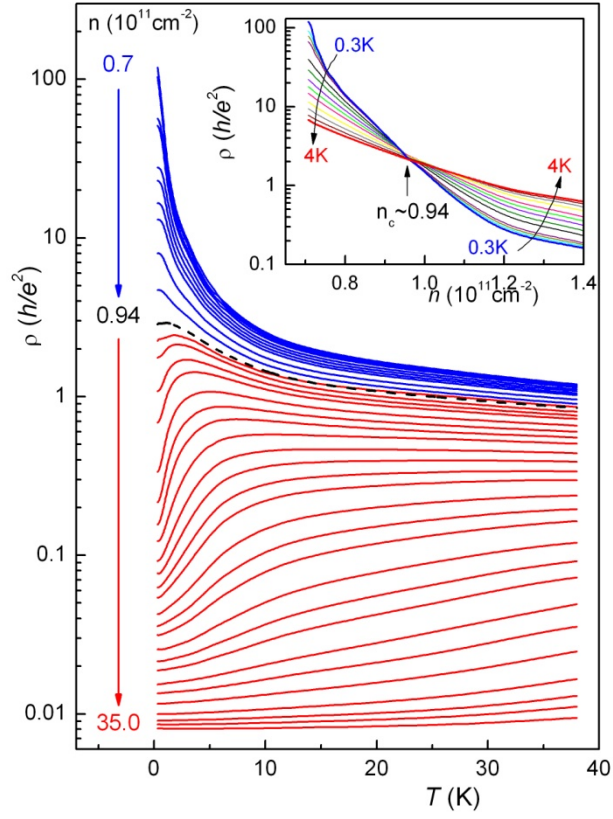


Figure 1.4. Temperature dependences of the resistivity of Si MOSFET for different electron densities ranging from  $0.707 \times 10^{11} \text{ cm}^{-2}$  to  $35 \times 10^{11} \text{ cm}^{-2}$ . The red curves correspond to the “metallic” regime ( $d\rho/dT > 0$ ), the blue curves correspond to the insulating regime ( $d\rho/dT < 0$ ). The dashed curve corresponds to a critical density range  $\delta n_c$ . The inset shows the resistivity as a function of electron density at different fixed temperatures ranging from 0.3 K to 0.4 K. (Adopted from Pudalov *et al.* circa 2000).

resistivity in dilute Si MOSFETs at some densities could be as large as a factor of 5-6 in magnitude<sup>12,13</sup>. It turned out that there exists a narrow critical density range  $\delta n_c$  (for high mobility Si MOSFETs this critical range lays between  $0.8 \times 10^{11} \text{ cm}^{-2}$  and  $1 \times 10^{11} \text{ cm}^{-2}$ ) such that with decreasing an electron density below  $\delta n_c$  the temperature dependence of  $\rho$  changes its sign from positive ( $d\rho/dT > 0$ , which corresponds to the metallic behavior) to negative ( $d\rho/dT < 0$ , which corresponds to

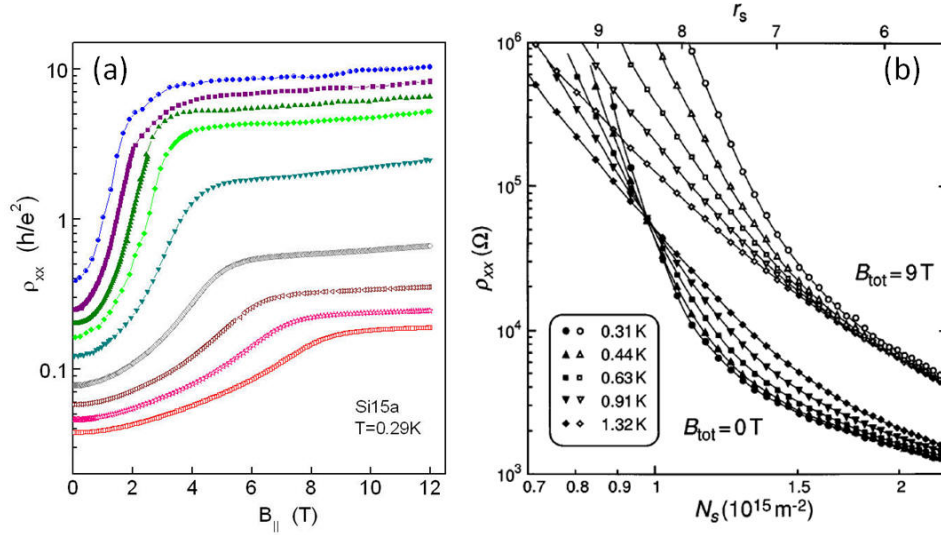


Figure 1.5. (a) In-plane magnetoresistance at  $T = 0.29 \text{ K}$  for a Si MOSFET with the peak mobility  $\mu_{\text{peak}} \approx 2 \text{ m}^2/\text{Vs}$ . Different symbols correspond to different electron densities varying from  $1.01 \times 10^{11} \text{ cm}^{-2}$  (the top curve) to  $2.17 \times 10^{11} \text{ cm}^{-2}$  (the bottom curve). (Adopted from Pudalov *et al.*<sup>15</sup>) (b) The longitudinal resistivity of a Si MOSFET ( $\mu_{\text{peak}} = 2.4 \text{ m}^2/\text{Vs}$ ) as a function of electron density at different temperatures. Closed and open symbols corresponds to  $B_{||} = 0$  and  $B_{||} = 9 \text{ T}$ , respectively. (Adopted from Okamoto *et al.*<sup>16</sup>)

the “insulating” behavior), thus showing the apparent 2D MIT. Typical temperature dependences for high-mobility Si MOSFET for different carrier densities are shown in Figure 1.4. Here the blue curves correspond to the “insulator” regime, whereas the red curves – to the metallic regime. A dashed curve corresponding to  $0.94 \times 10^{11} \text{ cm}^{-2}$  belongs to  $\delta n_c$ . The inset to Figure 1.4 shows the density dependence of the resistivity at several fixed temperatures. It is clear that the transition from  $d\rho/dT < 0$  to  $d\rho/dT > 0$  takes place in a narrow density range around  $n_c \approx 0.94 \times 10^{11} \text{ cm}^{-2}$ .

Another puzzle of 2D systems is their response to the in-plane magnetic field. It was found that an applied in-plane magnetic field causes an unexpected strong

magnetoresistance (MR) and suppresses the metallic behavior (Figure 1.5).<sup>14-19</sup> This observation indicated the importance of the spin effects.

The anomalous metallic behavior, the apparent MIT and the strong MR was later observed in practically all high mobility, low disorder, 2D systems in the low density regime.<sup>20-31</sup> The discovery of these phenomena defied a paradigm of the scientific community regarding the transport properties of 2D systems. It should be noted that the puzzle is the metallic behavior rather than the apparent MIT, since according the localization theory<sup>7</sup> there should be no metallic state in 2D. Although the metallic behavior was observed in many 2D systems, it is the most pronounced in high-mobility Si MOSFETs.

#### 1.4. Theoretical approach to the problem of the “metallicity” in 2D

EEI has always been the primary suspect in the metallic behavior of the conductivity in 2D. Indeed, as one goes deeper into the dilute regime (low  $n$ ) the energy of EEI  $E_{ee}$  becomes much larger than the Fermi energy  $E_F$ . The strength for unscreened Coulomb interactions between electrons can be characterized by the Wigner-Seitz parameter  $r_s$ , which is the average inter-electron spacing expressed in the Bohr radius  $a_B$ . The ratio of the energy of Coulomb interaction between two electrons at an average distance  $r_s a_B$  to their Fermi energy can be expressed in terms of  $r_s$ . In 2D  $r_s$  is equal to  $E_{ee}/E_F$  and varies with density as  $\propto 1/\sqrt{n}$ .<sup>6</sup> The metallic region in high-mobility Si MOSFETs corresponds to low electron densities ( $10^{11}$ - $10^{12}$  cm<sup>-2</sup>) and, hence, high  $r_s$  (varying from 2 to  $\sim 8$ ). This shows that EEI in Si MOSFETs are strong.

One of the first theories that described the EEI corrections to the conductivity of disordered 2D systems was developed by Altshuler and Aronov<sup>9</sup> and, later, Finkelstein<sup>10</sup>. The theory developed for weak interaction predicts a logarithmic *decrease* of  $\sigma(T)$  as  $T \rightarrow 0$  and is applicable only in the *diffusive* regime, corresponding to a condition  $T\tau \ll 1$ <sup>b</sup>, where  $\tau$  is the elastic scattering time. In contrast, at not-too-low temperatures almost linear *increase* of  $\sigma(T)$  with temperature cooling is observed in high-mobility 2D systems mostly in the *ballistic* regime, corresponding to a condition  $T\tau \gg 1$ <sup>b</sup>.

Early theoretical works, describing the metallic behavior of 2D systems in the ballistic regime, were developed by Stern,<sup>32</sup> Gold and Dolgoplov,<sup>33</sup> and Das Sarma<sup>34</sup>. The theories<sup>32-34</sup> explain the “metallicity” by considering the temperature-dependent screening of disorder by electrons, at relatively high temperatures ( $T\tau \gg 1$ ).<sup>c</sup>

In 2001 Zala, Narozhny and Aleiner<sup>35</sup> (ZNA) bridged the gap between the ballistic and the diffusive regimes. The theory considers the interference between electron waves, scattered back by the short-range scattering centers (this case is relevant to Si MOSFETs) and by the associated Friedel oscillations<sup>36</sup> of the electron density. Quantum corrections (QC) to the conductivity in the theory<sup>35</sup> are expressed in terms of the Fermi-liquid (FL) interaction parameter  $F_0^\sigma$  for an arbitrary value of  $T\tau$  ( $T \ll E_F$ ). Later Gornyi and Mirlin<sup>37</sup> extended the ZNA theory<sup>35</sup> for the case of a long-range scattering potential.

The temperature and magnetic behavior of the conductivity is affected by material-dependent details of a given structure, which is used for forming a 2D

---

<sup>b</sup> Here and below we set  $k_B = \hbar = 1$ .

<sup>c</sup> For high-mobility Si MOSFETs this corresponds to  $T \geq 0.5$  K.

electron or hole system. In particular, the transport properties of 2DEG in Si MOSFET is influenced by the band structure of Si. Although the conduction band of Si consists of six valleys, only two of them with major axes perpendicular to the (001) surface are relevant to an electron transport in (001) Si MOSFETs at ultralow temperatures and low carrier densities.<sup>6</sup> These two valleys strongly enhance the metallic behavior of  $\sigma(T)$  in Si MOSFETs compared to other 2D systems, where only one valley is present.<sup>38</sup> In actual inversion layers: the valleys are split with an energy splitting  $\Delta_V$ . Besides valley splitting, there exists intervalley scattering between the two valleys, which also influences the behavior of the conductivity in Si MOSFETs: at temperatures comparable to the intervalley scattering rate  $\tau_V^{-1}$  a crossover occurs between a band with two distinct valleys and a band where these two valleys are effectively unified due to intervalley scattering. The values of  $\Delta_V$  and  $\tau_V$  set the boundaries between regions, where the effect of valley splitting and intervalley scattering on  $\sigma(T)$  should be taken into account ( $T \ll \Delta_V, \tau_V^{-1}$ ), and where this effect can be neglected ( $T \gg \Delta_V, \tau_V^{-1}$ ). Thus, it is important to know the values of  $\Delta_V$  and  $\tau_V$ .

### 1.5. Summary of the results obtained in this dissertation

The aim of this work is to study the quantum effects in the transport properties of strongly-correlated disordered 2D systems, with a focus on a better understanding of the anomalous metallic conductivity observed in high-mobility Si MOSFETs. The relevant range of study of the anomalous metallicity corresponds to (i) low electron densities ( $n = (2-30) \times 10^{11} \text{ cm}^{-2}$ ), not too close to the critical density of the apparent 2D MIT, where the conductivity is relatively high ( $\sigma \gg e^2/h$ ), whereas QC are

small, compared to  $\sigma$ ; (ii) a wide temperature range ( $T = 30 \text{ mK} - 4 \text{ K}$ ) which is much lower than Fermi energy, but includes both the diffusive ( $T\tau \ll 1$ ) and the ballistic ( $T\tau \gg 1$ ) regimes, and (iii) a wide range of magnetic field ( $B_{\parallel} = 0 - 5 \text{ T}$ ) which is lower than the field of complete spin polarization ( $B_{pol} = 2E_F / g\mu_B$ , here  $g$  and  $\mu_B$  are Landé g-factor and the Bohr magneton, respectively). Within these ranges of parameters ( $\sigma \gg e^2 / h$ ,  $\Delta\sigma \ll \sigma$ ,  $n \gg n_c$ ,  $\{T, g\mu_B B / 2\} \ll E_F$ ), the experimentally measured conductivity can be compared with the theoretical prediction<sup>35</sup>.

We have measured the temperature and the magnetic field dependence of the conductivity in the metallic regime.<sup>40</sup> Extending the experimental temperature down to 30 mK allowed us to observe a nonmonotonic behavior of the conductivity at millikelvin temperatures (Figure 1.6) (prior to this result a saturation of  $\sigma(T)$  was observed at the lowest  $T$  most likely due to overheating of 2DEG by external noise).

To compare our results with the ZNA theory<sup>35</sup> we measured the parameters that are relevant in low-temperature electron transport in independent experiments, in particular, we have measured the intervalley scattering rate<sup>39</sup> and valley splitting<sup>40</sup> in Si MOSFETs.

The intervalley scattering plays an important role in the low-temperature phenomena in Si MOSFETs: it may determine the low-temperature cut-off of the metallic-like transport and could also modify 2D MIT in these structures. However, the systematic studies of the intervalley scattering in Si MOSFETs were missing until

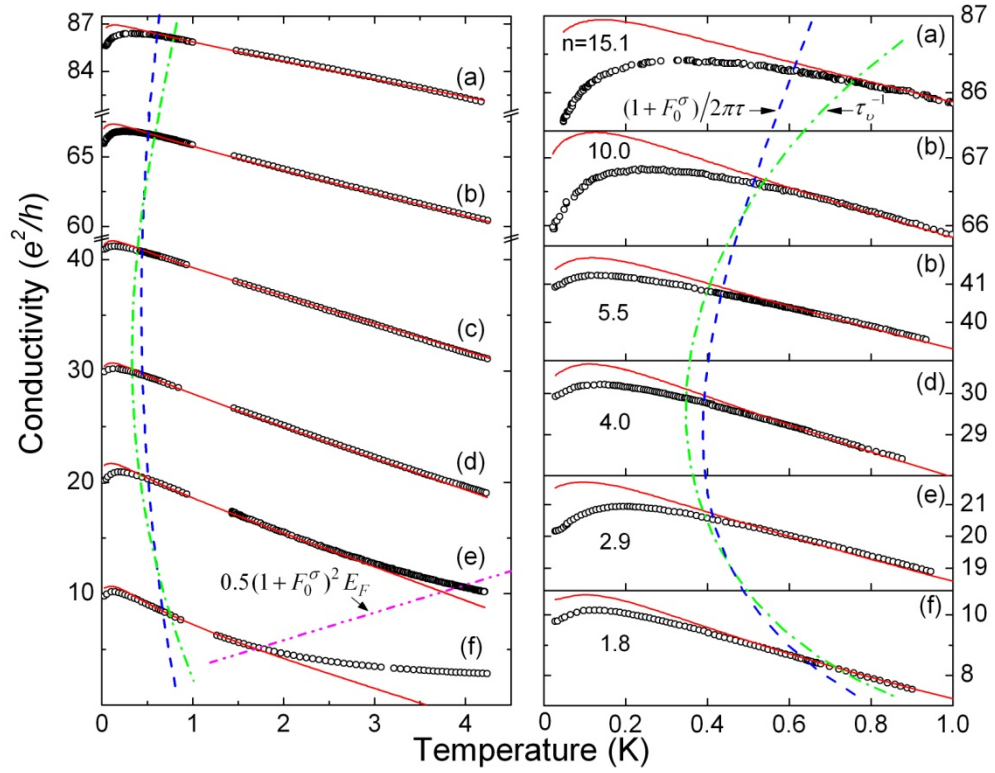


Figure 1.6. Temperature dependences of conductivity  $\sigma(T, B_{\parallel} = 0)$  for the Si MOSFET sample Si6-14 at various electron densities  $n = 15.1, 10.0, 5.5, 4.0, 2.9, 1.8$ , in units of  $10^{11} \text{ cm}^{-2}$ , from top to bottom. Circles show the experimental data, red curves - the theoretical fits with the ZNA theory. The dashed blue curve corresponds to the temperature of the crossover between ballistic and diffusive regimes,  $T^* = (1 + F_0^\sigma)/2\pi\tau$ . The dash-dot green curve corresponds to  $T = \tau_V^{-1}$ . On the left panel the dashed-dot-dot line corresponds to  $T = 0.5(1 + F_0^\sigma)^2 E_F$ , the applicability of the ZNA theory is violated at a higher  $T$ . The right panel shows the same data set within a narrower temperature interval.

recently<sup>39</sup>. We studied in details the intervalley scattering rate in Si MOSFET samples with different mobilities. Our experiments have shown that (i) the intervalley scattering is an elastic and temperature independent process, (ii) the intervalley scattering time  $\tau_V$  measured in units of transport time  $\tau$  increase monotonically as the electron density decreases (this observation suggests that the intervalley scattering is governed by the disorder at the Si-SiO<sub>2</sub> interface); and (iii) there is no simple

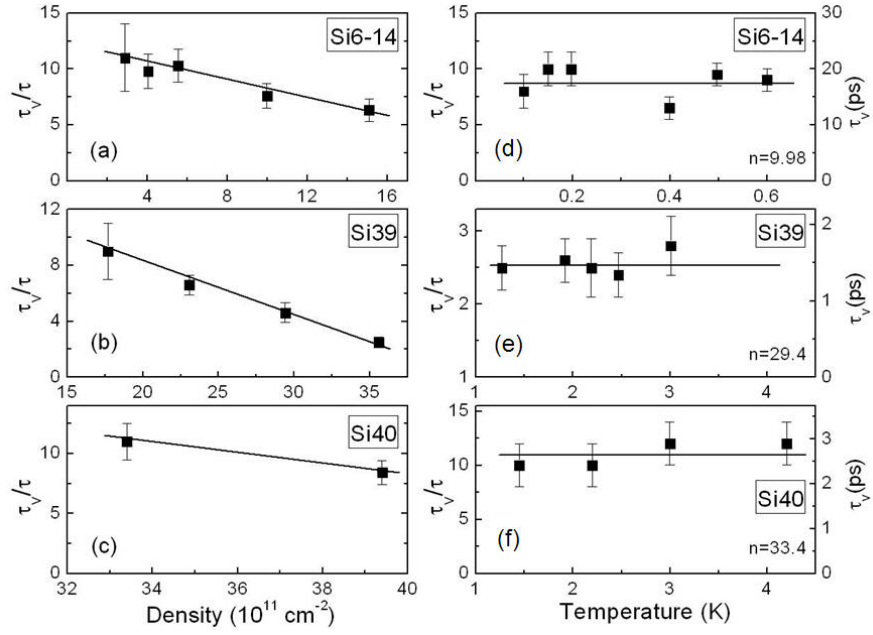


Figure 1.7.(a-c) Intervalley scattering time (averaged over temperature) for samples Si6-14, Si39, Si40. (d-f) Temperature dependence of  $\tau_V$  in units of  $\tau$  (left axes) and in picoseconds (right axes) for samples Si6-14, Si39, Si40. The densities are given in unit of  $10^{11} \text{ cm}^{-2}$ . Solid horizontal lines show the average  $\tau_V$ .

correlation between the intervalley scattering rate and the sample mobility. The latter observation points to a sample-specific rather than universal mechanism of the intervalley scattering (Figure 1.7).

The intervalley scattering rate  $\tau_V^{-1}$  measured in our Si MOSFET samples coincides with the temperature of the crossover (0.35 K to 0.7 K) from the ballistic to the diffusive regime (Figure 1.6). Thus, the intervalley scattering can affect the electron transport in the diffusive regime, and should be taken into account in comparison with the theory.

We estimated the valley splitting from the analysis of Shubnikov-de Haas (SdH) oscillations<sup>40</sup>; it turned out that its value is sample-dependent and, similar to the



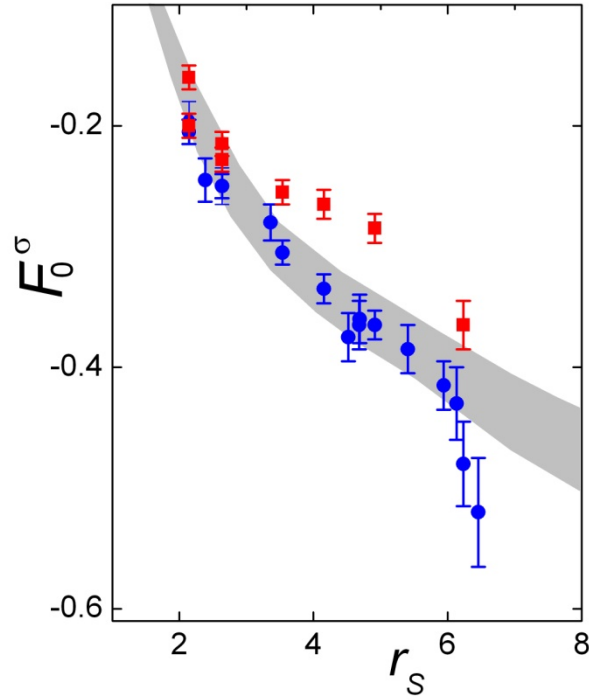


Figure 1.8. Renormalization of Fermi-liquid parameter  $F_0^\sigma$  in n-channel (001) Si MOSFETs. Circles and squares depict the  $F_0^\sigma$  values obtained from fitting the  $\sigma(T)$  and  $\sigma(B_{\parallel})$  dependences, respectively, with the ZNA theory<sup>35</sup>. The shaded region shows the  $F_0^\sigma(r_S)$  dependence (with the experimental uncertainty) extracted from the SdH data<sup>41</sup>.

intervalley scattering rate, is of the same order of magnitude as the temperature corresponding to the ballistic-diffusive crossover, what outlines the importance of taking  $\Delta_V$  into consideration in the analysis of  $\sigma(T, B)$  data.

We have compared our data with ZNA theory<sup>35</sup> and conclude that the metallic increase of  $\sigma$  with cooling, observed in the ballistic regime, as well as the downturn of  $\sigma(T)$  at low temperatures, are in-line with the theoretical predictions<sup>35</sup> and can be accounted for by the interaction effects in the electron liquid. However, for a quantitative analysis, especially at ultra-low temperatures, the thorough theory should

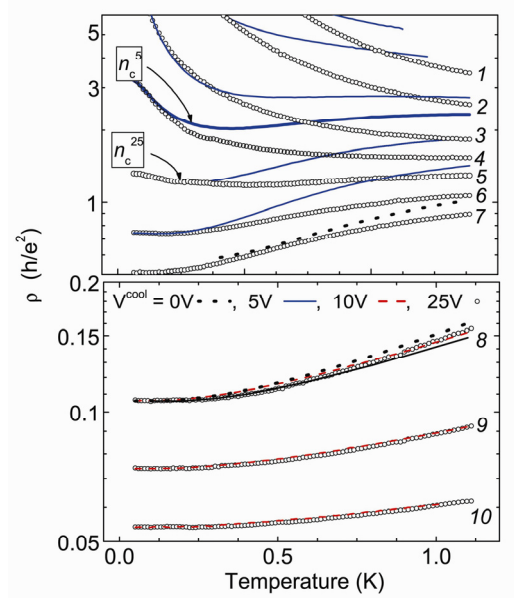


Figure 1.9. Temperature dependence of the resistivity for four different cooldowns. The densities, which correspond to curves 1 to 10, are as follow: 0.827, 0.0882, 0.942, 0.972, 1.00, 1.038, 1.07, 1.18, 1.31, 1.53 in units of  $10^{11}\text{cm}^{-2}$ .  $n_c^5$  and  $n_c^{25}$  mark two critical dependences for cooldowns at  $V_g = 5$  and  $25$  V, respectively.

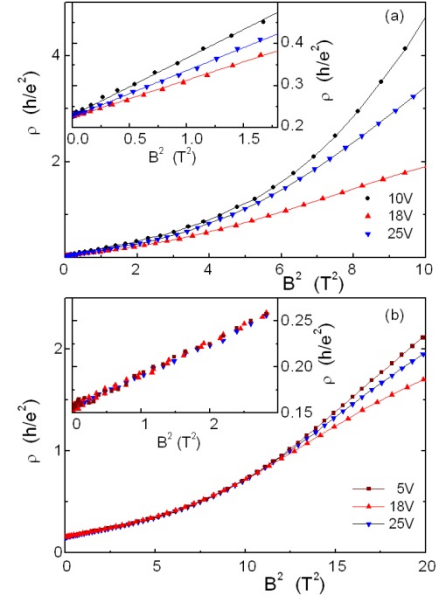


Figure 1.10. Examples of the dependences  $\rho(B_{\parallel}^2)$  at  $T = 0.3\text{K}$  for carrier density  $1.20 \times 10^{11}\text{cm}^{-2}$  (a) and  $1.34 \times 10^{11}\text{cm}^{-2}$  (b). The insets blow up the low-field region of the quadratic behavior. The values of  $V^{\text{cool}}$  are indicated for each curve.

take into account the finite intervalley scattering rate. Our observation suggests that the anomalous metallic conduction in 2D, at least for densities not-too-close to the critical density, is the finite-temperature phenomenon rather than a signature of a new ground state.

The  $F_0^\sigma$  values, obtained from the fitting  $\sigma(T, B)$ <sup>40</sup> with the ZNA theory<sup>35</sup>, are consistent with those obtained in independent measurements of SdH oscillations<sup>41</sup> in Si MOSFET samples (Figure 1.8).

In addition to the study of anomalous metallicity not-too-close to the apparent

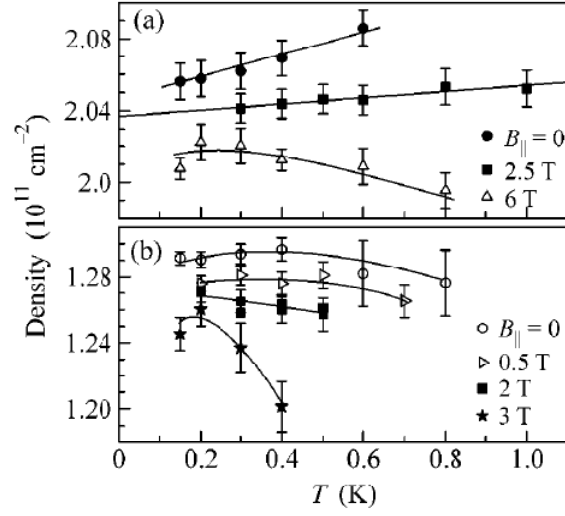


Figure 1.11. Temperature dependences of the frequency of SdH oscillations at two fixed values of the gate voltage. The different curves within each panel are shifted in  $y$ -axis for clarity.

2D MIT, we have explored the universality of the temperature and magnetic dependences of the resistivity in its vicinity of the MIT. In particular we studied the electron transport in the same Si MOSFET device after cooling it down to 4K at different fixed values of the gate voltage  $V^{\text{cool}}$ . We believe that this allows us to vary fine details of disorder – the structure of the resonant (localized) states – without affecting the type of disorder (the short-ranged), the scattering rate, and the strength of EEI in the system of mobile electrons.<sup>d</sup>

We have found that in the vicinity of the MIT ( $\rho \sim h/e^2$ ), the cooldown specific effects strongly affect  $\rho(T)$  (Figure 1.9); these effects vanish only when  $\rho$  is decreased below  $\sim 0.1h/e^2$  with increasing electron density.

---

<sup>d</sup> We have verified that both electron mobility (and thus the elastic scattering time), as well as the renormalization of the electron spin susceptibility and effective mass (and thus two Fermi-liquid coupling parameters) do not change for different cooldowns to within 5%. This indicated that EEI is not affected by different  $V^{\text{cool}}$ .

The non-universal behavior is also observed in in-plane magnetic fields  $B_{\parallel}$  at not too high electron densities (Figure 1.10). The effect of disorder on magnetoresistance becomes more pronounced as  $B_{\parallel}$  is increased and/or the electron density is decreased and approaches the critical density  $n_c$  of the 2D MIT.

We have also observed that the frequency of the weak field SdH oscillations varies with temperature and in-plane magnetic field (Figure 1.11); these variations grow as the density approaches  $n_c$ .

The observed temperature variation of the frequency of SdH oscillations demonstrates a weak exchange in electrons between the reservoirs of mobile electrons and resonant localized states. The large changes of  $\rho(T)$  at elevated temperature signify the development of a spatial inhomogeneity of the 2D system, which may result from either EEI or disorder. Our observation provides direct experimental evidence that near the 2D MIT the electron transport at finite temperatures in dilute systems becomes sample-specific and dependent on more subtle details of disorder.

## 2. Quantum effects in the conductivity of two-dimensional systems

At low temperatures, the “residual” resistance (i.e. classical resistance that does not take into account quantum effects) of disordered conductors (normal metals and strongly-doped (degenerate) semiconductors) is mostly determined by elastic scattering of electron from quenched disorder (impurities and defects). The elastic scattering from disorder is characterized by an average time between collisions - the transport elastic mean free time  $\tau$ . The residual conductivity in the case of weak disorder can be derived from the standard Fermi-liquid approach and the Boltzmann theory, and is given by the well known Drude formula:

$$\sigma_D = \frac{e^2 n \tau}{m}, \quad (2.1)$$

where  $v_F$  is a Fermi velocity,  $m$  and  $n$  denote electron effective mass and density, respectively. Taking into account that in 2D the diffusion constant  $D$  and the density of states at the Fermi level  $\nu$  have the forms  $D = v_F^2 \tau / 2$  and  $\nu = g_s g_v m / 2\pi \hbar^2$ , respectively (here  $g_s$  and  $g_v$  are the spin and valley degeneracy, respectively), the expression (2.1) in the case of 2D can be rewritten as follow:

$$\sigma_D = e^2 \nu D = G_0 g_v \pi k_F l, \quad (2.2)$$

here  $G_0 = e^2 / 2\pi^2 \hbar$ ,  $k_F = (4 / g_s g_v)^{1/2} \sqrt{\pi n}$  is the Fermi wavevector in 2D, and  $l = v_F \tau$  is the mean free path.

Different quantum effects modify the Drude result (2.1) by adding quantum corrections to the conductivity.<sup>9</sup> Conventional theories of quantum corrections are developed for the case when the Fermi wavelength  $\lambda_F = 2\pi / k_F$  is much smaller than

the mean free path  $l$ , or equivalently,  $k_F l \gg 1$ . Under this condition the QC are much smaller than  $\sigma_D$ . Even when QC are small, they determine all the temperature and magnetic field dependences of the conductivity at low temperatures.

According to their physical origin, QC can be divided into two distinct groups.<sup>9</sup> Both types of QC increase with decreasing temperature and/or increasing disorder and largely determine the low temperature transport in 2D systems. The first type of QC, known as the weak localization (WL) correction, is a single electron effect, which is caused by the quantum interference of electron wavefunctions propagating along a loop-like trajectory in opposite directions. For 2D systems without spin-spin and spin-orbit scattering, the WL QC is negative and logarithmically diverges as  $T \rightarrow 0$ . This divergence can be regularized either by a magnetic field, external high-frequency electromagnetic radiation, or by some other  $T$ -independent dephasing mechanism. At low  $T$ , electron-electron collisions govern the phase coherence (also known as phase relaxation, dephasing, or decoherence) time  $\tau_\phi$ , the characteristic time over which the phase coherence of electron wavefunction is preserved. The second type of QC, known as electron-electron interaction corrections, is determined by the interaction between electrons in the presence of disorder. The EEI can be interpreted<sup>35</sup> as interference between electron waves backscattered by single impurities and by Friedel oscillations<sup>36</sup> (oscillating inhomogeneous distribution of an electron density) induced by these impurities around themselves. These two types of QC can be separated from each other experimentally using the measurements in a magnetic field. EEI contributes to the longitudinal conductivity  $\sigma_{xx}$  only,<sup>9</sup> and this contribution does not depend on a magnetic field at  $g_b \mu_B B < T$  (here  $g_b$  and  $\mu_B$  are the band value of Landé  $g$ -factor and Bohr magneton, respectively), whereas the WL correction has a

sharp specific dependence in classically weak magnetic fields. The Hall resistivity  $\rho_{xy}$  is another quantity that helps separate experimentally the WL and interaction effects. In particular, there is no WL correction to the Hall resistivity<sup>42</sup>, whereas the interaction theory<sup>9</sup> predicts that  $\delta\rho_{xy}/\rho_{xy} = -2\delta\sigma_{xx}/\sigma_{xx}$ , since EEI does not contribute to  $\delta\sigma_{xy}$  (here  $\delta\sigma_{xx}$  is the EEI correction to the longitudinal conductivity  $\sigma_{xx}$ ).

## 2.1. Non-interacting 2D electron systems

### 2.1.1. Weak localization

There are two types of elementary scattering events, elastic and inelastic. In the case of elastic scattering, an electron conserves its energy, and, hence, a phase coherence of its wavefunction before and after a scattering event. Other than elastic processes, there exists inelastic scattering, e.g., collisions of electrons with phonons or other electrons. In such processes, in each scattering event an electron changes its energy, and, as a result, "forgets" about its quantum state over a phase coherence time  $\tau_\varphi$ . At low temperatures in the absence of magnetic impurities, the main source of inelastic scattering is the Coulomb electron-electron interaction. The characteristic length scale  $L_\varphi$  over which an electron loses the coherence of its wavefunction, is given by

$$L_\varphi = \sqrt{D\tau_\varphi} \approx l\sqrt{\tau_\varphi/\tau}. \quad (2.3)$$

If not limited by scattering from magnetic impurities, the phase coherence time is typically proportional to some power of temperature:

$$\tau_\varphi \propto T^{-P}. \quad (2.4)$$

The power  $p$  in Eq. (2.4) depends on the scattering mechanism, determined by the temperature range and the degree of disorder. Accordingly, the phase coherence length depends on  $T$  as

$$L_\phi \propto T^{-p/2}. \quad (2.5)$$

The WL QC is introduced under the condition that electrons move diffusively between the acts of inelastic scattering:

$$\tau_\phi \gg \tau \text{ or } L_\phi \gg l. \quad (2.6)$$

A qualitative physical interpretation of WL is given by the following argument. Consider an electron that moves diffusively in a good conductor ( $k_F l \gg 1$ ). The total probability for a transfer from  $A$  to  $B$  is determined by a squared modulus of the sum of all amplitudes  $A_i$  of the probability for an electron to pass along all possible paths, connecting points  $A$  and  $B$ :

$$w_{AB} = \left| \sum_i A_i \right|^2 = \sum_i |A_i|^2 + \sum_{i \neq j} A_i A_j^*. \quad (2.7)$$

The first sum in the right-hand part of Eq. (2.7) corresponds to the classical diffusion probability, whereas the second describes the quantum interference. For most paths, the interference is not essential, since their lengths differ strongly, and, hence, the corresponding phases of wave function differ substantially on these paths. As a result, after summing over all such paths, the interference term will vanish because of its oscillation nature. There are, however, paths of specific kind, namely, self-intersecting paths (Figure 2.1). Each such path can be assigned a pair of coherent amplitudes,  $A^+$  and  $A^-$ , corresponding to the passage of the loop clock- and counterclockwise. For a self-intersecting path, the probability of finding an electron at some intermediate point  $O$  is twice the classical result:



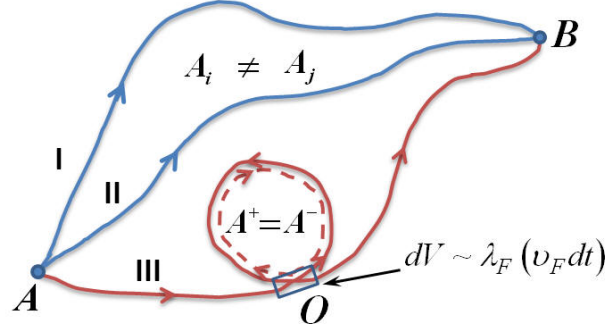


Figure 2.1. Mechanism of weak localization. The rectangular area depicts the phase volume  $dV$ , within which two reverse paths  $A^+$  and  $A^-$  meet.

$$|A^+ + A^-|^2 = |A^+|^2 + |A^-|^2 + 2 \operatorname{Re} A^+ A^- = 4 |A^\pm|^2. \quad (2.8)$$

On the other hand, the enhancement of the probability of finding an electron at point  $O$ , reduces the probability of finding a particle at point  $B$  (the point of observation). This mechanism reduces the diffusion constant and, hence, the conductivity.

An explicit form of the interference quantum correction to the conductivity was obtained by Gor'kov, Larkin and Khmel'nitskii<sup>43</sup> by summing the singular backscattering terms of the perturbation expansion in powers of the impurity concentration. The WL correction is small compared to Drude conductivity in the region of applicability of the perturbation theory:

$$\Delta\sigma_{WL} \ll \sigma_D. \quad (2.9)$$

Without going into details of the perturbation theory, the magnitude of WL QC can be estimated in the following way. Suppose that an electron moves diffusively with the mean free time  $\tau$  and the diffusion coefficient  $D$ . Over a time interval  $t \gg \tau$  an electron will move over a distance

$$L \simeq \sqrt{Dt}. \quad (2.10)$$

Starting from a point  $O$  an electron will return over time  $t$  to the phase volume  $dV$  around the starting point  $O$  (Figure 2.1) with the probability

$$dP = \frac{dV}{(\sqrt{Dt})^2}. \quad (2.11)$$

For the interference between two reverse paths  $A^+$  and  $A^-$  to be effective, the phase volume  $dV$  should be of the order  $\lambda_F(\nu_F dt)$ . To get a WL QC we need to sum over all self-intersecting trajectories:

$$\frac{\delta\sigma}{\sigma} \simeq -\int dP \simeq -\int_{\tau}^{\tau_{\phi}} \frac{\lambda_F \nu_F dt}{Dt}. \quad (2.12)$$

The integration in Eq. (2.12) should be done from the minimum time necessary for an electron to return to the origin  $O$  (the elastic scattering time  $\tau$ ) to the phase coherence time  $\tau_{\phi}$ .

After the integration, QC has the form:

$$\Delta\sigma_{WL} = -G_0 \ln \frac{\tau_{\phi}}{\tau} = -2G_0 \ln \frac{L_{\phi}}{l}. \quad (2.13)$$

$L_{\phi}$  and  $l$  appear as natural cutoffs for the size of closed electrons path when summing over all closed paths corresponding to a coherent electron propagation. According to Eqs. (2.4, 2.5, 2.13), the WL correction depends logarithmically on  $T\tau$  and diverges as  $T \rightarrow 0$ :

$$\Delta\sigma_{WL} \propto G_0 \ln(T\tau), \quad (2.14)$$

The WL correction is negative  $\Delta\sigma_{WL} < 0$  and diverges (decreases) with cooling.

It should be noted that for an actual high-mobility sample the phase coherence length  $L_{\phi}$  with decreasing temperature can become greater than the sample size  $L$ .

As a result the upper cutoff in Eq. (2.13) is given by  $L$  (as soon as  $L_\varphi > L$ ) and the WL QC does not depend on temperature.

### Effect of a magnetic field on weak localization

An application of a weak magnetic field  $B$ , normal to the plane of a 2D system, suppresses the WL correction. This occurs due to the breaking of the time reversal symmetry – a magnetic field  $B$  introduces a phase difference between clock- and counterclockwise paths along a loop-like trajectory:

$$\begin{aligned}\Delta\varphi &= \frac{1}{\hbar} \oint d\vec{r}_1 (\vec{p}_1 + \frac{e}{c} \vec{A}) - \frac{1}{\hbar} \oint d\vec{r}_2 (\vec{p}_2 + \frac{e}{c} \vec{A}) \\ &= \frac{2e}{\hbar c} \oint \vec{A} d\vec{r}_1 = 2\pi \frac{\Phi}{\Phi_0},\end{aligned}\tag{2.15}$$

where  $\Phi$  is a magnetic flux that threads a loop, and  $\Phi_0 = hc / 2e$  is a magnetic flux quantum. Since a magnetic flux threading a loop with a transverse dimension  $L$  is of an order of  $\Phi \simeq BL^2$ , the Eq. (2.15) can be written as

$$\Delta\varphi(B, L) \simeq 2\pi \frac{BL^2}{\Phi_0}.\tag{2.16}$$

Equation (2.16) shows that the phase difference of the order  $\Delta\varphi(B, L) \sim 1$  will occur for the loops with dimensions of an order of the magnetic length  $L_B$ :

$$L_B = \sqrt{\frac{\Phi_0}{2\pi B}} = \sqrt{\frac{\hbar c}{2eB}}.\tag{2.17}$$

The phase difference between two time-reverse paths along of the same loop modifies the relation (2.8):

$$\begin{aligned}|A^+ + A^-|^2 &= |A^+|^2 + |A^-|^2 + 2|A^+||A^-|\cos\Delta\varphi(B, L) \\ &= 2|A^\pm|^2 (1 + \cos\Delta\varphi(B, L)).\end{aligned}\tag{2.18}$$

For small loops  $L < L_B$  the corresponding phase shift is negligible  $\Delta\varphi(B, L) \ll 1$ , and the right-hand sides of Eq. (2.18) is given by

$$2|A^\pm|^2 (1 + \cos \Delta\varphi(B, L)) \approx 4|A^\pm|^2. \quad (2.19)$$

On the other hand, the phase shift for large loops  $L > L_B$  is not small ( $\Delta\varphi(B, L) > 1$ ) and, hence, cannot be neglected. As a result of averaging over such loops the second term on the right-hand side of Eq. (2.18) vanishes since  $\overline{\cos \varphi} = 0$ . Thus, an applied magnetic field  $B$  eliminates the interference contribution of all loops, whose transverse size is larger than the magnetic length  $L_B$ . Since  $L_B$  depends on magnetic field as  $1/\sqrt{B}$  [Eq. (2.17)], an increase of  $B$  reduces the number of self-intersecting trajectories on which the interference of electron wave functions can occur, leading to a decrease of the resistivity, the phenomenon of negative magnetoresistance (NMR). A typical example of NMR in 2D is shown in Figure 2.2, which illustrates a magnetoresistance of Mg films at different temperatures.<sup>44</sup> If we recall that a loop size cannot be smaller than the mean free path  $l$  and that only loops with  $L < L_\varphi$  (and thus  $L_B \leq L_\varphi$ ) can contribute to the WL, than it is clear that the range where the WL magnetoresistance can be observed is determined by the condition:

$$\frac{\Phi_0}{2\pi L_\varphi^2} \equiv B_\varphi \leq B \leq B_{tr} \equiv \frac{\Phi_0}{2\pi l^2}. \quad (2.20)$$

Since at low temperature  $L_\varphi$  typically depends on  $T$  as  $L_\varphi \propto T^{-p/2}$ ,  $B_\varphi$  decreases as  $T \rightarrow 0$ . Thus, the conductivity depends on  $B$  in the interval  $B_\varphi(T) \leq B \leq B_{tr}$  and only the low-field edge of this interval is temperature dependent. With decreasing temperature  $B_\varphi(T)$  decreases and the suppression of WL becomes more pronounced.

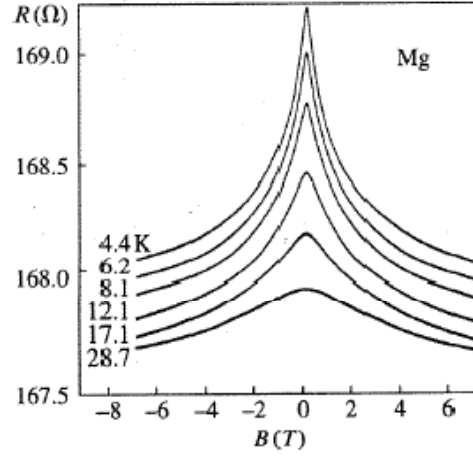


Figure 2.2. Magnetoresistance of thin Mg film for different temperatures. (Adopted from Ref. 44.)

In relatively weak magnetic fields  $B \ll B_{tr}$ , the magnetoconductance is described by Hikami-Larkin-Nagaoka (HLN) theory<sup>45</sup>:

$$\Delta\sigma_{HLN} = G_0 \left[ \psi \left( \frac{1}{2} + \frac{B_\varphi}{B} \right) + \ln \frac{B}{B_\varphi} \right], \quad (2.21)$$

here  $\psi$  is the digamma-function. It can be shown that

$$\frac{B_\varphi}{B} = \frac{\tau}{b\tau_\varphi} = \frac{1}{2} \left( \frac{L_B}{L_\varphi} \right)^2, \quad (2.22)$$

where  $b \equiv B / B_{tr}$ .

### 2.1.2. Scaling theory of localization

The fundamental difference between metals and disordered insulators is that electrons at the Fermi level in metals are mobile, whereas in insulators they are localized. Corresponding electron wavefunctions for metals are extended ( $|\Psi(\vec{r})| \propto \cos(k\vec{r})$ ), whereas for insulators they are spatially localized

$(|\Psi(\vec{r})| \propto \exp(-|\vec{r} - \vec{r}_0|/\xi))$ , where  $\xi$  is a localization length – the length scale on which the localized wavefunction decays exponentially) (Figure 2.3).

A transition between these two ground states, metal and insulator, as some system's parameter (disorder, electron density, pressure, etc.) is continuously varied is called a metal-insulator transition (MIT).<sup>46</sup>

There are two main factors that affect the electron wavefunctions of the ground state, and whose variation can give rise to the MIT. These are electron-electron interaction and disorder. Mott demonstrated that EEI can induce MIT even in the absence of disorder.<sup>46,47</sup> Anderson discovered that disorder, such as strong spatial fluctuations in the electrostatic potential caused by impurities, can cause localization of electrons and, thus the MIT, in a system of noninteracting electrons.<sup>48</sup> The situation when both effects, disorder and EEI, are present is one of the main unsolved problems in condensed matter physics. In 1979 Abrahams, Anderson, Licciardello and Ramakrishnan shed light on a problem of a ground state of disordered systems by developing the scaling theory of localization<sup>7</sup> based on the ideas proposed by Thouless<sup>49</sup>.

The scaling theory describes localization by considering the behavior of the dimensionless conductance  $g = G/(e^2/\hbar)$  (here  $G$  is the system conductance) as a function of only one parameter – the system size  $L$ . (It is assumed that the system size is large enough to have the well-defined mean free path  $l$ , i.e.  $L \gg l$ . In this case, the electron motion is diffusive.) The scaling theory of localization examines what would happen to the conductance of a system of noninteracting particles as  $L$  is gradually increased, i.e. how  $g(bL)$  is related to  $g(L)$ , where  $b$  is a scaling factor. In other words the main physical idea behind the scaling approach<sup>7,49,50</sup> is a gradual

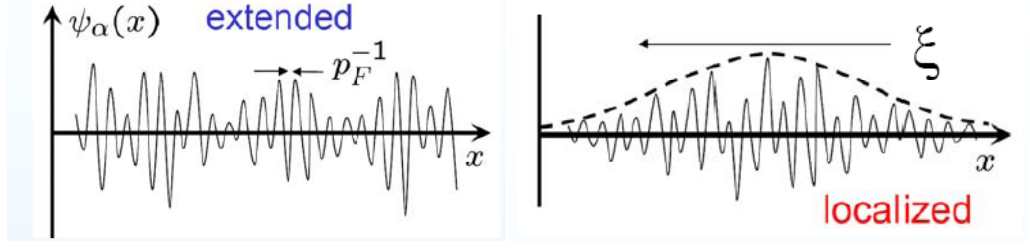


Figure 2.3. The wavefunctions corresponding to the extended (left) and localized (right) states.

transition from small cells of a system in the coordinate space, for which the problem can be solved at least approximately, to larger cells.

The authors of Ref. 7 proposed that the new  $g(bL)$  function is given by a function of the old  $g(L)$  and  $b$  only:

$$g(bL) = f[b, g(L)]. \quad (2.23)$$

Scaling assumption (2.23) can be expressed in a differential form by putting  $b = 1 + \varepsilon$ :

$$\beta(g) \equiv \frac{d \ln g(L)}{d \ln L} = \frac{[\partial f(b, g)/\partial b]_{b=1}}{g(L)}, \quad (2.24)$$

where a scaling function  $\beta$ , being a universal function of  $g$  solely, reflects the idea of the dependence of the conductance on only one parameter.

The asymptotic behavior of  $\beta(g)$  was calculated for very high and very low values of  $g$ . In the weakly localized regime ( $\xi > L$ ) corresponding to high  $g$  (weak disorder), the perturbation theory shows that the function  $\beta$  has the following form<sup>7,43,51</sup>:

$$\beta(g) = d - 2 + \frac{c_d}{g} + O\left(\frac{1}{g^2}\right), \quad g \gg 1. \quad (2.25)$$

The constant  $c_d$  is given by<sup>51</sup>  $c_d = (2/\pi) \left[ S_d / (2\pi)^d \right]$ , where  $S_d$  is a surface of the  $d$ -dimensional unit sphere. Equation (2.25) is consistent with the value of the conductance in the case of weak disorder, when the conductance of  $d$ -dimensional hypercube of size  $L \gg l$  is given by Ohm's law  $g(L) \propto L^{d-2}$ .

In the case of strong disorder all electrons are localized and their wavefunctions fade away within the localization length  $\xi$ :  $|\Psi(\vec{r})| \propto \exp(-|\vec{r} - \vec{r}_0|/\xi)$ . In the regime of strong localization ( $\xi < L$ ), the DC conductance falls exponentially within the size of the system:  $g(L) \propto \exp(-2L/\xi)$  ( $l \ll \xi \ll L$ ), and the scaling function has the following asymptotic:

$$\beta(g) = \ln g + O(\ln(\ln g^{-1})), \quad g \ll 1. \quad (2.26)$$

One may expect that between these two limits (weak and strong localization) the scaling function  $\beta$  should vary smoothly.<sup>e</sup> Figure 2.4 shows the behavior of the scaling function  $\beta$  as a function of its argument  $\ln g$ . Arrows show the flow of logarithmic conductance  $\ln g$  with an increase of  $L$ . According to the scaling hypothesis, this flow is controlled by only one parameter – the dimensionless conductance  $g$ .

In 3D there is a region where the scaling function changes its sign. The corresponding critical point  $g_c$  is a repulsion point or an “unstable critical point” in the renorm-group terminology. For low initial  $g < g_c$ , an increase of the size of the system will cause  $g$  to decrease and the behavior of the system corresponds to

---

<sup>e</sup> This assumption comes from the fact that with increasing disorder the system evolves continuously to the localized behavior.<sup>48</sup>



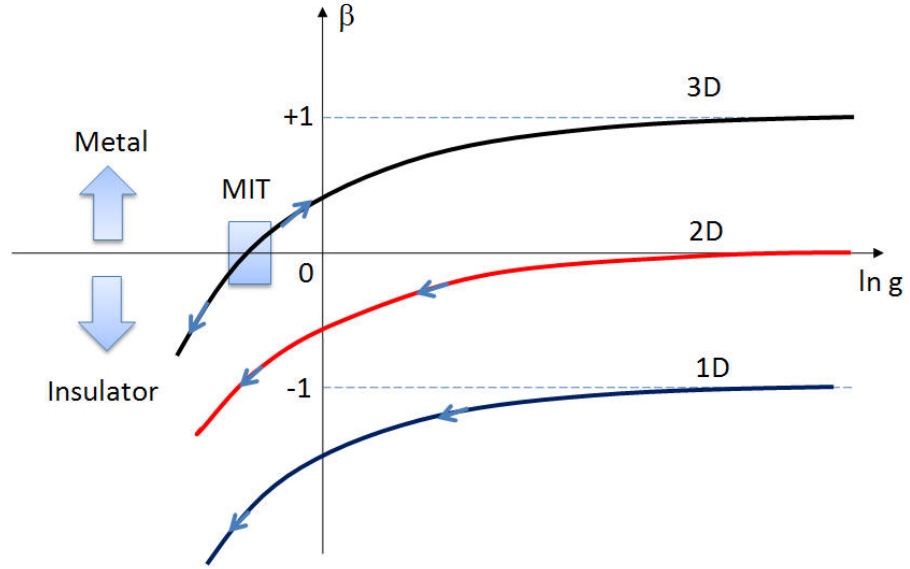


Figure 2.4. Schematic behavior of scaling function for non-interacting electrons in different dimensions.

localized states (insulator). In contrast, when the initial conductance is high  $g > g_c$  an increase of the system size will lead to Ohmic regime (metallic conductance). Thus, the point on a flow diagram (Figure 2.4) where  $\beta_{3D}$  changes its sign corresponds to the MIT.

In  $d \leq 2$   $\beta$  is always negative, and there is no true metallic conduction, i.e., in the limit of infinite system size, all states are localized no matter how weak the disorder is. For a finite system, the conductance can be non-zero. However, the state of such system approaches to a localization. The flow diagram (Figure 2.4) shows that for any initial system size  $L_0$ , the system moves towards strongly localized regime with increasing system size  $L$ .

Equations (2.25) shows that in the weakly localized regime in 2D, the scaling function is equal to  $\beta = -1/\pi^2 g$ , and thus the conductance is given by

$$G = \sigma_D - \frac{e^2}{\pi^2 \hbar} \ln \frac{L}{L_0}. \quad (2.27)$$

The scaling results, presented so far, are obtained for zero temperature. The theory can be extended to the case of non-zero  $T$  by replacing  $L$  with the phase dephasing length  $L_\phi$ . Since the length  $L_\phi$  depends on temperature [in the absence of magnetic impurities  $L_\phi$  is given by Eq. (2.5)], the predictions of Ref. 7 can be tested by varying temperature without actually changing the sample size.

It is worth to emphasize that in the scaling theory the dimensionality 2D is special in the sense that this is the lowest critical dimensionality, above which both the localized and extended states can exist. In contrast to 1D where the scaling function has a substantially larger amplitude  $|\beta| \geq 1$ , in 2D in the region of high conductance  $g \gg 1$  the scaling function is very close to zero and minor corrections, e.g. due to EEI<sup>10</sup> or spin-orbit scattering<sup>45</sup>, may potentially change the sign of  $\beta$ . Therefore, the problem of the 2D MIT and the metallic phase in 2D requires special attention.

## 2.2. Interacting 2D electron systems

### 2.2.1. Wigner-Seitz radius and the role of interaction in 2D systems

In 2D the average area occupied by each quasiparticle is the inverse density  $n^{-1}$  of 2D electron or hole gas. The dimensionless Wigner-Seitz parameter  $r_s$  is defined as the average dimensionless distance between charge carriers measured in units of the effective Bohr radii  $a_B$ :

$$r_s = \frac{1}{\sqrt{\pi n a_B}}. \quad (2.28)$$

Using the expression for the effective Bohr radius in semiconductor  $a_B = \varepsilon \hbar^2 / m_b e^2$  (where  $\varepsilon$  and  $m_b$  are dielectric permittivity and electron (or hole) effective band mass, respectively), Eq. (2.28) can be represented as follows:

$$r_s = \frac{1}{\sqrt{\pi n a_B}} = \frac{1}{\sqrt{\pi n} (\varepsilon \hbar^2 / m_b e^2)} = \frac{e^2 \sqrt{\pi n} / \varepsilon}{\hbar^2 k_F^2 / 2 m_b} = \frac{E_{ee}}{E_F}, \quad (2.29)$$

where the Fermi wavevector  $k_F = (4/g_S g_V)^{1/2} \sqrt{\pi n}$  is for two-spin ( $g_S = 2$ ) and one-valley ( $g_V = 1$ ) system. Eq. (2.29) shows that the parameter  $r_s$  can be interpreted as the ratio of the energy of Coulomb interaction  $E_{ee}$  between two electrons at an average inter-electron distance  $1/\sqrt{\pi n}$  to their Fermi energy.

For the 2DEG formed at the interface between (001) *Si* and amorphous *SiO<sub>2</sub>*, the band electron mass, dielectric constant, and the effective Bohr radius are equal to  $m_b \approx 0.19 m_e$ ,  $\varepsilon = 7.7$ , and  $a_B = 21.45 \text{ \AA}$ , respectively.<sup>6</sup> Thus,

$$r_s(n) = 8.319 n^{-1/2}, \quad (2.30)$$

where  $n$  is expressed in units of  $10^{11} \text{ cm}^{-2}$ .

In high-mobility Si MOFETs, where the most pronounced metallicity is observed, the metallic behavior corresponds to electron densities of the order of  $10^{11}$ - $10^{12} \text{ cm}^{-2}$ , and the apparent MIT occurs in a narrow critical range of electron densities around  $n_c \approx 1 \times 10^{11} \text{ cm}^{-2}$ . The corresponding values of  $r_s \sim 2-8$  are quite large.<sup>52</sup> Thus, the EEI might play an important role in the metallic behavior of the conductivity of high-mobility 2D systems.

Potentially, a strong interaction can modify the ground state of the system. Figure 2.5 shows a schematic phase diagram for 2DEG in Si MOSFETs. With

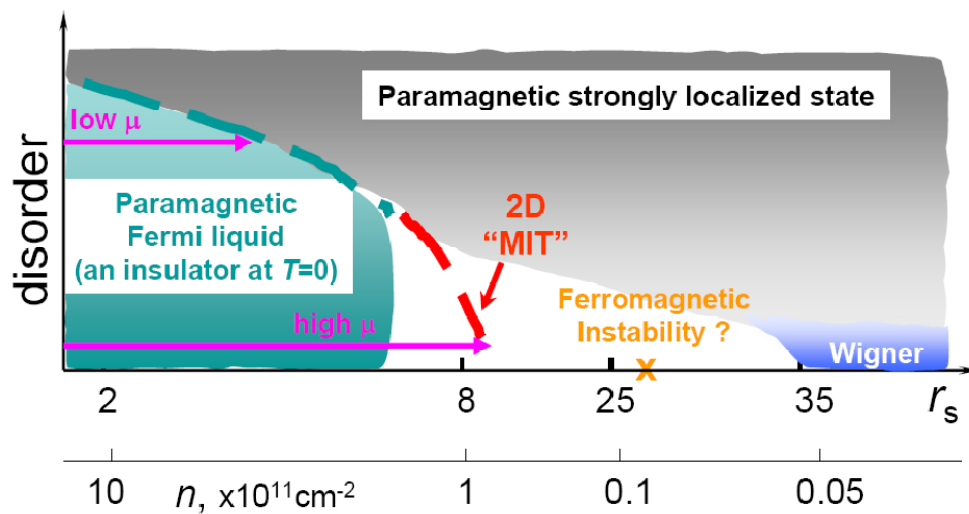


Figure 2.5. Phase diagram for Si MOSFETs.

variation of disorder and the strength of electron-electron interactions, a 2D system may go through several ground states that might exist between the limiting cases of a conventional paramagnetic Fermi-liquid<sup>53</sup> (high densities), electron solid - the Wigner crystal<sup>54</sup> characterized by spatial and spin ordering (low densities, weak disorder), and paramagnetic strongly localized state<sup>55,46</sup> (strong disorder). According to numerical simulations<sup>56</sup>, Wigner crystallization is expected to occur in a 2D system when disorder is weak and when  $r_s$  reaches  $\sim 37$ . One of the candidates for the ground state that occurs prior to Wigner crystallization is a strongly correlated ferromagnetic Fermi-liquid with spontaneous spin ordering. In a clean system the ferromagnetic instability is described by the Stoner criterion<sup>57</sup>, which defines the critical value of the spin-exchange interaction constant at which the system becomes unstable with respect to ferromagnetic ordering (the transition to a state with a non-zero total spin  $S$ ). Attacalite *et al.*<sup>58</sup> showed in their numerical simulations that the Stoner instability should take place prior to Wigner crystallization in the range of interaction parameter

$25 \leq r_s \leq 35$ . Besides the ferromagnetic instability, other ground states have been suggested between a conventional Fermi-liquid and the Wigner crystal.<sup>59</sup>

To enable observation of different quantum states the disorder should be weak. Since the mobility of 2D carriers at low temperature is inversely proportional to the strength of static disorder, the mobility should be high. Thus, only high mobility samples can give access to new physics and new possible ground states.

### 2.2.2. Electron-electron interaction in the diffusive regime

In addition to weak localization correction, interaction between electrons also modifies the conductivity of disordered 2D systems. Let us first consider the interaction between electrons that coherently diffuse due to impurity scattering and have close momenta and energies. For a degenerate electron gas only the electrons with energies that lie within the layer of width  $T$  near the Fermi level ( $E_F - T \leq E \leq E_F + T$ ) can be scattered. The average energy difference  $\Delta E$  between two such electrons is of the order of  $T$ . The electrons can interfere with each other during a time shorter or equal than the reciprocal difference in their energies  $\tau_{ee} \simeq (\Delta E)^{-1} \sim T^{-1}$ , since during that time electrons' states are indistinguishable. In the *diffusive* regime two interacting particles diffuse coherently, i.e. are scattered many times by impurities before they exchange an energy by  $\Delta E \sim T$ . In this regime the elastic momentum relaxation time  $\tau$  is small compared to the characteristic time  $\tau_{ee} = T^{-1}$  required for two interacting quasi-particles to change their energy by  $T$ :

$$T\tau \ll 1. \quad (2.31)$$

At finite temperatures in the presence of EEI the characteristic length scale on which the phase coherence of two electrons is preserved and the interference can

occur is the thermal diffusion length  $L_T \equiv \sqrt{D\hbar/T}$ . This length scale along with the phase relaxation length  $L_\phi$  determine the crossover from higher to lower dimensions: the crossover occurs when one dimension is of the order  $d \sim \min(L_T, L_\phi)$ . For example, if a film thickness  $d$  is much smaller than  $\min(L_T, L_\phi)$ , then the effective dimension is 2D.

The effect of interference between electrons that moves diffusively in disordered systems was first considered by Altshuler and Aronov<sup>9</sup> in the framework of the conventional Fermi-liquid (FL) theory. A more general approach to interacting systems based on generalization of the non-linear  $\sigma$ -model theory has been developed by Finkelstein<sup>10</sup>. It was discovered that the Coulomb interaction, enhanced by the diffusive motion of electrons, gives rise to quantum correction to the conductivity and tunneling density of states in the diffusive regime.<sup>9,10</sup> QC due to EEI in the diffusive regime ( $T\tau \ll 1$ ) can be written as follow:<sup>9,10</sup>

$$\delta\sigma = G_0 \left[ 1 + 3 \left\{ 1 - \frac{(1+F/2)\ln(1+F/2)}{F/2} \right\} \right] \ln(T\tau). \quad (2.32)$$

The first term in square brackets is the exchange term or the Fork contribution (the singlet channel that corresponds to interactions between two electrons with total spin zero), while the second is the Hartree contribution (the triplet channel that corresponds to interactions between two electrons with total spin one). Factor of 3 in front of the triplet channel corresponds to three different projection of total spin:  $-1, 0, +1$ . The interaction parameter  $F$  in the triplet channel is an angular average over the statically screened Coulomb interaction, which depends on the ratio of the inverse screening length  $\kappa$  ( $\kappa = 2\pi e^2 v / \varepsilon = 2g_V / a_B$ ) to the Fermi wave vector  $k_F$ :

$$F = \int_0^{2\pi} \frac{d\theta}{2\pi} \frac{1}{1 + (2k_F/\kappa) \sin \theta/2}. \quad (2.33)$$

Since the ratio  $\kappa/2k_F$  depends on Wigner-Seitz radius  $r_S$  ( $\kappa/2k_F = g_v^{3/2} 2^{-1/2} r_S$ ),  $F$  can be considered as a function of that depends  $r_S$ . Thus, the EEI correction in the diffusive regime has a  $\ln T\tau$  dependence, and the sign of the correction depends on the relative magnitude of the exchange and the Hartree terms, the latter being a function of  $F$ . The interaction parameter  $F$  is related to the Landau interaction parameter  $F_0^\sigma$  as

$$\frac{F}{2} = -Z \frac{F_0^\sigma}{1 + F_0^\sigma}, \quad (2.34)$$

where  $Z$  is a temperature (energy) renormalization parameter.<sup>10</sup> The Eq. (2.32) written in terms of  $F_0^\sigma$  has the form:

$$\delta\sigma = G_0 \left[ 1 + 3 \left\{ 1 - \frac{\ln(1 + F_0^\sigma)}{F_0^\sigma} \right\} \right] \ln(T\tau). \quad (2.35)$$

For a weak screening ( $\kappa/2k_F, r_S \ll 1$ ), the factor  $F$  is small ( $F \sim (\kappa/k_F) \ln(\kappa/k_F) \ll 1$ ) and the conductivity correction is dominated by the exchange term and is negative (since in the diffusive regime  $\ln T\tau < 0$ ). This leads to the logarithmic decrease of the conductivity in the diffusive regime with cooling:

$$\delta\sigma_{xx}^{ee} \approx G_0 \ln T\tau. \quad (2.36)$$

Equation (2.36) shows that EEI correction in the diffusive regime is similar to WL correction (2.13-2.14), though the characteristic length scale here is  $L_T$  rather than  $L_\phi$ . It is important that the EEI correction (2.36) in contrast to WL correction (2.14),

is independent of magnetic field at  $g\mu_B B/T < 1$ . This allows one to distinguish these two types of corrections by applying a weak magnetic field  $B_\varphi(T) \leq B \leq B_{tr}$ .

### 2.2.3. Electron-electron interaction in the ballistic regime

In the *ballistic* regime  $T\tau \gg 1$  the EEI is mediated by a single impurity scattering. The effect of EEI on the conductivity of 2D systems in the ballistic regime was first considered by Stern (1980),<sup>32</sup> Gold and Dolgoplov (1985),<sup>33</sup> and Das Sarma (1986),<sup>34</sup> who analyzed the correction to the conductivity in terms of the  $T$ -dependent screening<sup>32</sup> of the impurity potential.

The screening theory explains the anomalous metallic conductivity (an increase of  $\sigma$  as  $T \rightarrow 0$ ) observed in high-mobility 2D systems in terms of a temperature-dependent effective disorder arising from the strong temperature dependence of screening at low densities. The low temperature behavior of  $\sigma(T)$  is derived in terms of Boltzmann transport theory with random phase approximation screened disorder scattering and is described by a smooth and universal function of two variables: the dimensionless temperature  $t = T/E_F$  and the dimensionless screening parameter  $q_0 \equiv \kappa/k_F$ .

In the limit  $t \rightarrow 0$  interaction correction to the conductivity has the following form.<sup>33,34,60</sup>

$$\Delta\sigma(T)/\sigma_D \approx -C_1(q_0)t - C_{3/2}(q_0)t^{3/2}. \quad (2.37)$$

The coefficients  $C_1$  and  $C_{3/2}$ , being smooth functions of  $q_0$ , were first calculated by Gold and Dolgoplov<sup>33</sup> and later corrected by Das Sarma and Hwang<sup>34,60</sup>. Neglecting the higher order term in Eq. (2.37), the correction to the conductivity is linear in temperature and can be written as follows:



$$\delta\sigma(T) = -G_0 \frac{T}{E_F} f(r_s), \quad (2.38)$$

where  $f(r_s)$  is a smooth function of  $r_s$ .

According to the screening theory,<sup>33,34,60</sup> the effect of the anomalous 2D metallicity is not a signature of a new ground state, rather it is a finite-temperature effect. The theory<sup>33,34,60</sup> explains linear behavior of resistivity, which in Si MOSFETs occurs at a temperature range 0.5-4K<sup>f</sup>, as well as nonmonotonicity at relatively high temperature ( $T \geq 0.1T_F$ ), where  $\rho(T)$  seems to slowly decrease with increasing temperature. It is worth mentioning that the theory<sup>33,34,60</sup> is only valid for  $T_D \ll T \ll E_F$ , where  $T_D = 1/2\pi\tau_q$  (here  $\tau_q$  is the elastic quantum scattering time) is the Dingle temperature. Thus, the screening theory applies to the ballistic regime and describes the behavior of 2D systems on the metallic side of the 2D MIT.

#### 2.2.4. EEI in the crossover between the ballistic and diffusive regimes

In 2001 a considerable progress has been achieved in the theory of QC: Zala, Narozhny and Aleiner (ZNA)<sup>35</sup> calculated EEI corrections to the Drude conductivity [Eq. (2.1)] beyond the diffusive regime (for arbitrary value of  $T\tau$ ), in terms of FL interaction parameters. ZNA showed that the temperature-dependent screening<sup>32-34</sup> has in fact a common physical origin with the Altshuler-Aronov effect<sup>9,10</sup> but that the calculation in the screening theory<sup>32-34</sup> took only the Hartree term into account and missed the exchange contribution. Thus, according to the ZNA theory, EEI corrections in the ballistic ( $T\tau \gg 1$ ), diffusive ( $T\tau \ll 1$ ) and intermediate ( $T\tau \simeq 1$ ) regimes are

---

<sup>f</sup> As electron density approaches to the critical density of MIT (from the metallic side of the transition), the temperature range, corresponding to linear temperature behavior of resistivity, narrows down.

due to the same physical process: elastic scattering of electrons by the self-consistent potential from all other electrons. The ZNA theory has been developed for the short-range scattering potential (which is relevant to Si MOSFETs); later Gornyi and Mirlin (GM)<sup>37</sup> extended this theory for the case of the long-range scattering potential. The theories of Refs. 35,37 naturally incorporate the logarithmically divergent Altshuler-Aronov correction<sup>9,10</sup> to the conductivity [Eq. (2.35)] in the diffusive regime, and the linear temperature dependence of  $\sigma$ <sup>32-34</sup> in the ballistic regime [Eq. (2.38)]. The ZNA theory also makes specific predictions on the correction to the Hall coefficient  $\rho_{xy}/B$  at  $B \rightarrow 0$ , and the magnetoresistance in a parallel magnetic field.<sup>35</sup>

Recently the renormalization group (RG) based theory<sup>10</sup> that describes EEI in the diffusive interaction regime  $T\tau \ll 1$  was extended in the first order in  $1/\pi\sigma$  and in all orders in interaction<sup>38</sup>. The results of Refs. 10,38 have been compared with the conductivity of Si MOSFETs at low electron densities<sup>61-63</sup>. The RG equations<sup>10,38,64,65</sup> describe the length scale (temperature) evolution of the resistivity and interaction parameter for a 2D electron system in the diffusive regime. However, at high electron densities, the temperature range corresponding to the diffusive regime shrinks which limits the applicability of RG theory. In contrast, the theory of interaction corrections<sup>35,37</sup> is applicable in a wide  $T$  range provided  $\sigma \gg e^2/h$  and  $\Delta\sigma/\sigma \ll 1$ ; these assumptions are well justified at high densities.

The ZNA and GM theories offer the expressions for  $\Delta\sigma(T, B)$  that are valid in a wide range of  $T$ , including ballistic and diffusive interaction regimes. According to the theories of Ref. 35,37 the magnitude and sign of the quasi-linear  $\sigma(T)$  dependence is determined by the value of the Fermi-liquid parameter  $F_0^\sigma$  (which can be found by measuring the Shubnikov-de Haas oscillations in weak magnetic fields

normal to the plane of 2D structure<sup>16,41</sup> or the magnetoresistance in strong in-plane magnetic fields<sup>105-107</sup>). In particular, it is expected that  $\sigma(T)$  dependence becomes more metallic when  $F_0^\sigma$  is negative and its absolute value exceeds a certain threshold.

Since the ZNA theory<sup>35</sup> is relevant to Si MOSFETs (it takes into account the short-range random potential), we provide a more detailed overview of this theory below.

### 2.2.5. Interaction corrections to the conductivity within Zala-Narozhny-Aleiner theory

#### Temperature dependence of the conductivity in zero magnetic field

In a clean infinite system, electron density is homogeneous. In disordered or finite systems, however, electron density in the vicinity of impurities is modulated by the impurity potential and has an inhomogeneous term, which oscillates on the scale of the order of the Fermi wavelength  $\lambda_F$ . This oscillating term, called the Friedel oscillation<sup>36</sup>, can be considered as an additional scattering potential. The main mechanism leading to QC due to EEI is interference between two electrons: one scattered back by the impurity and the other scattered back by the Friedel oscillations induced by this impurity around itself (Figure 2.6).

In the case of a one-valley system<sup>g</sup> there are four spin channels that contribute to the conductivity: one “single” (the total spin of two electrons is zero) and three triplet channels (the total spin of two electron equals to unity), which are different from each other by a z-component of the total spin. EEI corrections  $\delta\sigma_{ee}(T, B=0)$  to the Drude

---

<sup>g</sup> The situation in the case of two valley system will be considered below.

conductivity  $\sigma_D$  in zero magnetic field can be considered as combination of the “charged”  $\delta\sigma_C$  term, which combines the Fock correction and the singlet part of the

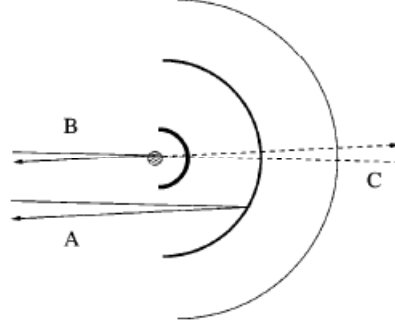


Figure 2.6. Scattering by Friedel oscillation. Paths A and B are due backscattering from Friedel oscillation, path C is due to backscattering from the impurity. Interference between A and B gives QC. (Adopted from Zala *at al.*<sup>35</sup>)

Hartree correction, and three equivalent “triplet” contributions  $\delta\sigma_T$  due to the triplet part of Hartree term:

$$\Delta\sigma_{ee}(T) = \delta\sigma_C(T) + 3\delta\sigma_T(T). \quad (2.39)$$

The charge term does not depend on detail of interaction:<sup>35</sup>

$$\delta\sigma_C = \frac{e^2}{\pi\hbar} \left\{ T\tau \left[ 1 - \frac{3}{8} f(T\tau) \right] - \frac{1}{2\pi} \ln \left( \frac{E_F}{T} \right) \right\}, \quad (2.40)$$

whereas the magnitude and sign of the triplet term is governed by the FL interaction parameter  $F_0^\sigma$ :<sup>35</sup>

$$\delta\sigma_T = \frac{e^2}{\pi\hbar} \left\{ \frac{F_0^\sigma}{1+F_0^\sigma} T\tau \left( 1 - \frac{3}{8} t(T\tau; F_0^\sigma) \right) - \left( 1 - \frac{1}{F_0^\sigma} \ln(1+F_0^\sigma) \right) \frac{1}{2\pi} \ln \left( \frac{E_F}{T} \right) \right\} \quad (2.41)$$

Figure 2.7 shows the dimensionless functions  $f(x)$  and  $t(x; F_0^\sigma)$ , which describe the crossover between the diffusive ( $\Delta\sigma_{ee} \propto \ln T$ ) and the ballistic ( $\Delta\sigma_{ee} \propto T$ ) regimes;

outside the crossover region,  $f$ - and  $t$ -functions change the value of  $\Delta\sigma_{ee}$  by a few

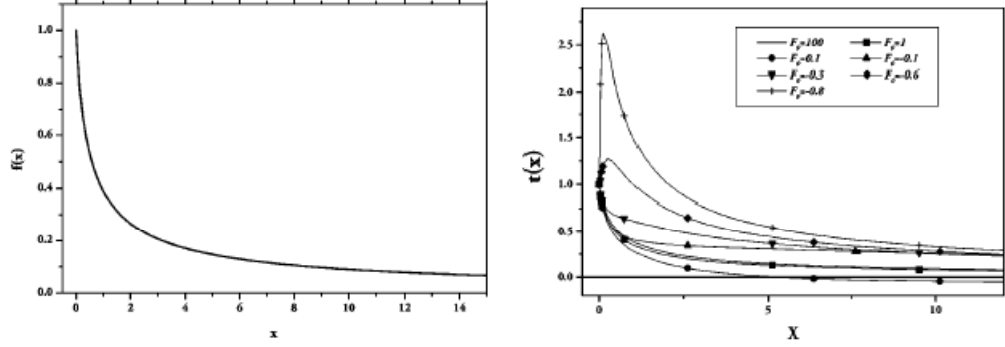


Figure 2.7. Dimensionless  $f(x)$  (left) and  $t(x; F_0^\sigma)$  (right) functions. (Adopted from Ref. 35.)

percents.<sup>h</sup> In the ballistic regime the correction is linear in  $T$ , and the slope  $d\sigma(T)/dT$  is determined by  $F_0^\sigma$ . The overall sign of the total correction to the conductivity is also determined by  $F_0^\sigma$  and can be both positive and negative (Figure 2.8).

The diffusive-ballistic crossover is expected over some temperature range near

$$T^* = \frac{(1 + F_0^\sigma)}{2\pi\tau}. \quad (2.42)$$

Equations (2.40-2.41) describe the quantum corrections in a system with conductance  $\sigma \gg e^2/h$  and at temperatures well below the Fermi energy

$$\left[ T \ll (1 + F_0^\sigma)^2 E_F \right].$$

---

<sup>h</sup> The explicit expressions  $f(T\tau)$  and  $g(T\tau, F_0^\sigma)$  functions are given in Appendix B.

Equations (2.39-2.41) were derived for a single-valley system. To adopt the theoretical result<sup>35</sup> to the case of (001) Si MOSFETs, one should take into account that the electron spectrum in this system has two almost degenerate valleys<sup>6</sup>. In the case of a two-valley system, the valley index can be considered as a pseudo-spin,<sup>38</sup>

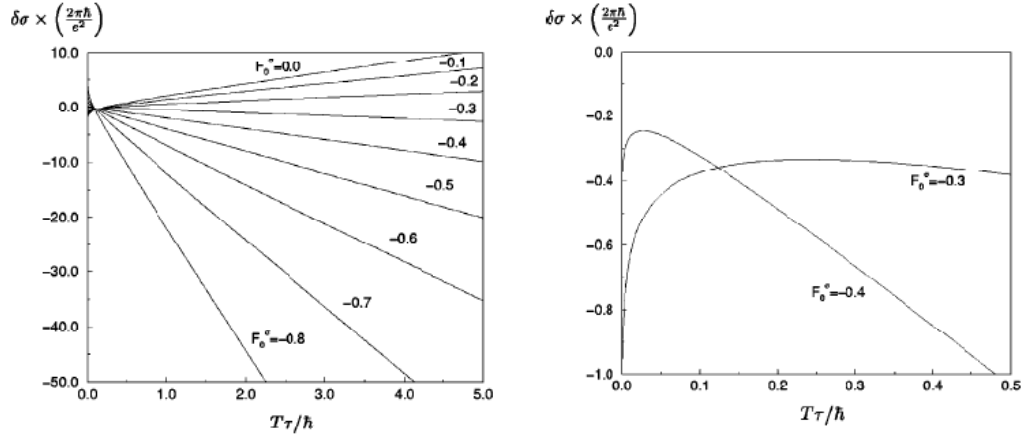


Figure 2.8. Total correction to conductivity for different parameters  $F_0^\sigma$  (left panel). Blow-up of curves with  $F_0^\sigma = -0.3$  and  $F_0^\sigma = -0.4$  (right panel). (Adopted from Ref. 35.)

and the valley degeneracy determines the number of triplet terms due to the spin exchange processes between electrons in different valleys. For a system with two degenerate valleys, the total number of channels of interaction is  $4 \times 4 = 16$ , among them 1 singlet and 15 triplet terms (for comparison, there are 1 singlet and 3 triplet terms for a single-valley system). Thus for a two-valley systems in the absence of intervalley scattering, EEI correction will be modified by changing the number of triplets channels from 3 to 15:

$$\Delta\sigma_{ee}(T) = \delta\sigma_c(T) + 15\delta\sigma_T(T) \quad (2.43)$$

Equations (2.40), (2.41) and (2.43) represent  $\Delta\sigma_{ee}$  in terms of one fitting parameter, the Fermi-liquid constant  $F_0^\sigma$ , which can be found in independent

experiments (see Sec. 5.3 for details). The sign and magnitude of  $\Delta\sigma_{ee}$  in both ballistic and diffusion regimes is controlled by the Fermi-liquid parameter  $F_0^\sigma$ . For a rough estimate, deeply in the ballistic regime the  $\ln T$  terms and the crossover functions  $t$  and  $f$  in Eqs. (2.40, 2.41) can be omitted. For example, at  $T\tau = 10$ , the function  $f$  and  $t$  contribute  $\approx 4\%$  and  $\approx 11\%$ , respectively, to the linear-in- $T\tau$  ballistic terms of Eqs. (2.40, 2.41). By neglecting these terms, one finds that for a single-valley system the linear dependence  $\Delta\sigma_{ee}(T)$  in the ballistic regime becomes metallic ( $d\sigma/dT < 0$ ) at  $3F_0^\sigma/(1+F_0^\sigma) < -1$  or  $F_0^\sigma < -0.25$ , whereas for a system with two degenerate valleys, the metallic  $\Delta\sigma_{ee}(T)$  dependence are expected at  $15F_0^\sigma/(1+F_0^\sigma) < -1$  or  $F_0^\sigma < -0.06$ . Thus, the valley degeneracy extends the range of  $F_0^\sigma(n)$ , and hence, the range of carrier densities  $n$  where the conduction exhibits the metallic behavior.

### **Magnetoconductivity in the in-plane magnetic field**

The in-plane magnetic field, being coupled to electron spins, provides a useful tool for exploring the interaction effects in the low-temperature conductivity of Si MOSFETs. One of the factors that affect the interaction correction to the conductivity is the magnetic field<sup>14,15</sup>. When the Zeeman energy  $E_Z = g_b\mu_B B$  ( $g_b = 2$  is the bare  $g$ -factor,  $\mu_B$  is the Bohr magneton) becomes much greater than  $T$ , the number of triplet terms that contribute to  $\Delta\sigma_{ee}(T)$  is reduced from 15 to 7. Similar reduction of triplet terms is expected for a valley splitting  $\Delta_v > T$ . These two effects have been accounted by the theory of interaction corrections<sup>35</sup>; in the presence

of a magnetic field and/or valley splitting the interaction correction to the conductivity can be expressed as follows:<sup>66</sup>

$$\begin{aligned} \Delta\sigma_{ee}(T, \tau, F_0^\sigma, B_\parallel, \Delta_V) = & \Delta\sigma_{ee}(T) + 2\Delta\sigma^Z(E_Z, T) \\ & + 2\Delta\sigma^Z(\Delta_V, T) + \Delta\sigma^Z(E_Z + \Delta_V, T) + \Delta\sigma^Z(E_Z - \Delta_V, T), \end{aligned} \quad (2.44)$$

where  $\Delta\sigma_{ee}(T)$  is given by Eq. (2.43) and all the terms  $\Delta\sigma^Z(Z, T)$  have a form

$$\begin{aligned} \Delta\sigma^Z(Z, T) \equiv & \sigma(Z, T) - \sigma(0, T) = \delta\sigma_b(Z) + \delta\sigma_d(Z) \\ = & \frac{e^2}{\pi\hbar} \left[ \left\{ \frac{2F_0^\sigma}{1+F_0^\sigma} (T\tau) K_b\left(\frac{Z}{2T}, F_0^\sigma\right) \right\} \right. \\ & \left. + \left\{ K_d\left(\frac{Z}{2\pi T}, F_0^\sigma\right) \right\} + m(Z\tau, T\tau; F_0^\sigma) \right], \end{aligned} \quad (2.45)$$

if the relevant energies  $Z \ll E_F$  ( $Z$  stands for  $E_Z, \Delta_V$  and combinations  $E_Z \pm \Delta_V$ ). The explicit expressions for the functions  $K_b$  and  $K_d$  are given in the Appendix B. In particular, Eq. (2.45) describes the interaction-driven magnetoconductivity in the magnetic fields which are much weaker than the field of a full spin polarization of a system. The function  $m(0, T\tau; F_0^\sigma)$ , which describes the crossover between the ballistic and diffusive regimes, can be neglected - it appears to be numerically small and does not modify the value of  $\Delta\sigma(Z, T)$  outside the ballistic-diffusive crossover region by more than one percent.

It is worth mentioning that in the framework of the RG theory, the magnetoconductance can also be described by the Castellani-Di Castro-Lee formula<sup>65,67</sup> which is equivalent to Eq. (2.44) in the diffusive limit at  $\Delta_V = 0$ . However, for the analysis of our magnetoconductivity data measured over a wide  $T$ -range that includes both diffusive and ballistic regimes, the interaction correction theory<sup>35</sup> is more appropriate than the RG theory<sup>65</sup>.



The interaction correction theory<sup>35</sup> (as well as the RG theory<sup>38</sup>) does not take into account intervalley scattering. This approximation is valid when the intervalley scattering rate  $\tau_V^{-1}$  is much smaller than  $T$ . In the low-temperature limit  $T \ll \tau_V^{-1}$ , the electron states in different valleys are completely intermixed at the time scale  $\sim T^{-1}$  and the correction  $\Delta\sigma_{ee}(T)$  for a two-valley system is expected to coincide with that for a single-valley system.

Since the interaction corrections to the conductivity  $\Delta\sigma_{ee}(T, B)$  depend on several parameters such as  $\tau, F_0^\sigma, \Delta_V$  and  $\tau_V$ , for testing the theoretical results, it is crucial to determine these parameters in independent measurements. This program is discussed in Sections 4.2.3, 5.3, 6, and 7.1.

### 3. Metal Oxide Semiconductor Field Effect Transistor

#### 3.1. Si MOSFET device

One of the most important semiconductor devices is a Si Metal-Oxide-Semiconductor Field Effect Transistor (Si MOSFET), which was successfully fabricated by Kahng and Atalla in 1960.<sup>68</sup> The integrated circuits based on this device now constitute about 90% of the semiconductor device market. This 2D electron system consists of a charge carriers confined within a two-dimensional potential well; the latter is formed at the interface between a semiconductor and an insulator.<sup>6</sup>

##### 3.1.1. Basic principles of operation of n-channel Si MOSFET

Let consider how a *n*-channel Si MOSFET operates. A prospective view of a Si MOSFET is shown in Figure 3.1. A device consists of a *p*-doped Si substrate, a thermally grown silicon oxide on top of the Si-substrate, a thin metal (aluminum) film deposited on top of SiO<sub>2</sub>, and two heavily *n*<sup>+</sup>-doped regions at the Si surface. The metal film (or a gate) and two other electrodes called the source (S) and the drain (D) located on top of the heavily doped regions form three terminals of the device.

A small negative bias  $V_g < 0$  applied to the metal gate relative to the source terminal (which is usually at a ground potential) causes the accumulation (induction) of the positively charged majority carriers at Si-SiO<sub>2</sub>. On the other hand, a small positive bias  $V_g > 0$  leads to a surface depletion near the metal-oxide interface, i.e. removing of the majority carriers near the Si-SiO<sub>2</sub> interface from the valence band (or

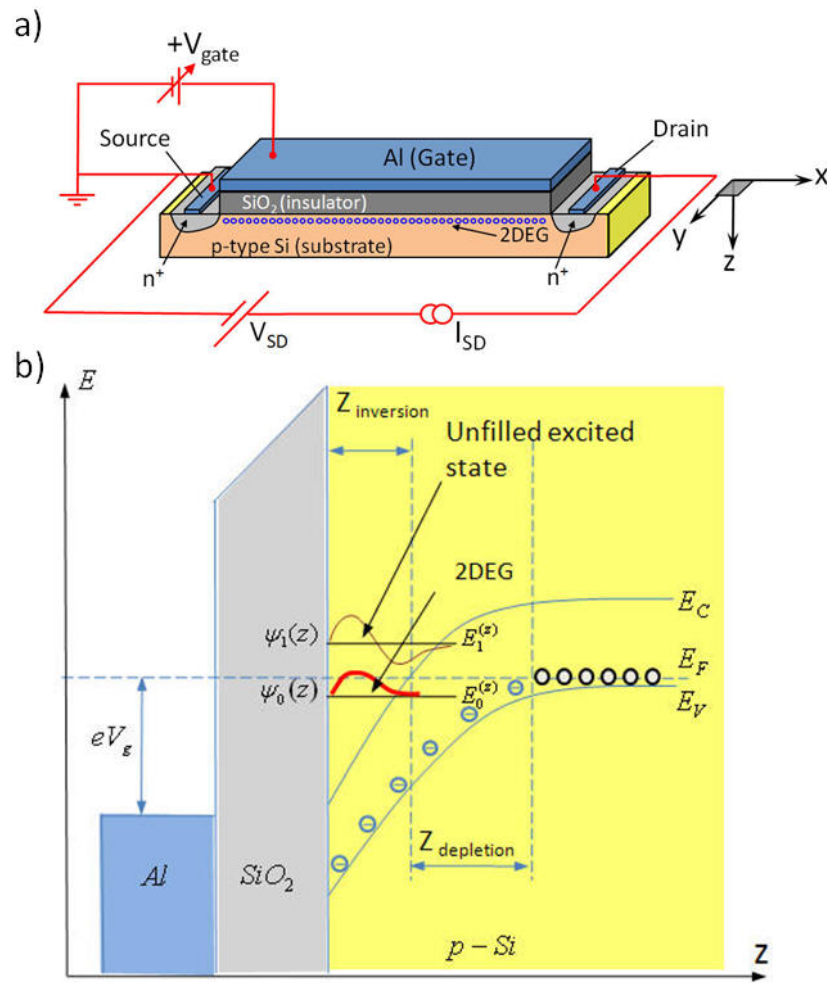


Figure 3.1. Si MOSFET: schematic (a) and the band-edge (b) diagrams.

from the neutral acceptors near the interface when they are deionized) leaving negatively charged ions. As a result, a space charge is created [Figure 3.1(b)], this *depletion layer* has a high electrical resistivity. An electrostatic potential associated with this negative space charge causes the conduction and valence band edges to bend downward at the interface. With increasing the positive gate voltage, the depletion layer and the corresponding bending of the energy levels near the interface increase further. At some point, the end of the conduction band crosses the Fermi level, and electrons near the interface will start occupying the states in the conduction band that

lies below the Fermi level, forming an *inversion layer* [Figure 3.1(b)]. The onset of strong inversion occurs when the electron concentration near the Si-SiO<sub>2</sub> interface exceeds the density of electron traps at the Si-SiO<sub>2</sub> interface and the substrate doping level. This happens when the gate voltage reaches the threshold voltage  $V_{th}$ . The typical width of the inversion layer is of the order 10 nm, whereas the width of the depletion layer is of the order of a few microns.

Electrons in the inversion layer are trapped in a triangular potential well [Figure 3.1(b)].<sup>69</sup> The energy levels of electrons are grouped in two-dimensional subbands, each of which corresponds to a quantized level  $E_n^{(z)}$  for the motion in the  $z$ -direction, with a continuum for the motion in the plane parallel to the Si-SiO<sub>2</sub> interface:

$$E(\mathbf{k}_{\parallel}) = E_n^{(z)} + \frac{\hbar^2 \mathbf{k}_{\parallel}^2}{2m_{\parallel}}, \quad (3.1)$$

here  $\mathbf{k}_{\parallel} = (k_x, k_y)$  and  $m_{\parallel}$  are the wave-vector and the electron effective mass for the motion parallel to the surface, respectively. Only those subbands that lie below the Fermi level can be occupied. As will be shown in the next section, at ultralow temperatures and not too high electron densities ( $n < (4-5) \times 10^{11} \text{ cm}^{-2}$ ), only the lowest energy subband is populated, and the confined electrons are able to move only parallel to the Si-SiO<sub>2</sub> interface, forming a pure two-dimensional electron gas (2DEG).

The  $n$ -channel Si MOSFET operates as follow.<sup>70</sup> When no voltage is applied to the gate, two facing each other  $p$ - $n$  junctions, formed by the heavily doped regions (located under S and D terminals) and the bulk semiconductor, block the current between the source and the drain and the device is in the “off” state. When a

sufficiently large positive bias is applied to the gate, a surface inversion layer (or channel) is formed between the two heavily  $n^+$ -doped regions. Electrons that form the inversion layer are trapped in the triangular potential well, at the Si-SiO<sub>2</sub> interface. The depth of the well, and thus the number of electrons that can be trapped by it, is controlled externally by the potential of the gate. Thus, the source and the drain are connected by a conducting 2D  $n$ -channel with a low resistivity when a positive  $V_g > V_{th}$  is applied (the “on” state of the device). With applying a small positive voltage  $V_D$  to the drain (relative to the source), a source-drain current  $I_{SD}$  flows through the inversion layer [Figure 3.1(a)].

A metal gate and a thin inversion layer form a parallel-plane capacitor. Since  $V_g$  drops partially across  $SiO_2$  oxide and partially across a space-charge layer in semiconductor, the MOSFET’s differential capacitance per unit area  $C = dQ/dV_g$  (where  $Q$  is a semiconductor space charge per unit area) is given by

$$\frac{1}{C} = \frac{1}{C_{ox}} + \frac{1}{C_{sc}}, \quad (3.2)$$

here  $C_{ox} = \epsilon_{ox}/d_{ox}$  is the capacitance of the oxide with a thickness  $d_{ox}$  and a dielectric constant  $\epsilon_{ox}$ ,  $C_{sc} = dQ/d\psi_s$  is the semiconductor capacitance ( $\psi_s$  is a potential at the interface). In the regime of strong inversion the charge induced by a further increase of  $V_g$  goes almost entirely into the inversion layer. As a result, the total capacitance  $C$  approaches the oxide capacitance  $C_{ox}$ . As a result, the density of electrons in the inversion layer depends on the applied gate voltage as follows

$$n(V_g) = \frac{C_{ox}}{e} \delta V_g = A(V_g - V_{th}), \quad (3.3)$$

here a linear coefficient  $A$  is given by  $A = \epsilon_{ox}/ed_{ox}$ .

### 3.1.2. Band structure of (001) Si MOSFET

Silicon is a multivalley system – there are six valleys in the conduction band that lie on the six equivalent  $\Delta$  -lines along [001]-directions, about 85% on the way from  $\Gamma$  to the six X points<sup>6</sup> [Figure 3.2(a)]. For each valley, the long axis corresponds to a longitudinal electron effective mass  $m_l \approx 0.92m_e$ , whereas the short axis corresponds to a transverse mass  $m_t \approx 0.19m_e$ .

On a (001) surface of Si, the degeneracy of six conduction valleys is removed by quantization in the surface potential well.<sup>71</sup> on this surface the electrons in the inversion layer occupy two different types of subbands. The confinement energy depends on the effective mass perpendicular to the Si-SiO<sub>2</sub> interface. Two valleys (shown by a red color on Figure 3.2) with long axes perpendicular to the surface give rise to one set of subbands (0,1,2,...) with a heavy mass  $m_{\text{heavy}} = \sqrt{m_l m_t} \approx 0.42m_e$ , for motion perpendicular to the (001) surface:

$$E(\mathbf{k}_{\parallel}) = E_n + \frac{\hbar^2 \mathbf{k}_{\parallel}^2}{2m_{\text{heavy}}}, \mathbf{k}_{\parallel} = (k_x, k_y). \quad (3.4)$$

The other four valleys (shown by a blue color on Figure 3.2(a)), whose long axes lie in the plane of the Si-SiO<sub>2</sub> interface, determine another set of subbands (0',1',2',...) with a lighter mass  $m_{\text{light}} = m_t$  for motion perpendicular to the (001) surface:

$$E(\mathbf{k}_{\parallel}) = E_n + \frac{\hbar^2 \mathbf{k}_{\parallel}^2}{2m_{\text{light}}}, \mathbf{k}_{\parallel} = (k_x, k_y). \quad (3.5)$$

A schematic representation of the constant-energy ellipses and the Brillouin zone for the (001) surface of Si is shown in Figure 3.2(b). Here two red concentric

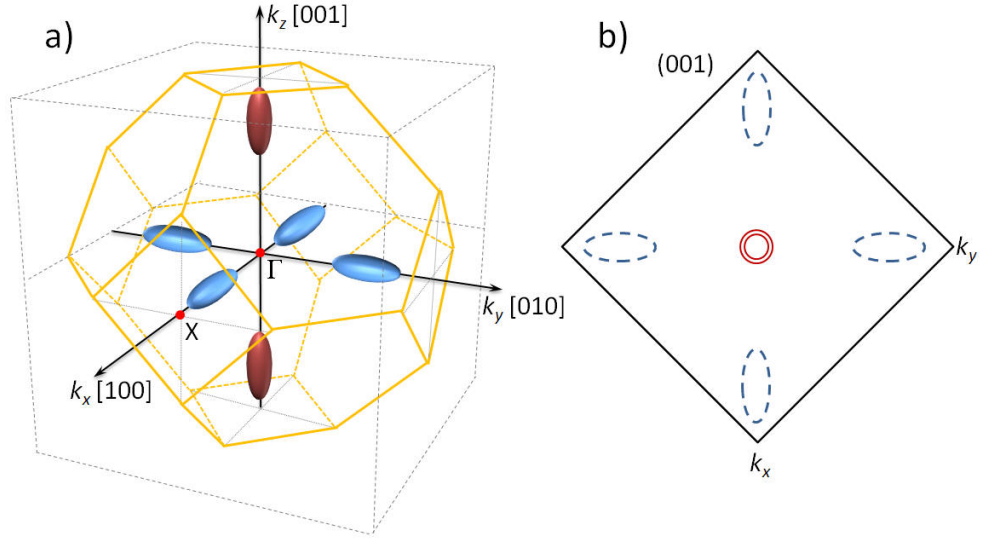


Figure 3.2 (a) Constant energy surfaces in  $k$  space for silicon. Each ellipsoid corresponds to a valley in the conduction band and a polyhedron represent the first Brillouin zone. The long axis of each ellipsoid corresponds to the longitudinal electron effective mass  $m_l \approx 0.92m_e$ , the short axis corresponds to the transverse effective mass  $m_t \approx 0.19m_e$ . For a (001) surface two valleys shown by red color have lower ground energy compared to the other four ellipsoids. (b) Constant energy ellipses and the Brillouin zone for a (001) surface of Si. Concentric ellipses show double degenerate levels.

ellipsoids correspond to two almost equivalent light-mass valleys, whereas four other dashed ellipsoids represent the heavy-mass valleys.

Thus, for a (100) Si surface there are two types of subbands: twofold subbands associated with two light-mass valleys, and fourfold subbands associated with four heavy-mass valleys. Both the fourfold degenerate ground subband  $E_0$  and the first excited twofold degenerate subband  $E_1$  are above the minima for the twofold degenerate ground subband  $E_0$  by  $\Delta E \approx (20 - 25) \text{ meV} \approx (200 - 300) \text{ K}$  (see, e.g., Ando *et al.*<sup>6</sup> and references therein). This indicates that the population of the higher subbands starts at  $n > (4-5) \times 10^{11} \text{ cm}^{-2}$ . To ensure that only the lowest size

quantization subband is filled, all measurements in this work were performed at  $n < 4 \times 10^{11} \text{ cm}^{-2}$ .

In a (001) Si MOSFET for a typical density  $\sim 10^{12} \text{ cm}^{-2}$  the corresponding Fermi energy is of the order  $E_F \approx 6 \text{ meV} \approx 70 \text{ K}$ , what is smaller than  $\Delta E = \{E_1, E_0\} - E_0$ . At not-too-high electron densities (such that  $E_F < \Delta E$ ) and ultralow temperatures ( $T \ll E_F$ ) only the ground-state subband associated with two light-mass valleys is occupied. Thus, only two valleys, whose long axes lie along the [001] direction, participate in the low temperature electron transport in a (001) Si MOSFET.

The valley degeneracy  $g_V = 2$  distinguishes (001) Si MOSFETs from other 2D systems: it significantly enhances the EEI effects in Si, which, in turn, gives rise to a large amplification of the temperature behavior of the conductivity of high-mobility Si MOSFET samples at low electron densities.<sup>38</sup>

Although the two valleys relevant in the low temperature transport of (001) Si MOSFETs are almost equivalent, there exists a relatively small energy splitting  $\Delta_V$  between them. This  $\Delta_V$  can be caused, for instance, by a slight misorientation of the plane of a 2D layer from the (001) crystallographic plane.<sup>6</sup>

The other important parameter of (001) Si inversion layers is the intervalley scattering between the two almost degenerate valleys. At temperatures comparable to the rate of the intervalley scattering,  $\tau_V^{-1}$ , a crossover occurs between a band with two distinct valleys and a band where the two valley are effectively unified due to the intervalley scattering. As will be shown in Sections 4.2.3 and 6, in a typical Si MOSFET sample the values of  $\tau_V^{-1}$  and  $\Delta_V$  fall within the experimentally relevant temperature interval. Thus, it is important to characterize those parameters and to know how they affect the electron transport.



### 3.2. Transport properties of Si MOSFETs

#### 3.2.1. Low $\mu$ , high $n$ Si MOSFETs

Si MOSFET devices with rather low mobility  $\mu$  and high carrier density  $n$  supported the scaling theory of localization<sup>7</sup> and Altshuler-Aronov<sup>9</sup> interaction theory. In 1980 Bishop *et al.*<sup>72</sup> studied the transport properties of low mobility ( $\mu \sim 0.2 \text{ m}^2/\text{Vs}$  at 4.2 K)  $n$ -channel Si MOSFETs in high density range ( $n \approx (1.8\text{-}5.6) \times 10^{11} \text{ cm}^{-2}$ ). The authors of Ref. 72 observed an increase of the resistivity with temperature cooling (Figure 3.3(a)): a smooth and graduate crossover from an exponential ( $R \sim R_0 \exp(A/T^{1/3})$ ) to a logarithmic ( $R \sim \ln T$ ) behavior occurred at  $R_{\square} \approx 10 k\Omega$ . Thus, in the studied density range, no evidence for the metallic state was observed. The saturation of the resistance at millikelvin temperatures was attributed to the heating effects.

Similar results were reported by Uren *et al.*<sup>73</sup> for low-mobility Si MOSFETs ( $\mu \sim (0.25\text{-}0.65) \text{ m}^2/\text{Vs}$ ). The authors of Ref. 73 also observed both strong and weak localization regimes. In the weak localization regime, the logarithmic decrease of the resistivity [Figure 4.6(b)] was consistent with interaction and localization theories<sup>7,9</sup>.

The magnetoconductance data<sup>73-76</sup> obtained for low- $\mu$  devices have also supported the scaling theory of localization<sup>7</sup>. The positive magnetoconductance due to the suppression of the WL correction by a magnetic field  $B_{\perp}$  normal to the plane of a 2D system was observed by Kawaguchi and Kawaji<sup>74</sup> and Wheeler<sup>75</sup> on  $n$ -channel (100) Si MOSFETs (Figure 3.4). The  $\sigma(B_{\perp})$  dependences were consistent with the Hikami-Larkin-Nagaoka theory<sup>45</sup>.

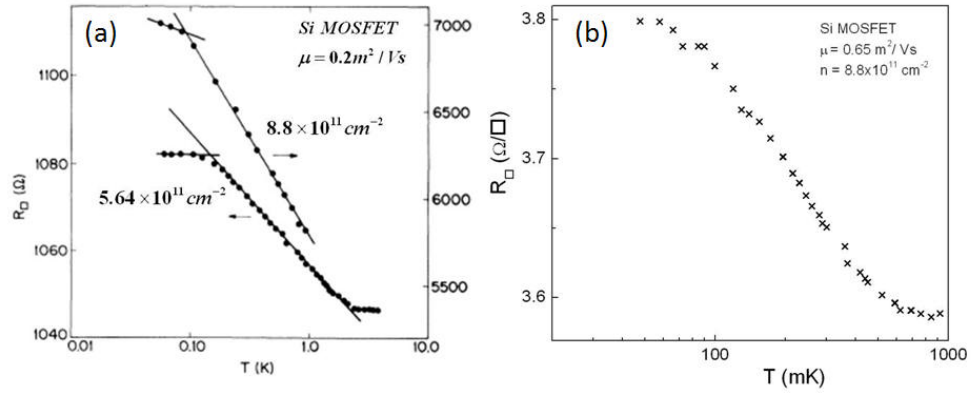


Figure 3.3. Zero magnetic field temperature dependence of the resistance for the inversion layers in Si MOSFETs (a) with densities of  $2.03 \times 10^{11} \text{ cm}^{-2}$  (right) and  $5.54 \times 10^{11} \text{ cm}^{-2}$  (left) (Bishop *et al.*<sup>72</sup>); (b) with peak mobility  $\mu \approx 0.65 \text{ m}^2/\text{Vs}$  and electron density  $8.8 \times 10^{11} \text{ cm}^{-2}$  (Uren *et al.*<sup>73</sup>).

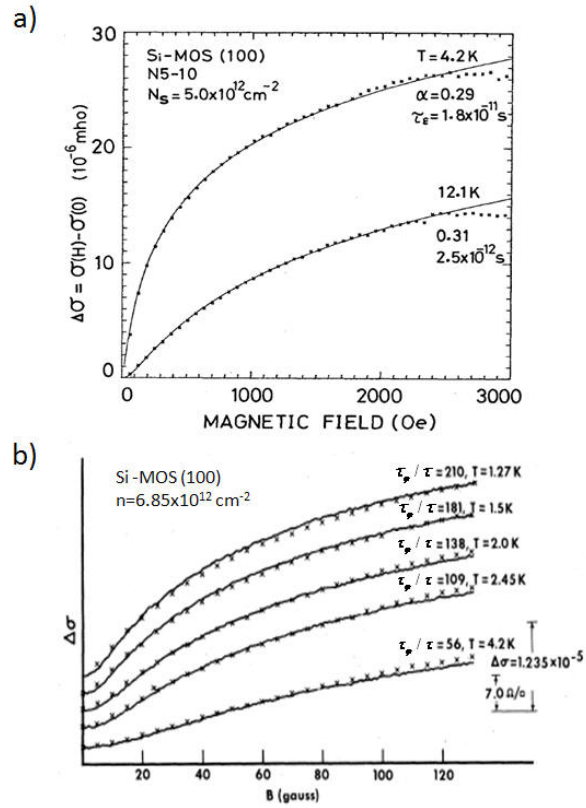


Figure 3.4. Magnetoconductance of the n-channel (100) Si MOSFET at different temperatures. The symbols represent the experimental data, the solid curves represent the fit with HLN formula. Reproduced from (a) Kawaguchi and Kawaji.<sup>74</sup> (b) Wheeler.<sup>75</sup>

Many other measurements<sup>77-79</sup> on low-mobility Si MOSFETs have also shown that both weak localization<sup>7</sup> and interaction<sup>9</sup> effects were present in Si inversion layers, and have confirmed the statement that there is no true metal state in 2D. However, though these data have supported qualitatively the theories of Refs. 7,9, there were quantitative discrepancies: unreasonably high value of the interaction parameter  $F$ , obtained in the parallel-field magnetoconductivity experiments<sup>78,79</sup>; lack of  $B/T$  scaling in the magnetoconductance data<sup>77</sup>, etc.

### 3.2.2. High $\mu$ , high $n$ Si MOSFETs

Although a number of experiments on low-mobility 2D systems supported the scaling theory of localization, the experiments on Si MOSFETs with higher mobility have brought some doubts in the validity of this theory.

In 1980, Cham and Wheeler<sup>80</sup> studied the transport properties of Si MOSFET with mobilities ranging from  $0.24 \text{ m}^2/\text{Vs}$  to  $2.2 \text{ m}^2/\text{Vs}$  at relatively high electron densities (of the order of  $1 \times 10^{12} \text{ cm}^{-2}$ ). In the experiments, a negative substrate bias  $V_{sub}$  was applied to increase the quality of the devices<sup>81,i</sup>. The authors of Ref. 80 observed that the resistivity of Si MOSFET decreased almost linearly with cooling instead of a logarithmic increase (Figure 3.5) as was predicted by the interaction and localization theories.<sup>7,9</sup>

---

<sup>i</sup> The increase of the quality of low- $\mu$  Si MOSFETs with applying  $V_{sub} < 0$  has been attributed to the reduction of scattering processes by electrons that occupy very long band tails associated with upper subbands. The reverse  $V_{sub} < 0$  increases the subband splitting and makes this scattering mechanism less important.<sup>81</sup>

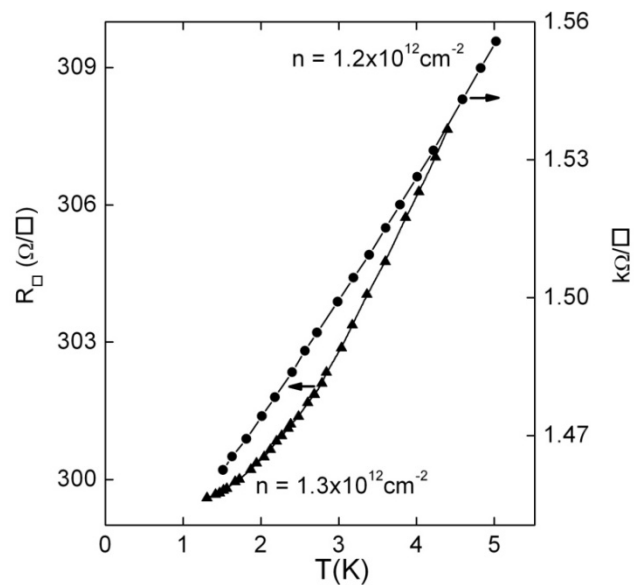


Figure 3.5. The temperature dependence of the resistivity of Si MOSFETs. circles - lower quality device ( $\mu_{\max}(4.2 \text{ K}, V_{\text{sub}} = 0) \approx 0.4 \text{ m}^2/\text{Vs}$ ),  $n = 1.2 \times 10^{11} \text{ cm}^{-2}$ ,  $V_{\text{sub}} = -9.42 \text{ V}$ ; triangulars - higher quality device ( $\mu_{\max}(4.2 \text{ K}, V_{\text{sub}} = 0) \approx 1.5 \text{ m}^2/\text{Vs}$ ),  $n = 1.3 \times 10^{11} \text{ cm}^{-2}$ ,  $V_{\text{sub}} = -17.6 \text{ V}$ . (Adopted from Cham and Wheeler.<sup>80</sup>)

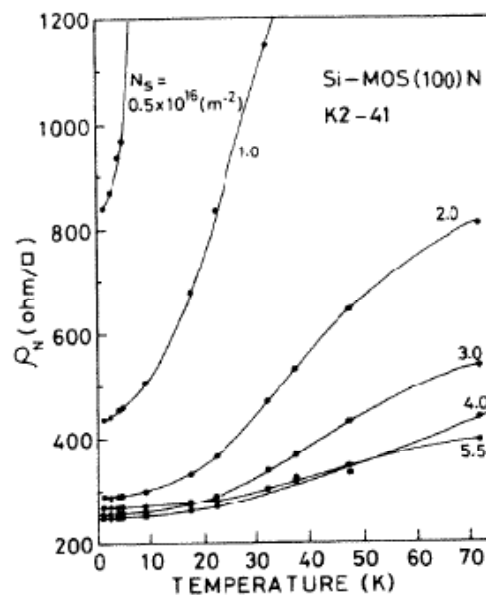


Figure 3.6. The temperature dependence of a (100) Si MOSFET with the peak mobility  $\mu_{\text{peak}} \approx 1.6 \text{ m}^2/\text{Vs}$  (Adopted from Kawaguchi *et al.*<sup>82</sup>)

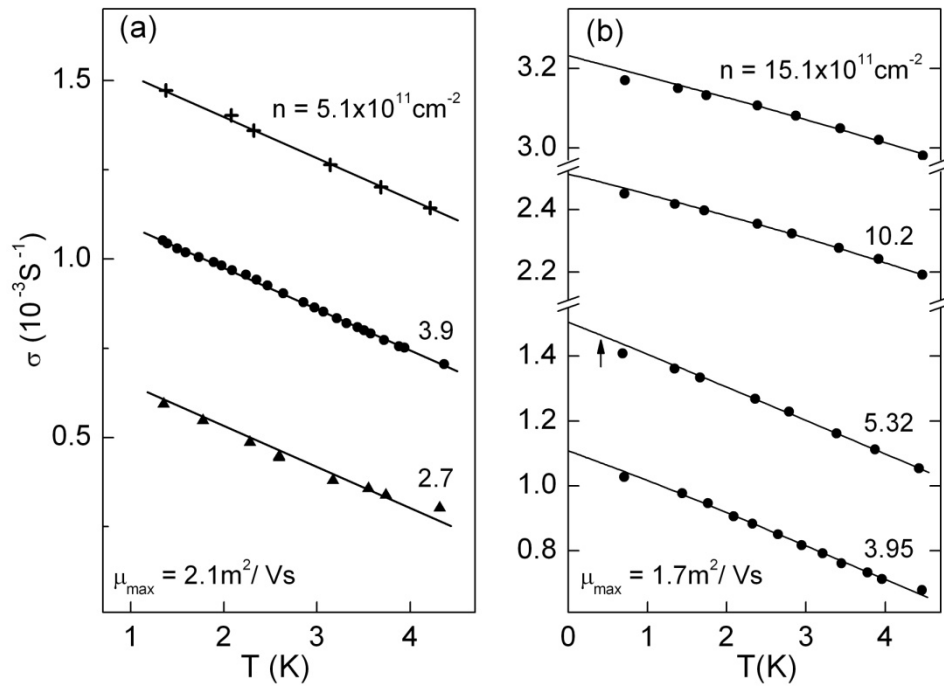


Figure 3.7. The temperature dependence of the conductivity of Si MOSFETs at different electron densities. Data from (a) Dorozhkin and Dolgoplov<sup>83</sup> for the sample with the peak mobility  $\mu_{\text{peak}} \approx 2.1 \text{ m}^2/\text{Vs}$ ; (b) Virodov, Dolgoplov, Dorozhkin, Zhitenev<sup>85</sup> for the sample samples with the peak mobility  $\mu_{\text{peak}} \approx 1.7 \text{ m}^2/\text{Vs}$ .

Kawaguchi *et al.*<sup>82</sup> have also reported a decrease of the resistivity of high-mobility Si MOSFETs with cooling (Figure 3.6).

Dorozhkin and Dolgoplov<sup>83</sup> have measured the conductivity of high-mobility Si MOSFETs (the peak mobilities of the studied samples were in the range  $\mu_{\text{peak}} \approx (1.2\text{-}2.5) \text{ m}^2/\text{Vs}$ ) at high electron densities ( $n \approx (3\text{-}8) \times 10^{11} \text{ cm}^{-2}$ ). Similar to the results of Cham and Wheeler<sup>80</sup> and Kawaguchi *et al.*,<sup>82</sup> the data obtained in Ref. 83 contradicted the expectations based on the WL theory: the conductivity increased almost linearly in the studied temperature range (1.3–4.2) K (Figure 3.7). The peculiar behavior of the conductivity of high-mobility Si MOSFETs was also reported in other experiments<sup>84,85</sup>.

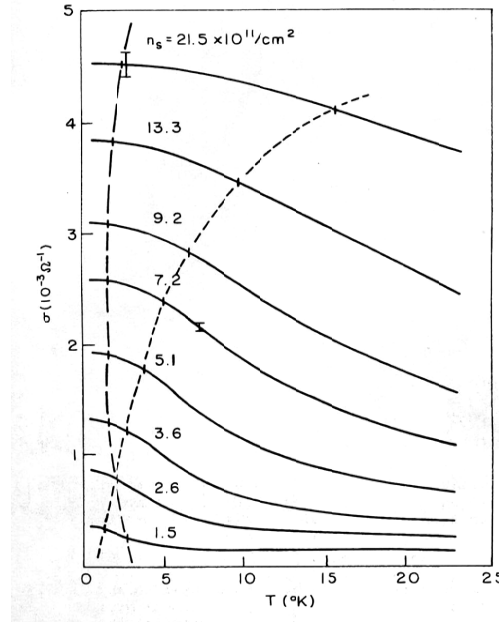


Figure 3.8. The temperature dependence of the conductivity for a Si MOSFET sample with the peak mobility  $\mu_{\text{peak}}(0.2\text{K}) \approx 2.4 \text{ m}^2/\text{Vs}$  for different electron densities. The dashed and dotted curves correspond to  $T = h/2\pi\tau$  and to  $T = 0.1E_F$ , respectively. (Adopted from Smith and Stiles.<sup>84</sup>)

### 3.2.3. High $\mu$ , low $n$ Si MOSFETs

#### Conductivity of high-mobility 2D systems at zero-magnetic field

Further improvement in the quality of Si MOSFETs allowed one to access lower densities without entering the strong localization regime. In 1987 Zavaritskaya and Zavaritskaya<sup>12</sup> reported a peculiar behavior in  $n$ - and  $p$ -type inversion channels in high-mobility Si MOSFETs. At carrier densities smaller than some critical density  $n_c$  ( $(n_c^{(1)} \cong 1 \times 10^{11} \text{ cm}^{-2}$  for electrons in  $n$ -type channels, and  $n_c^{(2)} \cong 3.5 \times 10^{11} \text{ cm}^{-2}$  for holes in  $p$ -channels) the conductivity decreased exponentially with cooling ( $\sigma = \sigma_0 \exp[-(T_0/T)^{1/3}]$ ). This behavior, corresponding to 2D hopping

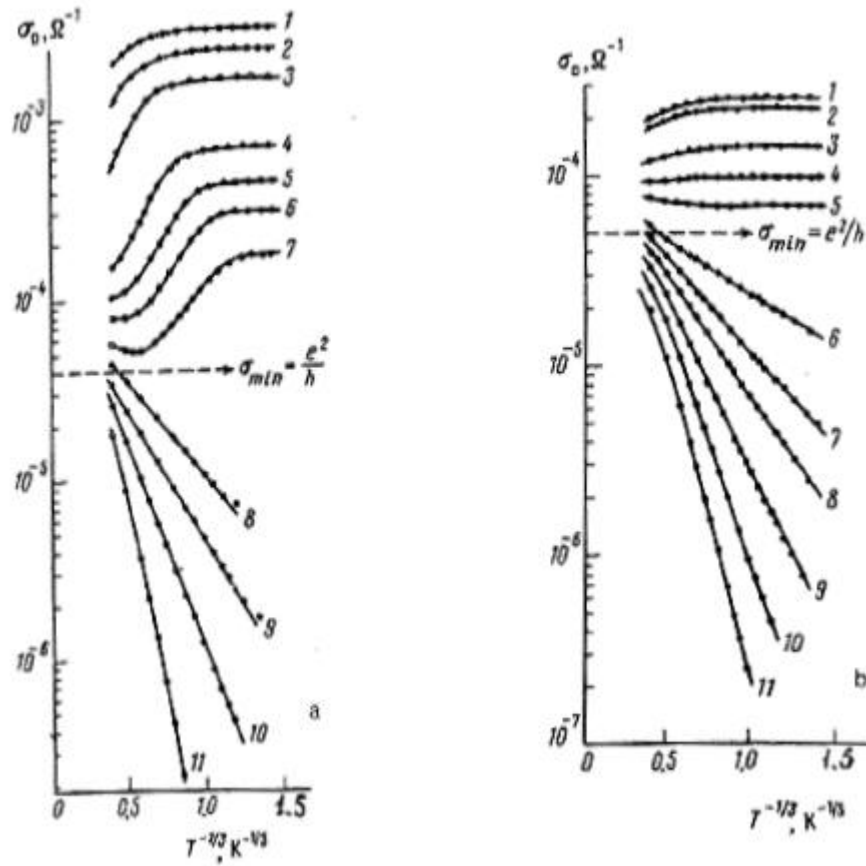


Figure 3.9. The electrical conductivity  $\sigma_{\square}$  versus reciprocal temperature in silicon inversion channels with various carrier densities  $n$  (in units of  $10^{11} \text{ cm}^{-2}$ ). (Left panel). Electrons: 1–10; 2–6; 3–3.8; 4–2.1; 5–1.6; 6–1.25; 7–1.05; 8–11 – less than 1. (Right panel). Holes: 1–12; 2–8; 3–6; 4–5; 5–4.5; 6–11 – less than 4. (Adopted from Ref. 12.)

conductivity<sup>86</sup>, was observed previously in 2D systems. At carrier densities slightly smaller than  $n_c$  the behavior of the conductivity was completely different:  $\sigma$  increased substantially with cooling. In both  $n$ - and  $p$ -inversion channels there was observed a critical conductivity  $\sigma_c \approx e^2/h$  that corresponded to the crossover between two regions: (i) the region  $\sigma_{\square} \geq \sigma_c$ , where the conductivity increased with cooling; and (ii) the region  $\sigma_{\square} \leq \sigma_c$ , corresponding to the decrease of the

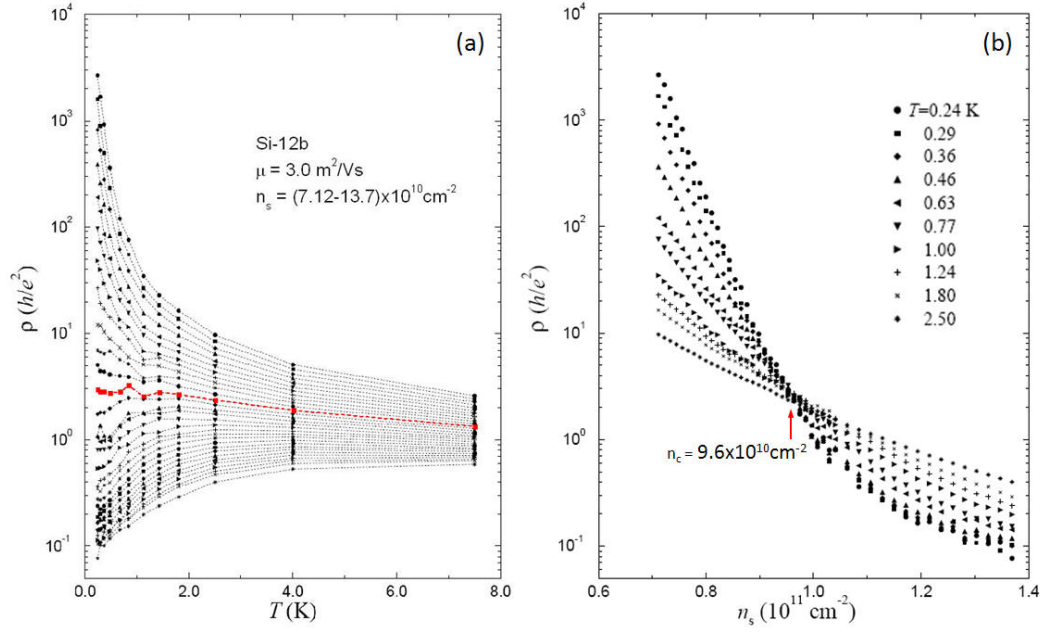


Figure 3.10. (a) The temperature dependence of the resistivity at  $B = 0$  of a high-mobility Si MOSFET (samples Si-12b) with the peak mobility  $\mu_{\text{peak}} = 3 \text{ m}^2/\text{Vs}$  at different electron densities ranging from  $17.12 \times 10^{10} \text{ cm}^{-2}$  (the top curve) to  $13.7 \times 10^{10} \text{ cm}^{-2}$  (the bottom curve). (b) The dependences of the resistivity on electron density for different temperatures at  $B = 0$  for sample Si-12b. (Adopted from Ref. 13.)

conductivity as  $T \rightarrow 0$ . Authors of Ref. 12 observed that in the devices with weaker disorder the metallic behavior was more pronounced. To our best knowledge, this was the first observation of the apparent 2D metal-to-insulator transition.

In 1994 the apparent 2D MIT in Si MOSFETs was rediscovered by Kravchenko *et al.*<sup>13</sup>, who conducted a more detailed study of the temperature dependence of the resistivity of high-mobility (up to  $7.1 \text{ m}^2/\text{Vs}$ ) Si MOSFETs at zero magnetic field. The authors of Ref. 13 have reported the apparent 2D MIT at the critical carrier density  $(0.85\text{-}0.96) \times 10^{11} \text{ cm}^{-2}$ .



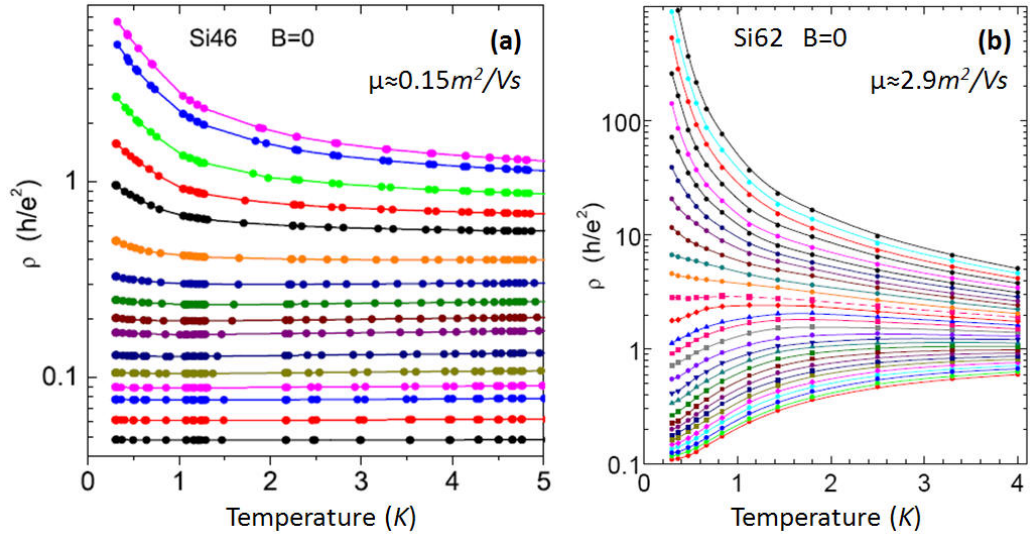


Figure 3.11. The resistivity vs. temperature for disordered Si MOSFET samples with the peak mobilities (a)  $\mu = 1.5 \text{ m}^2/\text{Vs}$  and (b)  $\mu = 2.9 \text{ m}^2/\text{Vs}$ . The densities (in units of  $10^{11} \text{ cm}^{-2}$ ) span (from top to bottom) (a) 3.85 to 37.0, (b) from 0.6936 to 1.326. (Adopted from Ref. 87.)

The main result of Ref. 13 is presented on Figure 3.10(a), which shows the temperature dependences of the resistivity at  $B = 0$  of a high-mobility Si MOSFET ( $\mu_{\text{peak}} = 3.0 \text{ m}^2/\text{Vs}$ ) for different electron densities varying from  $0.7 \times 10^{11} \text{ cm}^{-2}$  to  $1.4 \times 10^{11} \text{ cm}^{-2}$ . At low electron densities  $n < n_c = 0.96 \times 10^{11} \text{ cm}^{-2}$  the resistivity monotonically increases as  $T \rightarrow 0$ ; at  $n > n_c$  the temperature behavior of  $\rho$  becomes nonmonotonic: the resistivity increases at  $T \geq 2 \text{ K}$ , whereas below  $2 \text{ K}$  it decreases dramatically (by a factor of 5-7) with cooling. The presence of the critical density  $n_c$  is clearly seen on Figure 3.10(b), which shows the resistivity as a function of electron density for several temperatures. Here all  $\rho(n)$  curves intersect each other within a narrow density range around  $n_c = 0.96 \times 10^{11} \text{ cm}^{-2}$ . Here all  $\rho(n)$  curves

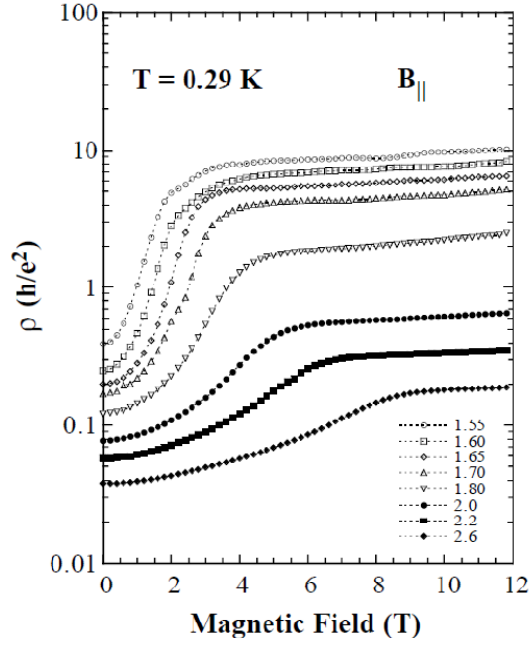


Figure 3.12. The resistivity versus in-plane magnetic field at  $T = 0.29$  K for a Si MOSFET sample. Different symbols correspond to gate voltages from 1.55 to 2.6 V, or, equivalently electron density from  $1.01$  to  $2.17 \times 10^{11} \text{ cm}^{-2}$ . (adopted from Ref. 15.)

intersect each other within a narrow density range around  $n_c \approx 0.96 \times 10^{11} \text{ cm}^{-2}$ , which separates two regimes: insulating ( $d\rho/dT < 0$ ) at  $n < n_c$  and metallic ( $d\rho/dT > 0$ ) at  $n > n_c$ .

Pronounced metallicity is peculiar to the samples with high mobility. Figure 3.11 shows for comparison the temperature dependences of the resistivity of low- and high-mobility samples.<sup>88</sup>

Later, the “metallic” behavior has been observed in practically all high-mobility systems in the low density regime: in conventional Si MOSFETs with low-mobilities ( $0.5\text{--}0.8 \text{ m}^2/\text{Vs}$ )<sup>20</sup>,  $p$ -type<sup>21-24</sup> and  $n$ -type<sup>25,26</sup> GaAs heterostructures, Si/SiGe<sup>27-29</sup>, AlAs quantum wells<sup>30</sup>, inverted Si-on-insulator structures<sup>31</sup>.

### Magnetoresistance of high-mobility 2D systems in a parallel magnetic field

An applied in-plane magnetic field causes dramatic increase of the resistivity of a high- $\mu$  2D system.<sup>14-18</sup> This magnetoresistance is especially pronounced in high-mobility Si SMOFETs:  $\rho$  varies by almost three orders of magnitude<sup>14,15</sup>. An example of MR data<sup>15</sup> is shown in Figure 3.12. In relatively weak fields, the resistivity increases abruptly depending on the electron density (by a factor of 4 for  $n \approx 2.6 \times 10^{11} \text{ cm}^{-2}$ , and more than an order of magnitude for  $n = 1.55 \times 10^{11} \text{ cm}^{-2}$ ). The resistivity saturates at high fields ranging from 2 T (for the lowest measured density) to 9 T (for the highest density), and remains almost constant up to highest field of 12 Tesla.<sup>15</sup> This giant positive magnetoresistance in Si MOSFETs varies continuously across the MIT:<sup>89</sup> it is qualitatively the same for carries densities above and below the zero-field critical density  $n_c$ .

### Suppression of the metallic state by a magnetic field

It was found that a magnetic field applied parallel to the plane of 2DEG in Si MOSFET destroys the metallic state: a high magnetic field drives a 2D system from a zero-field metallic behavior ( $d\rho_{xx}/dT > 0$ ) into a high-field insulating behavior ( $d\rho_{xx}/dT < 0$ ).<sup>14-19</sup> The suppression of the metallic state is shown in Figure 1.5(b), taken from Okamoto *et al.*<sup>16</sup> Similar to the data presented on Figure 3.10(b) an apparent MIT at  $B = 0$  is clearly observed at  $n_c \approx 1.0 \times 10^{11} \text{ cm}^{-2}$ ; the metallic behavior of the resistivity ( $d\rho_{xx}/dT > 0$ ) corresponds to the density range  $n > n_c$ . An in-plane magnetic field of 9 T destroys the metallic state: in the

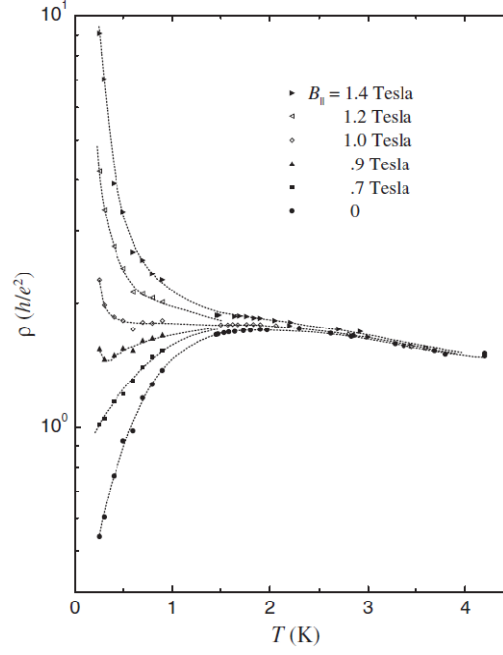


Figure 3.13. The resistivity versus temperature for five different magnetic fields applied parallel to the plane of a low-disordered Si MOSFET. The electron density is  $8.83 \times 10^{10} \text{ cm}^{-2}$ . The critical density of the MIT for this sample is  $n_c \approx 8.5 \times 10^{10} \text{ cm}^{-2}$ . (Adopted from Ref. 14.)

whole studied density range the resistivity shows only the insulating behavior ( $d\rho_{xx}/dT < 0$ ).

Another example of the suppression of the metallic behavior of a 2D system by a magnetic field is shown in Figure 3.13, where the resistivity is plotted as a function of temperature for different in-plane magnetic fields for a high-mobility Si MOSFET at an electron density slightly higher than the critical density for this sample.<sup>14</sup> For a zero-field (the lowest curve) the resistivity is slightly increasing with cooling down to  $T \approx 2 \text{ K}$ , then it decreases sharply as  $T$  continues to decrease. Applied in-plane magnetic field suppresses the metallic behavior completely: at  $B = 1.4 \text{ T}$  (the upper curve) the insulating behavior is observed over the entire temperature range. It was

suggested in Ref. 14 that the metallic state observed at densities  $n > n_c$  is unstable against an arbitrary weak magnetic field in the limit of  $T \rightarrow 0$ .

### Full spin polarization

Okamoto *et al.*<sup>16</sup> and Vitkalov *et al.*<sup>90,91</sup> concluded from the analysis of Shubnikov-de Haas oscillations in Si MOSFETs at relatively high densities that the onset of the saturation of MR corresponds to the field of complete spin polarization  $B_{pol.}$ :

$$g^* \mu B_{pol.} = 2E_Z, \quad (3.6)$$

where  $g^*$ ,  $\mu$ ,  $E_Z$  are effective  $g$ -factor, the Bohr magneton and the Fermi energy, respectively. Pudalov *et al.*<sup>92</sup> shown that, although the saturation field  $B_{sat.}$  is close to the field of full spin polarization ( $B_{sat.} \approx B_{pol.}$ ),  $B_{sat.}$  is actually a sample-dependent parameter: for different samples the saturation might occur at fields that lower, as well higher than  $B_{pol.}$ . In low-mobility Si MOSFETs, in which a metallic regime was not observed, a strong response to a parallel magnetic field is not observed either<sup>93</sup>. Similar results have been reported in  $p$ -GaAs/ $\text{Al}_x\text{Ga}_{1-x}$  heterostructures<sup>94</sup> confirming that strong MR is a characteristic of dilute conducting 2D systems<sup>93</sup>.

## 4. Experimental technique

### 4.1. Experimental set-up

The study of quantum effects in the conductivity of Si MOSFETs requires ultralow temperatures, strong magnetic fields, oriented both perpendicular and parallel to the plane of a 2D system. To get a reliable experimental data, the sample, and all parts of the electronic set-up have to be properly isolated from external electrical noise.

To cool the sample down to 30 mK, we have used S.H.E. He<sup>3</sup>/He<sup>4</sup> dilution refrigerator (model DRS-523), equipped with a gas handling system. The temperature can be controlled within the range 30 mK – 1.2 K. The sample and the ruthenium oxide (RO) thermometer are placed in a mixing chamber of the refrigerator. They are wired to the electronic set-up through two stages of low-pass filters. The electronic set-up consists of (i) LR-700 resistance bridge for measuring the sample's resistance<sup>j</sup> at 13 Hz AC;<sup>k</sup> (ii) AVS-47 resistance bridge for measuring the thermometer's resistance<sup>j</sup>; (iii) Keithley 2400 voltage source for applying a DC voltage to the gate contact of the sample; (iv) American Magnetics AMI-420 and Criomagnetics CS-4 bipolar superconducting magnet power supplies for running a DC current<sup>l</sup> through

---

<sup>j</sup> The resistance is measured using the standard four-terminal AC technique.

<sup>k</sup> Measurements of sample's resistance on our experimental set-up can be also done with a SR-830 lock-in amplifier in combination with differential preamplifier. This allows us to record not only the amplitude, but also the phase shift of the measured voltage across the sample. Besides that, the frequency of AC measurement current can be varied.

<sup>l</sup> American Magnetics AMI-420 and Criomagnetics CS-4 are able to provide a DC current of +/-100A.

two superconducting solenoids, which provide in-plane and normal magnetic fields. All the electronic devices are connected to a computer through GPIB cables.

Our experimental set-up allows us to measure (i) the temperature dependence of the resistivity at fixed magnetic fields  $[\rho(T; \{B_{\parallel}, B_{\perp}\} = \text{const})]$ , (ii) a magnetoresistance (in-plane or perpendicular) at fixed temperature  $[\rho(B_{\parallel}; \{T, B_{\perp}\} = \text{const})]$  or  $[\rho(B_{\perp}; \{T, B_{\parallel}\} = \text{const})]$ , (iii) the dependence of the resistivity on the gate voltage at fixed temperature and magnetic field  $[\rho(V_g; \{T, B_{\parallel}, B_{\perp}\} = \text{const})]$ . We implemented full automatization of each experiment through a set of LabVIEW programs to control all measurements remotely from a computer or even through the Internet.

Some details of the experimental set-up are given below.

#### 4.1.1. Ruthenium oxide thermometer

The temperature of  $\text{He}^3/\text{He}^4$  mixture is determined by a ruthenium oxide ( $\text{RuO}_2$ ) temperature sensor RO2254. This thick film resistor has a nominal resistance of  $1000\Omega$  at room temperature and about  $230\text{ k}\Omega$  at  $30\text{ mK}$ . The sensor can reliably measure temperature from  $40\text{ K}$  down to  $10\text{ mK}$ . Ruthenium oxide sensors have relatively small magnetoresistance: an error of determining millikelvin temperature due to a magnetoresistance effect is less than 3-4% at a magnetic field of  $5\text{ T}$ .<sup>95-97</sup> We have calibrated RO2254 using another calibrated  $\text{RuO}_2$  thermometer (RO600) over a temperature range  $50\text{ mK} - 0.8\text{ K}$  (Figure 4.1).

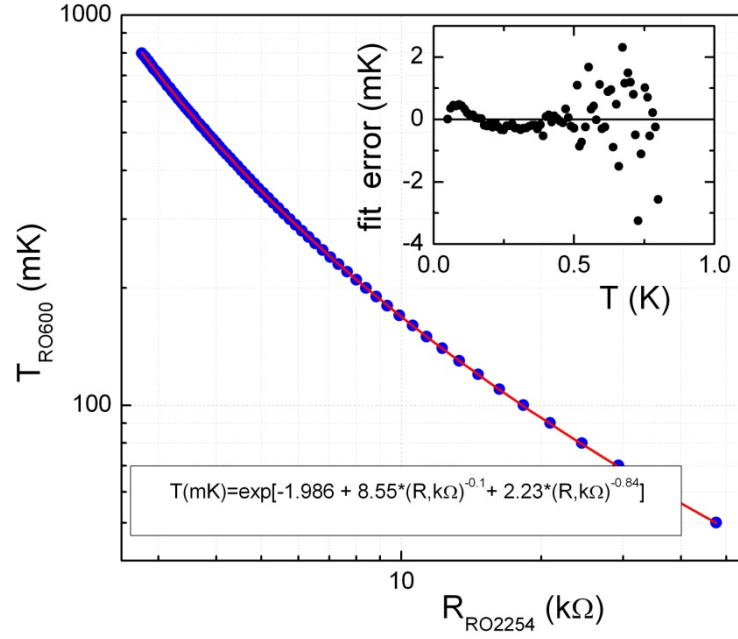


Figure 4.1. Calibration curve of  $RuO_2$  thermometer RO2254.

#### 4.1.2. Cross-magnetic field technique

In order to study orbital and spin effects in 2D electron systems we have used the cross-magnetic field technique<sup>98</sup>, which allowed us to independently control the in-plane component of the magnetic field,  $B_{||}$ , which is coupled to the electron spins, and the perpendicular component  $B_{\perp}$ , which affects both spins and orbital motion of electrons. This technique compares favorably with a more standard method that requires tilting the sample with respect to a fixed direction of the magnetic field (the latter method requires very accurate control of the sample position, which is challenging at ultra-low temperatures). The cross-field set-up consists of two superconducting solenoids made from Ni-Ti superconducting wire (Figure 4.2 and the inset to Figure 4.4). The smallest solenoid has a split-coil form. The axes of these solenoids are oriented at the right angle with respect to each other.



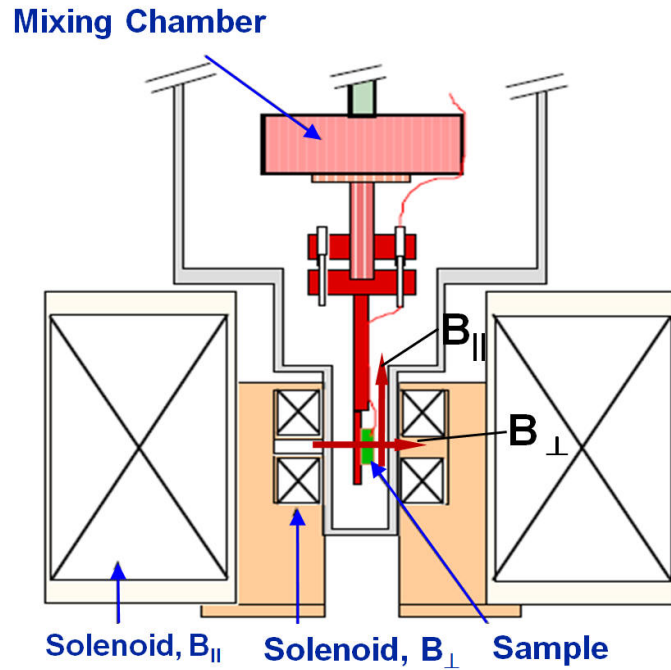


Figure 4.2. Cross-magnetic field set-up. (Adopted from Ref. 98.)

The large solenoid produces an in-plane magnetic field up to 8T, whereas a small split-coil solenoid generates a normal field up to 1.4 T. Two components  $B_{||}$  and  $B_{\perp}$  can be varied independently from each other. The solenoids were calibrated at 300K and 4.2 K using calibrated Hall-effect probes. The magnet constants for large and small solenoids are 0.138 T/A and 0.0270 T/A, respectively. The accessible range of magnetic fields is shown in Figure 4.3. The normalized magnetic field profiles inside solenoids are shown in Figure 4.4. It can be seen that in the center region of two solenoids the in-plane ( $x$ -direction) and normal ( $z$ -direction) fields vary by less than 10% within the volume of  $10 \times 10 \times 20 \text{ mm}^3$ , in the center of the sample holder. These variations are much smaller across our Si MOSFET samples with in-plane dimensions  $0.256 \times 2.5$  and  $0.8 \times 5.0 \text{ mm}^2$ . The described technique facilitates the analysis of the magnetic field dependence of the resistivity.

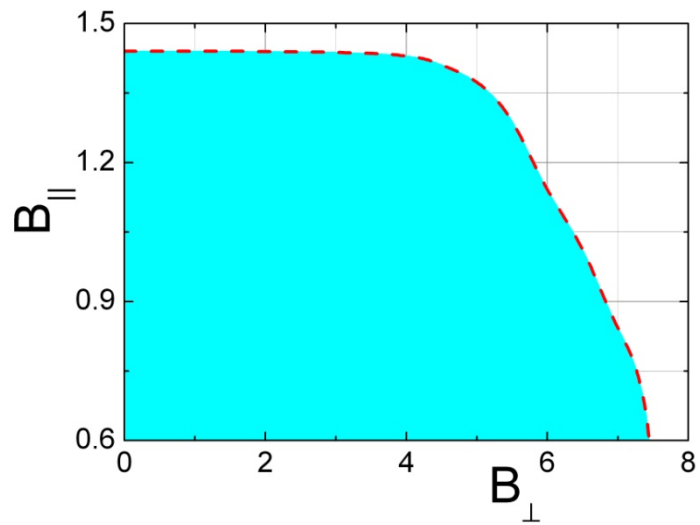


Figure 4.3. Available range of magnetic fields  $B_{\parallel}$  and  $B_{\perp}$ .

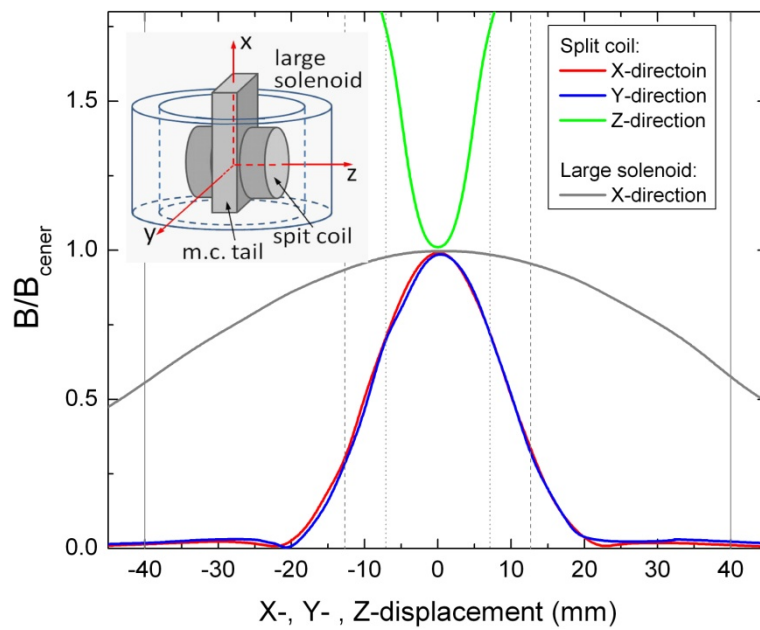


Figure 4.4. Magnetic field profiles for the split coil and the large solenoid. Thin solid lines correspond to the extension of the large solenoid in  $x$ -direction. Dash and dotted lines correspond to the dimensions of the sample space inside the split coil in  $x/y$ - and  $z$ -direction, respectively. The inset shows the schematic picture of two solenoids and a tailpiece of the mixing chamber (m.c.).

#### **4.1.3. Isolation of the experimental set-up from external electromagnetic noise (grounding and filtering)**

External electromagnetic noise can affect detrimentally the low-temperature measurements: it not only decrease the signal-to-noise ratio, but also might overheat the 2D electrons with respect to the  $\text{He}^3/\text{He}^4$  mixture.

There are numerous sources of noise in our laboratory environment, such as high-power machinery, as electrical  $^3\text{He}$  and  $^4\text{He}$  pumps and high-frequency radiation. Improper grounding of the experimental set-up can lead to parasitic currents in ground loops, and, thus also presents a source of noise.

To suppress the noise in our experimental set-up we (i) eliminated all possible ground loops by proper grounding of all electronic devices and the dilution refrigerator itself and made sure that there is only one common ground; (ii) galvanically isolated the pumps from the experimental set-up; (iii) isolated two power lines (for the electronic devices and the power supplies of the superconducting solenoids) from the main power line in the laboratory through uninterrupted power supply (UPS) and through two isolation transformers; (iv) installed an additional small isolation transformer for the LR-700 resistance bridge; (v) optically isolated the GPIB cable from a computer through GPIB-140 fiber optics extender; (vi) isolated a computer from the power line by installing a small UPS.

To improve thermal anchoring of all wires at the base temperature, and to reduce possible overheating of the sample by noise, we installed three silver-powder heat exchangers on Source, Drain and Gate contacts of our Si MOSFET samples. To further reduce the noise level in our dilution refrigerator, we added two stages of low-pass RC filters, at 1K stage, and inside the mixing chamber. The RC filters were

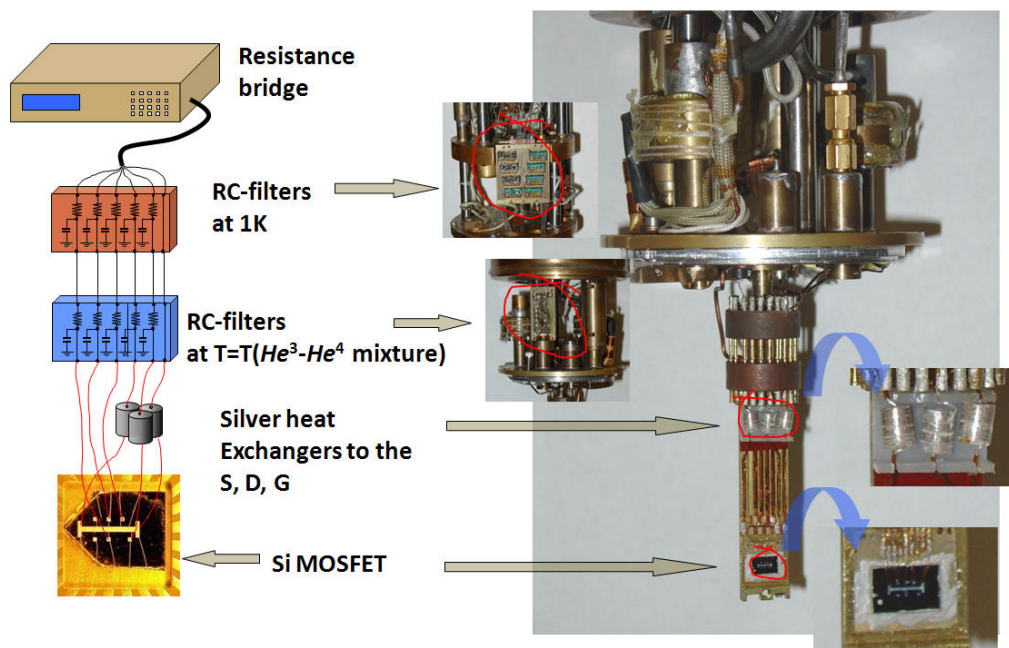


Figure 4.5. Filtering of wires connected to the Si MOSFET sample.

made from the metal film chip resistors ( $10\text{ k}\Omega$  each) and NPO type capacitors ( $4\text{ nF}$  each) with a low temperature coefficient of capacitance. The cut-off frequency of RC filter was  $\sim 4\text{ kHz}$ . Both filter stages were placed in shielded brass boxes to reduced a microwave noise. To suppress the noise from the magnet power supplies, we installed DC feed-through filters at the current leads of the superconducting solenoids.

Proper grounding of the experimental set-up, as well as careful sample's wiring significantly improved the signal-to-noise ratio and eliminated the overheating of 2DEG.<sup>m</sup> Only after these modifications of our experimental set-up the lowest electron temperature of  $30\text{ mK}$  was achieved. Previously in our set-up 2DEG had not been cooled down below  $\sim 150\text{ mK}$ .

<sup>m</sup> See more on electron overheating in Sec. 4.2.2.

#### 4.1.4. Samples studied in this work

The high-mobility Si MOSFET samples were provided by V. M. Pudalov (Lebedev Physical Institute, Moscow, Russia). The carrier density can be varied continuously by the top gate. The samples, studied in this dissertation are Si6-14 ( $\mu \approx 2 \text{ m}^2/\text{Vs}$  at 0.1 K), Si1-46 ( $\mu \approx 2 \text{ m}^2/\text{Vs}$  at 0.1 K), Si39 ( $\mu \approx 0.45 \text{ m}^2/\text{Vs}$  at 0.3 K), Si40 ( $\mu \approx 0.18 \text{ m}^2/\text{Vs}$  at  $T < 4.2 \text{ K}$ ). Typical parameters of 2DEG are listed in Table 1.

Our samples show the apparent 2D MIT at sample depending critical density ranging from  $0.9 \times 10^{11} \text{ cm}^{-2}$  (for high-mobility samples) to  $3.5 \times 10^{11} \text{ cm}^{-2}$  (for low mobility samples). For all samples, the oxide thickness is  $190 \pm 20 \text{ nm}$  and the aluminum gate thickness is approximately  $0.1 \mu\text{m}$ . The samples were fabricated on (001) Si wafer and had a source-drain orientation along [100]. All samples have a Hall bar geometry with in-plane dimensions  $0.256 \times 2.5 \text{ mm}^2$  (for the sample Si6-14) and  $0.8 \times 5.0 \text{ mm}^2$  (for the other samples) (Figure 4.6). Besides the source and the drain contacts, each sample has four potential contacts  $p_1$ ,  $p_3$ ,  $p_4$  and  $p_5$ <sup>n</sup> (Figure 4.6). Contacts  $p_1$ ,  $p_3$ ,  $p_5$  were used for measurements of the longitudinal resistance  $R_{xx} = V_{xx} / I_{SD}$ , whereas contacts  $p_3$  and  $p_4$  were used for measurements the Hall resistance  $R_{xy} = V_{xy} / I_{SD}$ . The homogeneity of the 2D system can be tested by comparing the longitudinal resistivity measured between contacts ( $p_1p_3$ ), ( $p_3p_5$ ) and ( $p_1p_5$ ).

Zero magnetic field measurements are complicated below 1.2 K because of superconductivity in aluminum current/voltage contacts pads and gate electrode.

---

<sup>n</sup> To provide a good Ohmic contact to the inversion layer the regions under all terminals (S, D,  $p_1$ ,  $p_3$ ,  $p_4$  and  $p_5$ ) were heavy  $n^+$ -doped.

Band electron mass down	$m_b$	$0.19m_e$
Dielectric constant at Si-	$\epsilon$	$7.7\epsilon_0$
Effective Bohr radius	$a_B = \epsilon\hbar^2 / m_b e^2$	2.1 nm
Density at the MIT	$n_c$	$1.22 \times 10^{11} \text{ cm}^{-2}$
Fermi wavevector	$k_F = \sqrt{\pi n}$	$(0.8 - 2.2) \times 10^6 \text{ cm}^{-1}$
Fermi wavelength	$\lambda_F = 2\pi / k_F$	(84-30) nm
Fermi velocity	$v_F = \hbar k_F / m$	$(0.4 - 1.2) \times 10^7 \text{ cm} / \text{s}$
Fermi energy	$E_F = (\hbar k_F)^2 / 2m$	1.0-8.8 meV
		12-100 K
Drude resistivity	$\rho_D$	4.4-0.30 k $\Omega$
Transport time	$\tau = m / n\rho_D e^2$	(0.9-1.6) ps
Diffusion constant	$D = v_F^2 \tau / 2$	(8.3 – 120) $\text{cm}^2 / \text{s}$
Mean free path	$l = v_F \tau$	(39-200) nm
Phase coherence time	$\tau_\phi$	56-800 ps
Phase coherence length	$L_\phi = (D\tau_\phi)^{1/2}$	$(210 - 3100) \text{ nm}(T / \text{K})^{-1/2}$
Thermal length	$L_T = (\hbar D / k_B T)^{1/2}$	$(80 - 310) \text{ nm}(T / \text{K})^{-1/2}$
Magnetic length	$L_B = (\hbar / 2eB)^{1/2}$	$18 \text{ nm}(T / \text{K})^{-1/2}$
	$k_F l$	3-43

Table 1. Electron properties of 2DEG in high-mobility Si MOSFET (sample Si6-14, the electron density range  $(1.8-15) \times 10^{11} \text{ cm}^{-2}$ ).

To quench the superconductivity in the Al contacts, the in-plane magnetic field  $B_{||} \approx 0.02 \text{ T}$  was applied for any “zero magnetic field” measurements below 1.2 K.

#### 4.2. Sample characterization

As we emphasized in Section 2.2.5, several parameters are to be determined for the detailed comparison of the low- $T$  behavior of the conductivity of Si MOSFETs with the ZNA theory<sup>35</sup>.

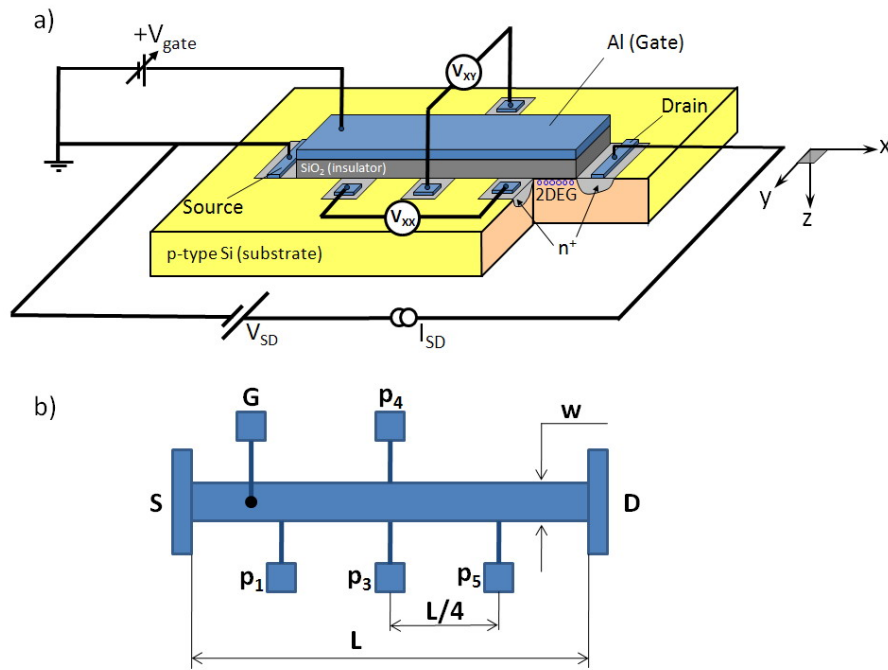


Figure 4.6. Si MOSFET sample: (a) schematic diagram; (b) Hall bar geometry.

A very useful tool in characterizing 2D systems is Shubnikov-de Haas oscillations<sup>o</sup> - SdH oscillation of longitudinal resistivity in a magnetic field, normal to the plane of a 2D system. SdH oscillations also allow us to control the temperature of electrons and, thus, avoid their overheating by measuring current (or noise).

#### 4.2.1. Density of 2D electrons

##### Electron density from the analysis of SdH oscillations

The density of 2DEG confined at the interface is controlled by a gate voltage  $V_g$  and is given by Eq. (3.3). The oxide capacitance  $C_{ox}$  and thus  $A = \epsilon_{ox}/ed_{ox}$ ,<sup>p</sup> is determined mostly by the oxide thickness  $d_{ox}$  and is fixed; whereas threshold voltage

<sup>o</sup> An overview of the phenomenon of Shubnikov-de Haas oscillations is given in Appendix A.

$V_{th}$  can change (within 0.3 V) for different cooldowns (depending on how fast the sample was cooled from room temperature to 4K, at what applied gate voltage this cooling was done, etc.) and remains fixed as long as the sample is maintained at low temperatures (up to a few months). Thus, for every experiment it is crucial to determine these parameters:  $A$  and  $V_{th}$ . The procedure of obtaining  $A$  and  $V_{th}$  is based on the analysis SdH oscillations using the Lifshitz-Kosevich (LK) formula [Eq. (A.6)]<sup>99</sup>. According to Eqs. (3.3) and (A.8), for a fixed density  $n_0(V_0)$  and varied  $B_{\perp}$  the longitudinal resistivity  $\rho_{xx}$  oscillates with the period

$$\Delta(B_{\perp}^{-1}) = \frac{4}{\Phi_0 n_0}, \quad (4.1)$$

and, thus, the parameter  $n_0$  can be found as

$$n_0 = \frac{4}{\Phi_0 \Delta(B_{\perp}^{-1})}. \quad (4.2)$$

The result of obtaining electron density  $n_0$  at some specific gate voltage  $V_0$  is shown in Figure 4.7(a). The solid line depicts the fit of using the LK formula [Eq. (A.8)]. The insert represents the  $(B^*)_{\perp}^{-1}$ -values, at which  $\rho_{xx}$  has local minima versus local minima order numbers (# min). The slope of linear fit to  $B_{\perp}^{*-1}(\# \text{ min})$  dependence gives the value of the period  $\Delta(B_{\perp}^{-1})$ , from which one can calculate  $n_0$  using Eq. (4.2). Both fits, shown in Figure 4.7(a) and on the insert to Figure 4.7(a), give the same value for the density:  $n_0 = 12.25 \times 10^{11} \text{ cm}^{-2}$ .

---

<sup>p</sup> In our Si MOSFET samples this geometric capacitance is of the order of  $\sim 700$  pF.



The expression for the parameter  $A$  can be obtained as follows. From the Eq. (A.8) one can obtain the period of SdH oscillations  $\Delta V_g$  for a fixed  $B_\perp$  and a varied density:

$$\Delta V_g = \frac{4B_\perp}{A\Phi_0}, \quad (4.3)$$

and, thus,

$$A = \frac{4B_\perp}{\Phi_0} \frac{1}{\Delta V_g}. \quad (4.4)$$

The insert on Figure 4.7(b) shows the dependence of the gate voltage values corresponding to the minima of the resistivity  $V_g^* = \{V_g : \rho = \text{local min}\}$  on the order numbers of such minima. The slope of  $V_g^*(\# \text{ min})$  gives the value of  $\Delta V_g$ .

Having determined the electron density  $n_0$  for some specific gate voltage  $V_0$ , the value of the threshold voltage can be obtained:

$$V_{th} = V_0 - \frac{n_0}{A}. \quad (4.5)$$

### Electron density from Hall measurements

Electron density can also be determined from Hall measurements in weak magnetic fields. When a magnetic field is applied normally to a 2D sample a flow of currents generates a Hall voltage in the direction perpendicular to the current flow. When a magnetic field is weak, the Hall voltage changes linearly with changing  $B$ . The flow of current between the source S and the drain D in the presence of a weak, oriented in  $z$ -direction, magnetic field (Figure 3.1), generates a Hall voltage  $V_{xy}$  between the contacts  $p_3$  and  $p_4$ :

$$V_{xy} = \frac{1}{ne} I_{SD} B_\perp \quad (4.6)$$

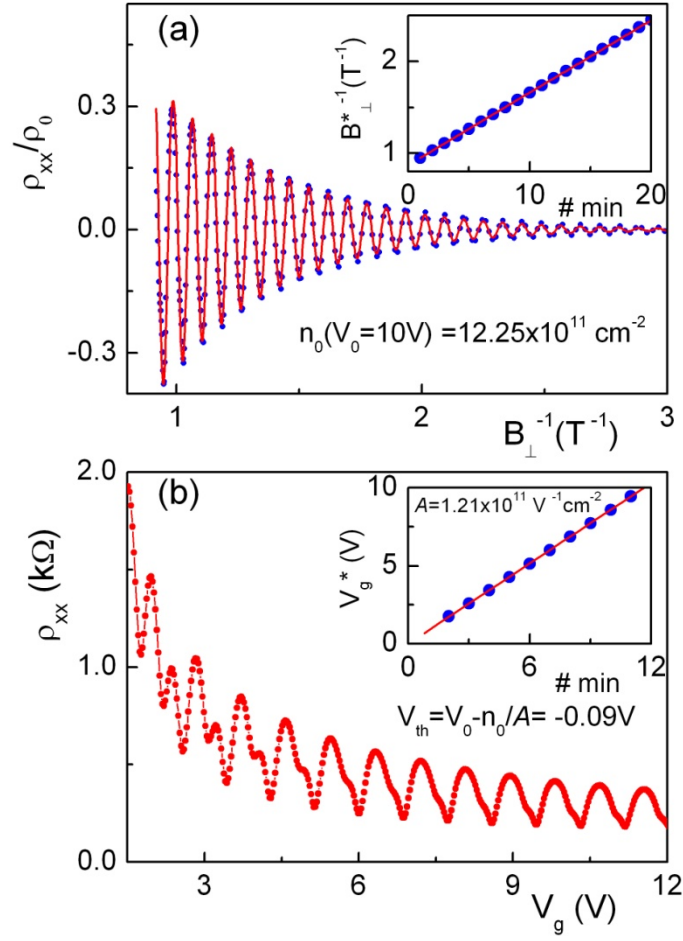


Figure 4.7. (a) The SdH oscillations for sample Si6-14 at  $T = 30$  mK and  $V_0 = 10$  V (circles) and the fit using the LK formula (A.6). The insert shows the dependence  $B_{\perp}^{*-1} = \{B_{\perp}^{-1} : \rho = \text{local min}\}$  as a function of local minimum order number (circles), and a linear fit (line). (b) The dependence of  $\rho_{xx}$  vs.  $V_g$  for sample Si6-14 at  $T = 30$  mK,  $B_{\perp} = 1.08$  T. The insert shows the dependence of  $V_g^* = \{V_g : \rho = \text{local min}\}$  as a function of local minimum order number (circles) and a linear fit (line).

According to Eq. (4.6), the Hall resistance  $\rho_{xy}(B_{\perp}) \equiv V_{xy} / I_{SD}$  in a weak magnetic

field is linear in  $B_{\perp}$ :

$$\rho_{xy} = \frac{B_{\perp}}{ne}. \quad (4.7)$$

By measuring the slope  $d\rho_{xy} / dB_{\perp}$  one can determine an electron density.

The density of 2DEG in our Si MOSFET samples was found from the period of SdH oscillations and the dependence of Hall resistance on a magnetic field. Both results were consistent with each other within 2% in the studied range of densities  $n = (2-30) \times 10^{11} \text{ cm}^{-2}$ ; this uncertainty of  $n$  is insignificant for the analysis of  $\sigma(T, B)$  dependences.

#### 4.2.2. Temperature of 2D electrons

As was mentioned in Section 4.1.3, 2D electrons can be easily overheated by external noise. Thus, one has to make sure that the reading of the RO thermometer coincide with the electron temperature and that the 2DEG is in a good thermocontact with the  $\text{He}^3/\text{He}^4$  mixture.

As an “internal” thermometer that measure the electron temperature, we have used SdH oscillations. For a fixed electron density, an amplitude of oscillations  $A$  monotonically decreases with temperature (Figure 4.8). Thus, to find out how cold the electrons are, one can measure the temperature dependence of the amplitude of SdH oscillations at some fixed density, and then analyze the result using the LK theory.

$$A(T) = \left[ \delta\sigma_{xx}(B_{\perp}^{\max}, T) - \delta\sigma_{xx}(B_{\perp}^{\min}, T) \right] / \sigma_0 \quad (4.8)$$

In Eq. (4.8)  $B_{\perp}^{\min}$  and  $B_{\perp}^{\max}$  determine the positions of the minimum and the maximum of a single oscillation. Each term is given by Eq. (A.8). Figure 4.9 shows that the temperature dependences of an amplitude of SdH oscillation for two different samples (circles) follow the theoretical dependences (solid curves) down to 30mK. Prior to the modification to the experimental set-up that evolved through filtering of all wires, the lowest achievable electron temperature was  $\sim 150 \text{ mK}$  (an experimental curve  $A(T)$

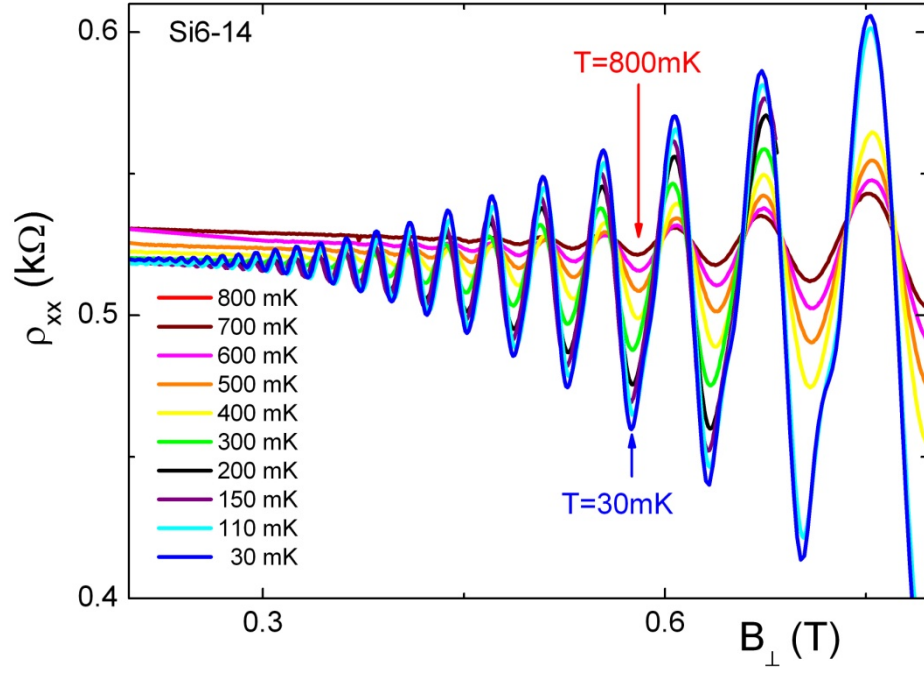


Figure 4.8. SdH oscillations for sample Si6-14 ( $n = 6.1 \times 10^{11} \text{ cm}^{-2}$ ) at different temperatures ranging from 800 mK (red curve) down to 30 mK (blue curve).

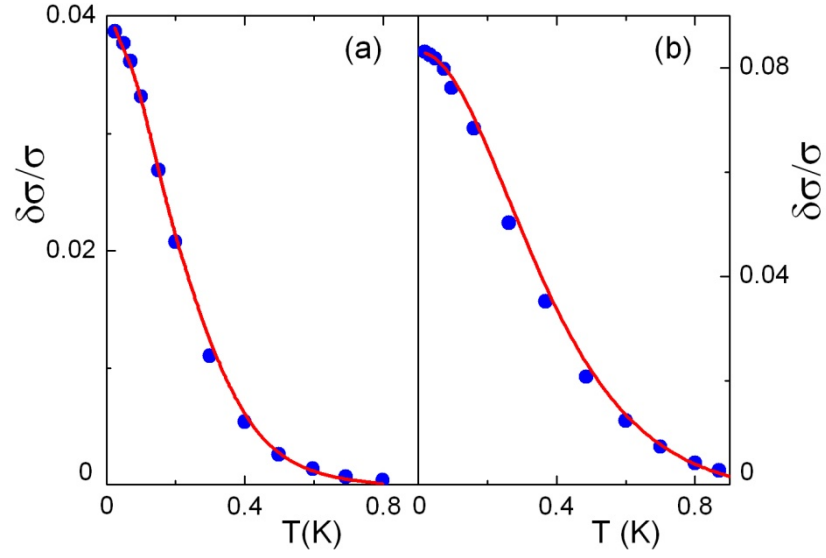


Figure 4.9. The temperature dependence of the amplitude of SdH oscillations for (a) Si6-14 ( $n = 5.5 \times 10^{11} \text{ cm}^{-2}$ ), and (b) Si1-46 ( $n = 6.1 \times 10^{11} \text{ cm}^{-2}$ ). Points show the experimental data, solid curves - the fits using the Lifshitz-Kosevich theory<sup>99</sup>.

saturated below 150 mK ). Thus, Figure 4.9 indicates that filtering and proper grounding indeed significantly reduces heating of 2D electrons in our samples.

Since other than external noise high measuring current  $I_{SD}$  can also overheat 2DEG<sup>100</sup>, in resistivity measurements we always choose (based on the temperature dependence of the amplitude of SdH oscillations) sufficiently small  $I_{SD}$  not to overheat 2DEG: of the order 1-5 nA depending on electron density.

#### 4.2.3. Valley splitting in (001) Si MOSFET

As it was mentioned in Sec. 3.1.2, only two valleys in the electron spectrum are relevant to the transport properties of (001) Si MOSFET at millikelvin temperatures. Those two valleys are in the “ideal” case degenerate: however, a non-zero energy splitting  $\Delta_V$  between the valleys can be caused, for instance, by a slight misorientation of the plane of a 2D layer with respect to the (001) crystallographic plane.<sup>6</sup>

Since a non-zero valley splitting results in the appearance of the beatings in SdH oscillation pattern<sup>101</sup>, the analysis of these beatings using the LK formula [Eq. (A.8)] allows us to estimate the energy splitting  $\Delta_V$ .<sup>40</sup> Figure 4.10 shows the SdH patterns for samples Si6-14 and Si1-46 (the electron densities are  $6.1 \times 10^{11} \text{ cm}^{-2}$  and  $10 \times 10^{12} \text{ cm}^{-2}$ , respectively). The amplitude of SdH oscillations normalized by the first harmonic  $A_1$  is expected to be field-independent if  $\Delta_V = 0$ . However, as Figure 4.10 shows, a noticeable reduction of the SdH amplitude is observed for both samples at small fields, which can be attributed to a finite valley splitting. Although the node of SdH oscillations (expected at  $B \approx 0.15 \text{ T}$ ) cannot be resolved at mobility

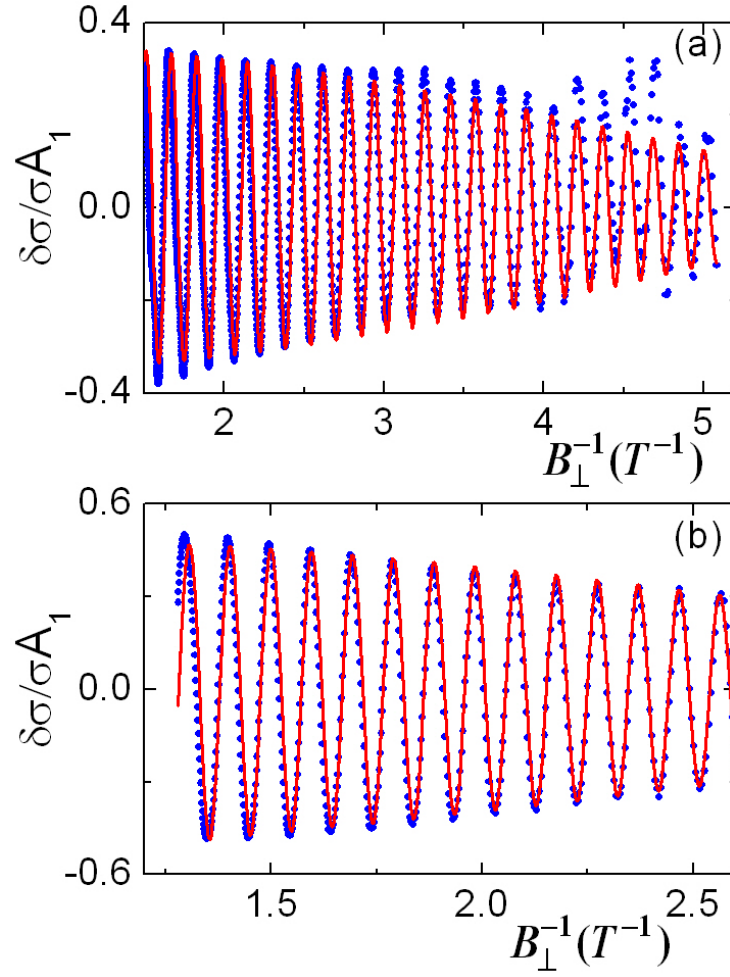


Figure 4.10. Shubnikov-de Haas oscillations normalized by the amplitude of the first harmonic  $A_1$ : (a) sample Si6-14,  $n = 6.1 \times 10^{11} \text{ cm}^{-2}$ ,  $T = 36 \text{ mK}$ ; (b) sample Si1-46,  $n = 1 \times 10^{12} \text{ cm}^{-2}$ ,  $T = 200 \text{ mK}$ . Dots represent the experimental data, solid curves – the theoretical dependences (A.8) modified for a finite  $\Delta_V$  and calculated for  $\Delta_V = 0.4 \text{ K}$  and  $0.7 \text{ K}$  for samples Si6-14 and Si1-46, respectively.

$\mu \approx 2 \text{ m}^2/\text{Vs}$ ,  $\Delta_V$  can be estimated from fitting of the  $B$ -dependence of the SdH amplitude with the equation (A.8), modified for the case of a finite  $\Delta_V$ :  $\Delta_V \cong 0.4 \text{ K}$  for sample Si6-14 and  $0.7 \text{ K}$  for Si1-46 (Figure 4.10). The estimate provides the upper limit for  $\Delta_V$  at  $B = 0$ : in non-zero  $B_\perp$  fields,  $\Delta_V$  may be enhanced by inter-level interaction effects<sup>6,102</sup>.

## 5. Renormalization of electron parameters due to electron-electron interactions

To understand the nature of the metallic behavior and the MIT in 2D, it is very important to characterize quantitatively electron-electron interactions, which are believed to be the main driving force in these phenomena<sup>35,38</sup>. Within the Fermi-liquid theory, the interaction-driven renormalization of electron parameters (such as spin susceptibility  $\chi^*$ , effective mass  $m^*$  and Landé factor  $g^*$ ),<sup>53</sup> are described by the Fermi-liquid parameters

$$F_0^\sigma = \frac{g_b}{g^*} - 1, \quad F_1^s = 2 \left( \frac{m^*}{m_b} - 1 \right). \quad (5.1)$$

$F_0^\sigma$  describes the interaction in the triplet channel,  $F_1^s$  – in the singlet channel. (Here  $g_b$  and  $m_b$  are the band values of  $g$ -factor and mass, respectively.) Below we present a brief review of the experimental data on renormalization of the effective quasiparticle parameters in Si MOSFETs. These data were obtained by different experimental technique and on different samples.

### 5.1. Spin susceptibility

The spin susceptibility can be expressed in terms of the effective mass and effective  $g$ -factor:

$$\frac{\chi^*}{\chi_b} = \frac{g^* m^*}{g_b m_b} = \frac{F_1^s + 2}{F_0^\sigma + 1} \quad (5.2)$$

where  $\chi_b$  is the band value of the spin susceptibility.

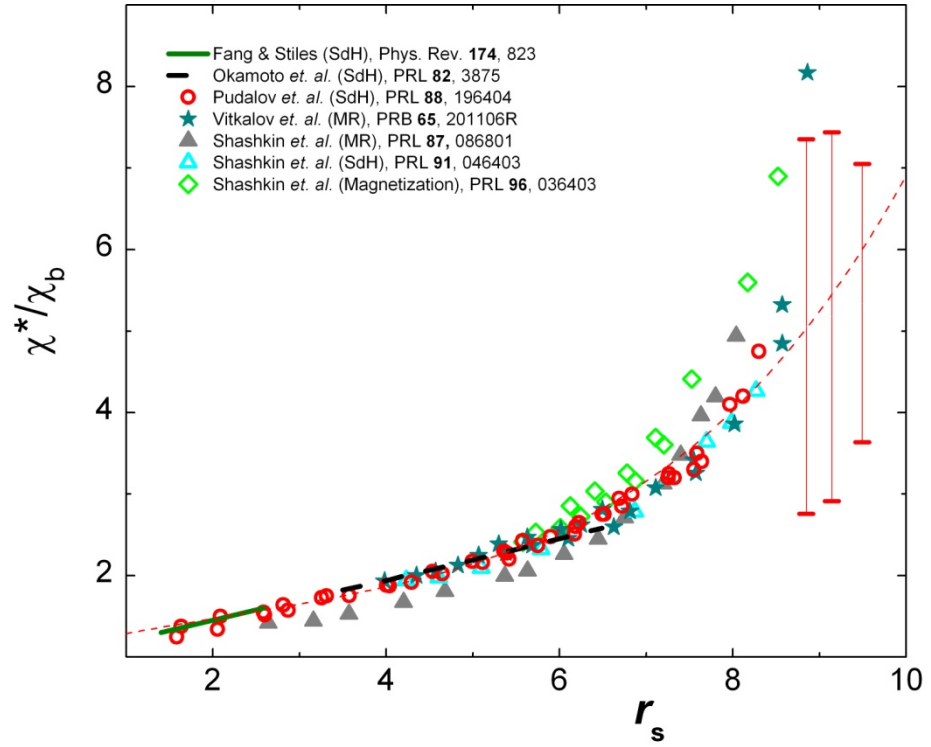


Figure 5.1. Renormalized spin susceptibility, obtained by different experimental groups on different Si MOSFET samples in tiled or crossed magnetic fields (“thick solid line” – Fang and Stiles<sup>104</sup>, “thick dashed line” – Okamoto *et al.*<sup>16</sup>, ○ – Pudalov *et al.*<sup>41,115,103</sup>, △ – Shashkin *et al.*<sup>114</sup>); in strong in-plane magnetic field (★ – Vitkalov *et al.*<sup>106</sup>, ▲ – Shashkin *et al.*<sup>105</sup>); in magnetization measurements (◇ – Shashkin *et al.*). Red bars depict the upper and lower limits on  $\chi^*$  values, determined in Ref. 103. Dashed thin curve shows a polynomial fit of the data measured by Pudalov *et al.*<sup>41,115,103</sup>.

Renormalized spin susceptibility in Si MOSFETs has been measured in different experiments: (i) the analysis of the beating pattern of SdH oscillations in tilted or crossed weak magnetic fields,<sup>16,104,41</sup> (ii) the magnetoresistance (MR) and magnetoconductivity (MC) analysis in strong in-plane magnetic field,<sup>92,105-107</sup> (iii) measuring of a thermodynamic magnetization<sup>108-110</sup>. The synopsis of the data is shown in Figure 5.1.

Taking into account that the data were obtained on different samples (fabricated by different manufactures<sup>16,41,104,105,107</sup>) with the values of peak mobility ranging



between  $1.5 \text{ m}^2/\text{Vs}$  and  $3.4 \text{ m}^2/\text{Vs}$ , there is a remarkable consistency among those data. This indicates that the effect of disorder on renormalization of  $\chi^*$  in the metallic regime is negligible, or at least weak.<sup>115</sup> Below we give an overview of the experimental results on renormalization of  $\chi^*$ .

### 5.1.1. $\chi^*$ from the analysis of SdH oscillations

Analysis of oscillation of the longitudinal resistivity in tilted<sup>16,104,114</sup>, or crossed (where perpendicular and in-plane field components can be varied independently)<sup>41</sup> weak magnetic fields provides information on renormalization of the spin susceptibility.

Fang and Stile<sup>104</sup> measured the spin susceptibility by analyzing the SdH oscillations in a tilted magnetic field. With varying a total magnetic field  $B_{\text{tot}}$  and the tilt angle  $\theta$  ( $B_{\perp} = B_{\text{tot}} \cos \theta$ ) the authors were able to resolve the spin splitting by observing the beating in the SdH pattern and the phase reversal of the fundamental (first harmonic) oscillations related to Landau quantization. The node of beatings and the phase reversal were noticed at some critical angle  $\theta_1$ . Since the value of  $\theta_1$  corresponds to the situation, when the spacing between two adjacent Landau levels is twice that of the spin splitting

$$\hbar \omega_c = 2E_Z \Rightarrow g^* m^* = m_e \cos \theta_1, \quad (5.3)$$

the  $\theta_1(n)$  dependence gave the authors the renormalized values of  $\chi^*(n) \propto \cos \theta_1(n)$ .

Okamoto *et al.*<sup>16</sup> studied the dependence of  $\chi^*(r_S)$  over an extended range of  $r_S$  also using measurements of SdH oscillations in a tilted magnetic field. The authors<sup>16</sup>

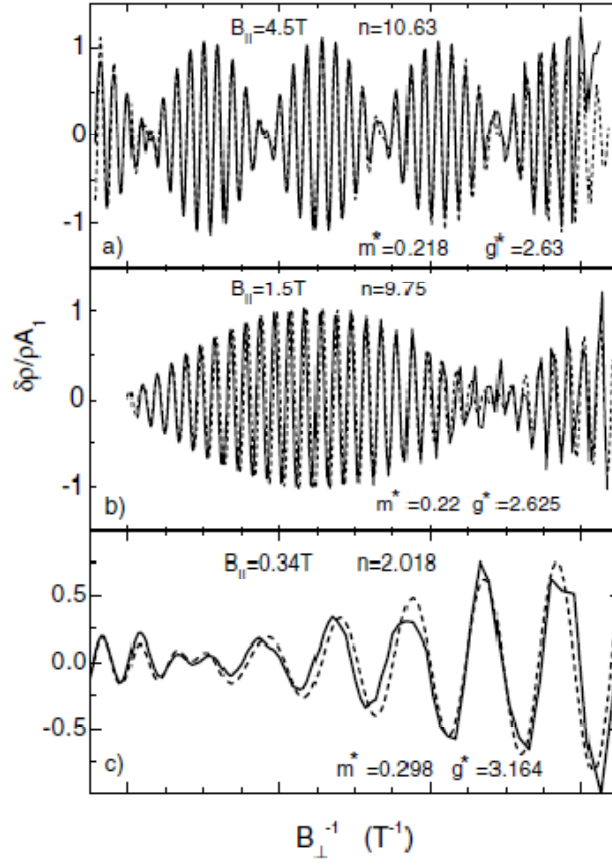


Figure 5.2. Examples of fitting SdH oscillations normalized by the first harmonic  $A_1(B_\perp)$  using the LK formula [Eq. (A.6)]: (a)  $n = 10.6 \times 10^{11} \text{ cm}^{-2}$ ,  $T = 0.35 \text{ K}$ ,  $B_\parallel = 4.5 \text{ T}$ ; (b)  $n = 9.75 \times 10^{11} \text{ cm}^{-2}$ ,  $B_\parallel = 1.5 \text{ T}$ ; (c)  $n = 2.02 \times 10^{11} \text{ cm}^{-2}$ ,  $T = 0.2 \text{ K}$ ,  $B_\parallel = 0.34 \text{ T}$ . The experimental data for samples Si6-14/10 are shown by the solid curves, the fit (with parameters shown) - by dashed curves. (Adopted from Ref. 41.)

extracted  $g^*m^*$  values from the measuring of a critical tilt angle, at which the energy

gap  $\Delta E_{\text{even}} = \hbar e B_\perp / m^* - g^* \mu_B B_{\text{tot}}$ , corresponding to even values of  $\nu/2$

( $\nu = n\Phi_0 / B_\perp$  - filling factor), was equal to the energy gap  $\Delta E_{\text{odd}} = g^* \mu_B B_{\text{tot}}$ ,

corresponding to odd values of  $\nu/2$ :

$$\Delta E_{\text{even}} = \Delta E_{\text{odd}} \Rightarrow g^* m^* = m_e B_\perp / B_{\text{tot}}. \quad (5.4)$$

Pudalov *et al.*<sup>41</sup> have measured the spin susceptibility for a wide range of  $r_s$  by analyzing a beating pattern of SdH oscillations in weak perpendicular and in-plane magnetic fields using a cross-magnetic field technique<sup>98</sup>. According to LK formula [Eq. (A.8)], the interference pattern (including the position of nodes) of SdH oscillations is determined by a term

$$Z_s(E_Z) = \cos \left[ \pi s \left( \frac{\hbar \pi n}{e B_{\perp}} \right) \frac{E_Z}{2 E_F} \right] = \cos \left[ \pi s \left( \frac{g^* m^*}{2 m_e} \right) \frac{B_{\text{tot}}}{B_{\perp}} \right], \quad (5.5)$$

which is a function of the product  $g^* m^*$ , and, hence,  $\chi^*$ . A systematic study of this interference patterns allowed the authors of Ref. 41 to determine  $g^* m^*$  values as a function of electron density with a high accuracy ( $\sim 2\text{-}5\%$ ). An example of a fitting procedure used in Ref. 41 is shown in Figure 5.2.

### 5.1.2. $\chi^*$ from measurement of the field of complete spin polarization

Another technique used to obtain  $\chi^*$  is based on the analysis of the field of complete spin polarization.<sup>16,90-92,105-107</sup> All electrons become fully spin polarized when

$$E_Z \equiv g^* \mu_B B_{\text{pol}} = 2 E_F \quad (5.6)$$

(here  $E_Z$  and  $E_F$  are the Zeeman and Fermi energies, respectively). Taking into account that the Fermi energy in 2D is equal to

$$E_F = \frac{\hbar^2 \pi n}{g_V m^*}, \quad (5.7)$$

(the valley degeneracy  $g_V = 2$  on a (001) surface of Si), one can relate the spin susceptibility to the field of full spin polarization as

$$g^* m^* = \frac{2n\pi\hbar^2}{B_{\text{pol}} g_V \mu_B}. \quad (5.8)$$

Monotonic MR in the in-plane magnetic field exhibits a well-defined saturation at  $B_{\parallel} > B_{\text{sat}}$  for the  $n$ -type Si MOSFETs.<sup>14-18,92,90</sup> Okamoto *et al.*<sup>16</sup> have shown that the saturation field  $B_{\text{sat}}$  corresponds to the field of complete spin polarization:

$$B_{\text{sat}} \approx B_{\text{pol}} = 2E_F / g^* \mu_B. \quad (5.9)$$

The authors<sup>16</sup> observed that the position ( $B_{\perp} / n\Phi_0$ ) of  $\rho_{xx}$  minima, corresponding to the filling factors 4 and 6 (these minima are produced by spin-up electrons), increased linearly with  $B_{\text{tot}}/B_{\text{pol}}$  at,  $B_{\text{tot}}/B_{\text{pol}} < 1$  but saturated for  $B_{\text{tot}}/B_{\text{pol}} > 1$  where the spin polarization is expected to be complete (see Fig. 6 from Ref. 16). Vitkalov *et al.*<sup>90,91</sup> also argued that the saturation of  $\rho_{xx}$  corresponds to the complete spin polarization. The authors of Refs. 90,91 drew this conclusion from the analysis of SdH oscillations in a tilted magnetic field: they observed an increase by a factor of 2 of the frequency of SdH oscillations (versus filling factor  $\nu$ ) for parallel fields greater than the saturation field  $B_{\text{sat}}$ . The abrupt changes in the period was attributed to the onset of full polarization of electron spins.

Another approach to the high-field measurements of  $\chi^*$  is based on the scaling of in-plane MR<sup>105</sup> or MC<sup>106,107</sup> data: the normalized magnetoresistivity  $\rho(n, B)/\rho(n, 0)$  or magnetoconductivity  $\sigma(n, B)/\sigma(n, 0)$  can be collapsed onto a single curve if a magnetic field is scaled to a density dependent field  $B_{\rho}$  (in case of MR measurements) or  $B_{\sigma}$  (in case of MC measurements). The scaling parameters ( $B_{\rho}$  and  $B_{\sigma}$ ) were attributed to the field of complete spin polarization. The authors of

Ref. 105 also claimed that their analysis of MR data shows that  $g$ -factor is practically density independent and is equal to  $g^* \approx 2.8$  (this is in odd with our observations, see below).

### 5.1.3. $\chi^*$ from the analysis of magnetization

Thermodynamic magnetization measurements was performed recently by Prus *et al.*<sup>108</sup>, Shashkin *et al.*<sup>109</sup>, and Anissimova *et al.*<sup>110</sup> The method is based on modulation the in-plane magnetic field, and measuring the imaginary component of AC current between the metal gate and a 2D electron system. This induced current is proportional to  $\partial\mu/\partial B$ , where  $\mu$  is a chemical potential). Using Maxwell relation  $\partial M/\partial n = -\partial\mu/\partial B$ , and then integrating  $\partial M/\partial n$  over electron density, one can obtain the magnetization  $M(B,n)$ . The spin susceptibility  $\chi$  was calculated from the slope  $M(B,n)$  versus  $B$  at small fields.

Magnetization, obtained by Prus *et al.*,<sup>108</sup> has shown a large (7.5 fold) enhancement of the susceptibility at critical density  $n_c$ . This enhancement is in good agreement with the one obtained from SdH measurements<sup>41</sup> (in the latter case, the upper estimate  $g^*m^*/2m_b \approx 7$  at  $n = (7.7-9) \times 10^{10} \text{ cm}^{-2}$  was obtained from the phase of SdH oscillations<sup>115</sup>): spin susceptibility  $\chi^*$  remains finite at  $n_c$ .

## 5.2. Effective mass

In many experiments the data on renormalization of the effective mass  $m^*$  in 2D have been obtained from the temperature dependence of SdH oscillations. Renormalization of the effective mass in Si MOSFETs, obtained in different experiments,<sup>111-115,41</sup> is shown in Figure 5.3.

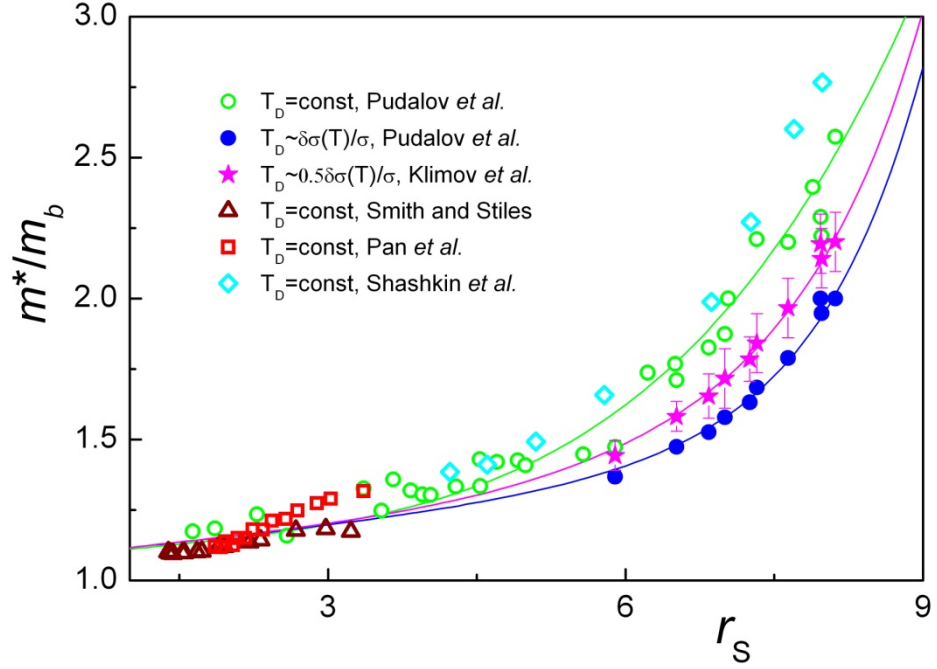


Figure 5.3. Renormalization of effective mass in Si MOSFET, obtained in different experiments.  $T_D = \text{const}$ :  $\circ$ -Pudalov *et al.*<sup>41</sup>,  $\triangle$ -Smith and Stiles<sup>111</sup>,  $\square$ -Pan *et al.*<sup>113</sup>,  $\diamond$ -Shashkin *et al.*<sup>114</sup>;  $T_D^* \approx [1 - \delta\sigma(T)/\sigma_D]$ :  $\bullet$ -Pudalov *et al.*<sup>41</sup>;  $T_D^* \approx [1 - \delta\sigma(T)/2\sigma_D]$ :  $\star$ -Ref. 40.

Whereas observation of the beating of SdH oscillations in crossed magnetic fields offers a straightforward (model-independent) method of finding  $g^* m^*$ <sup>41,98</sup>, an estimate of  $m^*$  is based on model-dependent analysis of the damping factor for the first harmonic of SdH oscillations,  $A_1(T, B_\perp = \text{const})$  given by Eq. (A.8). According to Lifshitz-Kosevich (LK) theory<sup>99</sup>, the damping factor  $A_1(T, B_\perp = \text{const})$  in the limit of  $T \gg \hbar\omega_c$  can be expressed as

$$-\frac{e\hbar}{2\pi^2} \ln \left[ A_1^{LK}(T, B_\perp) \right] B_\perp / m^* \approx (T + T_D). \quad (5.10)$$

Conventional procedure of calculating the effective mass is based on the assumption that the Dingle temperature  $T_D$  that describes broadening of the Landau levels due to collisions [Eq. (A.5)] is  $T$ -independent<sup>111-114</sup>

$$T_D \neq f(T). \quad (5.11)$$

Open symbols on Figure 5.3 correspond to this scenario. However the observed linearity of the dependence  $\ln A_1 \propto T$ <sup>41</sup> does not prove the applicability of the LK theory, which disregards the interaction effects. The assumption (5.11) becomes dubious at high  $r_s$ , where EEI is strong, and the conductivity varies significantly with temperature<sup>41</sup> owing to the interaction corrections<sup>35</sup>.

To take into account the interaction-induced temperature dependence of elastic scattering, Pudalov *et al.*<sup>41</sup> suggested that Dingle temperature should follow the temperature dependence of the conductivity

$$T_D^*(T) \approx T_D \left[ 1 - \frac{\delta\sigma_{xx}(T)}{\sigma_D} \right]. \quad (5.12)$$

The conjecture (5.12) was supported by the theoretical work of Martin *et al.*<sup>116</sup> according to which the damping of the magneto-oscillation is induced by the interplay of interaction and disorder.

Although the authors of Ref. 116 made an important step in understanding the effect of interaction and disorder on magneto-oscillations in 2DEG, their work is incomplete, as was pointed out in a more recent work of Adamov *et al.*<sup>117</sup> In particular, the authors of Ref. 117 have shown that the temperature dependence of damping of SdH oscillations stems from the temperature dependences of *both* the effective mass and the quantum scattering time ; whereas Martin *et al.*<sup>116</sup> argued that

the nonlinear  $T$ -dependence of the damping factor may be attributed either to a  $T$ -dependent renormalization of  $m^*$  or to a  $T$ -dependent  $T_D$ .

Recently, we reanalyzed the SdH data<sup>40</sup> previously measured by Pudalov *et al.*<sup>41</sup> with the theory of Adamov *et al.*<sup>117</sup>. The result of this analysis is presented below.

According to calculations of Adamov *et al.*<sup>117</sup> the damping factor acquires an additional term in both the diffusive and ballistic regimes due to the interference between electron-electron and electron-impurity interaction

$$\begin{aligned} -\frac{e\hbar}{2\pi^2} \ln[A_1(T, B_\perp)] B_\perp / m^* = \\ = T + T_D(1 - 2\pi \mathcal{A} T \tau) = T + T_D \left( 1 - \frac{1}{2} \frac{\delta\sigma(T)}{\sigma_D} \right), \end{aligned} \quad (5.13)$$

where

$$\alpha(T) = -T \frac{\delta m^*}{m^*} - T_D \left( \frac{\delta m^*}{m^*} - \frac{\delta \tau_q^*}{\tau_q^*} \right), \quad (5.14)$$

and

$$\begin{aligned} \frac{\delta m^*(T)}{m^*} &= -\mathcal{A} \times \ln\left(\frac{E_F}{T}\right), \\ \frac{\delta \tau_q^*}{\tau_q^*} &= \mathcal{A} \times \left[ 2\pi T \tau - \ln\left(\frac{E_F}{T}\right) \right], \\ \mathcal{A} &= \left( 1 + \frac{15F_0^\sigma}{1 + F_0^\sigma} \right) \frac{1}{4\pi^2 \sigma_D}, \end{aligned} \quad (5.15)$$

for a system with two degenerate valleys.

The equation for  $\delta m^*(T)/m^*$  resembles the one-loop renormalization of the effective mass (or  $Z$ ) in the RG theory<sup>10,38,64,65</sup>. Our numerical simulations show that within the relevant interval  $T = (0.03 - 0.8)$  K and  $r_S \leq 6$ , the  $\ln T$  terms in Eqs. (5.15) can be replaced with a  $T$ -independent constant. By combining the LK



result within our limited  $T$  range, we obtain the following equation in the ballistic regime for the short-range scattering ( $\tau_q \sim \tau$ ):

$$\begin{aligned} -\frac{e\hbar}{2\pi^2} \ln[A_1(T, B_\perp)] B_\perp / m^* &= \\ &= T + T_D(1 - 2\pi \mathcal{A} T \tau) = T + T_D \left( 1 - \frac{1}{2} \frac{\delta\sigma(T)}{\sigma_D} \right). \end{aligned} \quad (5.16)$$

In this case, the  $T$ -dependent correction to the Dingle temperature,  $\delta T_D(T)/T_D$ , is one half of the interaction correction to the conductivity<sup>q</sup>  $\delta\sigma(T)/\sigma$  (the factor 1/2 originates from the difference between the interaction corrections to the momentum relaxation and quantum scattering times<sup>r</sup>). We note that the empirical procedure used for finding  $m^*$  in Ref. 41 was based on the assumption (5.12), which differs from Eq. (5.16) by a factor 1/2.

Renormalization of  $m^*$ , which follows from the analysis of SdH oscillations data measured by Pudalov *et al.*<sup>41</sup> using the theory of Ref. 117, is shown by stars on Figure 5.3. These  $m^*(r_S)$  can be fitted by a polynomial

$$m^*(r_S) = 0.205m_e(1 + 0.035r_S + 1.2 \times 10^{-4}r_S^4 + 2 \times 10^{-10}r_S^{10})$$

The recalculated data lie in between the  $m^*$ -values obtained from the analysis (of the same SdH data<sup>41</sup>) with the assumptions (5.11) and (5.12), which are shown in Figure 5.3 by open and close circles, respectively.

---

<sup>q</sup> Interaction correction to the conductivity within the ZNA theory [Eqs. (2.43,2.40,2.41)] has the form  $\delta\sigma(T)/\sigma_D = T\tau \left[ 1 + 15F_0^\sigma / (1 + F_0^\sigma) \right] / \pi\sigma_D$ .

<sup>r</sup> The quantum correction to the transport scattering rate  $\tau^{-1}$  differs from that for the quantum scattering rate  $\tau_q^{-1}$  by the term  $(1 - \cos\phi)$  in the integrand, where  $\phi$  is the scattering angle. According to the ZNA theory<sup>35</sup>, the interaction corrections to the conductivity are determined by backscattering events for which  $\phi \approx \pi$ , or  $(1 - \cos\phi) \approx 2$ .

It is worth mentioning that the scattering of  $m^*$  obtained by different groups<sup>111-114,41</sup> is caused mainly by different interpretations of practically identical raw data. At present, the recipe (5.16) based on the theory [117] seems to be the best approach to the SdH data analysis. As will be shown below, the  $F_0^\sigma$ -values obtained from the SdH data using this approach agree with the renormalization of FL parameter  $F_0^\sigma$  determined from the temperature dependence of the conductivity  $\sigma(T)$  using the interaction theory<sup>35</sup> (see Sec. 7.2.5).

### 5.3. Renormalization of Landé $g$ -factor and the Fermi-liquid parameter $F_0^\sigma$

Renormalization of the effective  $g^*$ -factor can be obtained from independent measurements of  $\chi^*$  and  $m^*$ :

$$\frac{g^*}{g_b} = \frac{\chi^* / \chi_b}{m^* / m_b}. \quad (5.17)$$

Given the values of  $g^*$ , one can calculate the Fermi-liquid parameter  $F_0^\sigma$ , using Eq. (5.1). Renormalization of spin susceptibility, effective mass, effective  $g$ -factor and Fermi-liquid parameter  $F_0^\sigma$  in Si MOSFETs is shown in Figure 5.4. The values of  $m^*$ ,  $g^*$  and  $F_0^\sigma$  obtained by Pudalov *et al.*<sup>41</sup> under the assumptions (5.11) and (5.12) are shown in panels (b-d) by open and close circles, respectively. The  $\chi^*$ -values<sup>41</sup> are plotted on panel (a). The  $\chi^*$  values recalculated from the data measured in Ref. 41 using the assumption (5.16) are depicted by stars. On panels (b-d) for comparison we also plotted the  $g^*$  and  $F_0^\sigma$ -values obtained in Ref. 114, where only the assumption (5.11) was used.

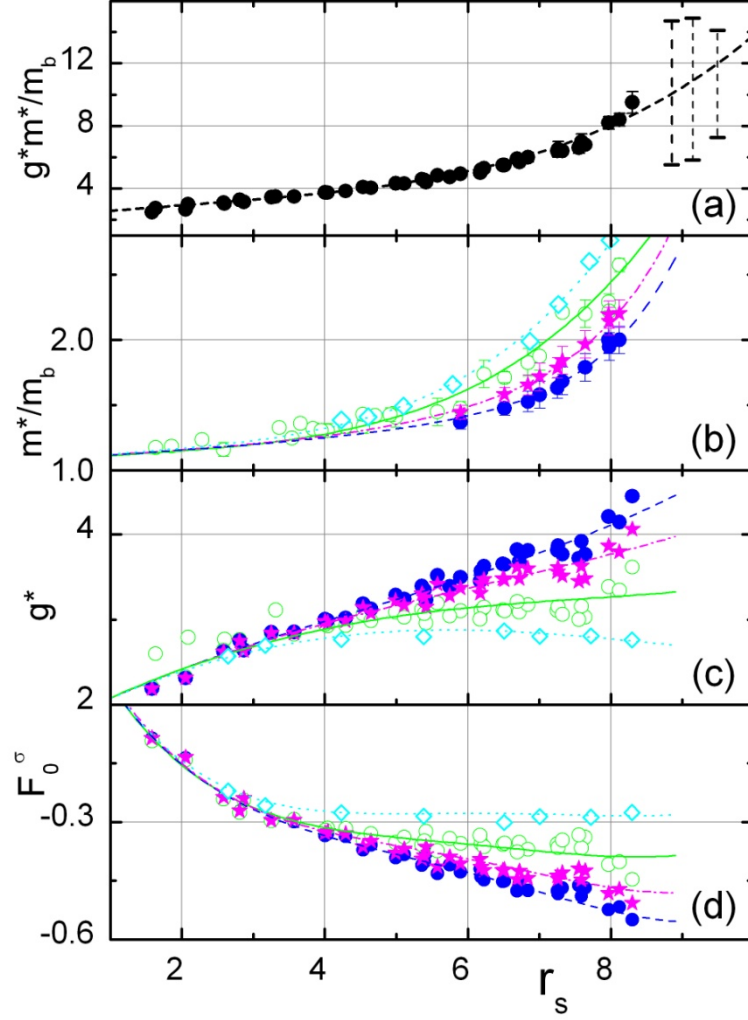


Figure 5.4. Renormalization of (a) the spin susceptibility, (b) the effective mass, (c)  $g$ -factor, and (d) the Fermi-liquid parameter  $F_0^\sigma$ . Symbols on panels b-d correspond to different assumptions as follows:  $\circ$  to assumption (5.11),  $\bullet$  - (5.12),  $\star$  - (5.16). On panels (b-d)  $\diamond$ - depict the data of Shashkin *et al.*<sup>114</sup> [assumption (5.11)].

## 6. Experimental study of intervalley scattering time and WL in Si-based 2D structures

### 6.1. Introduction

As was discussed in Sec. 3.1.2, (001) Si MOSFET is a multivalley system. At low temperatures and low electron densities, only two subbands in the electron spectrum are occupied. These low-energy valleys are almost equivalent: the valley splitting  $\Delta_V$  caused by an asymmetry of the confining potential is typically negligible in comparison with the Fermi energy.<sup>6</sup> When the intervalley scattering is weak, the valley degeneracy strongly affects both electron-electron interaction and weak localization effects in the conductivity. In particular, the interaction effects in Si MOSFETs are strongly amplified by the valley degeneracy,<sup>38</sup> this accounts for the anomalous metallic temperature dependence of the resistivity in high-mobility Si MOSFETs at intermediate temperatures.<sup>13,35</sup> Accordingly, the intervalley scattering plays an important role in the low-temperature phenomena in Si MOSFETs: it may determine the low-temperature cut-off of the metallic-like transport and could also modify the 2D MIT observed in these structures at low electron densities.<sup>13,38</sup> However, prior to our work<sup>39</sup>, there were no systematic study of the intervalley scattering in Si MOSFETs at low  $T$ .

The measurements of WL correction to the conductivity of two-valley systems allow one to study intervalley scattering. The effect of intervalley scattering on WL depends on the relationship between the intervalley scattering time,  $\tau_V$ , and the time of dephasing of the electron wave function,  $\tau_\phi$ . For weak intervalley scattering ( $\tau_V \gg \tau_\phi$ ), two valleys contribute independently to the WL correction to the conductivity, which in this case is expected to be twice as large that for a system with

strong intervalley scattering  $\tau_V \ll \tau_\phi$ <sup>9,118</sup>. In the opposite case ( $\tau_V \gg \tau_\phi$ ), the WL correction is the same as in a single-valley system because the valleys are completely intermixed at the  $\tau_\phi$  time scale.

In numerous measurements of the WL MR in Si MOSFETs,<sup>74-76,79,119,120</sup> the experimental data were fitted using the Hikami-Larkin-Nagaoka (HLN) theory.<sup>45</sup> Interestingly, the factor-of-two enhancement of the WL correction was never observed, indicating that intervalley scattering is rather strong. In order to extract the intervalley scattering time from the WL MR, the measurements should be extended towards higher magnetic fields. However, the HLN theory, which is used for fitting the WL MR, was developed within the diffusive approximation (i.e., small magnetic fields, see below). Therefore, for an adequate description of the effect of intervalley scattering on WL in Si MOSFETs, a theory applicable over a wider range of magnetic fields should be developed.

Only recently such a theory was developed by Averkiev and Taracenko<sup>39</sup> for the quantitative analysis of our experiment.

## 6.2. Experiment

The data for intervalley scattering time  $\tau_V$  were obtained on three representative Si MOSFET samples with high (sample Si6-14) intermediate (Si39) and low (Si40) mobilities (see section 4.1.4 for details). The transport times for these samples within the studied range of  $n$  were  $\tau \approx 2, 0.6$  and  $0.2$  ps, respectively.

The WL MR was measured at  $T = 0.05 - 0.6$  K for high-mobility sample Si6-14, and at  $T = 1.3 - 4.2$  K for samples Si39 and Si40. At these temperatures, the phase breaking time exceeds the transport time by one to two orders of magnitudes. The

magnetic field aligned perpendicular to the plane of Si MOSFET samples was varied from -1 to +1 kG (Si6-14) and from -3 to +3 kG (Si39 and Si40). When sample Si6-14 was measured at  $T < 1$  K, an additional in-plane field  $\sim 200$  G was applied to quench the superconductivity in the current/voltage contact pads and the gate electrode made of thin aluminum film. For reliable extraction of the phase relaxation time  $\tau_\phi$  from the WL MR, we have chosen a small field step size: 1 G for Si6-14 and 3 G for Si39 and Si40. The examples of  $\rho(B)$  data for Si6-14, Si29, and Si40 at fixed density and various temperatures are shown in Figure 6.1(a-c), respectively. Hereafter throughout this chapter we will use magnetoconductance  $\Delta\sigma \equiv \rho(B)^{-1} - \rho(B=0)^{-1}$ .

### 6.3. Fitting the data with Hikami-Larkin-Nagaoka theory

It is a common practice<sup>74-76,79,119-123</sup> to extract the phase breaking time from the WL magnetoconductance using the HLN theory<sup>45</sup>. The equation (2.21) can be expressed in terms  $\tau$  and  $\tau_\phi$ :

$$\Delta\sigma_{HLN}\left(b, \frac{\tau}{\tau_\phi}\right) = \frac{\alpha e^2}{2\pi\hbar^2} \left[ \psi\left(\frac{1}{2} + \frac{\tau}{b\tau_\phi}\right) + \ln \frac{b\tau_\phi}{\tau} \right]. \quad (6.1)$$

Here  $\psi$  is the digamma-function,  $b = B/B_{tr}$  is the dimensionless magnetic field,  $B_{tr} = \Phi_0/2\pi l^2$ ,  $\Phi_0 = \pi\hbar/e$ , and  $l$  is the transport mean free path.<sup>5</sup> The prefactor  $\alpha$  and the dimensionless ratio  $\tau_\phi/\tau$  are treated as fitting parameters. Note that with an increase of the magnetic field, the crossover from the diffusive regime ( $b \ll 1$ ) to the

---

<sup>5</sup> The transport mean free path  $l$  was determined from the formula  $\sigma_D = (e^2/2\pi\hbar) \times k_F l \times n_V$ , where  $k_F = \sqrt{2\pi/n_V}$ ,  $n_V = 2$  for a two-valley system,  $\sigma_D$  is the Drude conductivity, which for simplicity was taken equal to  $\sigma(B=0)$ , the simplification is justified for  $\sigma \gg e^2/2\pi\hbar$ .

ballistic regime ( $b \sim 1$ ) is expected in the WL correction. Equation (6.1) with prefactor  $\alpha = 1$  is the exact result for a single-valley system in the diffusive regime, i.e., at  $\tau_\phi \gg \tau$  and for sufficiently small magnetic fields  $b \ll 1$ .<sup>45</sup> On the other hand, the experimental data are often obtained beyond these limits and, therefore, should be described by more general ballistic theories.<sup>124,125</sup>

In Ref. 126, the HLN theory was numerically compared with the ballistic theory for a single-valley system for various values of  $\tau_\phi/\tau$  and magnetic fields  $b$ . It was found that both approaches agree with each other within a limited range of fields  $b < 0.15$  provided that  $\tau_\phi/\tau > 30$  and the conductivity is much greater than  $e^2/2\pi\hbar^2$ . Thus, within these limits, Eq. (6.1) can be used for extraction of  $\tau_\phi$  from the WL MR in a single-valley system, and the adjustable parameter  $\alpha$  is  $\approx 1$ . For a system with two valleys and weak intervalley scattering, the prefactor  $\alpha$  is expected to be two times larger, because each valley contributes the term  $\Delta\sigma_{HLN}$  with  $\alpha \approx 1$  to  $\Delta\sigma$ . Figure 6.2(a) shows a fit of our typical WL MC curve with Eq. (6.1). The fitting performed over the magnetic field range  $b=0-0.2$  gives  $\tau_\phi/\tau = 133$  and, contrary to the expectation for a two-valley system without intervalley scattering,  $\alpha = 1$ . Changing the magnetic field range, where the data are fitted, causes only minor variations of these parameters [see Figure 6.2(b)]. An attempt to analyze the MC curve using Eq. (6.1) with a fixed prefactor  $\alpha = 2$  results in a much worse fit [dashed line in Figure 6.2(a)]. Several reasons for the reduction of  $\alpha$  in a single-valley system have been considered in Ref. 121, including (i) Maki–Thompson correction, (ii) density-of-states correction, (iii) higher order corrections in  $(k_F l)^{-1}$ , where  $k_F$  is

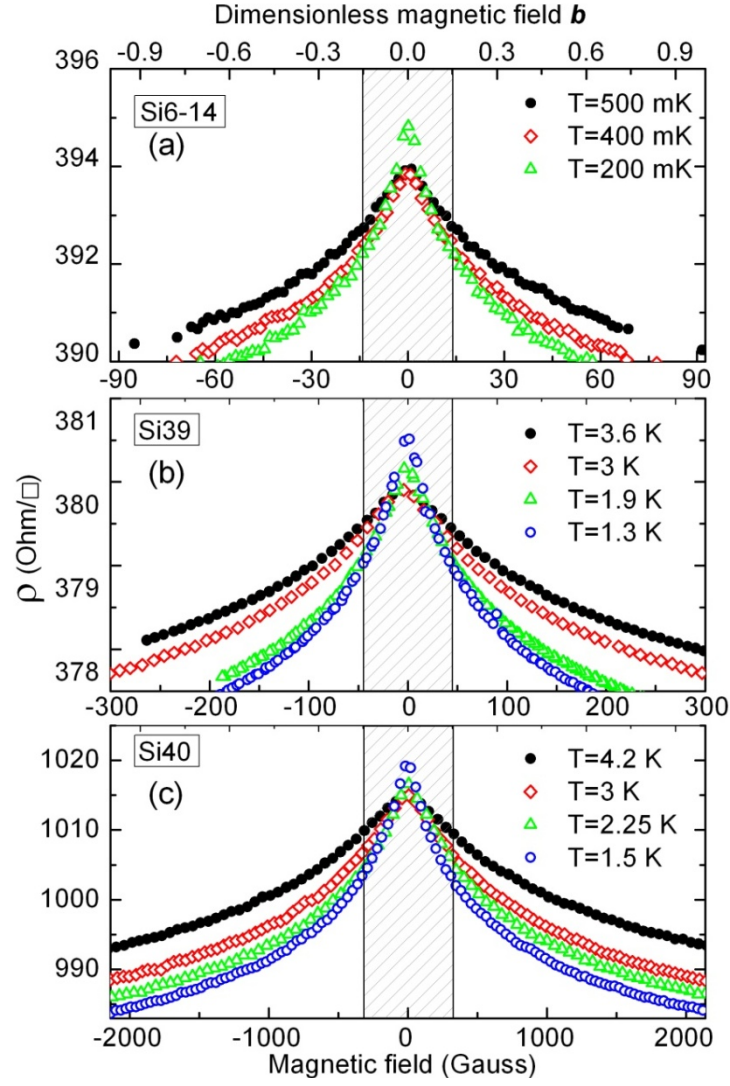


Figure 6.1. Examples of magnetoresistance  $\rho(B)$  data for Si6-14,  $n = 1 \times 10^{12} \text{ cm}^{-2}$  (a); Si39,  $n = 3.36 \times 10^{12} \text{ cm}^{-2}$  (b); and Si40,  $n = 3.5 \times 10^{12} \text{ cm}^{-2}$  (c). The data within the hatched regions have been used to extract the  $\tau_\phi$  value. Upper axes show the magnetic field in units of  $B_r = \Phi_0 / 2\pi l^2$ , lower axes show the field in Gauss.

the Fermi wave vector, and (iv) low  $\tau_\phi/\tau$  ratio. The corrections (i) and (ii) were shown to be small.<sup>121</sup> To ensure that the higher order corrections are also small, we have studied the WL MC only for large conductances ( $\sim 100 \times e^2/2\pi\hbar^2$ ). When the ratio  $\tau_\phi/\tau$  decreases, the HLN theory becomes inadequate, and the fitting procedure



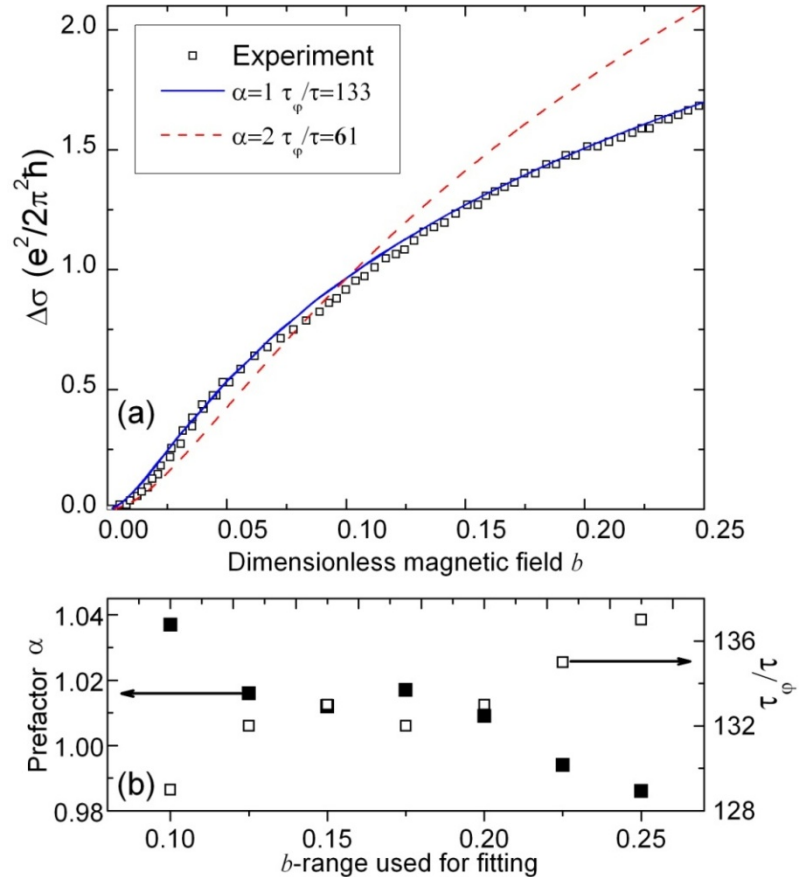


Figure 6.2. (a) Example of the MC data (points) for sample Si40,  $T=1.45$  K and  $n=3.34 \times 10^{12} \text{cm}^{-2}$ . Solid line is calculated using Eq. (6.1) with two fitting parameters  $\alpha=1$  and  $\tau_\phi/\tau=133$ . The dashed curve is an attempt to fit the same data over the same range of  $b$  with a fixed prefactor  $\alpha=2$  and  $\tau_\phi/\tau=61$ . (b) Dependences of the fitting parameters  $\alpha$  (solid squares) and  $\tau_\phi/\tau$  (open squares) on the magnetic field range  $0-b$  which was used for fitting.

results in an artificially reduced prefactor. Correspondingly, we performed measurements at such low temperatures that the inequality  $\tau_\phi/\tau > 30$  was satisfied.

We conclude, therefore, that the aforementioned reasons cannot account for a low value of the prefactor  $\alpha \approx 1$  in the studied multi-valley structures. It should be noted that  $\alpha \approx 1$  in Si MOSFETs was obtained in numerous previous experiments<sup>74-76,79,119</sup>.

We show below that the prefactor reduction can be well-described by the theory which explicitly takes the intervalley scattering into account.

## 6.4. Fitting the data with the ballistic theory

### 6.4.1. Ballistic theory of WL corrections for a two-valley system

A consistent theory that describes the WL correction over a wide range of magnetic fields has been developed by Averkiev and Tarasenko<sup>39</sup> in the framework of the diagram technique. The WL QC to the conductivity arise in the first order in the parameter  $(k_F v_F \tau)^{-1}$ , where the scattering time  $\tau$  is controlled by both *inter*-valley ( $\tau_V$ ) and *intra*-valley ( $\tau_i$ ) scattering processes,

$$1/\tau = 1/\tau_V + 1/\tau_i \quad (6.2)$$

The WL correction to the conductivity in the magnetic field has the form

$$\Delta\sigma(B) = \Delta\sigma^{(a)} + \Delta\sigma^{(b)}. \quad (6.3)$$

where the terms  $\Delta\sigma^{(a)}$  and  $\Delta\sigma^{(b)}$  correspond to the standard diagrams, which have been considered in detail in Refs. 125,127,128. Below we present the final result of calculations of WL QC with the theory of Averkiev and Tarasenko<sup>39</sup>. (The details of the ballistic theory of Averkiev and Tarasenko<sup>39</sup> of WL correction for a two-valley system is given in Appendix C.) We neglect both valley and spin-orbit splitting in Si MOSFETs.<sup>t</sup> Calculations show (see Appendix C) that the corrections have the form

$$\Delta\sigma^{(a)} = -\frac{e^2 b}{2\pi^2 \hbar} \sum_{N=0}^{\infty} C_N P_N^2, \quad (6.4)$$

---

<sup>t</sup> We neglected spin-orbit splitting because no signatures of the antilocalization were observed in our Si MOSFETs down to the lowest temperatures. The theory of Averkiev and Tarasenko<sup>39</sup> treats the valleys as equivalent, assuming  $\Delta_V \tau < 1$ . From the independent estimates (see Sec. 4.2.3) we have verified that the inequality  $\Delta_V \tau < 1$  is satisfied for all studied Si MOS structures. For samples Si6-14  $\Delta_V$  was estimated to be less than 0.4K, for Si39 – less than 2K, and for Si40 – less than 6K. In general, depending on the valley splitting, the weak localization should be described either by the theory developed in Ref. 39 or the theory of Ref. 128 ( $\Delta_V \tau \gg 1$ ).

$$\Delta\sigma^{(b)} = \frac{e^2 b}{2\pi^2 \hbar} \sum_{N=0}^{\infty} (C_N + C_{N+1}) Q_N^2 / 2, \quad (6.5)$$

$$C_N = \frac{2(1 + \tau/\tau_V)}{1 - (1 - \tau/\tau_V)P_N} + \frac{P_N}{1 - P_N} - \frac{(1 - 2\tau/\tau_V)^3 P_N}{1 - (1 - 2\tau/\tau_V)P_N}, \quad (6.6)$$

where the coefficients  $P_N$  and  $Q_N$  are given by

$$\begin{aligned} P_N &= \sqrt{\frac{2}{b}} \int_0^{\infty} \exp\left[-x\sqrt{\frac{2}{b}}\left(1 + \frac{\tau}{\tau_{\phi}}\right) - \frac{x^2}{2}\right] L_N(x^2) dx, \\ Q_N &= \sqrt{\frac{2}{b}} \int_0^{\infty} \exp\left[-x\sqrt{\frac{2}{b}}\left(1 + \frac{\tau}{\tau_{\phi}}\right) - \frac{x^2}{2}\right] \frac{L_N^1(x^2)}{\sqrt{N+1}} dx, \end{aligned} \quad (6.7)$$

here  $L_N$  and  $L_N^1$  are the Laguerre polynomials. Equations (6.3), (6.4), and (6.5) describe the WL MC over the whole range of classically weak magnetic fields  $\omega_c \tau \equiv \mu B < 1$ . In the limit of vanishing intervalley scattering ( $1/\tau_V = 0$ ), Eqs. (6.4) and (6.5) are reduced to the conventional expressions for the WL correction to the conductivity of a single-valley system<sup>127</sup> and, in particular, to the HLN formula<sup>45</sup> in the diffusion regime. The only difference is a prefactor of 2, which accounts for the valley degeneracy. To illustrate the effect of intervalley scattering on the magnetoconductance, we calculated the  $\Delta\sigma(b)$  dependence using Eqs. (6.3), (6.4), and (6.5) for a fixed  $\tau_{\phi}/\tau = 100$  and various values of  $\tau_V/\tau$ . The results are shown in Figure 6.3(a) by solid lines. For comparison, we also calculated the MC using a similar theory<sup>125</sup> developed for a single-valley system (dotted line). We then fitted these dependences over the range  $b < 0.15$  using the HLN theory [Eq. (6.1)] with two fitting parameters, the prefactor  $\alpha$  and  $\tau_{\phi}/\tau$ . In other words, we fitted the theoretical curve the same way as the experimental data have been fitted above in Sec. 6.3.

Figure 6.3(b) shows the resultant fitting parameters; for completeness, we also

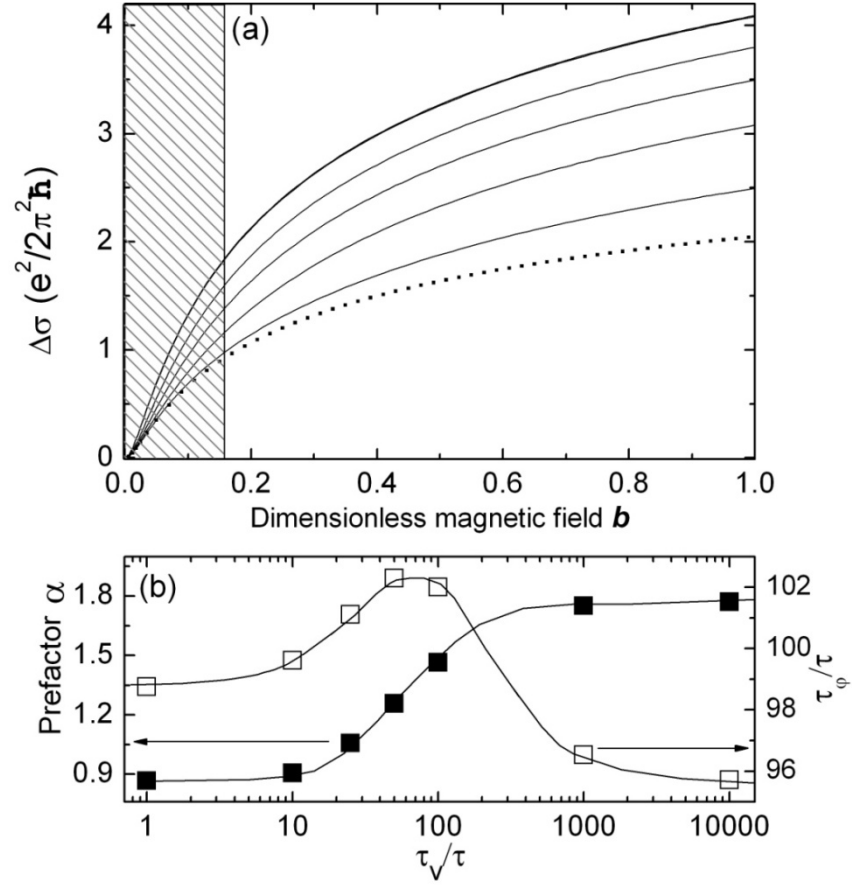


Figure 6.3. WL magnetoconductance calculated for a two-valley system using Eqs. (6.3), (6.4), and (6.5) (solid lines) and for a single-valley system (Ref. 125) (dotted line). For solid curves from bottom to top,  $\tau_V/\tau = 10, 25, 50, 100, 1000, 10000$ , respectively. Two upper curves are indistinguishable by eye. For all the curves  $\tau_\phi/\tau = 100$ . The hatched region was used for fitting with Eq. (6.1). (b) Dependences of the fitting parameters  $\alpha$ , and  $\tau_\phi/\tau$ , on  $\tau_V/\tau$ . The data points at  $\tau_V/\tau = 1$  correspond to a single-valley system.

depicted  $\alpha$  and  $\tau_\phi/\tau = 1$  for a single-valley system at  $\tau_V/\tau = 1$ . The main results of the fit are as follows: (i) the extracted phase breaking time  $\tau_\phi$  coincides with its preset value within a few percent (this uncertainty is insignificant for further analysis), and (ii) the observed prefactor increases from  $\approx 1$  to  $\approx 2$  as  $\tau_V$  increases and becomes greater than  $\tau_\phi$ . Therefore, the approximate equality  $\alpha \approx 1$  is simply a consequence of a large ratio  $\tau_\phi/\tau_V \gg 1$ .

### 6.4.2. Data analysis using the ballistic theory

It is intuitively clear and will be discussed in more detail below that the MC in low fields  $b \ll 1$  is predominantly determined by  $\tau_\phi$ . In principle, one could use the “ballistic” theory for fitting the MC data in the whole range of magnetic fields and, thus, for determining both  $\tau_\phi$  and  $\tau_V$  from a single fit. However, the series [Eqs. (6.4) and (6.5)] converge very slowly in small  $b$  region. Therefore, to determine  $\tau_\phi$ , it is more practical to use Eq. (6.1) in low fields. Figure 6.3 shows that this procedure provides the correct  $\tau_\phi$  value.

Consequently, we have used the following procedure of extracting  $\tau_V$  from the WL magnetoconductance. First, we analyzed the MR data in sufficiently weak magnetic fields and at low temperatures. In this regime (the hatched regions in Figure 6.1), the dephasing occurs at a time scale much greater than  $\tau_V$ , and we can apply Eq. (6.1) for extracting  $\tau_\phi$ ; the second adjustable parameter, prefactor  $\alpha$ , appears to be close to 1. At the next stage, we substitute  $\tau_\phi$  into the “ballistic” formulas [Eqs. (6.3), (6.4), and (6.5)] and calculate the MC curves in a wide range of fields ( $b < 1$ ) for various  $\tau_V$ . Figure 6.4 illustrates this procedure using as an example the same MC data as in Figure 6.2. We calculate  $\Delta\sigma(b)$  using the summation technique similar to that described in Ref. 129 for single-valley systems.

Figure 6.4 shows that the experimental MC (circles) is smaller than the MC for a system with two unmixed degenerate valleys (curve 1) and larger than MC for a single valley system (curve 5). This observation again indicates that the MC in the studied Si MOSFETs is affected by valley mixing. Curves 2, 3, and 4 in Figure 6.4

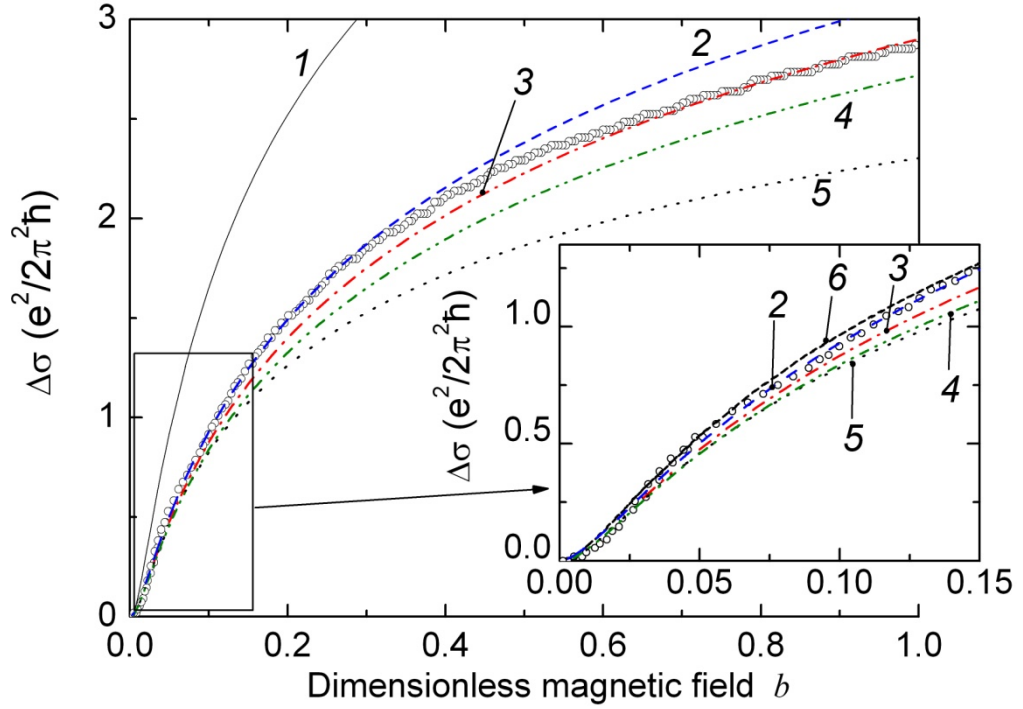


Figure 6.4. Comparison between the WL magnetoconductance for sample Si40,  $n = 33.4 \times 10^{11} \text{ cm}^{-2}$ ,  $T = 1.45 \text{ K}$ , and the ballistic theory. Different MC curves are calculated using Eqs. (6.3), (6.4), and (6.4): 1—for two unmixed valleys ( $\tau_V = \infty$ ); 2— $\tau_V/\tau = 15$ ; 3— $\tau_V/\tau = 12$ ; 4— $\tau_V/\tau = 9$ ; 5—MC for a single-valley system (equal to curve 1 divided by 2). Inset blows up the data in the range  $b < 0.15$ . Curve 6 is the HLN theory [Eq. (6.1)] with a prefactor  $\alpha = 1$  see Figure 6.2(a).  $\tau_\phi/\tau = 133$  for all calculated curves.

correspond to  $\tau_V/\tau = 15, 12$ , and  $9$ , respectively. Note that in the magnetic field range  $b < 0.15$ , these three curves, the experimental data, the HLN formula, and the ballistic result for a single valley system are almost indistinguishable from each other (see the inset to Figure 6.4). Therefore,  $\tau_V$  cannot be reliably found from the MC in low fields.

Figure 6.4 shows that the discrepancy between the curve 5 for a single-valley system and the curves, 2,3,4 for two mixed valleys ( $\tau_V/\tau = 15, 12$ , and  $9$ ) grows as  $b$  increases. This observation has a transparent physical explanation: with increasing  $b$ ,

the typical size of electron trajectories, which contribute to the WL correction diminishes, and the valley mixing over the time of travel along these trajectories becomes small when  $b > \Phi_0/D\tau_V$ . As a result, the WL magnetoconductance in strong magnetic fields approaches the theoretical prediction for a two-valley system with no intervalley scattering.

We also note that all calculated curves deviate from the experimental data. As Figure 6.4 shows, curve 4 calculated for  $\tau_V/\tau = 9$  at  $b > 0.4$  is approximately parallel to but lower than the experimental data in magnetic fields  $b > 0.4$ . On the other hand, curve 2 calculated for  $\tau_V/\tau = 15$  almost coincides with the data in low magnetic fields  $b < 0.4$ , though deviates substantially from them in higher fields. The minimal mean-square deviation of the calculated curve from the data is realized for  $\tau_V/\tau = 12$  (curve 3).

Thus, the value of  $\tau_V$  depends on the magnetic field interval  $(b_1, b_2)$  within which the MC data is fitted. The  $\tau_V/\tau$  values, obtained from fitting the difference  $\Delta\sigma(b_1) - \Delta\sigma(b_2)$  as a function of  $(b_1, b_2)$ , decrease as  $b = (b_1 + b_2)/2$  increases (see Figure 6.5). This monotonic dependence has been reproduced for all samples and temperatures. We believe that this apparent  $\tau_V(b)$  dependence is an artifact of the fitting procedure. In all above calculations we assumed  $\tau_\phi$  to be field independent. However,  $\tau_\phi$  should depend on a perpendicular magnetic field.<sup>35</sup> To the best of our knowledge, there are neither experimental nor theoretical systematic studies of this dependence beyond the diffusive limit. Ignoring this dependence in our fitting could lead to the observed monotonic variation in  $\tau_V$  with  $b$ .

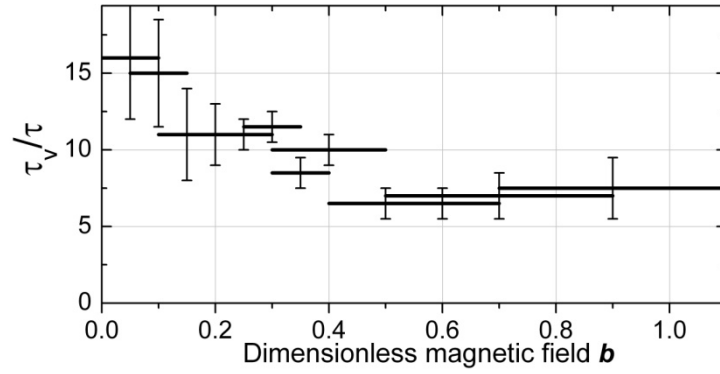


Figure 6.5. Intervalley scattering time determined from fitting the difference,  $\Delta\sigma(b_1) - \Delta\sigma(b_2)$ , for the same magnetoresistance curve as in Figure 6.4. The fitting ranges  $(b_1, b_2)$  are shown by the horizontal bars.  $\tau_\phi/\tau = 133$ .

A question arises, therefore: what range of magnetic fields should be chosen for  $\tau_V$  extraction? To answer this question we have analyzed errors of our method; the resulting root-mean-square sum of all errors is shown by the error bars in Figure 6.5. The error analysis is presented in detail in Sec. 6.5.5, where it is shown that neither small fields ( $b < 0.1$ ) nor large fields ( $b \sim 1$ ) should be used for  $\tau_V$  extraction. In weak fields, the MC is insensitive to  $\tau_V$ , whereas in strong fields one approaches the limits of applicability of the theory described in Sec 6.4.1.

Therefore, we conclude that an intermediate range of magnetic fields is most suitable for extracting  $\tau_V$ . For the further analysis, we choose the range  $b=0.2-0.4$ . We have verified that our conclusions on the temperature and density dependences of  $\tau_V$  are not affected if this range is changed.



## 6.5. Results and discussion

### 6.5.1. Phase breaking time

As we have already mentioned, at the first stage of the analysis we estimated the phase breaking time  $\tau_\phi$ . Comparison of the  $\tau_\phi(T)$  dependences with the theory of interaction effects<sup>35</sup> is shown in Figure 6.6(a-c). The uncertainty in the values of  $\alpha$  and  $\tau_\phi$  (shown as the error bars in Figure 6.6) reflects mainly the uncertainty in  $\sigma(b)$  in the weak fields  $b < 0.01$ . The magnitude of the phase breaking time and its temperature dependence are in good agreement with the theory for all samples within the studied ranges of electron density [Si6-14:  $n = (0.28-1.5) \times 10^{12} \text{ cm}^{-2}$ , Si39:  $n = (2-2.5) \times 10^{12} \text{ cm}^{-2}$ , Si40:  $n = (3-4) \times 10^{12} \text{ cm}^{-2}$ ]. Note that no adjustable parameters are involved in this comparison, since the Fermi-liquid parameter  $F_0^\sigma$  was obtained in independent measurements.<sup>41</sup>

The theoretical curves (solid lines in Figure 6.6) are calculated following Ref. 35 for 15 triplet channels,<sup>38</sup> which implies small valley splitting and relatively weak intervalley scattering ( $\Delta_V, \tau_V^{-1} < T$ ). For samples Si6-14 and Si39  $T \sim \tau_V^{-1}, \Delta_V$ , over the major part of the studied temperature range. Whether or not the condition  $\Delta_V, \tau_V^{-1} < T$  is fulfilled for low mobility samples Si39 and Si40 is not important, because the measurements were performed at such high densities that the amplitude of the triplet term in the interaction corrections to  $\tau_\phi$  was small in comparison with the singlet term: changing the number of triplet terms from 15 (two-valley case) to 3 (single-valley case) caused variation of  $\tau_\phi$  by less than 5% (dashed line in Figure 6.6). Interestingly, though the condition  $\tau_V^{-1}, \Delta_V < T$  is violated at temperatures lower than

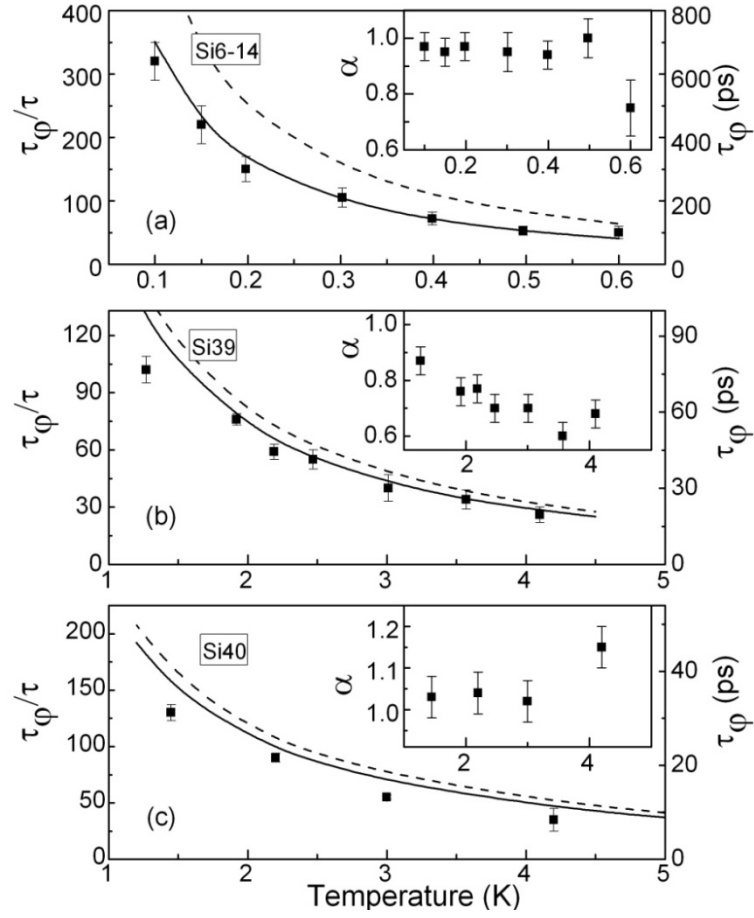


Figure 6.6. Temperature dependence of the extracted  $\tau_\phi$  value in units of  $\tau$  (left axes) and in picoseconds (right axes): (a) Si6-14,  $n = 9.98 \times 10^{11} \text{ cm}^{-2}$ , (b) Si39,  $n = 29.4 \times 10^{11} \text{ cm}^{-2}$ , (c) Si40,  $n = 33.4 \times 10^{11} \text{ cm}^{-2}$ . Solid lines show the  $\tau_\phi(T)$  dependence predicted by the theory of interaction corrections (Ref. 35) with 15 triplet terms, dashed line, with three triplet terms. The insets show the corresponding temperature dependences of the prefactor  $\alpha$ .

0.4K for sample Si6-14, the  $\tau_\phi(T)$  data still agree better with theory when 15 rather than 3 triplet terms are taken into account. The observed quantitative agreement of the experimental values of  $\tau_\phi$  with the theory suggests that  $\tau_\phi$  is weakly affected by intervalley scattering near the crossover  $T\tau_v \sim 1$ .

It is worth mentioning that the temperature dependence of the phase breaking time in Si MOSFETs has been previously investigated in Refs. 74-76,79,119. Our

agreement with theory<sup>35</sup> that takes more accurately EEI into account seems to be in-line with previous results.

### 6.5.2. Prefactor $\alpha$

By fitting the weak-field MC data with the HLN theory, we obtained the prefactor  $\alpha$  that is close to 1 for all samples (see the insets to Figure 6.6); this suggests that the valleys are intermixed on the  $\tau_\phi$  time scale. The decrease of  $\alpha$  from 0.9 to 0.6 with increasing temperature, obtained for sample Si39 (see the inset to Figure 6.6(b), we believe, is an artifact, because relatively small values  $\tau_\phi/\tau \sim 30$ , observed for this sample at high temperatures, make Eq. (6.1) inadequate. The complete theory described in Sec. 6.4.1 explains that small value of  $\alpha$  is a consequence of a fast phase relaxation. For the same reason, there is a larger scattering in the values of  $\alpha(T)$  for samples Si6-14 and Si40 at the highest temperatures (Figure 6.6), where  $\tau_\phi$  is small.

It is worth noting that the smallness of prefactor  $\alpha$  has been attributed to the intervalley scattering in Ref. 74. However, the MC data in this experiment were fitted with the theory,<sup>130</sup> which does not take into account the nonbackscattering correction Eq. (6.5). Our estimates show that for the parameters of samples studied in Ref. 74 ( $\tau_\phi/\tau = 20$ ,  $\tau_V/\tau = 4$ , and  $b=0.5-7$ ), the non-backscattering correction contributes about 50% to the extracted value of  $\tau_V$ .

### 6.5.3. Intervalley scattering time: Independence of temperature

Following the procedure described in Sec. 6.4.2, we have extracted  $\tau_V$  by fitting the WL MC data with “ballistic” Eqs. (6.3), (6.4), and (6.5). Figure 6.7 shows that the values of  $\tau_V$  are temperature-independent within the accuracy of our measurements.

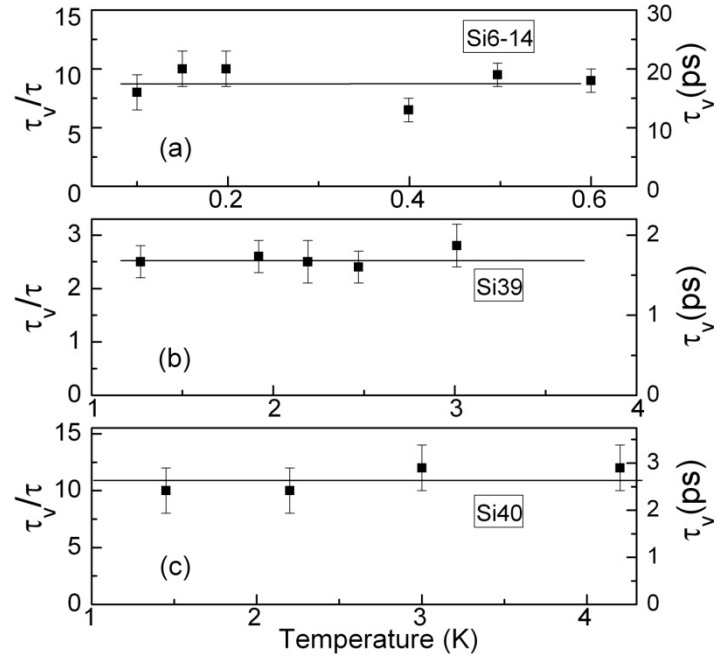


Figure 6.7. Temperature dependence of  $\tau_v$  in units of  $\tau$  (left axes) and in picoseconds (right axes): (a) Si6-14,  $n = 9.98 \times 10^{11} \text{ cm}^{-2}$ , (b) Si39,  $n = 29.4 \times 10^{11} \text{ cm}^{-2}$ , (c) Si40,  $n = 33.4 \times 10^{11} \text{ cm}^{-2}$ . Solid horizontal lines show the average  $\tau_v$ .

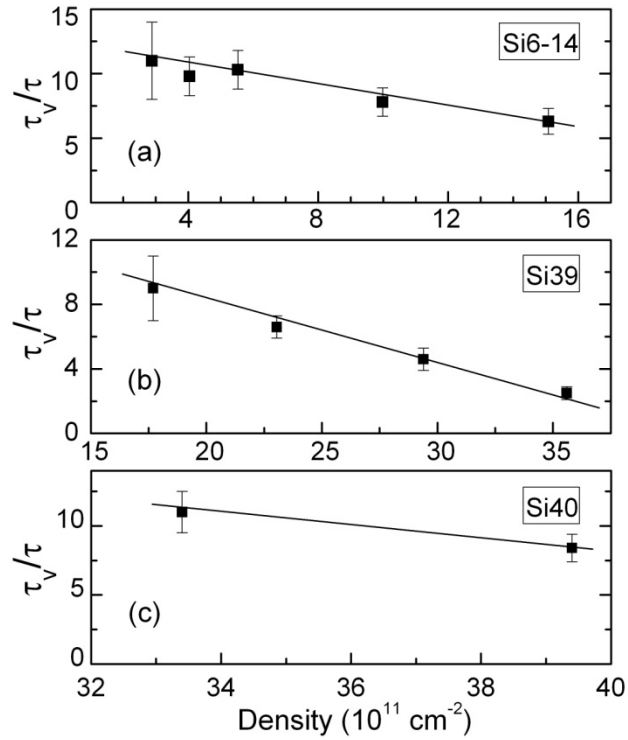


Figure 6.8. Density dependence of the intervalley scattering time (averaged over temperature) for samples Si6-14 (a), Si39 (b), and Si40 (c).

This observation suggests that the intervalley scattering is elastic, i.e., governed by static disorder. Similar conclusion can be also drawn from the fact that  $\alpha$  remains close to 1, while the extracted  $\tau_\phi$  exceeds  $\tau_V$  by far and grows without saturation as  $T$  decreases (see Figure 6.6). Indeed, were the intervalley scattering inelastic, one would have observed a prefactor  $\alpha \sim 2$  because the dephasing would occur in two valleys independently and the intervalley scattering would be just an additional dephasing mechanism. In the latter case, a cut-off of the dephasing time at the level  $\tau_\phi = \tau_V$  is also expected. The two observations, the absence of the cut-off and  $\alpha \approx 1$ , support the self-consistency of our analysis.

The intervalley transitions are expected to be elastic for the following reason. The intervalley scattering requires a large momentum transfer comparable to the vector of reciprocal lattice  $2\pi/a \sim 10^8 \text{ cm}^{-2}$  ( $a$  is the interatomic distance). At liquid helium temperatures, only static disorder can cause these transitions, as the momenta of electrons  $k_F \sim 10^6 \text{ cm}^{-1}$   $k_F \sim 10^6 \text{ cm}^{-1}$  for the studied range of densities and phonons  $k_{ph} \sim T/(\hbar v_s)$  (here  $v_s$  is the sound velocity) are much smaller than  $2\pi/a$ . Static disorder can lead only to elastic scattering because it changes momentum of scattered electrons but does not change their energy.

#### 6.5.4. Intervalley scattering time: density and sample dependence

Figure 6.8 shows the density dependence of  $\tau_V$  values averaged over the temperature. For all three samples, the *relative* rate of the intervalley transitions (with respect to the momentum relaxation rate) increases with density. This points to the dominant role of the Si-SiO<sub>2</sub> interface in the intervalley transitions. The electron wave function  $\Psi$  in Si MOSFETs is positioned mostly in the bulk silicon and exponentially

decays in SiO<sub>2</sub>.<sup>6</sup> When the gate voltage (and, hence, the density  $n$ ) is increased, the electrons are “pushed” towards the Si-SiO<sub>2</sub> interface, and the amplitude of the wave function at the interface,  $\Psi_0$ , increases. The probability of the interface scattering is proportional to  $|\Psi_0|^2$  and increases with  $n$ ;<sup>6</sup> this is in line with the behavior shown in Figure 6.8.

In the experiments we used samples with the mobilities, which vary over a decade. We find no correlation between  $\tau_V$  and the mobility for different samples. This suggests that the intervalley scattering is determined by a sample-specific interface disorder, namely, the surface roughness at the atomic length scale, which might be different for the samples fabricated on different wafers. In contrast to the intervalley scattering, the mobility is governed mostly by impurities in the bulk and by the interface roughness at a large length scale,  $\sim 2\pi/k_F$ .

The measured values of  $\tau_V$  for all samples are within the interval  $(3-12)\tau$ , which indicates that the valley index remains a good quantum number at the time scale  $\sim \tau$ .

#### 6.5.5. Analysis of possible errors in $\tau_v$

We present here an analysis of errors in the fitting procedure, which determine the size of error bars in Figure 6.5. As discussed in Section 6.4.1,  $\tau_V$  was found from the following equation:

$$\begin{aligned} \Delta\sigma(b_1)_{\text{exp}} - \Delta\sigma(b_2)_{\text{exp}} &= \Delta\sigma(b_1, \tau_\phi / \tau, \tau_V / \tau)_{\text{th}} \\ &\quad - \Delta\sigma(b_2, \tau_\phi / \tau, \tau_V / \tau)_{\text{th}} \end{aligned} \quad (6.8)$$

Here subscript “exp” denotes experimental data, subscript “th” denotes calculation using Eqs. (6.3), (6.4), and (6.5). Consequently, the uncertainty in  $\tau_V$  is determined by (i) uncertainty in  $b$ , (ii) uncertainty in  $\tau_\phi$ , and (iii) uncertainty in the conductivity.

To estimate each contribution to the error, we varied the corresponding parameter ( $b$ ,  $\tau_\varphi$ , or  $\Delta\sigma$ ) within its uncertainty and determined the variation in  $\tau_V$  by solving Eq. (6.8).

The uncertainty  $\delta b$  in  $b = 2\pi l^2/\Phi_0$  value is determined by the uncertainty in the mean free path  $l$ .<sup>8</sup> The latter is about 2–3% due to the uncertainties in electron density  $n$  and Drude conductivity. However,  $\delta b$  affects  $\tau_V$  rather weakly for the following reason: MC in the studied magnetic field range behaves approximately as  $\ln b$ , therefore  $\Delta\sigma(b_1) - \Delta\sigma(b_2) \sim \ln(b_1/b_2) = \ln(B_1/B_2)$ .

The error related to the uncertainty in  $\tau_\varphi$  is essential in low magnetic fields where magnetoconductance is sensitive to  $\tau_\varphi$ . Correspondingly, the error bars in low fields  $b < 0.15$  in Figure 6.5 are determined predominantly by the uncertainty in  $\tau_\varphi$ .

Another source of errors is related to the precision of the absolute value of WL MC (“calibration error”). Indeed, the accuracy of our measurements of the absolute magnetoresistance value is  $\sim 0.5\%$ . Higher order corrections, Maki–Thompson and DoS corrections<sup>121</sup> can modify MC by approximately 2–3% (as shown in Ref. 121,  $\delta(\Delta\sigma)/\Delta\sigma \approx 2e^2\rho_D/2\pi^2\hbar \approx 0.25$ ). In order to estimate this error, we artificially changed our experimental data by 3% and studied the corresponding change in  $\tau_V$ . The error appears to grow in small magnetic field where magnetoconductance is weakly sensitive to  $\tau_V$ . Therefore, small fields should not be used for the extraction of  $\tau_V$ . In large magnetic fields ( $b \sim 1$ ) MC becomes again weakly sensitive to  $\tau_V$ , and the latter error grows as  $b$  increases, as shown by the error bars in Figure 6.5. The calibration error is minimal in intermediate magnetic fields, where MC is most sensitive to  $\tau_V$ .

Our attempts to analyze the WL MC data in strong fields  $b > 1$  using Eqs. (6.3), (6.4), and (6.5) resulted in a large uncertainty of the fitting parameter  $\tau_V/\tau$  (large scattering of extracted  $\tau_V/\tau$  for various electron densities and temperatures). In large magnetic fields, there are several other error mechanisms, which are difficult to take into account. For example, at  $b \sim 1$ ,  $\tau_\phi$  differs from its small-field value.<sup>35</sup> Moreover, in Ref. 133 the MC for  $b > 1$  was shown to behave in a nonuniversal manner: it strongly depends on details of scattering potential, whereas our theory assumes an uncorrelated short-range disorder. Some other mechanisms of magnetoconductance (such as classical memory effects, interaction corrections, Maki–Thompson corrections, etc.) may also become essential in large fields where the shape of WL MC curve flattens. Therefore, we believe that the intermediate field range  $b=0.2\text{--}0.4$  is optimal for the extraction of the intervalley scattering rate.

## 6.6. Conclusions

To summarize, we have studied the weak localization magnetoconductance in Si MOSFETs over wide ranges of the electron densities, mobilities, and temperatures. In order to quantitatively analyze the experimental data, we have used the theory of weak localization for two-dimensional multivalley systems, which is valid in both the diffusion and ballistic regimes. The theory of Averkiev and Tarasenko<sup>39</sup>, which explicitly takes the intervalley scattering into account, allowed us to conduct the first detailed study of the intervalley scattering in the Si MOSFETs. It was found that:

(1) Intervalley scattering in Si MOSFETs is an elastic and temperature-independent process.



(2) The ratio  $\tau_V/\tau$  monotonically increases as the electron density decreases. This observation suggests that the intervalley scattering is governed by the disorder at the Si-SiO<sub>2</sub> interface.

(3) There is no simple correlation between the intervalley scattering rate and the sample mobility (or the momentum relaxation rate); this points to a sample-specific rather than universal mechanism of the intervalley scattering.

(4) The smallness of the prefactor  $\alpha \sim 1$ , that is obtained from fitting the experimental WL data with the HLN formula, is a consequence of a fast intervalley relaxation rate, which exceeds the phase relaxation rate.

(5) The temperature dependence of the phase relaxation time in Si MOSFETs is in quantitative agreement with the theory of EEI effects in disordered 2D systems.<sup>35</sup>

We note that the approach of the analysis of WL MC can be used for studies of intervalley relaxation in other multi-valley 2D electron systems, such as AlAs-AlGaAs heterostructures,<sup>131</sup> Si MOX structures,<sup>132</sup> and Si-SiGe quantum wells.<sup>133</sup>

## 7. Experimental study of the low-temperature conductivity of high- $\mu$ Si MOSFETs

### 7.1. Introduction

This chapter is devoted to a detailed study of the conductivity of 2D electron liquid in high-mobility (001) Si MOSFETs over a wide temperature range ( $T = 0.03$ -4.2 K) that includes both the *diffusive* and *ballistic* regimes. In particular, we observed for the first time that the metallic increase of  $\sigma$  with cooling is followed by the downturn of  $\sigma(T)$  at lower temperatures. For the purpose of comparison with the ZNA theory<sup>35</sup>, we studied the range of not-too-low densities,  $n = (1.8$ -15) $\times 10^{11}$  cm<sup>-2</sup>, where the temperature and magnetic field dependences  $\Delta\sigma(T, B)$  can still be treated as small corrections to the Drude conductivity  $\sigma_D$ . In principle, no fitting parameters are required for comparison with the theory, because we have measured  $F_0^\sigma$ ,  $\Delta_V$ , and  $\tau_V$  in independent experiments (see Secs. 4.2.3, 5.3, 6 for details). However, below we take a slightly different approach: we obtain the  $F_0^\sigma(n)$  values from fitting the  $\Delta\sigma(T, B_{||})$  dependences with the ZNA theory<sup>35</sup>, and show that these values are consistent with the corresponding values extracted from the analysis of SdH oscillations<sup>41,40</sup>. We have also revealed shortcomings of earlier analysis of  $\Delta\sigma(T)$ , reanalyzed the available data, and compared the extracted values of  $F_0^\sigma(n)$  with corresponding values from other measurements. We conclude that the experimental data are well described by the theory of interaction corrections<sup>35</sup> at intermediate temperatures  $T \approx 0.03$ -4.2 K. For a quantitative analysis at ultra-low

temperatures ( $T \leq 0.3$  K), the interaction correction theory should be modified by taking into account finite intervalley scattering rates.

## 7.2. Sample characterization and data analysis

### 7.2.1. Samples characterization

We have studied the temperature and magnetic field dependences of the conductivity for high-mobility (001) Si MOSFETs, which demonstrated the metallic quisi-linear  $\sigma(T)$  dependences at intermediate temperatures over a wide range of electron densities  $n$ . Below we present the data for high- $\mu$  (001) Si MOSFET samples, Si6-14 and Si1-46, (see Sec. 4.1.4 for samples' description). The  $\sigma(T, B_{\parallel})$  dependences were measured in a wide ranges of temperatures ( $T = 0.03 - 4$  K), magnetic fields ( $B_{\parallel} \leq 5$  T) and electron densities ( $n = (1.8-15) \times 10^{11} \text{ cm}^{-2}$ ).<sup>u</sup>

Electron density  $n$  was determined from the period of SdH oscillations (Sec. 4.2.1). Analysis of SdH oscillations was also used to verify that electrons are in a good thermocontact with  $\text{He}^3/\text{He}^4$  mixture and are not overheated by external noise and/or measuring current (Sec. 4.2.2). Figure 4.9 shows that temperature dependence of amplitude of SdH oscillation for samples Si6-14 and Si1-46 follow Lifshitz-Kosevich theory<sup>99</sup> down to 30 mK, the base temperature of our dilution  $\text{He}^3/\text{He}^4$  refrigerator.

---

<sup>u</sup> The experimental technique is described in Chapter 4.

### Valley splitting and intervalley scattering

We have estimated the energy splitting  $\Delta_V$  between two valleys from the analysis of SdH oscillations:  $\Delta_V \cong 0.4$  K for sample Si6-14 and 0.7 K for Si1-46 (see Sec. 4.2.3 for details).

We have measured the intervalley scattering rate for sample Si6-14 (see Chapter 6 for more details) by analyzing the WL magnetoresistance. It was found that  $\tau_V$  is temperature-independent and the ratio  $\tau_V/\tau$  decreases monotonically with increasing electron density. For Si6-14 at  $n = (3-6) \times 10^{11} \text{ cm}^{-2}$ , ( $\tau_V^{-1} \cong 0.36$  K)  $\tau_V \cong 20$  ps is approximately ten times greater than the transport time  $\tau \cong 2$  ps.

### Relaxation time $\tau$ and the band mass

The momentum relaxation time  $\tau$  was determined from the Drude conductivity  $\sigma_D = e^2 n \tau / m_b$ , which was found by extrapolating the quasi-linear  $\sigma(T)$  dependence observed in the ballistic regime to  $T = 0$ . Note that in order to extract  $\tau$  from the Drude conductivity, one should use the bare mass  $m_b$ : according to the Kohn theorem, the response of a translationally-invariant system to the electromagnetic field is described by  $m_b$  in the presence of electron-electron interactions; this result also holds for weak disorder ( $E_F \tau \gg 1$ ). It is worth mentioning that several prior publications<sup>66,134,135</sup>, incorrectly used  $m^*$  instead of  $m_b$  to estimate  $\tau$  from  $\sigma_D$ ; this affects the value of the fitting parameters extracted from comparison with the ZNA theory<sup>35</sup> as shown below.

The textbook value<sup>6</sup> for the light electron mass in a bulk Si is  $m_b^{(3D)} \approx 0.19m_e$ . For inversion layers on (001) Si-surface, Kunze and Lautz<sup>136</sup> have obtained  $m_b^{(2D)} / m_e = (0.19-0.22) \pm 0.02$  from tunneling measurements. The recent  $m^*(n)$  data obtained from the analysis of SdH oscillations over a wide range of densities  $n = (1-35) \times 10^{11} \text{ cm}^{-2}$  ( $r_s = 1.4-8.5$ )<sup>41,40</sup> can be fitted with a polynomial

$$m^*(r_s) = 0.205m_e(1 + 0.035r_s + 1.2 \times 10^{-4}r_s^4 + 2 \times 10^{-10}r_s^{10}).$$

These  $m^*/m_e$  data agree well with earlier values of  $m^*$  extracted from SdH oscillations<sup>104,111,112</sup> in narrower ranges of densities. By extrapolating the polynomial  $m^*(r_s)$  to  $r_s = 0$  we obtain  $m_b^{(2D)} / m_e = 0.205 \pm 0.005$ , the value, which we adopted for the analysis  $\sigma(T, B)$ <sup>v</sup>; available measurements of the cyclotron resonance<sup>w</sup> do not contradict and do not refine this value.

In principle, the aforementioned complete characterization of samples allows us to compare the  $\Delta\sigma(T, B)$  dependences with the ZNA theory<sup>35</sup> without any fitting parameters (with a caveat that the theory<sup>35</sup> does not take into account the intervalley scattering, see the discussion below). However, we adopt an equivalent, but more convenient procedure: for each electron density,  $F_0^\sigma(n)$  will be considered as a single

---

<sup>v</sup> Our revision of the analysis of SdH data<sup>40</sup> (described in the subsection 5.2) modifies the  $m^*$  values only at low densities  $r_s > 4$  and does not affect  $m^*(r_s \rightarrow 0) = 0.205m_e$ , adopted as the best estimate for  $m_b$ .

<sup>w</sup> The chosen value  $m_b = 0.205m_e$  does not contradict the cyclotron resonance data. Due to the Kohn theorem, the mass measured in the cyclotron resonance experiments is believed to be unrenormalized and equal to the band mass (and hence, independent of density). Abstreiter *et al.* [Phys. Rev. B **14**, 2480 (1976)] observed the far-infrared cyclotron resonance and obtained  $m_c = (0.197 \pm 0.005)m_e$  independent of  $n$  for  $n > 1 \times 10^{12} \text{ cm}^{-2}$ . However, for  $n > 1 \times 10^{12} \text{ cm}^{-2}$ , they observed a sample-dependent noticeable increase of  $m_c$  with decreasing density (up to  $0.215m_e$  at  $n = 5 \times 10^{12} \text{ cm}^{-2}$ ), which was attributed to the localization effects.

parameter for fitting  $\Delta\sigma(T, B)$ , and these values of  $F_0^\sigma(n)$  will be compared with the corresponding values obtained from the SdH oscillations<sup>41,40</sup>.

### 7.2.2. Temperature dependence of the conductivity at $B_{||}=0$

The temperature dependences of the conductivity  $\sigma(T)$  for sample Si6-14 are shown in Figure 7.1. In these measurements, we applied a fixed  $B_{\perp} = 0.1T$  that is sufficient to suppress the temperature dependence of the WL correction in the studied temperature range. The  $\sigma(T)$  dependences are non-monotonic for all studied densities  $[n = (1.8-15) \times 10^{11} \text{ cm}^{-2}]$  for Si6-14 and  $[n = (10-15) \times 10^{11} \text{ cm}^{-2}]$  for Si1-46: a quasi-linear increase of  $\sigma$  with cooling, observed down to  $\sim 0.5 \text{ K}$ , is replaced at lower  $T$  with a decrease of  $\sigma$ . Note that in the previous experiments of  $\sigma(T)$ -study in high- $\mu$  Si MOSFETs (including Si6-14 – the sample studied in this work)<sup>135</sup>, a trend of  $\sigma(T)$  saturation was observed at  $T < 0.4 \text{ K}$  rather than the decrease of the conductivity. One of the reasons for this might have been “heating” of electrons by high frequency noise: only after thorough filtering of all leads connected to the sample were we able to decrease the electron temperature down to  $\sim 30 \text{ mK}$  (see Secs. 4.1.3 and 4.2.2). Similar downturn of  $\sigma(T)$ , although at much lower temperatures, has been recently observed in high- $\mu$  GaAs FETs at low electron densities<sup>137</sup>.

Below we use the following strategy for analyzing the  $\Delta\sigma(T)$  dependences. First, we find  $F_0^\sigma$  by fitting the quasi-linear  $\sigma(T)$  dependences observed in the ballistic regime ( $T > 0.5 \text{ K}$ ) with Eqs. (2.43), (2.40), (2.41). The effect of valley splitting and

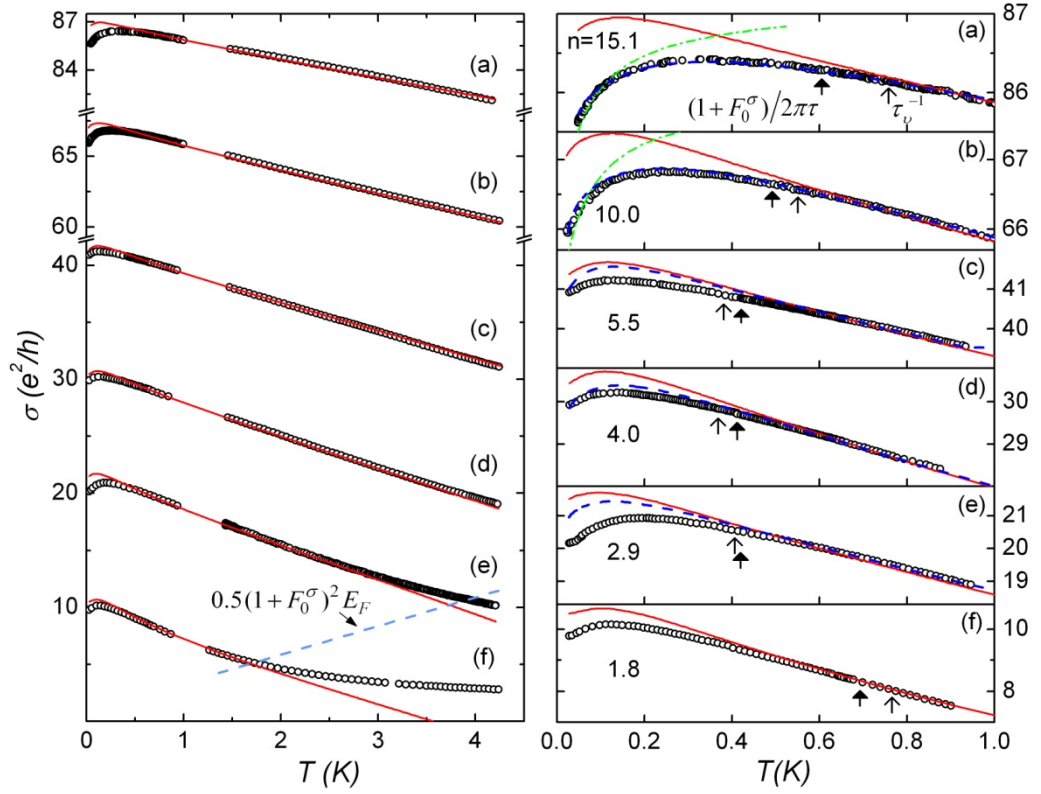


Figure 7.1. Temperature dependences of the conductivity  $\sigma(T, B_{\parallel} = 0)$  for the sample Si6-14 at various electron densities  $n = 15.1, 10.0, 5.5, 4.0, 2.9, 1.8$ , in units of  $10^{11} \text{ cm}^{-2}$ , from top to bottom. Circles show the experimental data, red curves - the theoretical dependences Eq. (2.44) calculated with  $\Delta_V = 0.4 \text{ K}$ . On the left panel the dashed blue curve corresponds to  $T = 0.5(1 + F_0^{\sigma})^2 E_F$ , the applicability of the ZNA theory is violated at a higher  $T$ . The right panel shows the same data set within a narrower temperature interval, the thin arrows correspond to  $T = \tau_V^{-1}$  and the thick arrows - to the temperature of the crossover between ballistic and diffusive regimes,  $T^* = (1 + F_0^{\sigma})/2\pi\tau$ . The dash-dotted green curves on the right panel were calculated with three triplet components [Eq. (2.39)] (the valleys are completely intermixed), the blue dashed curves -  $\sigma(T, B) = \sigma_D + \delta\sigma_C + N_{\text{triplet}}(T\tau_V) \times \delta\sigma_T(T)$  with  $N_{\text{triplet}}$  continuously varying between 3 (for  $T \ll \tau_V^{-1}, \Delta_V$ ) and 15 (for  $T \gg \tau_V^{-1}, \Delta_V$ ).

intervalley scattering on  $\Delta\sigma_{ee}(T)$  can be neglected at  $T \gg \Delta_V, \tau_V^{-1}$  and the analysis is significantly simplified. The corresponding values of  $F_0^{\sigma}(n)$  are shown in Figure 7.4. The  $T$  range available for fitting in this regime “shrinks” rapidly at low  $n$ : the growth of  $|F_0^{\sigma}|$  and decrease of  $E_F$  with decreasing  $n$ , lead to violation of the

condition  $T \ll (1 + F_0^\sigma)^2 E_F$  (e.g., at  $n = 1.8 \times 10^{11} \text{ cm}^{-2}$  this occurs at temperatures above 2K). This might be one of the reasons for the observed deviation of the high-temperature  $\sigma(T)$  from the linear-in- $(T/E_F)$  theory<sup>35</sup>. Also, the higher-order corrections might become significant at low  $n$  when  $\Delta\sigma(T)/\sigma_D \sim 1$  (see Figure 7.1).

After finding the  $F_0^\sigma$  values (which are temperature-independent in the studied temperature range), we proceed with the analysis of the low- $T$  part of the  $\sigma(T)$  dependences, where the crossover from  $d\sigma/dT < 0$  to  $d\sigma/dT > 0$  was observed. We note that the crossover occurs when temperature becomes smaller than two characteristic temperature scales -  $\Delta_V$  and  $\tau_V^{-1}$  - which are of the same order of magnitude for the studied structures. We emphasize that according to the ZNA theory<sup>35</sup>, the ballistic-diffusive crossover should not lead to the change of the sign of  $d\sigma/dT$ . In contrast, the valley splitting and the intervalley scattering may result in the sign change for  $d\sigma/dT$  because these processes reduce the number of triplet components at  $T < \Delta_V$  and  $T < \tau_V^{-1}$ .

The theory<sup>35</sup> takes into account a finite  $\Delta_V$  but not  $\tau_V^{-1}$ . The solid red curves in Figure 7.1 are calculated for  $\Delta_V = 0.4 \text{ K}$ , the estimated value of  $\Delta_V$  for sample Si6-14 (see Sec. 4.2.3 for details), and  $\tau_V^{-1} = 0$ . It is clear that the change in the number of triplet components from 15 ( $T \gg \Delta_V$ ) to 7 ( $T \ll \Delta_V$ )<sup>66,x</sup> [see also Eq. (2.44)] is not sufficient to explain the shape of the  $\sigma(T)$  downturn. The effect of strong intervalley scattering is illustrated in Figure 7.1 by dashed green curves calculated with 3 triplet

---

<sup>x</sup> For a two-valley system with  $\Delta_V \gg T$ , the total number of interaction channels is  $4 \times 4 = 8$ , among them 1 singlet and 7 triplet terms.



components (to model roughly the case of  $T \ll \tau_V^{-1}$  when the valleys are completely intermixed). In the absence of a detailed theory that would account for intervalley mixing, we attempted to fit the experimental data with an empirical crossover function for the number of triplet components

$$N_{\text{triplet}}(x) = 9 + 6[\exp(-0.3/x) - \exp(-30x)]$$

where  $x = T\tau_V$ . This crossover function provides correct asymptotic limits for  $N_{\text{triplet}}$ : 3 at  $T \ll \tau_V^{-1}$  and 15 at  $T \gg \tau_V^{-1}$ . Figure 7.1 shows that using this function, we can reasonably well describe the shape of experimental  $\sigma(T)$  dependences for all studied electron densities. Qualitatively, the data agree with the theoretical dependences  $\Delta\sigma_{ee}(T)$ , calculated for the experimentally determined  $\Delta_V$  value. In particular, the downturn of  $\sigma(T)$  at  $T < 0.4$  K temperature can be explained by suppression of the triplet contribution to  $\Delta\sigma_{ee}(T)$  due to valley splitting and/or intervalley scattering. We stress that in the above analysis we modeled the theoretical dependences only qualitatively. For a more detailed quantitative analysis of the experimental data at low  $T$ , one needs a rigorous theory extended to the case of a finite intervalley scattering rate.

### 7.2.3. Temperature dependence of the conductivity at non-zero $B_{\parallel}$

Better understanding of different contributions to  $\Delta\sigma(T)$  can be achieved by measuring the conductivity in strong in-plane magnetic fields  $B_{\parallel} \gg T/g_b\mu_B$ . The evolution of experimental dependences  $\Delta\sigma(T)$  with  $B_{\parallel}$  is shown in Figure 7.2 for two samples at different electron densities. The steps in  $B_{\parallel}$  were chosen in such a way that the corresponding increase of the Zeeman energy  $E_Z = g_b\mu_B B_{\parallel}$  was of the order

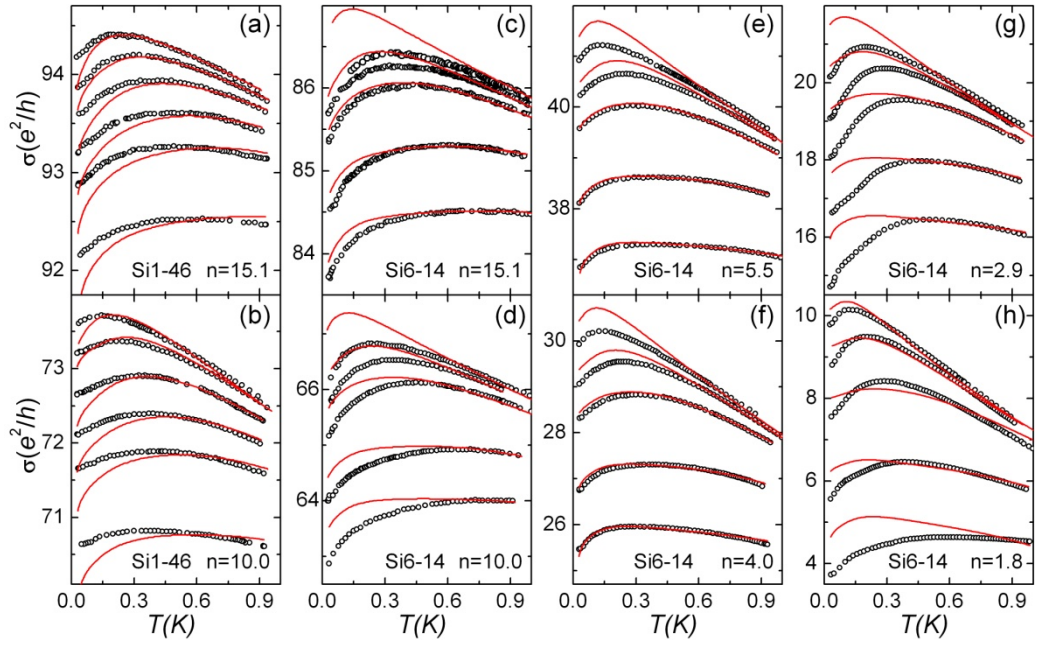


Figure 7.2. Temperature dependences of the conductivity for samples Si1-46 [(a) and (b)] and Si6-14 [(c)-(h)] in different in-plane magnetic fields (from top to bottom,  $B_{\parallel} = 0, 0.6, 1, 2, 3$  T). Experimental data are shown as circles, the solid curves show the theoretical dependences calculated for sample Si6-14 with  $\Delta_V = 0.4$  K and for sample Si1-46 with  $\Delta_V = 0.7$  K. The  $F_0^\sigma$  value is the only fitting parameter in comparison with the theory<sup>35</sup>, the corresponding values of  $F_0^\sigma$  are shown in Figure 7.4. The values of  $n$  are shown in units of  $10^{11} \text{ cm}^{-2}$ .

of 1K. The theoretical curves in Figure 7.2 were calculated using the  $F_0^\sigma(n)$  values extracted from the analysis of  $\delta\sigma_{ee}(T, B_{\parallel} = 0)$  (see Figure 7.1). The transport time  $\tau$  was calculated for each  $B_{\parallel}$  value from the Drude conductivity  $\sigma_D(B_{\parallel})$ , which in turn was estimated by extrapolating the quasi-linear part of the  $\sigma(T, B_{\parallel})$  dependence to  $T = 0$ . The observed behavior is in line with our analysis of the  $\sigma(T)$  dependences in Section 7.2.2. Indeed, the magnitude of the triplet contribution is expected to be reduced when the Zeeman energy becomes greater than  $T$ . This effect is more pronounced within the range  $\{\Delta_V, \tau_V^{-1}\} < T < g_b \mu_B B$ , where a strong magnetic field

reduces the number of triplet components from 15 to 7. For example, at  $n = 1 \times 10^{11} \text{ cm}^{-2}$  [see Figure 7.2(d)] the metallic behavior disappears at  $T < 1 \text{ K}$  and  $B_{\parallel} = 3 \text{ T}$ , which is in agreement with the theory<sup>35</sup>. At lower  $T$ , the number of triplet components is smaller than 15 even at  $B_{\parallel} = 0$  due to valley splitting and intervalley scattering, and the effect of  $B_{\parallel}$  on  $\Delta\sigma(T)$  is less prominent.

#### 7.2.4. Magnetoconductivity

To test the theoretical predictions on the magnetoconductivity induced by in-plane magnetic fields, we also measured the  $\sigma(B_{\parallel})$  dependences at fixed  $T$ . Similar measurements have been performed in the past (see, e.g., Refs. 66,135,138), but no detailed comparison with the theory was carried out at that time. The MC for sample Si6-14 over the field range  $-4.5 < B_{\parallel} < 4.5 \text{ T}$  is shown for different densities and temperatures in Figure 7.3. In these measurements, special care was taken to reduce the magnetic field component perpendicular to the plane of the structure: even a  $1^\circ$  misalignment between the sample's plane and the magnet axis (which results in  $B_{\perp} \sim 50 \text{ G}$  at  $B_{\parallel} \sim 3 \text{ T}$ ) may be sufficiently strong for suppressing the WL corrections at low  $T$ . To eliminate  $B_{\perp}$ , we used the cross-magnetic-field set-up<sup>98</sup> (see Sec. 4.1.2 for details). For each value of  $B_{\parallel}$ , we measured the dependence  $\sigma(B_{\perp})$  by sweeping  $B_{\perp}$  and recorded the minimum value of  $\sigma(B_{\perp})$  which corresponded to the zero WL magnetoconductance and, thus,  $B_{\perp} = 0$ . This method allowed us to compensate  $B_{\perp}$  with accuracy better than 10G.

The theoretical  $\Delta\sigma(B_{\parallel})$  dependences [Eqs. (2.44), (2.45)], plotted in Figure 7.3 as solid curves, describe the observed MC very well in not-too-strong magnetic fields

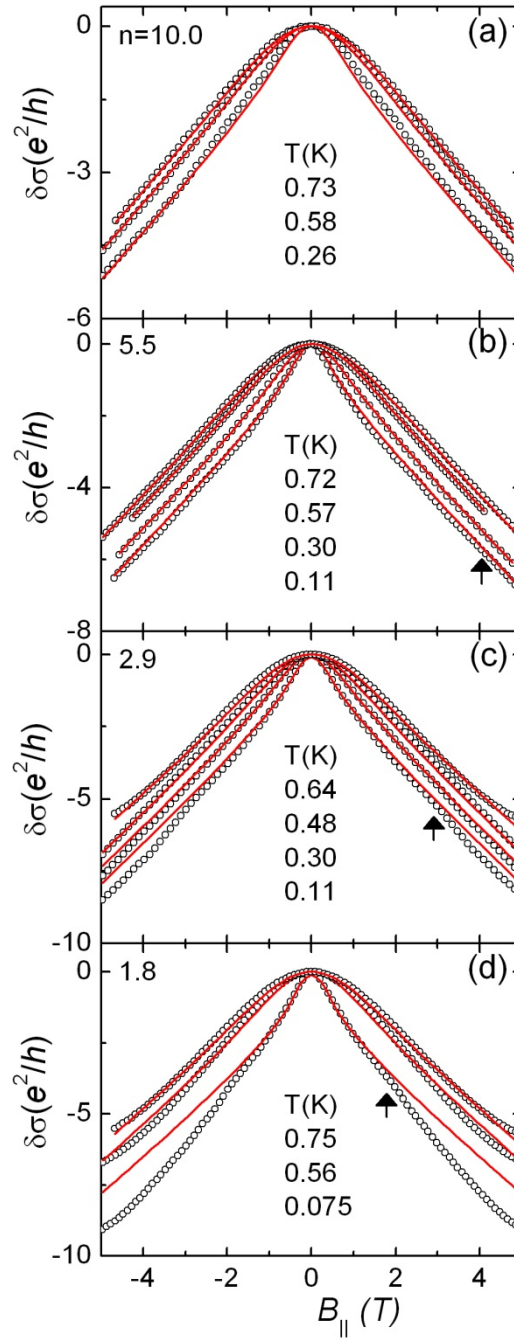


Figure 7.3. Magnetoconductance for sample Si6-14 at different electron densities and temperatures. Experimental data are shown by dots, the theoretical dependences calculated according to Eqs. (2.44), (2.45), - by solid curves. The  $F_0^\sigma$  value is the only fitting parameter in comparison with the theory<sup>35</sup>, the corresponding values of  $F_0^\sigma$  are shown in Figure 7.4. Arrows indicate the fields corresponding to the condition  $g\mu_B B_{||} / 2E_F = 0.1$ . The values of  $n$  are shown in units of  $10^{11} \text{ cm}^{-2}$ .

$g_b \mu_B B_{\parallel} < 0.2 E_F$ . Again, as in the case of fitting the  $\Delta\sigma(T)$  dependences, the only adjustable parameter was the  $F_0^{\sigma}(n)$  value extracted for each density from fitting the MC at high temperatures ( $\sim 0.7\text{K}$ ) where the effects of valley splitting or intervalley scattering on  $\Delta\sigma_{ee}(T, B)$  can be neglected. Note that all the theoretical curves plotted in Figure 7.3 for the same  $n$  were calculated for a fixed  $F_0^{\sigma}(n)$ , i.e. neglecting possible dependence  $F_0^{\sigma}(B_{\parallel})$ . The detailed analysis of the spin susceptibility  $\chi^* \propto g^* m^*$  in strong magnetic field, presented in Ref. 115, shows that the product  $g^* m^*$  decreases with an increase of  $B_{\parallel}$  by as much as  $\sim 20\%$ . Our estimate shows that by ignoring the  $g^*(B)$  dependence, we might reduce the value of  $|F_0^{\sigma}|$  by  $\sim 10\%$  (see below), which is close to the accuracy of extraction of  $F_0^{\sigma}$  from the data in strong magnetic fields. As  $B_{\parallel}$  grows and/or  $n$  decreases, the data start deviating from the theoretical curves [see Figure 7.3(d)]; this deviation can be attributed to the violation of the condition  $g_b \mu_B B \ll E_F$  required for applicability of Eqs. (2.44) and (2.45).

### 7.2.5. The $F_0^{\sigma}(n)$ dependence

The  $F_0^{\sigma}$  values obtained from fitting the  $\Delta\sigma(T)$  and  $\Delta\sigma(B_{\parallel})$  dependences with the theory<sup>35</sup> are shown in Figure 7.4. For comparison, we have also plotted the  $F_0^{\sigma}$  values obtained from the analysis of SdH oscillations (measured for sample Si6-14) using the theories of Refs. 99,117 (see Section 5.3). The  $F_0^{\sigma}$  values obtained from fitting  $\Delta\sigma(T)$  are in good agreement with the corresponding values extracted from the analysis of SdH data.

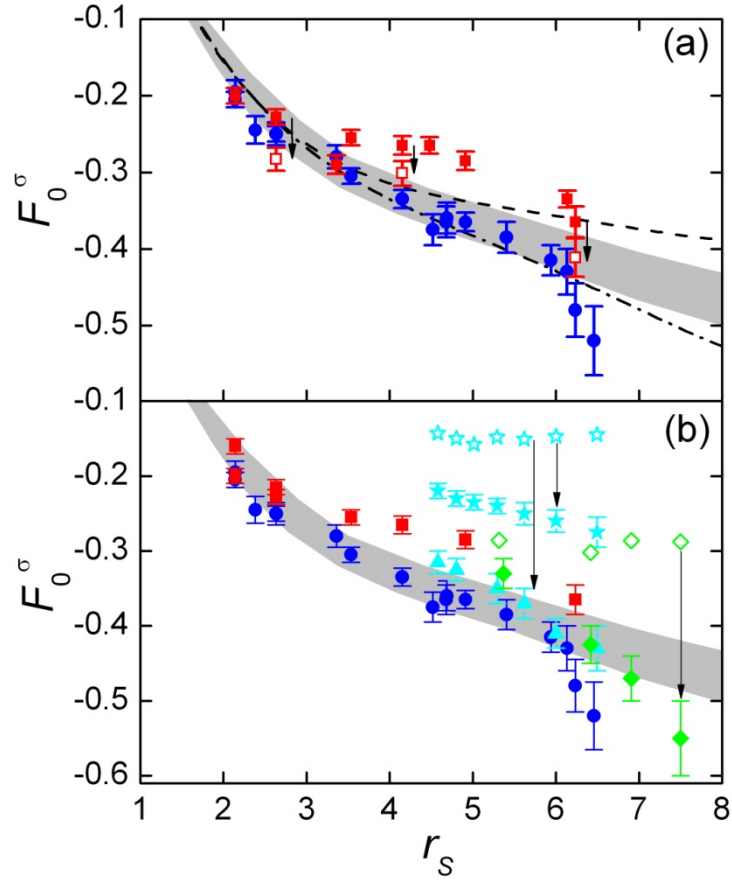


Figure 7.4. The  $F_0^\sigma$  values obtained from fitting the  $\sigma(T)$  and  $\sigma(B_\parallel)$  dependences with the ZNA theory<sup>35</sup> (blue and red symbols, respectively). Open red squares show the shift of several  $F_0^\sigma$  values extracted from  $\sigma(B_\parallel)$  if one takes into account the  $g(B_\parallel)$  dependence and the suppression of the WL corrections by  $B_\parallel$  (see the text). The dashed curve corresponds to  $F_0^\sigma(r_s)$  extracted from the SdH data<sup>41</sup> using the LK theory<sup>99</sup>, the dash-dotted curve - to the empirical approach used in Ref. 41. The shaded regions in panels (a) and (b) show the  $F_0^\sigma(r_s)$  dependence (with the experimental uncertainty) obtained from fitting the SdH data (measured by Pudalov *et al.*<sup>41</sup>) with the theory<sup>117</sup>. (b) Comparison of  $F_0^\sigma$  values calculated from  $\sigma(B_\parallel)$  and  $\sigma(T)$  using the same fitting procedure (see the text): ●, ■ - present work, ☆ and ◇ -  $F_0^\sigma$  reported in Refs. 134 and 66, respectively; ★ and ▲ -  $F_0^\sigma$  recalculated from  $\sigma(B_\parallel)$  and  $\sigma(T)$  data<sup>134</sup>, respectively; ◆ -  $F_0^\sigma$  recalculated from  $\sigma(T)$  data<sup>66</sup>.

At the same time, the  $|F_0^\sigma|$  values obtained from fitting the  $\Delta\sigma(B_\parallel)$  dependences at  $r_s > 4$  are systematically smaller than the corresponding values obtained from

fitting  $\Delta\sigma(T)$  and SdH oscillations. This trend was earlier reported in Refs. 66,135. There are at least two factors that can reduce this discrepancy. One of them, a potential decrease of  $g^*$  in strong  $B_{\parallel}$ , was mentioned in Section 7.2.4. The other factor is more subtle. In our analysis, we neglected the dependence of the WL correction  $\delta\sigma_{\text{WL}}$  on  $B_{\parallel}$ . However, our measurements show that  $\delta\sigma_{\text{WL}}$  decreases with an increase of the in-plane magnetic field, which leads to a positive magnetoconductance. There are at least two potential reasons for this dependence: (a) the Si-SiO<sub>2</sub> interface roughness transforms a uniform in-plane field into a random perpendicular field (see, e.g., Refs. 139,140,141 and references therein), and (b) a finite extent of electron wave functions in the direction perpendicular to the plane of a 2D system causes sub-band mixing by the magnetic field and disorder (see, e.g., Ref. 142 and references therein).

Phenomenologically, both effects can be described in terms of a decrease of the dephasing length  $L_{\varphi}$  with  $B_{\parallel}$ . For example, from the analysis of the WL magnetoresistance measured for different values of  $B_{\parallel}$  for sample Si6-14 at  $n = 1 \times 10^{11} \text{ cm}^{-2}$  and  $T = 0.3 \text{ K}$ , we have extracted  $L_{\varphi}(B_{\parallel} = 0) = 1.3 \mu\text{m}$  and  $L_{\varphi}(B_{\parallel} = 3 \text{ T}) = 0.8 \mu\text{m}$ . Our estimates show that the positive magnetoconductance associated with the suppression of  $\delta\sigma_{\text{WL}}$  by  $B_{\parallel}$  can account for  $\sim 10\%$  magnetoconductance. After taking the dependences  $g^*(B_{\parallel})$  and  $\delta\sigma_{\text{WL}}(B_{\parallel})$  into account, the  $|F_0^{\sigma}|$  values extracted from the MC should be increased by  $\sim 20\%$ . The corresponding downshift of the  $F_0^{\sigma}$  values extracted from the  $\Delta\sigma(B)$  data is shown by arrows in Figure 7.4(a), it significantly reduces the discrepancy between the values of  $F_0^{\sigma}$  extracted from the  $B_{\parallel} = 0$  data and the data measured at  $B_{\parallel} = 1\text{-}5 \text{ T}$ .

Finally, in order to compare our data with other available  $\Delta\sigma(T)$  data for high-mobility Si MOSFETs, we have used Eqs. (2.40-2.45) to estimate the  $F_0^\sigma$  values from the quasi-linear  $\sigma(T, B=0)$  dependences measured by Shashkin *et al.*<sup>134</sup> and Vitkalov *et al.*<sup>66</sup>. We also reanalyzed  $\sigma(B_{||})$  data presented in Ref. 66. In this analysis, we estimated  $\tau$  from  $\sigma(T \rightarrow 0)$  using the band mass rather than  $m^*$ . As for the valley splitting, we have used  $\Delta_V$  0.6 K and 1 K for the analysis of data from Ref. 134 and 66, respectively. (The value  $\Delta_V \sim 1$ -2 K used in Ref. 134 seems to be too large, as it would lead to the appearance of beating of SdH oscillations in the field range studied in Ref. 143). We have also taken into account the WL correction neglected in both Ref. 134 and 66. Figure 7.4(b) shows that the  $F_0^\sigma(r_s)$  values estimated for  $\sigma(T)$  data measured on different Si MOSFETs using the ZNA theory<sup>35</sup> are in good agreement with each other. The values of  $|F_0^\sigma|$  extracted from MC data of Vitkalov *et al.*<sup>66</sup> are smaller compared to  $|F_0^\sigma|$  estimated from  $\sigma(T, B=0)$ .

The  $F_0^\sigma$  values obtained on the basis of the interaction correction theory and plotted in Figure 7.4 may be compared also with the values of  $F_0^\sigma = -\gamma_2/(1+\gamma_2)$  predicted by the RG theory and measured experimentally in Refs. 61,62. Extrapolation of our  $F_0^\sigma(r_s)$  data to lower densities, provides the value  $F_0^\sigma \approx -0.5$  at  $n \approx 1 \times 10^{11} \text{ cm}^{-2}$  ( $r_s \approx 8$ ), which is *smaller* than the value  $F_0^\sigma = -0.31$  ( $\gamma_2 = 0.45$ ) predicted by the one-loop RG theory for the temperature  $T^{\text{max}}$  corresponding to the  $\rho(T)$  maximum<sup>38,61,62</sup> (e.g.,  $T^{\text{max}} \approx 3$  K For  $n = 1.2 \times 10^{11} \text{ cm}^{-2}$ ).

The experimental test<sup>61,62</sup> of the RG theory was conducted at temperatures higher than that in the experiments described in the present work. Within the framework of



the RG theory, the interaction parameter  $\gamma_2$  is expected to increase with decreasing  $T$ <sup>38,61,62</sup> and, in principle, it can reach at  $T < 1\text{K}$  the value of  $\sim 1$  which corresponds to  $F_0^\sigma = -0.5$ . (Note that the factor-of-two increase of  $\gamma_2$  (from 0.45 to 1) is beyond the range of the applicability of the one-loop RG theory.) However, the spin susceptibility  $\chi^* \propto g^* m^*$  obtained from the SdH data is almost  $T$ -independent<sup>115</sup>, in contrast to the expected increase of  $\gamma_2$  (and, hence,  $|F_0^\sigma|$  and  $g^*$ ) with cooling. This contradiction can be resolved if the  $T$ -dependence of  $g^*$  is exactly compensated by the opposite  $T$ -dependence of  $m^*$ , so that  $\chi^* \propto g^* m^*$  remains almost constant. The reason for this compensation is not clear and requires both experimental and theoretical studies.

### 7.3. Conclusion

Our experiments show that the low- $T$  behavior of the conductivity of high-mobility (001) Si MOSFETs is well described by the theory of interaction effects in systems with short-range disorder<sup>35</sup>. Over a wide range of intermediate temperatures ( $\Delta_V, \tau_V^{-1}, g_b \mu_B B < T \ll E_F$ ), the interaction effects are strongly enhanced in Si MOSFETs due to the presence of two valleys in the electron spectrum. This factor, in combination with the interaction-driven renormalization of the Fermi-liquid parameter  $F_0^\sigma$ , leads to an increase of  $\sigma$  with decreasing  $T$ . At lower temperatures ( $T < \Delta_V, \tau_V^{-1}, g_b \mu_B B, E_F$ ), the triplet contribution to  $\Delta\sigma_{ee}(T)$  is significantly reduced due to valley splitting and/or intervalley scattering. As a result, the metallic behavior of  $\sigma$  is replaced with a more conventional, insulating behavior. The  $F_0^\sigma$  values obtained from fitting the experimental data with the theory<sup>35</sup> agree well with the  $F_0^\sigma$

data obtained from the analysis of SdH oscillations in these samples. However, it remains unclear how to reconcile the  $F_0^\sigma$  values obtained at low  $n$  from fitting the  $\sigma(T)$  and SdH data by using the interaction correction theory with the corresponding values obtained within framework of the RG theory.

We emphasize the detailed analysis of the interaction-induced contributions to the conductivity, it is important to measure such parameters as the valley splitting and intervalley scattering rate in independent experiments.

Finally, for a quantitative description of the interaction effects to the conductivity  $\Delta\sigma_{ee}$  at low temperatures, both the interaction correction theory and RG theory should be extended to the case of a finite intervalley scattering rate.

## 8. Quenched disorder effects in electron transport in Si MOSFETs in the dilute regime

### 8.1. Introduction

One of the central problems in the phenomenon of the apparent 2D MIT and related metallic behavior is an understanding of the individual roles of the two major driving forces: disorder and EEI. A great body of experimental data demonstrates that, at sufficiently large carrier densities, the low-temperature behavior of disordered systems is governed by the universal quantum interaction corrections to the conductivity.<sup>9,35,37</sup> These interaction effects between mobile 2D electrons have been intensively studied both theoretically<sup>9,10,35-38,60,64,65</sup> and experimentally<sup>41,66,135,144,145</sup>.

Much less frequently another important issue is addressed, namely the interactions between localized and mobile electrons.<sup>46,93,146-148</sup> There are clear observations that, near the apparent 2D MIT, the behavior of dilute systems is very rich and does not necessarily follow the same pattern.<sup>92,93,149</sup> Also one might expect that the sample-specific disorder might become more important as the electron density decreases and approaches the critical density of the 2D MIT.

Usually, the presence of the localized states themselves in 2D transport is masked by mobile electrons. In order to reveal their contribution in the vicinity of the 2D MIT, we have studied electron transport in the same Si MOSFET sample that was slowly cooled down from room temperature to  $T = 4$  K at different fixed values of the gate voltage  $V_g = V^{\text{cool}}$ . Changing the cooling conditions primarily affects the

thickness of the potential well.<sup>y</sup> We believe that this allowed us to vary the fine details of disorder - the structure of the resonant (localized) states - without affecting the type of disorder (short-ranged), the scattering rate, and the strength of EEI in the system of mobile electrons. We focused on two key features of the 2D MIT: the strong dependences of the resistivity on temperature and the parallel magnetic field, and studied them in the density range  $n = (0.7-3) \times 10^{11} \text{ cm}^{-2}$ .

We have observed that, at relatively high densities (where the resistivity is smaller  $\rho \leq 0.1 h/e^2$ ), the dependences  $\rho(T)$  and  $\rho(B_{\parallel})$  in weak parallel magnetic fields  $B_{\parallel}$  are very similar for different cooldowns. This “universal” behavior of transport at high densities agrees with earlier observation<sup>135</sup> of the sample-independent  $\rho(T\tau, n)$  for samples with different mobility ( $\mu \propto \tau$ ). In contrast, at low densities [ $\rho \sim (0.1-1) h/e^2$ ], or in moderate and strong parallel fields  $g\mu_B B_{\parallel} \sim E_F \geq T$ , the cooling conditions dramatically affect transport even though the main parameters of disorder and of the electron interactions remain unchanged. This observation provides direct experimental evidence that, near the 2D MIT, electron transport at finite temperatures in dilute systems becomes sample-specific and dependent on more subtle details of disorder.

We have also observed that the frequency of SdH oscillations varies with temperature and in-plane field; these variations (of the order of a few %) grow as the density approaches the 2D MIT critical density. The SdH frequency is directly related to the density of mobile electrons, regardless of the interaction strength. Therefore,

---

<sup>y</sup>  $V^{\text{cool}}$  determines the depth of the confining potential well and, simultaneously, the number of interface traps sunk under the Fermi level. At low temperatures, as  $V_g$  is varied, the potential well  $V^{\text{cool}} = 0, 5, 10, 18$  and  $25$  V. The peak mobility for different  $V^{\text{cool}}$  varies by less than remains almost unchanged and “memorizes” the quenched disorder formed during the cooldown.

the observed variations of the mobile charge density at a fixed total charge in the metal-oxide-semiconductor capacitor gives evidence for the redistribution of electrons between mobile and localized states. The weak  $T$  dependence of this electron exchange, if it is attributed to activation processes, indicates the presence of very low energy barriers ( $\sim 1$  K) between the mobile and localized electron states. We relate the finite temperature cooldown effects to the hybridization of the mobile and (spatially separated) resonant localized states present at the Fermi energy at low densities.

## 8.2. Experiment

The resistivity measurements were performed on a high-mobility Si MOSFET sample Si6-14 (see Sec. 4.1.4 for details) in a temperature range of 0.05-1.2 K. The crossed magnetic field technique<sup>98</sup> was used to accurately align the magnetic field parallel to the plane of the 2D electron system (for more details see Sec. 4.1.2). The resistance was measured using the standard four-terminal AC technique using resistance bridge LR700. Five different cooldowns were performed with  $V^{\text{cool}} = 0, 5, 10, 18$  and 25 V. The electron density, found from the period of SdH oscillations (Sec. 4.2.1), varied linearly with  $V_g$ :  $n = A(V_g - V_{th})$ , where  $A$  ( $1.2 \times 10^{11} / (\text{Vcm}^2)$  for the studied sample) is determined by the oxide thickness. The threshold voltage  $V_{th}$  varied little (within 0.15 V) for different cooldowns and remained constant (within a few %) in the overall studied range of densities.

## 8.3. Temperature dependence of resistivity for different cooldowns

Figure 8.1 shows the mobility  $\mu$  versus  $V_g$  for five different cooldowns with  $\sim 7\%$ ; this demonstrates that the momentum relaxation time  $\tau$  is not strongly affected

by the cooling conditions. Comparing the  $\mu(n)$  curves with the conventional transport theory<sup>6,150</sup> we concluded that the density of charged impurities varies by less than  $10^{10} \text{ cm}^{-2}$  for different cooldowns. We also observed that the amplitudes of the SdH oscillations are similar for different cooldowns, as shown in the inset to Figure 8.1. These two observations are consistent with each other since the quantum lifetime  $\tau_q$  is nearly equal to  $\tau$  for Si MOSFETs.

Figure 8.2 shows that the  $\rho(T)$  dependences for several different cooldowns and different electron densities (in the vicinity and far from the 2D MIT). Far from the transition ( $\rho \ll h/e^2$ ) (see, e.g., curves 8-10). However, in the vicinity of the transition ( $\rho \sim h/e^2$ ), a dramatically different behavior is observed as temperature is decreased. The irreproducibility of  $\rho(T)$  for different cooldowns is clearly seen for curves in Figure 8.2, which correspond to nearly the same  $\rho$  at the lowest  $T$ : these curves, being different at higher temperatures, converge with decreasing  $T$ . We have verified that renormalized spin susceptibility and effective mass (and, thus, the two Fermi-liquid coupling parameters [Eq. (5.1)] do not change for different cooldowns to within 5%. Thus, EEI effects also cannot account for the change in  $\rho(T)$ .

The sample specific variations vanish at sufficiently low temperatures: this suggests that, in addition to universal effects, a sample-specific mechanism, which strongly affects the resistivity, comes into play at intermediate  $T$ .

If the behavior shown in Figure 8.2 were characterized by the critical density  $n_c$ , which correspond to the transition, the latter would have been cooldown-dependent. The labels on Figure 8.2 mark two  $\rho(T)$  dependences, which correspond to  $n = n_c$  for two different cooldowns: they were estimated from linear extrapolation to zero of

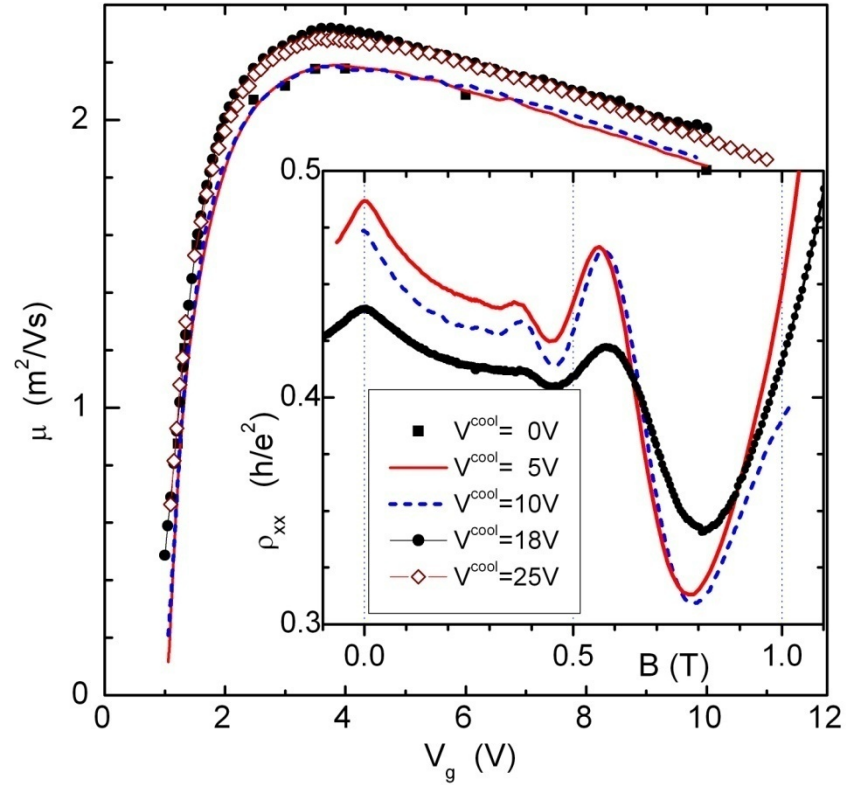


Figure 8.1. Mobility versus the gate voltage for different cooldowns. The  $V^{\text{cool}}$  for both the main panel and the inset are shown in figure. Examples of the SdH oscillations, shown in the inset for the same gate  $V_g = 1.15$  V,  $T = 0.1$  K,  $B_{||} = 0.03$  T, demonstrate that the quantum time  $\tau_q$  is not very sensitive to the cooling conditions. The carrier densities are (from top to bottom)  $n = 1.081, 1.092, 1.070$  in units  $10^{11} \text{cm}^{-2}$ .

the activation energy  $\Delta(n)$  measured in the insulating regime<sup>149,151</sup>

$\rho(T) \propto \exp(\Delta/T)$  away from the critical regime. It is clear that the critical

dependences  $\rho(T, n = n_c)$  are nonmonotonic (see also Ref. 151,100). The

nonmonotonicity is not caused by electron overheating: we applied sufficiently low source-drain current in order to reduce the excess electron temperature  $\delta T_e$  to a few

mK. For example, for the curve " $n_c^{25}$ " (the source-drain resistance are  $150 k\Omega$  each;

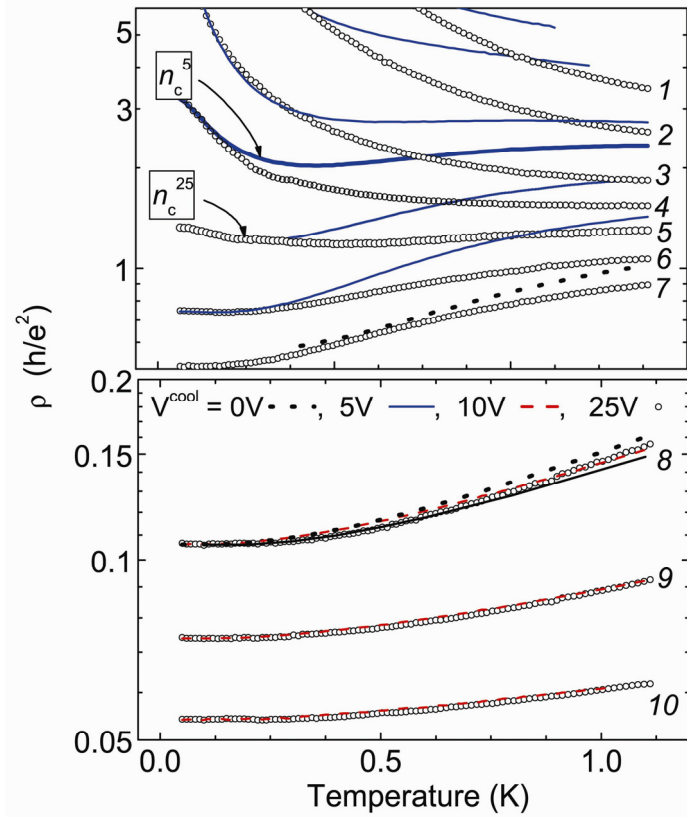


Figure 8.2. Temperature dependence of the resistivity for four different cooldowns. The densities, which correspond to curves 1 to 10, are as follow: 0.827, 0.0882, 0.942, 0.972, 1.00, 1.038, 1.07, 1.18, 1.31, 1.53 in units of  $10^{11} \text{ cm}^{-2}$ .  $n_c^5$  and  $n_c^{25}$  mark two critical dependences for cooldowns at  $V_g = 5$  and  $25 \text{ V}$ , respectively.

the channel resistance  $\sim 30 \text{ k}\Omega/\square$ ), the chosen the source-drain excitation  $10 \mu\text{V}$  corresponds to the dissipation  $\sim 10^{-15} \text{ W}$ , which might cause electron overheating  $\lesssim 1 \text{ mK}$ .<sup>100</sup>

Since the cooldown-specific changes in  $\rho(T)$  vanish with decreasing temperature, we have attempted to analyze the variations  $\delta\rho(T) = \rho(V_1^{\text{cool}}, T) - \rho(V_2^{\text{cool}}, T)$  in terms of exponential  $\exp(-\Delta/T)$  dependence as demonstrated in Figure 8.3. The corresponding activation energy  $\Delta$  is very low: it varies within the range  $\sim (0.7\text{-}1) \text{ K}$ .



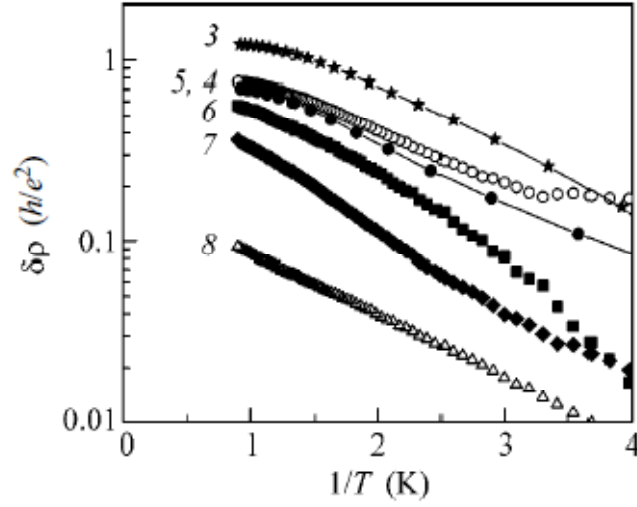


Figure 8.3. Difference between resistivity values for two different cooldowns (shown in Figure 8.2) versus inverse temperature. The numbers label the curves for the densities the same as in Figure 8.2.

This proves that the low-lying band of localized states (located close to the bottom of the conduction band,  $\approx 8$  K below the Fermi level) is irrelevant. The smallness of  $\Delta$ , therefore, points to the involvement of localized states that are located close to the Fermi Level. Similar resonant localized states are known in narrow band-gap semiconductors and must be spatially separated from the mobile states.

#### 8.4. In-plane magnetoresistance for different cooldowns

The in-plane MR data for different cooldowns are shown in Figure 8.4 and Figure 8.5. This MR is associated with spin effects.<sup>115,152,92</sup> In the theoretical models that describe in-plane MR in terms of  $EEI$ <sup>35,37</sup>, the MR is controlled by the FL parameter and the momentum relaxation time  $\tau$ . An important advantage of our method is that, as was mentioned above, cooling of the same sample at different  $V^{cool}$  does not affect these parameters. Thus, one might expect to observe a sample-

independent behavior if the MR is controlled solely by the universal interaction effects.

Firstly, we consider the range of field much weaker than the field of complete spin polarization ( $g\mu_B B_{\parallel}$ ). The insets to Figure 8.4 show that the MR is proportional to  $B_{\parallel}^2$  at  $g\mu_B B_{\parallel} \leq 1$ . We found that the slope  $d\rho/dB^2$  is nearly cooldown independent (i.e., universal) only for densities  $n > 1.3 \times 10^{11} \text{ cm}^{-2}$  (which are 30% greater than the critical density  $n_c$ ) or for the resistivity  $\rho(0) < 0.16h/e^2$  (compare two insets to Figure 8.4): this is consistent with earlier observation<sup>135</sup>. With approaching  $n_c$ , this universality vanishes: Figure 8.4(a) shows that even when the zero-field resistivity is as small as  $0.22h/e^2$ , the slope varies by a factor 1.3 for different  $V^{cool}$ .

For intermediate field,  $T < g\mu_B B_{\parallel} < E_F$ , the  $\rho(B_{\parallel})$  behavior is not universal over the whole density range  $n = (1-3) \times 10^{11} \text{ cm}^{-2}$  (Figure 8.4). As  $n$  decreases and approaches  $n_c$ , the cooldown dependent variations of  $\rho(B_{\parallel})$  increases progressively.

The influence of the cooldown conditions on the MR becomes even more dramatic in strong field;  $B_{\parallel} > E_F/g\mu_B$ . Despite the fact that the dependences  $\mu(n) \propto \tau(n)$  for different cooldowns were very similar (Figure 8.1), we observed very large variations in the high-field MR. Figure 8.5 shows  $\rho(B_{\parallel})$  for two different cooldowns at two values of  $n$ . The cooldown conditions cause factor-of-five changes in MR in strong field and factor-of-two changes in the values of  $B_{\parallel} = B_{sat}$  at which the MR saturates at a given electron density. The latter quantity was determined from the intercept of the tangents at the field below and above the MR saturation.<sup>92</sup>

The nonuniversal, sample-dependent behavior  $\rho(B_{\parallel})$  agrees with earlier

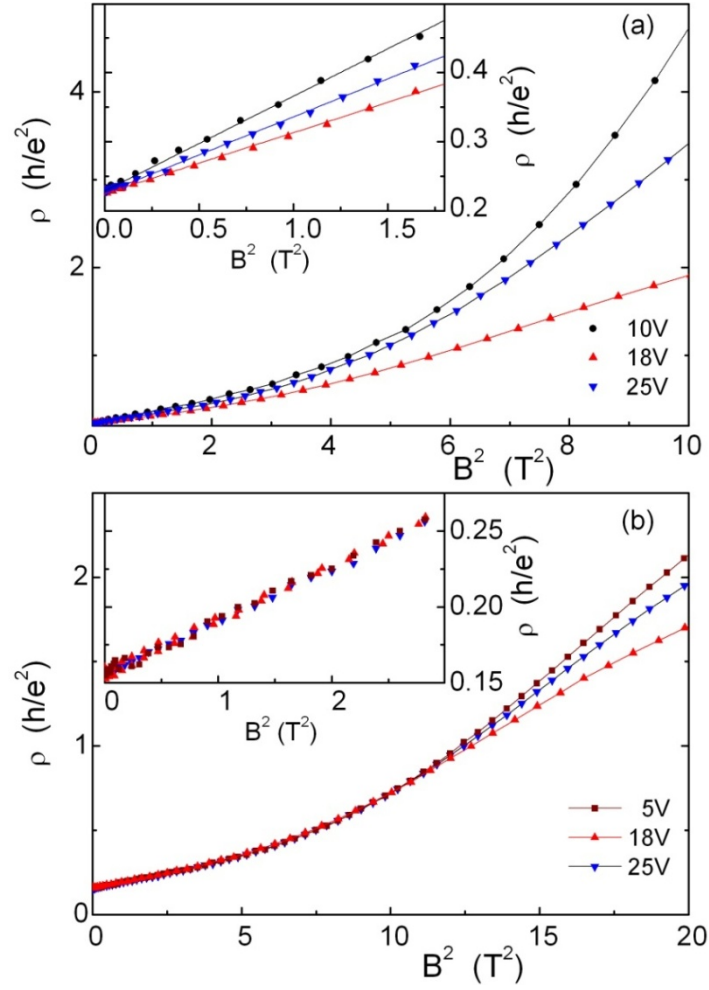


Figure 8.4. Examples of the dependences  $\rho(B_{\parallel}^2)$  at  $T = 0.3$  K for carrier density (a)  $1.2 \times 10^{11} \text{ cm}^{-2}$  and (b)  $1.34 \times 10^{11} \text{ cm}^{-2}$ . The insets blow up the low-field region of the quadratic behavior. The values of  $V^{\text{cool}}$  are indicated for each curve.

observations made on different samples.<sup>92</sup> We emphasize that the curves for different  $V^{\text{cool}}$  [in both Figure 8.5(a,b)] nominally correspond to the same density. The fact that  $B_{\text{sat}}$  is a cooldown dependent parameter proves that the MR in strong parallel fields is not solely related to the spin-polarization of mobile electrons. The fact that the variations arise in strong fields  $g\mu_B B_{\parallel} \sim E_F$  hints that a deep tail of localized states located near the bottom of the conduction band (or near the bottom of the upper

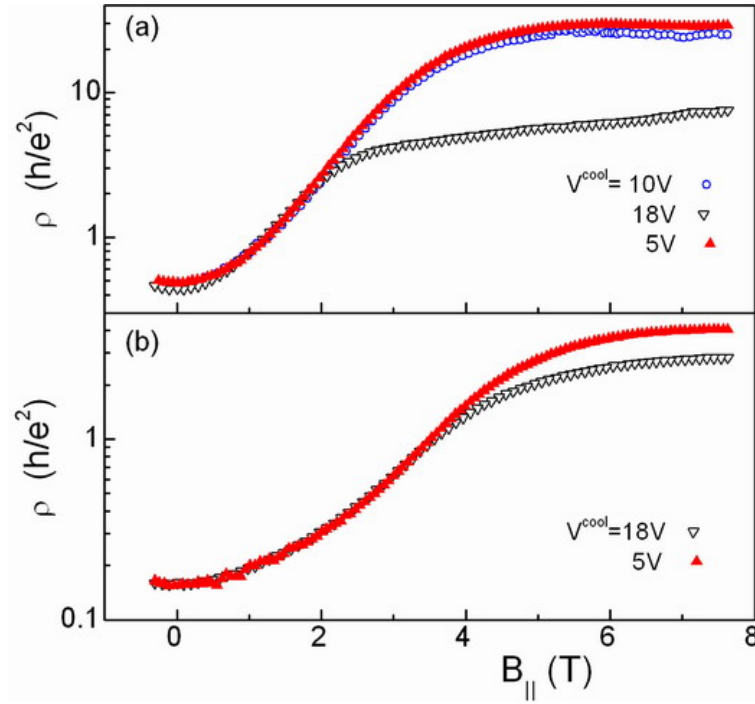


Figure 8.5. Resistivity vs. in-plane magnetic field for three cooldowns at two densities: (a)  $1.09 \times 10^{11} \text{ cm}^{-2}$  and (b)  $1.33 \times 10^{11} \text{ cm}^{-2}$ .

spin subband)<sup>46,148,106,153</sup> is responsible for the magnetoresistance variations. We note that, at low temperatures  $T \leq 1 \text{ K} \ll E_F$  and at zero field, temperature activation of carriers from the tail of localized states to the Fermi level (across the energy gap  $\sim E_F$ ) is negligibly weak and could not affect the data shown in Figure 8.2. In contrast, at higher temperatures  $T \sim E_F$ , the thermal activation of carriers from the tail of localized states to the Fermi level produces noticeable effects, which are detected in the Hall voltage.<sup>154</sup>

It is worth mentioning that the influence of variable disorder on transport and magnetotransport in Si MOSFETs has been studied earlier. Both temperature dependence  $\rho(T)$  and magnetoresistance  $\rho(B_{\parallel})$  were found to be different in samples with different mobility,<sup>149,92</sup> in samples cooled down with different values of

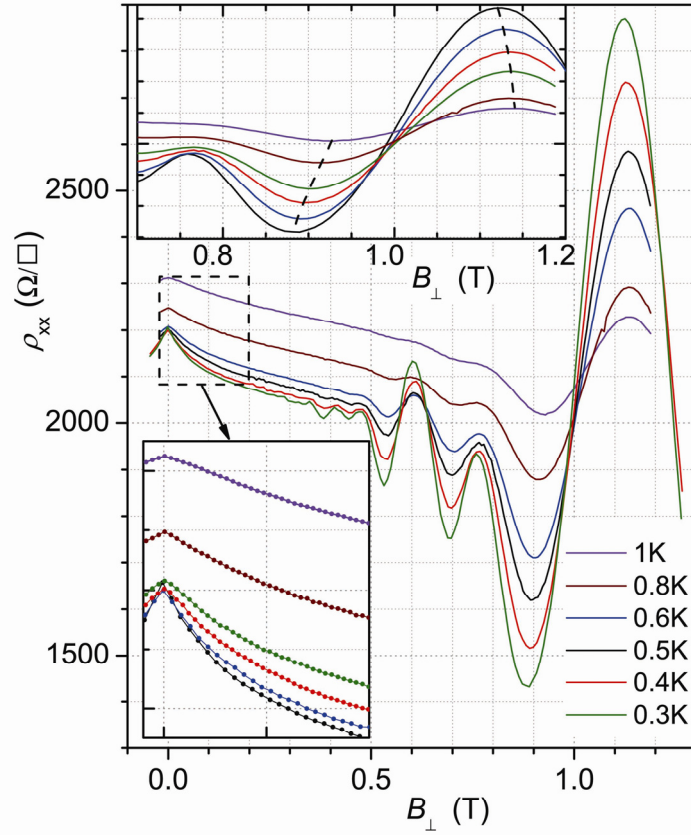


Figure 8.6. Typical SdH oscillations at six temperatures (indicated on the main panel) and in in-plane field  $B_{\parallel} = 0.02$  T. The nominal density value is  $n \approx 2 \times 10^{11} \text{ cm}^{-2}$ . The lower left inset demonstrates the precise control of the zero magnetic field position, and upper inset magnifies one of the oscillations to show its shifting with  $T$ .

the substrate bias voltage,<sup>155</sup> and with an intentionally varied oxide charge.<sup>6</sup> In contrast, in our studies, we kept constant the scattering time, the quantum time, the phase breaking time, the interface charge, and the parameters relevant to EEI. Even under such conditions, strong nonuniversal variations in  $\rho(T)$  and  $\rho(B_{\parallel})$  occur.

In order to elucidate the origin of the observed variations in disorder, we have analyzed SdH oscillations at weak perpendicular magnetic fields versus temperature

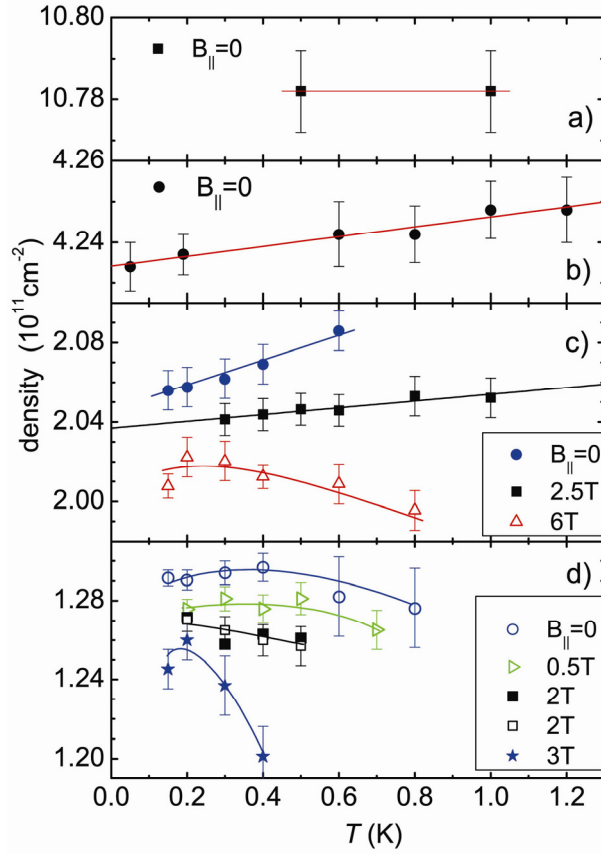


Figure 8.7. Temperature dependences of the frequency of SdH oscillations at four fixed values of the gate voltage. The different curves within panels (c) and (d) are shifted in  $y$ -axis for clarity.

and in-plane magnetic field. Figure 8.6 shows typical  $\rho_{xx}(B_{\perp})$  curves for six temperatures that were measured during the same cooldown for a fixed gate voltage value. The  $\rho_{xx}$  minima occur when the Fermi energy coincides with the middle of the energy gap. The upper-left inset clearly shows that the minima of the oscillations shift with temperature, thereby, providing evidence for the changes in the density of mobile carriers. The lower-left inset demonstrates that the shift of the  $\rho_{xx}$  minima is not caused by variations in the residual field of the superconducting magnet (maintained at 4 K).

We fitted the total oscillatory picture with the theoretical dependence (similar to that

In Ref. 41) using the frequency of oscillations  $n_{\text{sdH}}$  for each of the curves as a fitting parameter. The resulting temperature dependences of  $n_{\text{sdH}}$  are shown in Figure 8.7. The error bars on the figure correspond to relative changes of the frequency with temperature; the absolute frequencies are determined with about three times lower precision. At a higher density  $n > 5 \times 10^{11} \text{cm}^{-2}$  the oscillation frequency was independent of temperature within the 0.5% uncertainty. The  $n_{\text{sdH}}(T)$  changes become noticeable at a density  $\leq 4 \times 10^{11} \text{cm}^{-2}$  (which is four times larger than the critical density of the 2D MIT); they increase progressively with an in-plane field, as Figure 8.7(c,d) shows.

## 8.5. Conclusions

The measured density values  $n_{\text{sdH}}$  refer to the density of mobile electrons that participate in the Landau quantization. The weak temperature variations of the density of mobile electrons do not involve a large energy scale on the order of  $E_F \sim 8 \text{ K}$ . This points to the presence of resonant localized states at the Fermi level, which are separated spatially and by a small energy barrier from the mobile states. The density variations are then caused by exchange of electrons between those two states via either overbarrier transitions, or tunneling.

The temperature induced exchange of electrons between the bands of mobile and localized states, by itself, cannot produce a significant effect on the resistivity. Indeed, the appearance (disappearance) of  $10^9 \text{cm}^{-2}$  charged scatterers (which corresponds to the 0.5% variations of density in Figure 8.7) may, correspondingly, cause 0.5% changes in  $\rho$ . However, in the critical regime, the localized states are expected to occupy a significant share of the total 2D layer by forming clusters. The periphery of

the cluster is assumed to consist of the resonant states that may emit and absorb electrons. As a result, the overall area available for motion of mobile electrons changes with temperature, similar to that in the known percolation picture<sup>156</sup>. The resonant states, thus, may control transport through the saddle points separating neighboring areas occupied by mobile electrons and, thus, indirectly trigger the strong changes in  $\rho$ .

In the  $B_{\parallel}$  field, the resonant state should split and move relative to the band of mobile states. This model can potentially explain both the strong variations of  $\rho(T)$  and  $\rho(B_{\parallel})$  in the critical regime and the weak changes in the mobile carrier density. Formation of the two-phase state may be caused by either disorder or EEL. Spontaneous formation of the heterophase state in the vicinity of the phase transition was established for quasi-1D systems;<sup>157</sup> in 2D electron systems, the two-phase state is also intrinsic to some theoretical models.<sup>158</sup>

To summarize, by cooling the same high-mobility Si MOSFET sample at different fixed values of the gate voltage, we tested the universality of temperature and magnetic field dependences of the resistivity near the 2D MIT. An important advantage of this approach is that the different cooldown procedures do not alter the interaction effects between mobile carriers. It has been found that, in the vicinity of the transition ( $\rho \sim h/e^2$ ), the specific cooldown effects strongly affect  $\rho(T)$ ; these effects vanish only when  $\rho$  decreases below  $\sim 0.1h/e^2$  with increasing electron density; they also vanish as  $T$  decreases. The nonuniversal behavior is especially dramatic in strong  $B_{\parallel}$  fields, where it extends to much higher electron densities (we observed pronounced nonuniversality of  $R(B_{\parallel})$  over a range of  $n = (1-3) \times 10^{11} \text{ cm}^{-2}$ ).



Our results reveal the existence of the resonant (shallow) localized states near the Fermi energy. The observed temperature variation of the frequency of SdH oscillations demonstrates a weak exchange of electrons between the reservoirs of mobile and resonant localized states. The large changes of  $\rho(T)$  at elevated temperature signify the development of a spatial inhomogeneity of the 2D system, which may result from either interactions between electrons or disorder.

## 9. Summary

### INTERACTION EFFECTS IN HIGH-MOBILITY Si MOSFETs AT ULTRA-LOW TEMPERATURES

The experimental observation of the metallic behavior and the apparent 2D MIT in almost all dilute 2D electron and hole systems studied so far defies the main statement of the scaling theory of localization that in 2D at zero temperature all electron states are localized and there exists no true metallic phase.

A high-mobility Si MOSFET stands out of all other 2D systems since its transport properties are especially pronounced. In particular, two almost degenerate valleys strongly amplify the anomalous metallic dependence of  $\sigma(T)$ .

Recently, Zala, Narozhny and Aleiner<sup>35</sup> have explained the metallic behavior of the conductivity in terms of EEI using the Fermi-liquid approach. The authors of Ref. 35 linked the theory of Altshuler and Aronov<sup>9</sup> and Finkelstein<sup>10</sup> (diffusive regime) and the screening theory<sup>32,33,34</sup> (ballistic regime). The ZNA theory predicts that the magnitude and sign of interaction correction  $\Delta\sigma(T, B)$  is determined by the value of the Fermi-liquid parameter  $F_0^\sigma$ . The metallicity in various low-carrier-density 2D systems is enhanced at low  $n$  due to the renormalization of  $F_0^\sigma$ .

In the present work, we have studied the interaction effects responsible for the anomalous metallic conductivity over wide ranges of electron densities, temperatures and magnetic fields.

The interaction theory predicts the conductivity to depend on several parameters such as the elastic transport scattering time  $\tau$ , the Fermi-liquid parameter  $F_0^\sigma$  and the

valley splitting  $\Delta_V$ . Although the effect of the intervalley scattering is not considered in the interaction theory<sup>35</sup>, it might also affect the behavior of  $\sigma(T, B)$  since at temperatures smaller than intervalley scattering rate  $\tau_V^{-1}$  two valleys are effectively unified and the enhancement of the metallicity is diminished. As a result, with decreasing of  $T$ , the metallic dependence of  $\sigma(T)$  is expected to become weaker or even to be replaced with the insulating one. Thus, it is crucial to determine these parameters in independent experiments.

Before analyzing the temperature and magnetic behavior of the conductivity with the existing interaction theory<sup>35</sup> we have measured in independent experiments the parameters, which might affect the low-temperature transport: valley splitting and intervalley scattering.

The analysis of SdH oscillations allowed us to estimate the energy splitting  $\Delta_V$  between two valleys. In particular, a noticeable reduction of the SdH amplitude was attributed to a non-zero valley splitting. The measured values of  $\Delta_V$  (0.4K and 0.7K) for two our samples indicate that the effect of the valley splitting on  $\sigma$  is indeed important at low temperatures.

Based on the analysis of measured WL magnetoresistance, we have studied in details the intervalley scattering in Si MOSFET samples with different mobilities. In the analysis of our WL MR data we used a recent theory developed by Averkiev and Tarasenko<sup>39</sup> that extends the ballistic (i.e., applicable to arbitrary classically-weak magnetic fields) theory of WL QC to the case of two degenerate valleys. Our experiments have shown that the intervalley scattering is elastic and rather strong. The intervalley scattering rate is temperature independent and the ratio  $\tau_V/\tau$  decreases monotonically with increasing the electron density. We found no simple correlation

between  $\tau_V$  and the mobility of different samples, what points to a sample specific mechanism of the intervalley scattering. The measured  $\tau_V^{-1}$  values correspond  $T = (0.4-0.8)$  K what indicates the importance of extending the existent interaction theories to the case of finite intervalley scattering rate.

We have also reanalyzed previously measured SdH oscillations using the available theory of magneto-oscillations<sup>117</sup> that extends the Lifshitz-Kosevich theory<sup>99</sup> to 2D interacting systems. This allowed us to correct previously reported  $F_0^\sigma(n)$ -values.

Proper grounding of the experimental set-up and filtering of all leads connected to the sample extended the experimental temperature down to 30 mK, what, in turn, allowed us to observe the nonmonotonic behavior of the conductivity at millikelvin temperatures. In particular, we observed for the first time that the metallic increase of  $\sigma$  with cooling in Si MOSFETs is followed by the downturn of  $\sigma(T)$  at lower temperatures.

We made a thorough comparison of our experimental  $\sigma(T, B_{||})$  dependences with the interaction theory<sup>35</sup> in both the ballistic and diffusive regimes [ $T\tau \sim (0.1-15)$ ]. We have also revealed shortcoming of the earlier analysis of  $\Delta\sigma(T)$ , reanalyzed the available data, and compared the  $F_0^\sigma(n)$  extracted from the fitting  $\Delta\sigma(T, B_{||})$  with corresponding values from other measurements. Our experiments show that the low- $T$  behavior of the conductivity in high-mobility (001) Si MOSFETs is well described by the theory of interaction effects in systems with short-range disorder. For a quantitative description of the EEI corrections the conductivity  $\Delta\sigma_{ee}$  at low temperatures ( $T \leq 0.3$  K) the theory should be modified by taking into account a finite intervalley scattering rate. We conclude that the metallic behavior of the

conductivity not-too-close to the apparent 2D MIT can be accounted for by the interaction effects in 2D systems at intermediate temperatures including both the ballistic and diffusive regimes.

In addition to the study of the anomalous metallicity not-too-close to the apparent 2D MIT, we have explored the universality of the temperature and magnetic dependencies of the resistivity in the vicinity of the transition. We have varied fine details of the effective disorder (the structure of the localized states) in 2DEG by cooling down the same Si MOSFET sample at different fixed values  $V^{\text{cool}}$  of the gate voltage. (We have shown that different values of  $V^{\text{cool}}$  do not alter the type of disorder (short-ranged), the scattering rate, and the strength of EEI between mobile electrons.)

Our experiments have shown that at relatively high densities ( $n \geq 1.3 \times 10^{11} \text{ cm}^{-2}$ ) the dependences  $\rho(T)$  and  $\rho(B_{\parallel})$  in the fields that are much weaker than the field of complete spin polarization ( $g\mu_B B_{\parallel} \ll 2E_F$ ) are “universal”, i.e. practically independent of the  $V^{\text{cool}}$  value. On the other hand, at low  $n$  or in moderate and strong magnetic fields this universality is violated. This observation provides direct experimental evidence that near the 2D MIT the electron transport at finite temperatures in dilute systems becomes sample-specific and dependent on more subtle details of disorder.

We have also observed that the frequency of SdH oscillations varies with temperature and magnetic field; these variations grows as  $n$  is decreased towards  $n_c$ . This points to the presence of the resonant localized states at the Fermi level, separated spatially and by a small energy barrier from the mobile states.

## APPENDIX A (Shubnikov-de Haas oscillations)

Shubnikov-de Haas (SdH) effect is an oscillatory behavior of the longitudinal resistivity  $\rho_{xx}$  in varied magnetic field normal to the plane of a 2D sample. This phenomenon is caused by the changing occupation of Landau levels in the vicinity of the Fermi level. Below we present the main formulas used in the analysis of Shubnikov-de Haas oscillations.

In the presence of magnetic field  $B_{\perp}$ , normal to a 2D sample, the electron spectrum is quantized; the Landau levels are formed at energies:

$$E_k = \left(k + \frac{1}{2}\right) \hbar \omega_c, k = 0, 1, 2, \dots \quad (\text{A.1})$$

where  $\omega_c = eB_{\perp}/m$  is a cyclotron frequency (Figure A1). The number of degenerate states  $n_L$  in each Landau level per unit area is proportional to a magnetic field:

$$n_L = \frac{B_{\perp}}{\Phi_0} = \frac{eB_{\perp}}{h} = \frac{m}{2\pi\hbar^2} \hbar \omega_c. \quad (\text{A.2})$$

Here  $\Phi_0 = h/e$  is the magnetic flux quantum. The gap between two consecutive Landau levels  $\hbar \omega_c$  increases with increasing magnetic field, so does the “capacity”  $n_L$  of each Landau level. Thus, an applied magnetic field transforms a continuous density of states for 2DEG ( $m/2\pi\hbar^2$ ) into a series of  $\delta$ -functions of weights  $n_L$  at the energies  $(k + 1/2)\hbar \omega_c$  as shown in Figure A1. Each Landau state contains the same number of states as the original 2D band over a range of  $\hbar \omega_c$ .

In a disordered system,  $\delta$ -functions are smeared: they acquire a finite width  $\Gamma$  because of scattering of electrons by impurities [Figure A1(b)].

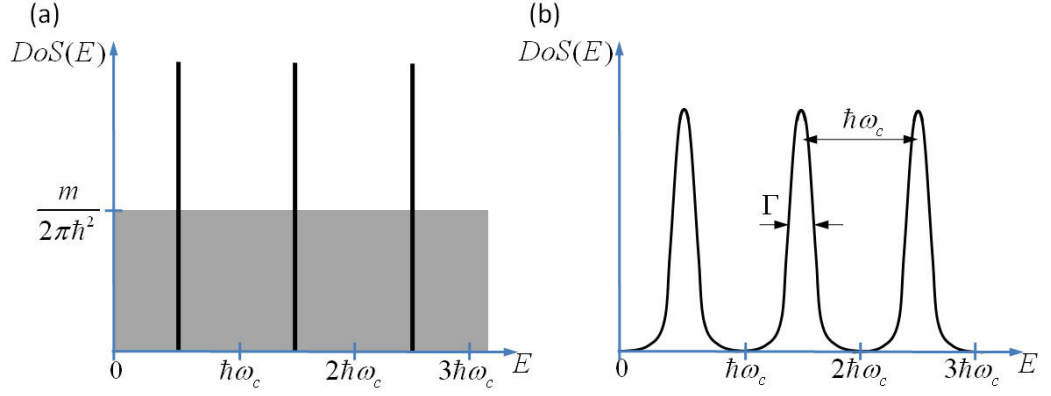


Figure A1. Density of states in a perpendicular magnetic field (spin splitting is neglected). (a) for an ideal system (without scattering processes), (b) realistic picture with finite level broadening. The Landau levels in case (b) are distinct when the interlevel distance  $\hbar\omega_c$  is greater than the level width  $\Gamma$  :  $\hbar\omega_c > \Gamma$ .

The number of occupied Landau levels is characterized by a filling factor  $\nu$ , which is the ration of the density of a 2DEG  $n_{2D}$  to the number of states in each Landau level  $n_L$  :

$$\nu = \frac{n_{2D}}{n_L} = \frac{\hbar n_{2D}}{eB_{\perp}} = \frac{\Phi_0 n_{2D}}{B_{\perp}} = 2\pi l_B^2 n_{2D}. \quad (\text{A.3})$$

Here  $2\pi l_B^2$  is a an area occupied by each state in Landau level ( $l_B = \sqrt{\hbar/eB_{\perp}}$  is called the magnetic length). The integer part of the filling factor  $[\nu]$ , is the number of completely filled Landau levels, while the reminder  $\nu - [\nu]$  determines the population of the highest occupied Landau level, partially filled by electrons.

As electron density or magnetic field is varied, the number of occupied Landau levels changes as well. Usually in the experiments it is easier to keep electron density constant and to vary a magnetic field. Suppose that  $n_{2D}$  is maintained constant and  $B_{\perp}$  is varied. Let us also assume that at a given magnetic field  $B_{\perp}^0$  the number of

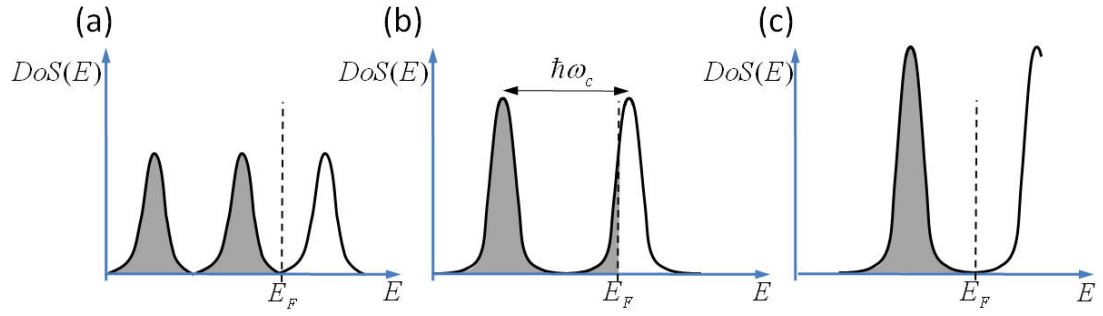


Figure A2. Occupation of Landau levels in a perpendicular magnetic field (spin splitting is neglected).

filled Landau levels is an integer number  $\nu^0 = i_0$ . In this case the Fermi energy lies in region between Landau levels, corresponding to zero density of states  $DoS(E) = 0$  and is equal to its value  $E_F^0$  before a magnetic field was applied [Figure A2(a)]. With increasing  $B_\perp$  the separation between Landau levels  $\hbar\omega_c$  and the degeneracy of each level  $n_L$  will increase. This will result in depopulating the upper ( $i_0$ -th) Landau level: the number of occupied states will become  $(\nu - [\nu])n_L$  instead of  $n_L$  [Figure A2(b)]. The Fermi level will move with the density of states to keep the number of electrons constant. When  $B_\perp$  is increased slightly ( $i_0 - 1 < \nu < i_0$ ) the Fermi level is approximately equal to  $E_F \approx (i_0 + 1)\hbar\omega_c$  and lies inside the  $i_0$ -th level within the width  $\Gamma$ , i.e.  $E_F$  rises linearly with  $B_\perp$ . With further increase of  $B_\perp$  the  $i_0$ -th level will become completely depopulated ( $\nu = i_0 - 1$ ), at this point  $E_F$  falls back to ( $i_0 - 1$ )-th level. The movement of  $E_F$  with magnetic field is schematically shown in a fan diagram (Figure A3) for a perfect system with  $\delta$ -function Landau levels.



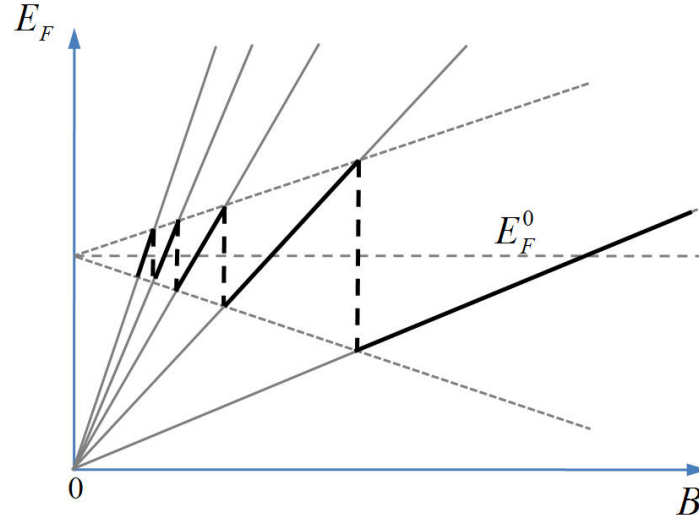


Figure A3. Variation of Fermi level as a function of magnetic field for 2DEG. The fan of thin lines shows Landau levels, while the discontinuous thick line is  $E_F$ . (This picture corresponds to an ideal 2D system in the absence of scattering ( $\delta$ -function Landau levels). For a realistic system the sharp jumps are smeared by Landau level broadening.)

When the Landau levels are broadened due to different scattering mechanisms we expect the longitudinal conductivity  $\sigma_{xx}$  roughly to follow the density of state at the Fermi level with a maximum when each level is half-filled. The density of state at the Fermi level and, hence,  $\sigma_{xx}$  have a periodic structure when considered as a function of  $1/B_{\perp}$  - the Shubnikov-de Haas effect.

The Shubnikov-de Haas oscillations are described by Lifshitz-Kosevich (LK) formula<sup>99</sup>, which is valid for non-interacting 2D electrons if the amplitude of oscillations is small<sup>116</sup>:

$$\frac{\delta\sigma_{xx}(\omega_c, T)}{\sigma_D} = \sum_s A_s^{LK}(\omega_c, T) \cos\left(\pi s \frac{2E_F}{\hbar\omega_c} - \pi s\right), \quad (\text{A.4})$$

$$A_s^{LK}(\omega_c, T) = -4 \exp\left(-\frac{2\pi^2 s T_D}{\hbar\omega_c}\right) \frac{(2\pi^2 s T / \hbar\omega_c)}{\sinh(2\pi^2 s T / \hbar\omega_c)}.$$

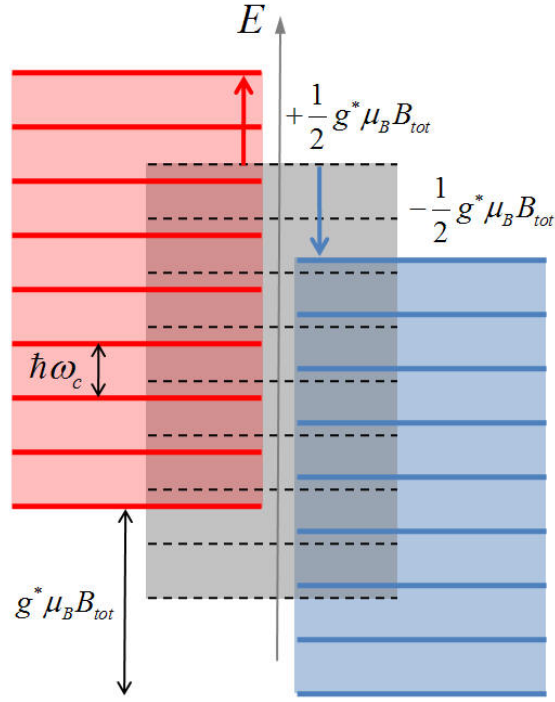


Figure A4. Zeeman splitting of Landau levels for spin up (red lines) and spin down (blue lines) states. Grey lines represent Landau levels neglecting spin-splitting.

Here  $\sigma_D = e^2 n \tau / m_b$  is the Drude resistivity ( $m_b$  - electron band mass),  $\omega_c = e B_{\perp} / m^*$  is the cyclotron frequency expressed through the effective mass  $m^*$ ,  $E_F = \hbar^2 \pi n / 2 m_b$  is the Fermi energy. Parameter  $T_D$  is the Dingle temperature,<sup>6,159</sup> that describes a broadening of Landau levels due to collisions:

$$T_D = \frac{\Gamma}{2\pi} = \frac{1}{2\pi\tau_q}. \quad (\text{A.5})$$

Here  $\tau_q$  is the elastic quantum scattering time. While only backscattering processes contribute to the transport time  $\tau$ , all scattering processes enter the  $\tau_q$ . The ratio  $\tau_q / \tau$  was studied in Ref. 160-162.

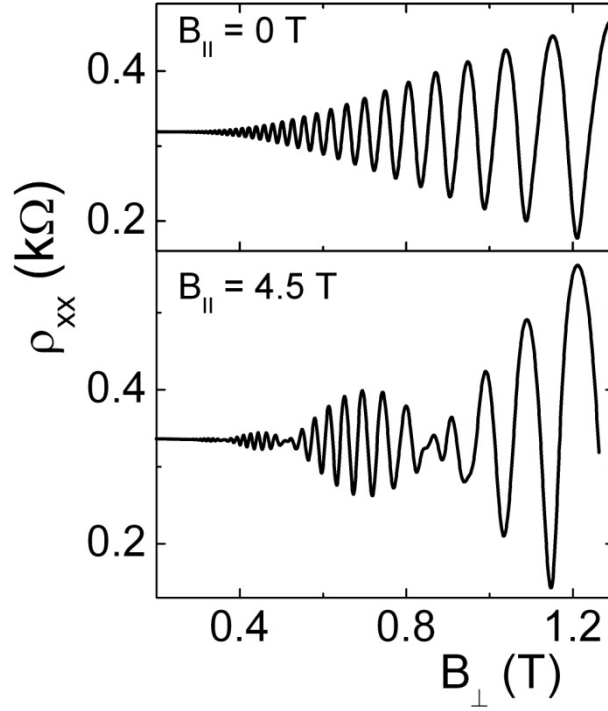


Figure A5. Typical SdH oscillations with and without in-plane magnetic field for electron density  $n = 10.6 \times 10^{11} \text{ cm}^{-2}$  (sample Si6-14/10) at  $T=0.35\text{K}$ . (Adopted from Ref. 41.)

The in-plane magnetic field  $B_{||}$  lifts the spin degeneracy by introducing an energy splitting for spin-up and spin-down electrons equal to the Zeeman energy  $E_Z = g\mu_B B_{tot}$  (See Figure A4), where  $\mu_B$  is a Bohr magneton and  $B_{tot} = \sqrt{B_{\perp}^2 + B_{||}^2}$  is a total magnetic field.

Although the two valleys relevant to the low temperature transport of (001) Si MOSFETs are almost equivalent, there exists a relatively small energy splitting  $\Delta_V$  between them.

Nonzero  $B_{||}$  and  $\Delta_V$  modify Eq. (A.1) as follow

$$E_k = \left(k + \frac{1}{2}\right) \hbar \omega_c \pm \frac{1}{2} E_Z \pm \frac{1}{2} \Delta_V, \quad k = 0, 1, 2, \dots \quad (\text{A.6})$$

This results in appearance of beating in the SdH pattern (Figure A5).

The complete expression of the LK formula ( $B_{\parallel}, \Delta_V \neq 0$ ) is given by

$$\frac{\delta\sigma_{xx}(\omega_c, T)}{\sigma_D} = \sum_s A_s^{LK}(\omega_c, T) \cos\left(\pi s \frac{2E_F}{\hbar\omega_c} - \pi s\right) Z_s(E_z) Z_s(\Delta_V),$$

$$Z_s(X) = \cos\left[\pi s \left(\frac{\hbar\pi n}{eB_{\perp}}\right) \frac{X}{2E_F}\right]. \quad (\text{A.7})$$

Or equivalently

$$\frac{\delta\sigma_{xx}(B_{\perp}, T)}{\sigma_D} =$$

$$\sum_s A_s^{LK}(\omega_c, T) \cos\left[\pi s \frac{\hbar\pi n}{eB_{\perp}} - \pi s\right] \cos\left[\pi s \left(\frac{g^* m^*}{2m_e}\right) \frac{B_{tot}}{B_{\perp}}\right] \cos\left[\pi s \left(\frac{\hbar\pi n}{eB_{\perp}}\right) \frac{\Delta_V}{2E_F}\right], \quad (\text{A.8})^z$$

$$A_s^{LK}(\omega_c, T) = -4 \exp\left(-\frac{2\pi^2 s T_D}{\hbar\omega_c}\right) \frac{(2\pi^2 s T / \hbar\omega_c)}{\sinh(2\pi^2 s T / \hbar\omega_c)}.$$

To summarize, SdH oscillations is a valuable tool in characterizing electronic structure in 2D: it can provide information on electron effective mass, spin susceptibility, electron density and electron temperature. A detailed analysis of extracting renormalized effective mass and  $g$ -factor is given in Ref. 41.

---

<sup>z</sup> For small values of  $\delta\sigma_{xx}/\sigma$  the corrections to the longitudinal resistivity  $\rho_{xx}$  can be expressed as  $\delta\rho_{xx}/\rho = -\delta\sigma_{xx}/\sigma$ .

## APPENDIX B (ZNA theory)

### ***f*- and *t*-functions:**

Explicit formulas for *f*- and *t*-function

$$\begin{aligned}
 f(x) = & \frac{8}{3} \int_0^\infty dz \left[ \frac{\partial}{\partial z} (z \coth z) - 1 \right] \\
 & \times \left\{ \frac{xz}{\pi} H(2xz) \ln 2 + \frac{1}{\pi} [1 + H(2xz)] \arctan \frac{1}{2xz} \right. \\
 & \left. + \frac{xz}{\pi} \left[ \frac{1}{2} + H(2xz) \right] \ln \left( 1 + \frac{1}{(2xz)^2} \right) + \frac{2}{\pi} \arctan(2xz) - 1 \right\}
 \end{aligned} \tag{B.1}$$

$$\begin{aligned}
 t(x; F_0^\sigma) = & \frac{8}{3} \int_0^\infty dz \left[ \frac{\partial}{\partial z} (z \coth z) - 1 \right] \\
 & \times \left\{ \frac{xz}{\pi} \{ [H(2xz) + h_1(2xz)] \ln 2 + h_4(2xz) \} \right. \\
 & + \frac{1}{\pi} [1 + H(2xz) + 4x^2 z^2 h_3(2xz)] \arctan \frac{1}{2xz} \\
 & \left. + \frac{xz}{\pi} \left[ \frac{1}{2} + H(2xz) + h_2(2xz) \right] \ln \left( 1 + \frac{1}{(2xz)^2} \right) + \left[ \frac{2}{\pi} \arctan(2xz) - 1 \right] \right\}
 \end{aligned} \tag{B.2}$$

$$\begin{aligned}
 h_1(x) &= \widetilde{H}(x; 1 + 2F_0^\sigma) [5 + 6F_0^\sigma - 4(2 + 3F_0^\sigma)H(x)] \\
 h_2(x) &= h_1(x) + \widetilde{H}(x; F_0^\sigma) \left[ -\frac{1}{2}(1 + F_0^\sigma) + F_0^\sigma x^2 \left( \frac{1}{2} - (1 + F_0^\sigma) \widetilde{H}(x; F_0^\sigma) \right) \right] \\
 h_3(x) &= \widetilde{H}(x; 1 + 2F_0^\sigma) [-1 - 2F_0^\sigma + (2 + 3F_0^\sigma) \widetilde{H}(x; F_0^\sigma)] \\
 &+ \frac{F_0^\sigma}{2} \widetilde{H}(x; F_0^\sigma) [1 + F_0^\sigma x^2 \widetilde{H}(x; F_0^\sigma)] \\
 h_4(x) &= \widetilde{H}(x; F_0^\sigma) \left( \frac{5F_0^\sigma - 3}{2} + \frac{1 - (F_0^\sigma)^2}{F_0^\sigma} \ln(1 + F_0^\sigma) \right) + h_5(x) \frac{1 + F_0^\sigma}{F_0^\sigma} \ln(1 + F_0^\sigma) \\
 h_5(x) &= \\
 & (2F_0^\sigma - 1) \widetilde{H}(x; 1 + 2F_0^\sigma) + \widetilde{H}^2(x; F_0^\sigma) \left[ \left( \frac{1}{2} - 2F_0^\sigma \right) (1 + F_0^\sigma)^2 - (F_0^\sigma)^2 x^2 \left( \frac{1}{2} + 2F_0^\sigma \right) \right] \\
 H(x) &= \frac{1}{4 + x^2}; \quad \widetilde{H}(x; y) = \frac{1}{(1 + y)^2 + (xy)^2}
 \end{aligned} \tag{B.3}$$

### $K_d$ and $K_b$ functions:

The exact formulas for  $K_d$  and  $K_b$  are the following.

$$\begin{aligned}
 K_b(x, F_0^\sigma) &= K_1(x) + K_2(x, F_0^\sigma) \\
 K_1(x, F_0^\sigma) &= x \coth(x) - 1 \\
 K_2(x, F_0^\sigma) &= \frac{1 + F_0^\sigma}{2F_0^\sigma} \int_x^{x/(1+F_0^\sigma)} dy \frac{\partial}{\partial y} (y \coth y) \\
 &\quad \times \left( y - \frac{x}{1 + F_0^\sigma} \right) \left[ \frac{1}{y} + \frac{2F_0^\sigma}{(1 + 2F_0^\sigma)y - x} \right] \\
 K_d(h, F_0^\sigma) &= -\frac{1}{4\pi F_0^\sigma} \sum_{L_z = \pm 1} \operatorname{Re} \int_{-\infty}^{\infty} \frac{dx}{x^2} \left[ \frac{\partial}{\partial x} (x \coth \pi x) \right] \\
 &\quad \times (x - L_z h) \ln \frac{x - L_z h}{x - L_z h / (1 + F_0^\sigma)} = \\
 &= -\frac{1}{4\pi F_0^\sigma} \sum_{n=1}^{\infty} \left\{ \frac{1}{n} \left( \ln \frac{n^2 + h^2}{n^2 + \frac{h^2}{(1 + F_0^\sigma)^2}} \right) - \frac{4h}{n^2} \left( \arctan \frac{h}{n^2} - \arctan \frac{h}{n(1 + F_0^\sigma)} \right) \right\} \\
 &\quad - \frac{1}{\pi} \left[ C + \operatorname{Re} \psi \left( 1 - \frac{ih}{1 + F_0^\sigma} \right) \right] \quad (B.4)
 \end{aligned}$$

Here  $C = 0.577\dots$  is Euler's constant,  $\psi(x)$  is the digamma function.

Although in the analysis of our experimental data we used exact formulas from ZNA theory, here we present the asymptotics for  $K_b$ ,  $K_d$ ,  $f$  and  $t$ :<sup>35</sup>

$$K_b(x, F_0^\sigma) = \begin{cases} \tilde{f}(F_0^\sigma) \frac{x^2}{3}, & x \ll 1 + F_0^\sigma \\ \tilde{g}(F_0^\sigma) x - 1 + O\left(\frac{1}{x}\right), & 1 \ll x \end{cases} \quad (B.6)$$

$$\begin{aligned}
 \tilde{f}(F_0^\sigma) &= 1 - \frac{F_0^\sigma}{1 + F_0^\sigma} \left[ \frac{1}{2} + \frac{1}{1 + 2F_0^\sigma} - \frac{2}{(1 + F_0^\sigma)^2} + \frac{2 \ln 2(1 + F_0^\sigma)}{(1 + F_0^\sigma)^3} \right] \\
 \tilde{g}(F_0^\sigma) &= \frac{1}{2F_0^\sigma} \ln(1 + F_0^\sigma) + \frac{1}{2(1 + 2F_0^\sigma)} + \frac{F_0^\sigma \ln 2(1 + F_0^\sigma)}{(1 + F_0^\sigma)^2}
 \end{aligned}$$

$$K_d(h) \approx \begin{cases} \frac{3F_0^\sigma \zeta(3)}{2\pi(1+F_0^\sigma)^2} h^2, & 1+F_0^\sigma \ll h \\ -\frac{1}{2\pi} \ln^2 \frac{h}{1+F_0^\sigma} + O\left(\ln \frac{h}{1+F_0^\sigma}\right), & 1+F_0^\sigma \ll h \ll 1 \\ \frac{1}{\pi} \left\{ 1 - \frac{1}{F_0^\sigma} \ln(1+F_0^\sigma) \right\} \ln \frac{1}{1+F_0^\sigma} - \frac{1}{2\pi F_0^\sigma} \ln^2 \frac{1}{1+F_0^\sigma}, & 1 \ll h \end{cases} \quad (\text{B.7})$$

$\zeta(x)$  is the Riemann zeta-function ( $\zeta(3) = 1.202\dots$ ).

$$f(x) \approx \begin{cases} 1 - \gamma_1 x - \frac{\pi}{6} x \ln x, & x \ll 1 \\ \frac{1}{3\pi x} \left( 2(\ln x - 1) \ln 2 - \frac{7}{2} \ln(2x) \right), & 1 \ll x \end{cases} \quad (\text{B.8})$$

$$\gamma_1 = -\frac{\zeta'(2)}{\pi} + \frac{\pi}{6} \left( C + \frac{1}{3} \ln 2 \right) \approx 0.7216$$

$$t(x \ll 1 + F_0^\sigma) \approx 1 - \gamma_2 x + \frac{\pi}{18} x \ln x \left( 3 + \frac{1}{1 + F_0^\sigma} \right),$$

$$\gamma_2 = -\frac{\zeta(2)}{3\pi} \left( 3 + \frac{1}{1 + F_0^\sigma} \right) - \frac{\pi \gamma_3}{9(1 + F_0^\sigma)} + \frac{\pi}{18} \left[ C \left( 3 + \frac{1}{1 + F_0^\sigma} \right) + \ln 2 \left( 1 + \frac{3}{1 + F_0^\sigma} \right) \right], \quad (\text{B.9})$$

$$\gamma_3 = 1 - \frac{5F_0^\sigma - 3}{1 + F_0^\sigma} - \left( \frac{5}{2} - 2F_0^\sigma \right) \frac{\ln(1 + F_0^\sigma)}{F_0^\sigma}.$$

## APPENDIX C (WL theory for a two-valley system)

In this section we give a short review of the theory of Averkiev and Tarasenko<sup>39</sup> that describes the WL magnetoconductance of a two-valley system over the whole range of classically weak magnetic fields  $\omega_c \tau \equiv \mu B < 1$ .

The WL QC to the conductivity in the magnetic field has the form

$$\Delta\sigma(B) = \Delta\sigma^{(a)} + \Delta\sigma^{(b)} \quad (\text{C.1})$$

where the terms  $\Delta\sigma^{(a)}$  and  $\Delta\sigma^{(b)}$  correspond to the diagrams, which have been considered in detail in Refs. 125,127,128. For the short-range scattering potential,<sup>aa</sup> one obtains

$$\begin{aligned} \Delta\sigma^{(a)} &= \frac{\hbar}{\pi} \sum_{\alpha\beta} \int J_x^2(\boldsymbol{\rho}, \boldsymbol{\rho}') C_{\beta\alpha}^{(3)\beta\alpha}(\boldsymbol{\rho}, \boldsymbol{\rho}') d\boldsymbol{\rho} d\boldsymbol{\rho}', \\ \Delta\sigma^{(b)} &= \frac{\hbar}{\pi} \sum_{\alpha\beta\gamma\delta} \int J_x(\boldsymbol{\rho}, \boldsymbol{\rho}') J_x(\boldsymbol{\rho}'', \boldsymbol{\rho}) W_{\gamma\delta}^{\alpha\beta} C_{\beta\gamma}^{(2)\delta\alpha}(\boldsymbol{\rho}', \boldsymbol{\rho}'') d\boldsymbol{\rho} d\boldsymbol{\rho}' \\ &\quad \times [G^R(\boldsymbol{\rho}, \boldsymbol{\rho}') G^R(\boldsymbol{\rho}', \boldsymbol{\rho}'') + G^A(\boldsymbol{\rho}, \boldsymbol{\rho}') G^A(\boldsymbol{\rho}', \boldsymbol{\rho}'')] d\boldsymbol{\rho}' d\boldsymbol{\rho}''. \end{aligned} \quad (\text{C.2})$$

Here  $\alpha, \beta, \gamma, \delta = 1, 2$  are the valley indices;  $J_x(\boldsymbol{\rho}, \boldsymbol{\rho}')$  is the  $x$ -component of the current vertex, which is defined as

$$J_x(\boldsymbol{\rho}, \boldsymbol{\rho}') = ie \frac{k_F \tau}{m^*} \frac{\boldsymbol{\rho} - \boldsymbol{\rho}'}{|\boldsymbol{\rho} - \boldsymbol{\rho}'|} [G^A(\boldsymbol{\rho}, \boldsymbol{\rho}') + G^R(\boldsymbol{\rho}, \boldsymbol{\rho}')]. \quad (\text{C.3})$$

$G^A(\boldsymbol{\rho}, \boldsymbol{\rho}')$  and  $G^R(\boldsymbol{\rho}, \boldsymbol{\rho}')$  are the advanced and related Green functions,

$$G^{R(A)}(\boldsymbol{\rho}, \boldsymbol{\rho}') = \sum_{s, k_y} \frac{\psi_{s, k_y}(\boldsymbol{\rho}) \psi_{s, k_y}^*(\boldsymbol{\rho}')}{E_F - E_s \pm i\hbar / (2\tau) \pm i\hbar / (2\tau_\varphi)}. \quad (\text{C.4})$$

---

<sup>aa</sup> As follows from our SdH measurements for all samples, as well from numerous other experiments,<sup>6</sup> the ratio of the large-angle scattering time  $\tau$  to the quantum time (or any-angle scattering time)  $\tau_q$  is close to unity in the studied range of electron densities. This result implies that the scattering in the studied samples is short-range.



$\psi_{s,k_y}(\boldsymbol{\rho})$  is the wave function of an electron subject to an external magnetic field  $\mathbf{B}$ , which is normal to the plane of a 2D structure,  $s$  and  $k_y$  are the quantum numbers ( $s$  is the Landau level number and  $k_y$  is the in-plane wave vector),  $E_s = \hbar\omega_c(s + 1/2)$  is the energy of the  $s$ th Landau level;  $C_{\gamma\delta}^{(2)\alpha\beta}(\boldsymbol{\rho}, \boldsymbol{\rho}')$ , and  $C_{\gamma\delta}^{(3)\alpha\beta}(\boldsymbol{\rho}, \boldsymbol{\rho}')$  are the Cooperons which depend on four valley indices. The parameters  $W_{\gamma\delta}^{\alpha\beta}$ , are determined by intervalley and intravalley correlators of the scattering potential and are defined by

$$\langle V_{\alpha k_1, \beta k_2}, V_{\gamma k_3, \delta k_4} \rangle N_{\text{imp}} = W_{\gamma\delta}^{\alpha\beta} \delta_{k_1+k_2+k_3+k_4}, \quad (\text{C.5})$$

where  $V_{\alpha k_1, \beta k_2}$  is the matrix element of scattering between electron states  $(\beta, \mathbf{k}_2)$  and  $(\alpha, \mathbf{k}_1)$  in zero magnetic field,  $k_j$  ( $j = 1, \dots, 4$ ) are wave vectors in the plane of a 2D system,  $N_{\text{imp}}$  is the two-dimensional density of impurities, and the angle brackets stand for the averaging over impurity spatial distribution. The Cooperons  $C_{\gamma\delta}^{(2)\alpha\beta}(\boldsymbol{\rho}, \boldsymbol{\rho}')$  and  $C_{\gamma\delta}^{(3)\alpha\beta}(\boldsymbol{\rho}, \boldsymbol{\rho}')$  represent the sums of internal parts of the fan diagrams starting with two and three lines, respectively.<sup>125,127,128</sup> They can be found from the following equations:

$$\begin{aligned} C_{\gamma\delta}^{(2)\alpha\beta}(\boldsymbol{\rho}, \boldsymbol{\rho}') &= \sum_{\nu\mu} W_{\gamma\mu}^{\alpha\nu} W_{\mu\delta}^{\nu\beta} P(\boldsymbol{\rho}, \boldsymbol{\rho}') \\ &+ \sum_{\nu\mu} W_{\gamma\mu}^{\alpha\nu} \int P(\boldsymbol{\rho}, \boldsymbol{\rho}') C_{\mu\delta}^{(2)\nu\beta}(\boldsymbol{\rho}'', \boldsymbol{\rho}') d\boldsymbol{\rho}', \\ C_{\gamma\delta}^{(3)\alpha\beta}(\boldsymbol{\rho}, \boldsymbol{\rho}') &= C_{\gamma\delta}^{(2)\alpha\beta}(\boldsymbol{\rho}, \boldsymbol{\rho}') - \sum_{\nu\mu} W_{\gamma\mu}^{\alpha\nu} W_{\mu\delta}^{\nu\beta} P(\boldsymbol{\rho}, \boldsymbol{\rho}') \end{aligned} \quad (\text{C.6})$$

where  $P(\boldsymbol{\rho}, \boldsymbol{\rho}') = G^A(\boldsymbol{\rho}, \boldsymbol{\rho}') G^R(\boldsymbol{\rho}, \boldsymbol{\rho}')$ .

It is assumed that the impurity potential is the same for particles in different valleys and, thus, the electron scattering in the valleys is strongly correlated. In particular, in the (001)-oriented Si-based structures the nonzero correlators are

$$W_{11}^{11} = W_{22}^{22} = W_{11}^{22} = W_{22}^{11}, \quad W_{12}^{21} = W_{21}^{12}. \quad (\text{C.7})$$

Other correlators vanish due to averaging over the impurity positions because the lowest conduction-band valleys in silicon are located in the  $\Delta$ -points of the Brillouin zone and, therefore, the Bloch functions contain oscillatory factors. The intravalley and intervalley scattering times are determined by these correlators:  $1/\tau_i = m^*W_{11}^{11}/\hbar^3$ ,  $1/\tau_V = m^*W_{12}^{21}/\hbar^3$ . Using the standard procedure (see Refs. 127 and 130), one can expand  $P(\boldsymbol{\rho}, \boldsymbol{\rho}')$  and the Cooperons in the series of eigenfunctions of a particle with the double charge in a magnetic field and derive equations for the WL correction  $\Delta\sigma^{(a)}$  and  $\Delta\sigma^{(b)}$ .

Calculations show that the correction have the form

$$\Delta\sigma^{(a)} = -\frac{e^2b}{2\pi^2\hbar} \sum_{N=0}^{\infty} C_N P_N^2, \quad (\text{C.8})$$

$$\Delta\sigma^{(b)} = \frac{e^2b}{2\pi^2\hbar} \sum_{N=0}^{\infty} (C_N + C_{N+1}) Q_N^2 / 2, \quad (\text{C.9})$$

$$C_N = \frac{2(1+\tau/\tau_V)}{1-(1-\tau/\tau_V)P_N} + \frac{P_N}{1-P_N} - \frac{(1-2\tau/\tau_V)^3 P_N}{1-(1-2\tau/\tau_V)P_N}, \quad (\text{C.10})$$

where  $P_N$  and  $Q_N$  are coefficients which are given by

$$\begin{aligned} P_N &= \sqrt{\frac{2}{b}} \int_0^{\infty} \exp\left[-x\sqrt{\frac{2}{b}}\left(1+\frac{\tau}{\tau_\phi}\right) - \frac{x^2}{2}\right] L_N(x^2) dx, \\ Q_N &= \sqrt{\frac{2}{b}} \int_0^{\infty} \exp\left[-x\sqrt{\frac{2}{b}}\left(1+\frac{\tau}{\tau_\phi}\right) - \frac{x^2}{2}\right] \frac{L_N^1(x^2)}{\sqrt{N+1}} dx, \end{aligned} \quad (\text{C.11})$$

here  $L_N$  and  $L_N^1$  are the Laguerre polynomials.

## References

- 
- <sup>1</sup> Bardeen J., Brattain W. H., Phys. Rev. **71**, 230 (1948).
  - <sup>2</sup> Schockley W., Bell Syst. Tech. J. **28**, 435 (1949).
  - <sup>3</sup> Bardeen J., Brattain W. H., Phys. Rev. **71**, 230 (1948).
  - <sup>4</sup> Calaeys C., Simoen E., “Germanium-based thecnology. From material to devices.” (Eslsevier, 2007).
  - <sup>5</sup> P. Bai, et al., 65 nm Logic Technology Featuring 35 nm Gate Lengths, Enhanced Channel Strain, 8 Cu Interconnect Layers, Low-k ILD, and 0.57  $\mu\text{m}^2$  SRAM Cell (*IEDM Proceedings*, 2004).
  - <sup>6</sup> Ando T., Fowler A. B., Stern F., Rev. Mod. Phys. **54**, 437 (1982).
  - <sup>7</sup> Abrahams E., Anderson P. W., Licceardello D. C., Ramakrishnan T. V., Phys. Rev. Lett. **42**, 673 (1979).
  - <sup>8</sup> Anderson P.W., Abrahams E. and Ramakrishnan T.V., Phys. Rev. Lett. **43**, 718 (1979); Gor'kov L.P., Larkin A.I. and Khmel'nitskii D.E., Zh. Eksp. Teor. Fiz. Pis'ma Red. **30**, 248 (1979) [JETP Lett. **30**, 248 (1979)].
  - <sup>9</sup> Altshuler B. L. and Aronov A. G., in *Electron-Electron Interactions in Disordered Systems*, edited by A.L. Efros and M. Pollak (North-Holland, Amsterdam, 1985); Solid State Comm. **46**, 429 (1983); Altshuler B. L., Aronov A. G., Lee P. A., Phys. Rev. Lett. **44**, 1288 (1980);
  - <sup>10</sup> Finkel'stein A. M., Zh. Eksp. Teor. Fiz. **84**, 168 (1983) [Sov. Phys. JETP **57**, 97 (1983)]; Z. Phys. B **56**, 189-196 (1984); Sov. Sci. Rev. A **14**, 3 (1990).
  - <sup>11</sup> Altshuler B. L., Aronov A. G., Gershenson M. E., and Sharvin Yu. V., Sov. Sci. Rev A Phys **9**, 223-354 (1987).
  - <sup>12</sup> Zavaritskaya T. N., Zavaritskaya E. I., Zh. Eksp. Teor. Fiz. **45**, 476 (1987); [Sov. Phys. JETP Lett. **45**, 609 (1987)].
  - <sup>13</sup> Kravchenko S. V., Kravchenko G. V., Furneaux J. E., Pudalov V. M., and D'Iorio M., Phys. Rev. B **50**, 8039 (1994); Kravchenko S. V., Mason W. E., Bowker G. E., Furneaux J. E., Pudalov V. M., and D'Iorio M., Phys. Rev. B **51**, 7038 (1995).
  - <sup>14</sup> Simonian D., Kravchenko S. V., Sarachik M. P., and Pudalov V. M., Phys. Rev. Lett. **79**, 2304 (1997).

- 
- <sup>15</sup> Pudalov V. M., Brunthaler G., Prinz A., and Bauer G., Pis'ma Zh. Eksp. Teor. Fiz. **65**, 887 (1997) [JETP Lett. **65**, 932 (1997)].
  - <sup>16</sup> Okamoto T., Hosoya K., Kawaji S., and Yagi A., Phys. Rev. Lett. **82**, 3875 (1999).
  - <sup>17</sup> Mertes K. M., Sharachik M. P., Kravchenko S. V., Klapwijk T. M., Phys. Rev. B **60**, R5093 (1999).
  - <sup>18</sup> Eng K., Feng X. G., Popovic' D., Washburn S., Phys. Rev. Lett. **88**, 136402 (2002).
  - <sup>19</sup> Yoon J., Li C. C., Shahr D., Tsui D. C., Shayegan M., Phys. Rev. Lett. **84**, 4221 (2000).
  - <sup>20</sup> Popovic' D., Fowler A. B., and Washburn S., Phys. Rev. Lett. **79**, 1543 (1997); Li K. P., Popovic' D., Washburn S., in *Proceedings EP2DS-12*, Tokyo (1997).
  - <sup>21</sup> Hanein Y., Meirav U., Shahr D., Li C. C., Tsui D. C., and Shtrikman H., Phys. Rev. Lett. **80**, 1288 (1998); Hanein Y., Shahr D., Yoon J., Li C. C., Tsui D. C., and Shtrikman H., Phys. Rev. B **56**, R7520 (1998); Hamilton A. R., Simmons M. Y., Pepper M., Linfield E. H., Rose P. D., and Ritchie D. A., Phys. Rev. Lett. **82**, 1542 (1999); Mills A. P., Ramirez A. P., Pfeiffer L.N., and West K., preprint cond-mat/9905176.
  - <sup>22</sup> Simmons M. Y., Hamilton A. R., Pepper M., Linfield E. H., Rose P. D., Ritchie D. A., Savchenko A. K., and Griffiths T. G., Phys. Rev. Lett. **80**, 1292, (1998); Yoon J., Li C. C., Shahr D., Tsui D. C., And Shayegan M., Phys. Rev. Lett. **82**, 1744 (1999).
  - <sup>23</sup> Papadakis S. J., De Poortere E. P., Manoharan H. C., Shayegan M., and Winkler R., Science **283**, 2056 (1999).
  - <sup>24</sup> Hanein Y., Shahr D., Shtrikman H., Yoon J., Li C. C., and Tsui D. C., Nature **400**, 735 (1999).
  - <sup>25</sup> Hanein Y., Shahr D., Yoon J., Li C. C., Tsui D. C., and Shtrikman H., Phys. Rev. B **58**, R13338 (1998).
  - <sup>26</sup> Ribeiro E., Jaggi R. D., Heinzl T., Ensslin K., Medeiros-Ribeiro G., and Petroff P. M., Phys. Rev. Lett. **82**, 996 (1999).
  - <sup>27</sup> Coleridge P. T., Williams R. L., Feng Y., and Zawadzki P., Phys. Rev. B **56**, R12764 (1997); Lam J., D'Iorio M., Brown D., and Lafontaine H., Phys. Rev. B **56**, R12741 (1997).
  - <sup>28</sup> Brunthaler G., Prinz A., Pillwein G., Bauer G., Brunner K., Abstreiter G., Dietl T. and Pudalov V. M., in Proc. ICPS-25 (Berlin, Springer-Verlag, 2001) p.785.

- 
- <sup>29</sup> Coleridge P. T., Zawadzki P., Sachrajda A., Feng Y., and Williams R. L., preprint cond-mat/9909292.
- <sup>30</sup> Papadakis S. J. and Shayegan M., Phys. Rev. B **56**, R15068 (1998).
- <sup>31</sup> Brunthaler G., Prinz, A. Pillwein G., Bauer G., Pudalov V. M., Lindelof P. E. and Ahopelto J., Physica E **13**, 691 (2002).
- <sup>32</sup> Stern F., Phys. Rev. Lett. **44**, 1469 (1980).
- <sup>33</sup> Gold A., Dolgoplov V. T., J. Phys. C **18**, L463 (1985); Phys. Rev. B **33**, 1076 (1986).
- <sup>34</sup> Das Sarma S., Phys. Rev. B **33**, 5401 (1986).
- <sup>35</sup> Zala G., Narozhny B. N., Aleiner I. L., Phys. Rev B **64**, 214204 (2001); Phys. Rev. B **65**, 020201(R) (2001); Phys. Rev. B **65**, 180202 (2002).
- <sup>36</sup> Friedel J., Phys. Mag. **43**, 153 (1952); Mahan G., Many Particle Physics. (Plenum, New York, 1990).
- <sup>37</sup> Gornyi I. V., Mirlin A. D., Phys. Rev. B **69**, 045313 (2004).
- <sup>38</sup> Punnoose A. and Finkel'stein A. M., Phys. Rev. Lett. **88**, 016802 (2002); Science **310**, 289 (2005).
- <sup>39</sup> Kuntsevich Yu. A., Klimov N. N., Tarasenko S. A., Averkiev N. S., Pudalov V. M., Kojima H., Gershenson M. E., Phys. Rev. B **75**, 195330 (2007).
- <sup>40</sup> Klimov N. N., Knyazev D. A., Omel'yanovskii O. E., Pudalov v. M., Kojima H., Gershenson M. E., ArXiv.0809.2750v1.
- <sup>41</sup> Pudalov V. M., Gershenson M. E., Kojima H., Butch N., Dizhur E. M., Brunthaler G., Prinz A., Bauer G., Phys. Rev. Lett. **89**, 196404 (2002).
- <sup>42</sup> Fukuyama H., J. Phys. Soc. Japan **48**, 2169 (1980).
- <sup>43</sup> Gor'kov L.P., Larkin A.I. and Khmel'nitskii D.E., Zh. Eksp. Teor. Fiz. Pis'ma Red. **30**, 248 (1979) [JETP Lett. **30**, 248 (1979)].
- <sup>44</sup> Bergmann G., Phys. Rep. **107**, 1 (1984).
- <sup>45</sup> Hikami S, Larkin A. I., Nagaoka Y., Prog. Theor. Phys. **63**, 707 (1980).
- <sup>46</sup> Mott. N. F., Metal-Insulator Transitions. (London, Tailor & Hobson, 1990).
- <sup>47</sup> Mott N. F., Phil. Mag. **22**, 7 (1970).
- <sup>48</sup> Anderson, P. W., Phys. Rev. **109**, 1498 (1958).
- <sup>49</sup> Thouless D. J., Phys. Rep. (Phys. Lett. C) **13**, 93 (1974); Phys. Rev. Lett. **39**, 1169 (1977).

- 
- <sup>50</sup> Wegner F. J., Phys. Rev. B **19**, 783 (1979).
- <sup>51</sup> Vollhardt D., Wölfle P., Phys. Rev. Lett. **45**, 842 9 (1980); Phys. Rev. B **22**, 4666 (1980).
- <sup>52</sup> Pudalov V.M., D'Iorio M., Campbell J.W., Kravchenko S.V., Phys. Rev. Lett. **70**, 1866 (1993).
- <sup>53</sup> Landau L. D., Zh. Eksp. Teor. Fiz. **32**, 59 (1957) [Sov. Phys. JETP **3**, 920 (1957)].
- <sup>54</sup> Wigner E., Phys. Rev. B **46**, 1002 (1934).
- <sup>55</sup> Shklovskii B. I. and Efros A. L., *Electron Properties of Doped Semiconductors* (Springer, 1984).
- <sup>56</sup> Tanatar B. and Ceperley D. M., Phys. Rev. B **39**, 5005 (1989).
- <sup>57</sup> Stoner E. C., Rep. Prog. Phys. **11**, 43-112 (1947).
- <sup>58</sup> Attacalite B. C., Moroni S., Gori-Georgi P., Bachelet G., Phys. Rev. Lett. **88**, 256601 (2002).
- <sup>59</sup> Spivak B., Phys. Rev. B **67**, 125205 (2003).
- <sup>60</sup> Das Sarma S and Hwang E. H., Phys. Rev. Lett. **83**, 164 (1999); Phys. Rev. B **69**, 195305 (2004).
- <sup>61</sup> Knyazev D. A., Omel'yanovskii O. E., Pudalov V. M., Burmistrov I.S., JETP Lett. **84**, 662 (2006).
- <sup>62</sup> Anissimova S., Kravchenko S. V., Punnoose A., Finkel'stein A. M., Klapwijk T. M., Nature Phys. **3**, 707 (2007).
- <sup>63</sup> Knyazev D. A., Omel'yanovskii O. E., Pudalov V. M., Burmistrov, Phys. Rev. Lett. **100**, 046405 (2008).
- <sup>64</sup> Castellani C., Di Castro C., Lee P. A., Ma M., Phys. Rev. B **30**, 527 (1984).
- <sup>65</sup> Castellani C., Di Castro C., Lee P. A., Phys. Rev. B **57**, 9381 (1998).
- <sup>66</sup> Vitkalov S. A., James K., Narozhny B. N., Sarachik M. P., Klapwijk T. M., Phys. Rev. B **67**, 113310 (2003).
- <sup>67</sup> Burmistrov I. S., Chetchevkatchev N. M., JETP Lett. **84**, 558 (2006); Phys. Rev. B **77**, 195319 (2008).
- <sup>68</sup> Kahng D. and Atalla M. M., "Silicon-Silicon Dioxide Surface Device," in *IRE Device Conference*, Pittsburgh, 1960.

- 
- <sup>69</sup> Schrieffer, J. R., 1957, "Mobility in inversion layers: Theory and experiment," in *Semiconductor Surface Physics*, edited by Kingston R. H. (University of Pennsylvania Press, Philadelphia), pp. 55-69.
- <sup>70</sup> Sze S. M., Kwon K. Ng, *Physics of Semiconductor Devices*. (John Wiley & Sons, Inc., 3<sup>rd</sup> edition, 2007).
- <sup>71</sup> Stern F., Howard W. E., *Phys. Rev.* **163**, 816 (1967).
- <sup>72</sup> Bishop D. J., Tsui D. C., and Dynes R. C., *Phys. Rev. Lett.* **44**, 1153 (1980).
- <sup>73</sup> Uren M. J., Davies R. A., Kaveh M., and Pepper M., *J. Phys. C* **14**, 5737 (1981).
- <sup>74</sup> Kawaguchi Y., Kawaji S., *J. Phys. Soc. Jpn.* **48**, 699 (1980); **53**, 2868 (1984).
- <sup>75</sup> Wheeler R. G., *Phys. Rev. B* **24**, 4645 (1981).
- <sup>76</sup> Davies R. A., Pepper M., *J. Phys. C* **16**, L353 (1983).
- <sup>77</sup> Dolgoplov V. T., Dorozhkin S. I., Shashkin A. A., *Sol. State Commun.* **50**, 273 (1984).
- <sup>78</sup> Burdis M. S., Dean C. C., *Phys. Rev.* **15**, 3269 (1988).
- <sup>79</sup> Bishop D. J., Tsui D. C., and Dynes R. C., *Phys. B* **26**, 773 (1982).
- <sup>80</sup> Cham K. M., Wheeler R. G., *Phys. Rev. Lett.* **44**, 1472 (1980).
- <sup>81</sup> Fowler A. B., *Phys. Rev. Lett.* **34**, 15 (1975).
- <sup>82</sup> Kawaguchi Y., Suzuki T., Kawaji S., *Sol State Comm.* **36**, 257 (1980).
- <sup>83</sup> Dorozhkin S. I., Dolgoplov V. T., *JETP Lett.* **40**, 1019 (1984).
- <sup>84</sup> Smith, Stiles, *Sol. State Commun.* **58**, 511 (1986).
- <sup>85</sup> Virodov E. A., Dolgoplov V. T., Dorozhkin S. I., Zhitenev N. B., *Sov. Phys. JETP Lett.* **67**, 998 (1988).
- <sup>86</sup> Mott N. F., *Adv. Phys.* **16**, 49 (1976); Mott N. F., Davis E. A., *Electronic Processes in Non-Crystalline Material*, Oxford press, New York, (1979).
- <sup>87</sup> Pudalov V. M., cond-mat/0405315.
- <sup>88</sup> Pudalov V. M., Brunthaler G, Prinz A., Bauer G, *Physica E* **3**, 79 (1998).
- <sup>89</sup> Simonian K. M., Sarachik M. P., Kravchenko S. V., Klapwijk T. M., *Phys. Rev. B* **60**, 5093 (1999).
- <sup>90</sup> Vitkalov S. A., Zheng H., Mertes K. M., Sarachik M. P., and Klapwijk T. M., *Phys. Rev. Lett.* **85**, 2164 (2000).
- <sup>91</sup> Vitkalov S. A., Sarachik M. P., and Klapwijk T. M., *Phys. Rev. B* **64**, 073101 (2001).

- 
- <sup>92</sup> Pudalov V. M., Brunthaler G., Prinz A., Bauer G., Phys. Rev. Lett. **88**, 076401 (2002).
- <sup>93</sup> Pudalov V. M., Brunthaler G., Prinz A., Bauer G., cond-mat/0103087.
- <sup>94</sup> Simmons M. Y. *et al.*, Phys. Rev. Lett. **80**, 1292 (1998).
- <sup>95</sup> “Magnetoresistance of RuO<sub>2</sub>-based resistance thermometer below 0.3K”, by Watanabe *et al.*, Cryogenics **41**, 143 (2001).
- <sup>96</sup> Briggs A., “Characterization of RO chip resistors at low temperatures,” Cryogenics **31**, 932 (1991).
- <sup>97</sup> Uhlig K., “Magnetoresistance of thick-film chip resistors at millikelvin temperatures,” Cryogenics **35**, 525 (1995).
- <sup>98</sup> Gershenson M. E., Pudalov V. M., Kojima H., Butch N., Dizhur E. M., Brunthaler G., Prinz A., Bauer G., Physica E **12**, 585 (2002).
- <sup>99</sup> Lifshitz I.M., Kosevich A.M., Zh. Eksb. Teor. Fiz. **29**, 730 (1955); Isihara A., SmrWcka L., J. Phys. C **19**, 6777 (1986).
- <sup>100</sup> Prus O., Reznikov M., Sivan U., Pudalov V. M., Phys. Rev. Lett. **88**, 016801 (2002).
- <sup>101</sup> Pudalov V. M., Punnoose A., Brunthaler G., Prinz A., Bauer G., cond-mat/0104347.
- <sup>102</sup> Pudalov V. M., Semenchinskii S. G., Edelman V. S., Pis'ma v ZhETF, **41**(6), 265 (1985). [JETP Lett. **41**, 325 (1985)].
- <sup>103</sup> Pudalov V. M., Gershenson M. E., Kojima H., cond-mat/0110160.
- <sup>104</sup> Fang F. F., Stiles P. J., Phys. Rev. **174**, 823 (1968).
- <sup>105</sup> Shashkin A. A., Kravchenko S. V., Dolgoplov V. T., Klapwijk T. M., Phys. Rev. Lett. **87**, 086801 (2001).
- <sup>106</sup> Vitkalov S. A., Sarachik M. P., Klapwijk T. M., Phys. Rev. B **65**, 201106R (2002).
- <sup>107</sup> Vitkalov S. A., Zheng H., Mertes K. M., Sarachik M. P., and Klapwijk T. M., Phys. Rev. Lett. **87**, 086401 (2001).
- <sup>108</sup> Prus O., Yaish Y., Reznikov M., Sivan U., and Pudalov V. M., Phys. Rev. B **67**, 205407 (2003).
- <sup>109</sup> Shashkin A. A., Anissimova S., Kravchenko S. V., Dolgoplov V. T., Klapwijk T. M., Phys. Rev. Lett. **96**, 03403 (2006).
- <sup>110</sup> Anissimova S., Venkatesan A., Shashkin A. A., Sakr M. R., Kravchenko S. V., Phys. Rev. Lett **96**, 046409 (2006).
- <sup>111</sup> Fang F. F., Fowler A. B, Hartstein A., Phys. Rev. B **16**, 4446 (1977).



- 
- <sup>112</sup> Smith J. L., Stiles P. J., Phys. Rev. Lett **29**, 102 (1972).
- <sup>113</sup> Pan W., Tsui D. C., Draper B. L., Phys. Rev. B **59**, 10208 (1999).
- <sup>114</sup> Shashkin A. A., Rahimi M., Anissimova S. , Kravchenko S.V., Dolgoplov V.T., and Klapwijk T.M., Phys. Rev. Lett. **91**, 046403 (2003).
- <sup>115</sup> Pudalov V. M., Gershenson M. E., Kojima H., cond-mat/0401396; “On the Electron-Electron Interactions in Two Dimensions”, Chapter in: “Fundamental problems of mesoscopic physics”, Ed. by I. Lerner, B. Altshuler, and Y. Gefen, p.309-327 (Kluwer Academic Publ., Boston/London 2004).
- <sup>116</sup> G. W. Martin, D. L. Maslov, M. Yu. Reizer, Phys. Rev. B **68**, 241309 (2003).
- <sup>117</sup> Adamov Y., Gornyi I. V., Mirlin A. D., Phys. Rev. B **73**, 045426 (2006).
- <sup>118</sup> Altshuler B. L., Aronov A. G., Larkin A. I., and Khmel'nitskii D. E., Zh. Eksp. Teor. Fiz. **81**, 768 (1981); Sov. Phys. JETP **54**, 411 (1981).
- <sup>119</sup> Brunthaler G., Prinz A., Bauer G., Pudalov V. M., Phys. Rev. Lett. **87**, 096802 (2001).
- <sup>120</sup> Rahimi M., Anissimova S., Sakr M. R., Kravchenko S. V., and Klapwijk T. M., Phys. Rev. Lett. **91**, 116402 (2003).
- <sup>121</sup> Minkov G. M., Germanenko A. V., and Gornyi I. V., Phys. Rev. B **70**, 245423 (2004).
- <sup>122</sup> Minkov G. M., Germanenko A. V., Rut O. E., Sherstobitov A. A., Larionova V. A., Bakarov A. K., Zvonkov B. N., Phys. Rev. B **74**, 045314 (2006).
- <sup>123</sup> Minkov G. M., Germanenko A. V., Rut O. E., Sherstobitov A. A., Zvonkov B. N., Phys. Rev. B **75**, 193311 (2007).
- <sup>124</sup> Wittman H-P. and Schmidt A., J. Low Temp. Phys. **69**, 131 (1987).
- <sup>125</sup> Dmitriev A. P., Kachorovskii V. Yu., and Gornyi I. V., Phys. Rev. B **56**, 9910 (1997).
- <sup>126</sup> Minkov G. M., Germanenko A. V., Larionova V. A., Negashev S. A., and Gornyi I. V., Phys. Rev. B **61**, 13164 (2000).
- <sup>127</sup> Gasparian V. M. and Zyuzin A. Yu., Fiz. Tverd. Tela (Leningrad) **27**, 1662 (1985); [Sov. Phys. Solid State **27**, 1580 (1985).]
- <sup>128</sup> Averkiev N. S., Golub L. E., Tarasenko S. A., and Willander M., Phys. Rev. B **64**, 045405 (2001).

- 
- <sup>129</sup> Mc Phail S., Yasin C. E., Hamilton A. R., Simmons M. Y., Linfield E. H., Pepper M., and Ritchie D. A., *Phys. Rev. B* **70**, 245311 (2004).
- <sup>130</sup> Kawabata A., *J. Phys. Soc. Jpn.* **53**, 3540 (1984).
- <sup>131</sup> Vakili K., Shkolnikov Y. P., Tutuc E., DePoortere E. P., and Shayegan M., *Phys. Rev. Lett.* **92**, 186404 (2004).
- <sup>132</sup> Takashina K., Fujiwara A., Horiguchi S., Takahashi Y., and Hirayama Y., *Phys. Rev. B* **69**, 161304R (2004).
- <sup>133</sup> Germanenko A. V., Minkov G. M., Sherstobitov A. A., and Rut O. E., *Phys. Rev. B* **73**, 233301 (2006).
- <sup>134</sup> Shashkin A. A., Kravchenko S. V., Dolgoplov V. T., Klapwijk T. M., *Phys. Rev. B* **66**, 073303 (2002).
- <sup>135</sup> Pudalov V. M., Gershenson M. E., Kojima H., Brunthaler G., Prinz A., and Bauer G., *Phys. Rev. Lett.* **91**, 126403 (2003).
- <sup>136</sup> Kunze and Lautz, *Surface Sci.* **143**, 314 (1984).
- <sup>137</sup> Huang J., Xia J. S., Tsui D. C., Pfeiffer L. N., and West K. W., *Phys. Rev. Lett.* **98**, 226801 (2007).
- <sup>138</sup> Gao Xuan P.A., Mills A. P., Ramirez A. P., Pfeiffer L. N., West K. W., *Phys. Rev. Lett.* **88**, 166803 (2002).
- <sup>139</sup> P.M. Mensz and R.G. Wheeler, *Phys. Rev. B* **35**, 2844 (1987).
- <sup>140</sup> H. Mathur and H.U. Baranger, *Phys. Rev. B* **64**, 235325 (2001).
- <sup>141</sup> G.M. Minkov *et al.*, *Phys. Rev. B* **70**, 035304 (2004).
- <sup>142</sup> J.S. Meyer, V.I. Fal'ko, and B.L. Altshuler, in NATO Science Series II, vol. 72, eds. I.V. Lerner, B.L. Altshuler, V.I. Fal'ko, and T. Giamarchi (Kluwer Academics, Dordrecht, 2002), pp. 117-164.
- <sup>143</sup> Kravchenko S. V., Shashkin A. A., Bloore D. A., Klapwijk T. M., *Solid Ste Comm.* **116**, 495 (2000).
- <sup>144</sup> Proskuryakov Y. Y., Savchenko A. K., Safonov S. S. *et al.*, *Phys. Rev. Lett.* **89**, 076406 (2002).
- <sup>145</sup> Zhu J., Stormer H. L., Pfeiffer L. N., *et al.*, *Phys Rev. Lett.* **90**, 056805 (2003).
- <sup>146</sup> Klapwijk T. M., Das Sarma S., *Solid State Commun.* **110**, 581 (1999).
- <sup>147</sup> Altshuler B. L., Maslov D. L., *Phys. Rev. Lett.* **83**, 2092 (1999).
- <sup>148</sup> Kozub V. I., Agrinskaya N. V., *Phys. Rev. B* **64**, 245103 (2001).

- 
- <sup>149</sup> Pudalov V. M., Brunthaler G., Prinz A., Bauer G., JETP Lett. **68**, 442 (1998).
- <sup>150</sup> Gold A., Götze W., Phys. Rev. B **33**, 2495 (1986).
- <sup>151</sup> Altshuler B. L., Maslov D. L., Pudalov V. M., Physica E **9**, 209 (2001).
- <sup>152</sup> Abrahams E., Kravchenko S., Sarachik M.P., Rev. Mod. Phys. **73**, 251 (2001).
- <sup>153</sup> Gold A., Dolgoplov V. T., Phys. Rev. Lett. **89**, 129701 (2002).
- <sup>154</sup> Kuntsevich A. Yu., Knyazev D. A., Kozub V. I., *et al.*, JETP Lett. **81**, 409 (2005).
- <sup>155</sup> Lewalle A., Pepper M., Ford C. J. B., *et al.*, cond-mat/0108244.
- <sup>156</sup> Meir Y., Phys. Rev. Lett. **83**, 3506 (1999).
- <sup>157</sup> Kornilov A. V., Pudalov V. M., Kitaoka Y., *et. al.*, Phys. Rev. B **69**, 224404 (2004).
- <sup>158</sup> Spivak B., Phys. Rev. B **64**, 085317 (2001).
- <sup>159</sup> Schoenberg D., Magnetic Oscillations in Metals, Cambridge University Press, Cambridge (1984).
- <sup>160</sup> Das Sarma S., and Stern F., Phys. Rev. B **32**, 8442 (1985).
- <sup>161</sup> Gold A., Phys. Rev. B **38**, 10798 (1988).
- <sup>162</sup> Gold A., Fabie L., Dolgoplov V. T., Appl. Phys. Lett. **91**, 052112 (2007).

## Curriculum Vitae

**Nikolai N. Klimov**

### EDUCATION

- 2000** B.Sc. in Applied Mathematics and Physics, *Summa Cum Laude Diploma*, Moscow Institute of Physics and Technology (The State University), Russia
- 2002** M.Sc. in Applied Mathematics and Physics, *Summa Cum Laude Diploma*, Moscow Institute of Physics and Technology (The State University), Russia
- 2008** Ph.D. in Physics, Rutgers, The State University of New Jersey

### PUBLICATIONS

1. *Interaction effects in the conductivity of a two-valley electron system in high-mobility Si inversion layers*  
Klimov N. N., Knyazev D. A., Omel'yanovskii O. E., Pudalov V. M., Kojima H., Gershenson M. E., preprint ArXiv.0809.2750v1, submitted to Phys. Rev. B.
2. *Intervalley scattering and weak localization in Si-based two-dimensional structures*  
 Kuntsevich Yu. A., Klimov N. N., Tarasenko S. A., Averkiev N. S., Pudalov V. M., Kojima H., Gershenson M. E., Phys. Rev. B **75**, 195330 (2007).
3. *Quenched disorder effects in electron transport in Si inversion layers in the dilute regime*  
 Pudalov V. M., Gershenson M. E., Klimov N. N., Kojima H., Pis'ma v ZhETF **82**, iss. 6, 412 (2005); [JETP **82**, iss. 6, p371, (2005)].
4. *Unexpected negative nonmonotonic magnetoresistance of the two-dimensional electrons in Si in a parallel magnetic field*  
 V.M. Pudalov V. M., Kirichenko A. S., Klimov N. N., Gershenson M. E., Kojima H., Pis'ma v ZhETF **80**, iss. 5, 408 (2004); [JETP, 80, iss. 5, p359 (2004)].